ABSTRACT

Title of dissertation: IDENTIFICATION OF STATE-SPACE ROTOR WAKE MODELS WITH APPLICATION TO COAXIAL ROTORCRAFT FLIGHT DYNAMICS AND CONTROL

Sean Hersey
Doctor of Philosophy, 2019

Dissertation directed by: Professor Roberto Celi
Department of Aerospace Engineering

Modern aerodynamic analysis tools, such as free-vortex wake models and CFD-based techniques, include fewer theoretical limitations and approximations than classical simplified schemes, and represent the state-of-the-art in rotorcraft aerodynamic modeling, including for coaxial and other advanced configurations. However, they are impractical or impossible to apply to many flight dynamics problems because they are not formulated in ordinary differential equation (ODE) form, and they are often computationally intensive. Inflow models, for any configuration type, that couple the accuracy of high-fidelity aerodynamic models with the simplicity and ODE form of dynamic inflow-type theories would be an important contribution to the field of flight dynamics and control. This dissertation presents the methodology for the extraction of linearized ODE models from computed inflow data acquired from detailed aerodynamic free-vortex wake models, using frequency domain system identification. These methods are very general and applicable to any aerodynamic

model, and are first demonstrated with a free wake model in hover and forward flight, for a single main rotor, and subsequently for the prediction of induced flow off the rotor as well, at locations such as the tail or fuselage.

The methods are then applied to the extraction of first order linearized ODE inflow models for a coaxial rotor in hover. Subsequent analysis concluded that free-vortex wake models show that the behavior of the inflow of a coaxial configuration may be higher-order. Also, tip-path plane motion of a coaxial rotor causes wake distortion which has an impact on the inflow behavior. Therefore, the methodology is expanded to the identification of a second order inflow representation which is shown to better capture from all of the relevant dynamics from free-vortex wake models, including wake distortion. With ODE models of inflow defined for an advanced coaxial configuration, this dissertation then presents a comparison of the fully-coupled aircraft flight dynamics, and the design of an explicit modeling-following feedback controller, with both a free-vortex wake identified model and a momentum theory based approach, concluding that accurate inflow modeling of coaxial rotor inflow is essential for investigation into the flight dynamics and control design of advanced rotor configurations.

IDENTIFICATION OF STATE-SPACE ROTOR WAKE MODELS WITH APPLICATION TO COAXIAL ROTORCRAFT FLIGHT DYNAMICS AND CONTROL

by

Sean Hersey

Dissertation submitted to the Faculty of the Graduate School of the
University of Maryland, College Park in partial fulfillment
of the requirements for the degree of
Doctor of Philosophy
2019

Advisory Committee:
Professor Roberto Celi, Chair/Advisor
Professor Inderjit Chopra
Professor James Baeder
Professor Robert Sanner
Professor Shapour Azarm

Acknowledgments

I would first like to thank my advisor, Dr. Roberto Celi, who first convinced me that helicopters are cooler than rockets (this is not an opinion; rockets are, in fact, very hot). His dedication and support means a lot to me. His joy and enthusiasm for research was contagious and motivational, even during tough times. His guidance was invaluable to this work, and in general to my development as a student.

This research was supported by the U.S. Army Aviation Development Directorate, under grant NNX13AR72A, Technical Monitor Dr. Mark B. Tischler. I would like to especially thank him for all his insight and advice, and also his previous work and expertise, without which this project would not have been possible. I'd also like to thank Dr. Ondrej Juhasz, also from the U.S. Army Aviation Development Directorate, for all of his incredible support.

I'd like to thank my friends and family for there love and support, and also their understanding as I embarked on this long journey. I am very grateful to Christine who provided me moral and emotional support throughout these years.

I'd like to thank the students and coworkers in the Alfred Gessow Rotorcraft Center for their help and support and general willingness to let me bounce ideas off them.

Lastly I'd like to thank God for giving me this opportunity to learn and understand, and I hope to be able to make something with this knowledge.

Thanks for all your encouragement!

Table of Contents

List of Tables

List of Figures

Nomenclature

$\boldsymbol{\cdots}$ Bold symbols indicate vector quantities

$[\cdot]$ indicates matrices

Subscripts and Superscripts

$(\cdot)^U$ Term corresponds to the upper rotor on a coaxial rotor

$(\cdot)^L$ Term corresponds to the lower rotor on a coaxial rotor

$(\cdot)_{ij}$ subscript indicates i$^{\text{th}}$ row and j$^{\text{th}}$ column element of the matrix

$(\cdot)_{eq}$ Term corresponds to the trim or equilibrium value

$\overset{*}{(\ )}$ $d(\ )/d\psi$, derivative with respect to azimuth

Symbols

$\boldsymbol{x}$ State vector

$\boldsymbol{y}$ Output vector; also state vector when $[C] = \mathbb{1}$

$\boldsymbol{u}$ Control vector

β Blade flap angle

β_0 Zeroth harmonic of the blade flap angle

β_{1S} First sine harmonic of the blade flap angle

β_{1C} First cosine harmonic of the blade flap angle

θ_0 Swashplate collective

θ_{1C} Swashplate longitudinal cyclic

θ_{1S} Swashplate lateral cyclic

$\boldsymbol{\theta}$ Array containing $\{\theta_0 \ \ \theta_{1S} \ \ \theta_{1C}\}^\intercal$ for single main rotor
or $\left\{\theta_0^U \ \ \theta_{1S}^U \ \ \theta_{1C}^U \ \ \theta_0^L \ \ \theta_{1S}^L \ \ \theta_{1C}^L\right\}^\intercal$ for coaxial rotor

$\Delta\boldsymbol{\theta}$ Perturbation of $\boldsymbol{\theta}$

$\overset{*}{\boldsymbol{\beta}}$ Array containing cyclic flap rates $\left\{\overset{*}{\beta}_{1s} \ \ \overset{*}{\beta}_{1c}\right\}^\intercal$ for single main rotor
or $\left\{\overset{*}{\beta}_{1S}^U \ \ \overset{*}{\beta}_{1C}^U \ \ \overset{*}{\beta}_{1S}^L \ \ \overset{*}{\beta}_{1C}^L\right\}^\intercal$ for coaxial rotor

ρ Air density

a Lift curve slope

c Blade chord

R Rotor radius

r Radial blade station; $\tilde{r} = r/R$

I_b Blade moment of inertia

γ Lock number; $= \rho a c R^4 / I_b$

e Hinge offset

N_b Rotor number of blades

A_b Planform area of a blade; $= c * R$ for rectangular blades

σ Solidity; $= N_b A_b / \pi R^2$

ψ Blade azimuth position

λ_i, v_i Induced velocity; $\tilde{v}_i = \lambda_i = v_i / \Omega R$

λ_0 Average induced inflow coefficient

λ_{1S} Lateral induced inflow coefficient

λ_{1C}	Longitudinal induced inflow coefficient
$\boldsymbol{\lambda}$	Array containing $\{\lambda_0 \;\; \lambda_{1S} \;\; \lambda_{1C}]^\intercal$ for single main rotor or $\left\{\lambda_0^U \;\; \lambda_{1S}^U \;\; \lambda_{1C}^U \;\; \lambda_0^L \;\; \lambda_{1S}^L \;\; \lambda_{1C}^L\right\}^\intercal$ for a coaxial rotor
$\Delta\boldsymbol{\lambda}$	Perturbation of $\boldsymbol{\lambda}$
$\boldsymbol{\lambda}_{eq}$	Equilibrium or trim value of $\boldsymbol{\lambda}$
$[M]$	Induced inflow M matrix
$[L]^{-1}$	Inverse of induced inflow L matrix ($[L_{nl}]^{-1}$ non-linear version)
C_T	Aerodynamic rotor thrust coefficient; $T/\rho\pi R^2(\Omega R)^2$
C_L	Aerodynamic rotor roll moment; $L/\rho\pi R^3(\Omega R)^2$
C_M	Aerodynamic rotor pitch moment coefficient; $M/\rho\pi R^3(\Omega R)^2$
$\Delta C_T, \Delta C_L, \Delta C_M$	Thrust, roll and pitch perturbation
$\mathbf{C}$	Array containing $\{C_T \;\; C_L \;\; C_M\}^\intercal$ for single main rotor and $\left\{C_T^U \;\; C_L^U \;\; C_M^U \;\; C_T^L \;\; C_L^L \;\; C_M^L\right\}^\intercal$ for coaxial main rotor
$\Delta\mathbf{C}$	Perturbation of $\mathbf{C}$
$\mathbf{C}_{eq}$	Equilibrium or trim value of $\mathbf{C}$
$[\tau]$	Time delay matrix
μ	Advance ratio
ρ	Air density
σ	Rotor solidity ($N_b c/\pi R$)
ψ_n,$\bar{\psi}$	The n^{th} blade azimuth angle; $\bar{\psi} = \tilde{\omega}\psi_1$
Ω	Rotor angular velocity (rad/sec)
H_{uy}	Frequency response of input u to output y
$\hat{H}_{uy}$	Approximate frequency response of input u to output y
G_{uy}	Spectral density of u to y
$\hat{G}_{uy}$	Approximate spectral density of u to y
γ_{uy}	Coherence from input u to output y
$[T]$	Transfer function matrix
J	Frequency response fitting cost function
θ_0^S	Symmetric swashplate collective
θ_0^D	Differential swashplate collective
θ_{1C}^S	Symmetric swashplate longitudinal cyclic
θ_{1S}^S	Symmetric swashplate lateral cyclic
$\bar{v}_x$	x-component of non-dim. off-rotor inflow
$\bar{v}_y$	y-component of non-dim. off-rotor inflow
$\bar{v}_z$	z-component of non-dim. off-rotor inflow
$\bar{\boldsymbol{v}}$	Vector containing $\{\bar{v}_x \;\; \bar{v}_y \;\; \bar{v}_z\}^\intercal$
ζ	Damping ratio

List of Abbreviations

ODE	Ordinary differential Equation
PDE	Partial Differential Equation
S.S.	State space
MFW	Maryland Free Wake
RFW	RAPiD Free Wake
VTM	Vorticity Transport Model
VVPM	Viscous Vortex Particle Method
BEMT	Blade Element Momentum Theory
CFD	Computational Fluid Dynamics
HeliUM	Helicopter University of Maryland flight dynamics simulation
DDE	Delay differential equation
CIFER	Comprehensive Identification from Frequency Responses software package
SISO	Single Input Single Output
SIMO	Single Input Multiple Output
MIMO	Multiple Input Multiple Output
D.C.	Dynamic Climb inflow model
EMF	Explicit Model Following Control Architecture
PID	Proportional Integral Derivative feedback controller
DMO	Design Margin Optimization
GM	Gain Margin
PM	Phase Margin
DRB	Disturbance Rejection Bandwidth
DRP	Disturbance Rejection Peak

Chapter 1: Introduction

The next generation of military and commercial rotorcraft is expected to reach substantially higher speeds than platforms currently in production, through the use of advanced configurations. One possible configuration is a coaxial helicopter with thrust and/or lift compounding, obtained through the addition of pusher propellers and/or wings.

1.1 Coaxial Rotorcraft

Coaxial helicopters have their rotors placed in a specific configuration in which the two rotors lie on the same axis of rotation, yet spin in opposite directions. Because coaxial rotors spin in opposite directions, they can provide a rotor system that has zero net torque on the aircraft, provided that each rotor is operated at the same torque, or equivalently power (assuming equivalent rotor RPM). Conversely, the coaxial rotor can induce a yaw moment on the aircraft by modifying the controls to produce dissimilar rotor torques. This affords them one advantage over conventional single main rotor helicopters by not requiring a tail rotor for anti-torque. The second advantage is that two combined rotors tend to have high solidity which results in rotors that have a smaller radii for a given weight and therefore aircraft

may have a smaller footprints. These benefits historically come at the cost higher complexity of the rotor and transmission system, and higher hub drag reducing the efficiency of the rotorcraft. Traditional coaxial rotors have flap hinges and so the rotors have to be sufficiently separated to avoid rotor on rotor blade strikes during maneuvers. This leads to rather large and unwieldy rotor hubs with complicated swashplate assemblies.

More recently, Lift-offset coaxial rotorcraft have been gaining interest. Lift-offset coaxial rotorcraft typically forgo the flap hinge in favor of stiff hingeless blades. This allows for the rotors to be much more closely spaced, as the amount of flapping observed is much smaller, reducing their ability to strike a blade of the other rotor. This also allows for the hub to be much more compact due to its overall height being reduced, which leads to better aerodynamic qualities. The advantages of lift offset in forward flight was first shown with the Sikorsky Advancing Blade Concept [1, 2]. Lift offset refers to an offset in the location of the center of lift of each rotor. A rotor that is moment balanced can be described as having its center of lift at the center of rotation. A rotor that is carrying a lateral moment would have its center of lift laterally offset to the left or right side, depending on the sign of the roll moment. Lift offset for coaxial rotors almost always refers to lateral lift offset.

With a lateral lift offset, the advancing side of the rotors are allowed to carry more lift than the retreating side. In forward flight, this allows the rotor to not balance the natural dissymmetry of lift experienced by each rotor, and instead just balance the total moment experienced by both rotors. Unlike single main rotors, their maximum speed is not limited by retreating blade stall. Lift offset allows an

increased stall margin on each rotor, which in turn increases efficiency in forward flight. The difficulties with such a design tend to involve creating blades that are strong and stiff enough. Not only do the blades not have flap hinges, and so must carry the entire coning moment, but they also must be able to handle large one per rev bending moments in forward flight to achieve lateral lift offset. Recent advances in design have made it feasible and worthwhile to overcome the challenges of coaxial rotors, including the higher complexity, hub drag, flap bending moments and vibratory loads. Very recently, Sikorsky has demonstrated various lift offset coaxial rotorcraft, including the X-2 Technology demonstrator [3–5], the S-97 Raider [6], and the SB>1 Defiant [7].

Significant gaps remain in the fundamental understanding of coaxial compound rotorcraft configurations. Strong aerodynamic interactions exist between the two rotors, and between the rotors, empennages, and pusher propeller. The role of these interactions in steady flight and maneuvers has not been studied in depth and is not fully understood. Additionally, compound configurations create control redundancy and possibly novel strategies to trim and perform maneuvers. There have been studies into the performance, structural load, and vibratory loads of coaxial helicopter, but not so many studies into the flight dynamics and control characteristics of coaxial rotor, due to difficulties in this field of analysis.

There are three broad categories of analysis that provide solutions of the equations of motion, and are applicable to all helicopters. These are:

1. Steady-state analysis

2. Transient analysis

3. Linearized analysis

1.1.1 Steady-State Analysis

Steady state analysis refers to the calculation of a steady-state equilibrium condition, or trim. The equations of motion are formulated as a system of nonlinear algebraic equations. One or more solutions can be found that satisfy these equations. Because the solution is steady, equations of motion that are expressed as ordinary differential equations (ODE) can have their state derivatives set to zero. Equations of motion that are in partial differential equation (PDE) can be used so long as they can be time marched to a steady (or periodically steady) solution. This includes higher order aerodynamic models that model the flow-field in time and space. If the PDE can be time marched to a steady solution that is consistent with the steady solution of the remaining equations of motion, then a trimmed state is achieved. Therefore, many types of equations of motion may be used and it is not required that the mathematical model be in ODE form.

Steady state analysis is useful for a wide array of calculations necessary for the design and analysis of helicopters. A trimmed solution provides the performance of an aircraft at each steady flight condition. It also can provide steady and vibratory load predictions on the helicopter components (blades, pitch links, shaft, etc). Likewise it will calculate the blade flap, lag and pitch bending (or rotation with a

hinge) in the non-rotating frame. It can provide estimates of the vibration that the pilot may experience.

1.1.2 Transient Analysis

Transient analysis describes the solution of the equations of motion in time. The equations for the helicopter are formulated as a system of ordinary differential equations. Various algorithms exist to march these equations forward in time, primarily ODE solvers. Higher aerodynamic models in PDE form typically have their own solvers allowing a time-marching solution in time and space. These can often be time-marched in parallel, with information being passed between the different algorithms at discrete time steps, allowing the two algorithms to simultaneously solve all of the equations of motion, both the ODEs and PDEs.

These solutions are useful for a different set of explorations into helicopter capabilities. Transient analysis is useful for determining the time histories of aircraft responses to pilot inputs or to gusts. It is useful for verification of control systems by checking that the aircraft behaves as expected when trying to follow a given trajectory. It is useful for simulating unsteady maneuvers that can not be characterized by trim. It, in general, allows exploration of any operation a helicopter can perform in the time domain.

1.1.3 Linearized Analysis

Linearized Analysis allows for exploration of behavior in the frequency domain. Linearized analysis is a procedure that calculates linear perturbation models through finite difference calculations about a given equilibrium condition. This is essential for describing how the helicopter behaves when it is disturbed a small amount from the trim condition found through steady state analysis. The form of the state-space linear perturbation model is given by Eq.(1.1):

$$\dot{\boldsymbol{y}} = [A]\boldsymbol{y} + [B]\boldsymbol{u} \tag{1.1}$$

The state-vector $\boldsymbol{y}$ for a helicopter contains the body velocities, body rates, Euler angles, rotor states and inflow states (if the inflow system is in state-space form). The control vector $\boldsymbol{u}$ contains the rotor controls and other optional controls such as propeller, tail elevator, or tail rotor controls. The derivation for identifying the state and control matrices ($[A]$ and $[B]$) is shown in more detail in Appendix A.

This form is very useful for flight dynamics purposes. The eigenvalues of the $[A]$ matrix define the poles of the system, which provide the stability, damping, and natural frequency of the various aircraft responses. The full equations can also be utilized to define the transfer functions of the aircraft responses. These describe, in the frequency domain, the linear relationship between the inputs and outputs of a helicopter, while it is operating within small perturbations from a trim condition.

Linearized perturbation analysis requires all of the equations of motion to be in ODE state-space form. Higher fidelity aerodynamic methods that are in PDE

form do not have states in the way written in Eq.(1.1). If a system does not have states that can be included in the linearization, then the dynamic effect of that system cannot be determined through perturbations. If states available are time-varying, even in trim, and a specific transform is not known that removes the time dependency then the procedure will not capture the correct effects. And if the equations of motion contain partial differential equations, but somehow the states are defined, then there is a question of how to actually perform perturbations. How long and in what way should the simulation be run in order to accurately determine the change and rate of change of the states?

A quasi-steady linearization can be performed on the aircraft coupled with a PDE form wake model. In this case, there are not any actual wake states, however the aircraft states and controls do effect the wake behavior which in turn couples back into the aircraft dynamics through the aerodynamic loading. In this procedure, perturbations are performed to the states, state derivatives and controls, and the wake is time marched to a new steady condition to determine the effect of the wake on the aircraft. This will modify the aerodynamic loading which will in turn change parts of the $[A]$ and $[B]$ matrices. But it is important to note that this will not add poles and zeros to the perturbation model of the full aircraft, as a state-space model of inflow would. This can only change the gains of certain aircraft transfer functions. The lack of poles and zeros caused by the wake is what makes this quasi-steady linearization an approximation and is why it does not accurately capture the dynamics that are present in the high fidelity aerodynamic models.

1.2 Review of Coaxial Rotorcraft Modeling

1.2.1 Aerodynamic Modeling of Coaxial Rotors

Rotors impart velocity to a mass of air in order to generate thrust. The velocity imparted in the vertical direction in the rotor frame of reference is referred to as the induced velocity or induced inflow. The mutual interactions between the rotors of a coaxial configuration create complexities that are not easily approximated through simplified approaches such as momentum theory. Momentum theory makes several assumptions about the flow field which are not easily extended to systems of two rotors. Nevertheless, there are several momentum theory based models that try to predict the inflow on each rotor.

Harington [8] was the first to model coaxial rotors as a single rotor with equivalent solidity, using momentum theory analysis. This analysis was used to predict the performance of a coaxial rotor, and compared to experimental data of a coaxial rotor in a wind tunnel (which will be referred to as the Harrington Rotor experiments). Inflow is not measured or computed directly, but it is implied by the form of the analysis that there would be an equivalent uniform inflow. He concluded that the equivalent solidity rotor theory was adequate to predict the performance of the experimental coaxial data, and was just as accurate as the single main rotor prediction. Dingeldein [9] tested the equivalent solidity rotor theory of coaxial rotors in forward flight. He found that the theory tends to overpredict power requirements of a coaxial rotor by up to 14%. Payne [10] repeats this analysis while coming to inflow

and performance solutions for tandem configuration rotors, and also compared with the wind tunnel test data from Refs. 8,9. These models predict equal thrust on each rotor and predict the rotors to each have an equivalent uniform inflow velocity of:

$$(v_i)_e = \sqrt{\frac{W}{2\rho A}} \tag{1.2}$$

Though the equivalent solidity models may be close for overall performance prediction, they do not accurately describe the true flow characteristics.

Sweet [11] performs a similar analysis for a coaxial rotorcraft on which a pilot stands and leans in order to provide control moments. In this work the inflow is described as uniform with a longitudinal variation in forward flight (due to this configuration carrying a aerodynamic pitching moment). The coaxial rotor is analyzed as a single main rotor with equivalent solidity. The rotor forces and moments are compared with an experimental wind tunnel test. The theory under predicts thrust across the flight envelope by as much as 15%, does not capture the proper hub drag force. Even though the paper concludes that the longitudinal variation in inflow is necessary to capture the pitching moment, and indeed it is an improvement, the pitching moment from theory is still mismatches the wind tunnel data by up to 45% at certain flight conditions.

The next extensions of the momentum theory model were to operate the lower rotor in a climb based on the upper rotor inflow. These "climbing rotor" models made varying assumptions about the contraction of the upper rotor's wake. They also assumed that the upper rotor was not affected by the lower rotor's behavior. Paglino [2] first described this theory for application to modeling the Sikorsky XH-

59 “Advancing Blade Concept” (ABC) Helicopter. Two different dual rotor theories were compared with measured wind tunnel test data. The first (undeveloped wake) assumed the spacing was small compared to the contraction of the upper rotor’s wake and therefore the whole lower rotor operated in a climb equal to the upper rotors induced velocity. The second (developed wake) instead assumed the spacing was large enough that the upper rotor’s wake would fully contract and only impact upon half of the lower rotor’s area, but with twice the velocity. Therefore the lower rotor operated in a climb equivalent to twice the upper rotor’s induced velocity. Paglino noted that both models produces better results than single rotor (equivalent solidity) theory, in terms of matching torque and thrust coefficients to experiment. The developed wake was concluded to be slightly better at capturing the experimental results.

Leishman et al. [12–14] further expanded on this developed wake approach with analytical solutions. Figure 1.1 from Ref. 12 shows a schematic of this rotor representation. Following this representation through to an inflow solution for coaxial rotors operating at equal power (which covers almost all practical coaxial configurations, as it also implies torque balance) shows that the inflow induced by the lower rotor v_l should be:

$$v_l = 0.4375 v_u \tag{1.3}$$

where v_u is the upper rotor induced inflow. The total inflow over the center half of the lower rotor is the combination of the vena contracta of the upper rotor and the

lower rotors induced velocity, leading to:

$$v_{lower\ center} = 2v_u + 0.4375v_u = 2.4375v_u \tag{1.4}$$

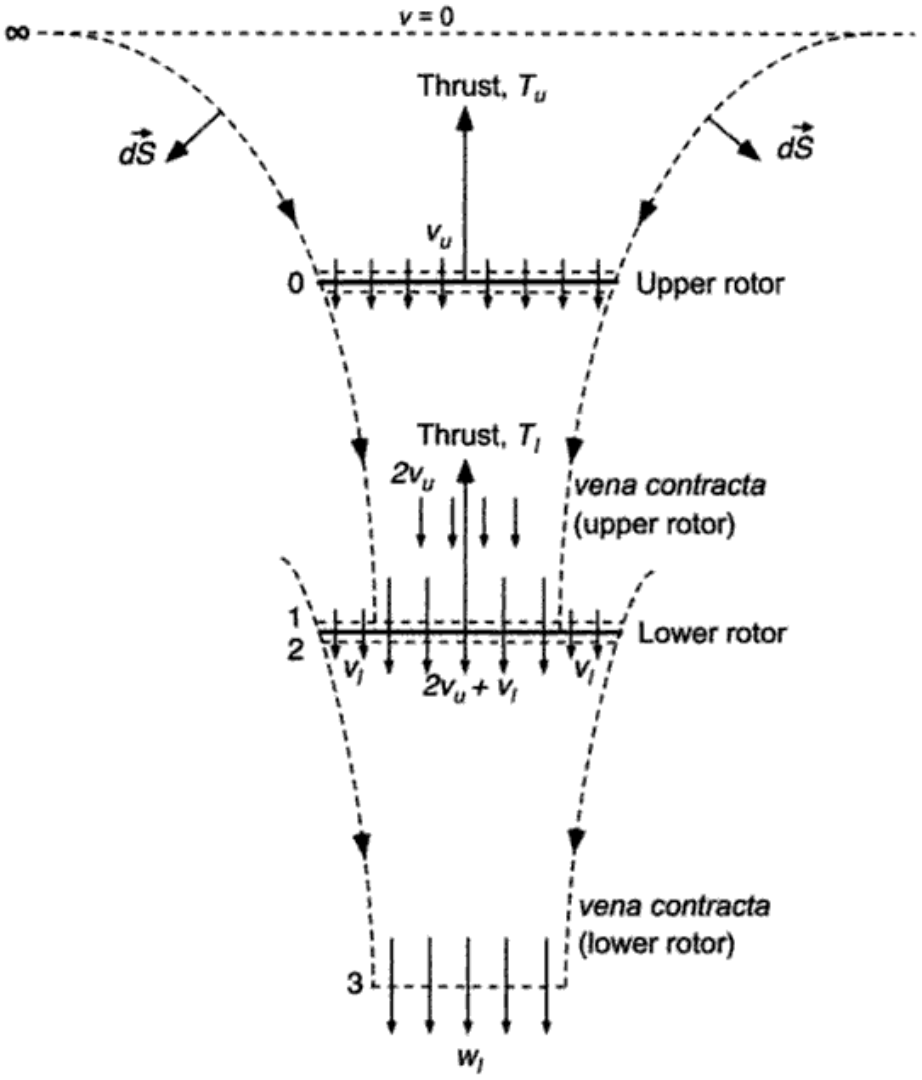

Figure 1.1: Flow model of coaxial rotorcraft (from Ref. 12).

These models tend to overpredict the induced velocities and therefore the power requirements. Also the assumption that the wake is fully contracted is usually not quite valid because rotors are not sufficiently separated [12]. Finally, it is

concluded that these overpredictions may occur because "swirl recovery" allows the lower rotor to recapture some of the upper rotor's inflow momentum [2].

Johnson [15] tries to make a more realistic assumption for the contraction of the upper rotor's wake, allowing for the wake to contract by different amounts depending on the spacing. The upper rotor's induced velocity v_u is assumed to be uniform and unaffected by the lower rotor (momentum theory solution). The lower rotor's induced velocity v_l is nonuniform. The theory introduces a term $\bar{\alpha}$ which describes the average of the disk loading on the lower rotor weighted by the induced velocity on the lower rotor. This is given by:

$$\bar{\alpha} = \int \frac{\Delta p_l v_l dA}{T_l \bar{v}_l} \tag{1.5}$$

Where Δp_l and v_l are the change in pressure and the induced velocity, both on a given annular portion of the lower rotor. T_l is the thrust on the lower rotor. $\bar{v}_l$ is the lower rotor's mean induced velocity calculated as an integral over the lower rotor's disk area (A):

$$\bar{v}_l = \int v_l dA/A \tag{1.6}$$

This term also controls the area of the lower rotor that is subjected to the upper rotors wake. Uniform loading on the lower rotor corresponds to a value $\bar{\alpha} = 1$. In general the loading on the lower rotor is higher towards the outboard sections, leading to $\bar{\alpha} > 1$. Ref. 15 lists a table with a few values of $\bar{\alpha}$, sorted in order of rotor spacing, which can be used for analysis.

Next the variable τ is defined as the ratio between the lower and upper thrust:

$$\tau = T_l/T_u \tag{1.7}$$

Given this parameter, Ref. 15 shows that, for the case of equal power on each rotor, the ratio between the lower rotor's mean induced velocity and the upper rotor's uniform velocity s is:

$$s = \bar{v_l}/v_u = \frac{(1+\tau)^2}{2} \tag{1.8}$$

The actual nonuniform inflow distribution on the lower rotor would be deduced from $\bar{v_l}$, $\bar{\alpha}$, and the other parameters of the model. While the lower rotor's mean velocity (for equal power case) would not depend on the contraction (and hence $\bar{\alpha}$), the inflow distribution across the lower rotor would. The difficulty with this model is that $\bar{\alpha}$ is a tuning parameter. Instead of there being a defined correct value, it is rather left to the user to tweak the value to match the desired contraction ratio, presumably from flight test / wind tunnel data, assuming any such data exists.

Other models exist that try to expand upon this contracted flow "climbing rotor" theory. Nagashima and Nakanishi [16] presents two theories, one using the contracted rotor momentum theory, and the other using a simplified vortex analysis, as shown in Fig. 1.2. The first theory is unique in that the outboard region of the lower rotor experiences a small upwash from the upper rotor's wake, and the upper rotor experiences some interference from the lower rotor's wake. In addition, swirl velocities are also calculated across both rotor disks. The mutual interference terms were computed from potential theory and from experimental results. The second theory modeled the blades as lifting lines with nonuniform circulation and the wake

was model as a set of discrete circular vortices with strengths set by the bound circulation. These theories were compared and match quite well with thrust sharing ratios obtained from an experimental coaxial rotor in hover, at different control settings.

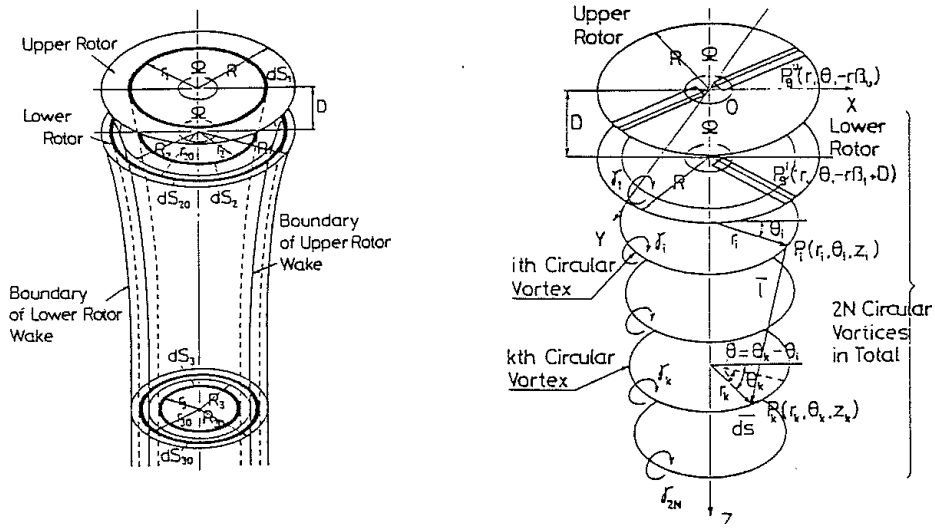

Figure 1.2: Flow model of coaxial rotorcraft (from Ref. 16).; left shows theoretical wake boundaries and the impingement of the upper rotor wake on the lower rotor; right shows simplified circular vortex wake analysis

Valkov [17] presented a wake superposition theory for coaxial rotors, in which the rotors are plunged in each other's wake. The slipstream of each wake is calculated using helical tip vortices and Biot-Savart law. This gives the velocity and contraction ratio of each wake at the other rotor plane. In this way interference velocities are calculated. This theory is compared with hover and forward flight data from a Canadair CL-227 remotely piloted vehicle, and showed good agreement with performance metrics.

Bourtsev et al. [18] presented a model used for Kamov Helicopters that proposed that the coaxial rotor could be modeled as a single rotor with a larger effective "active" area. As shown in Fig. 1.3, The upper rotor and the portion of the lower rotor residing within the upper rotors slipstream can be considered one active area of area $F = \pi D^2/4$. The annulus lying outside of the upper rotors wake is considered an extra active area.

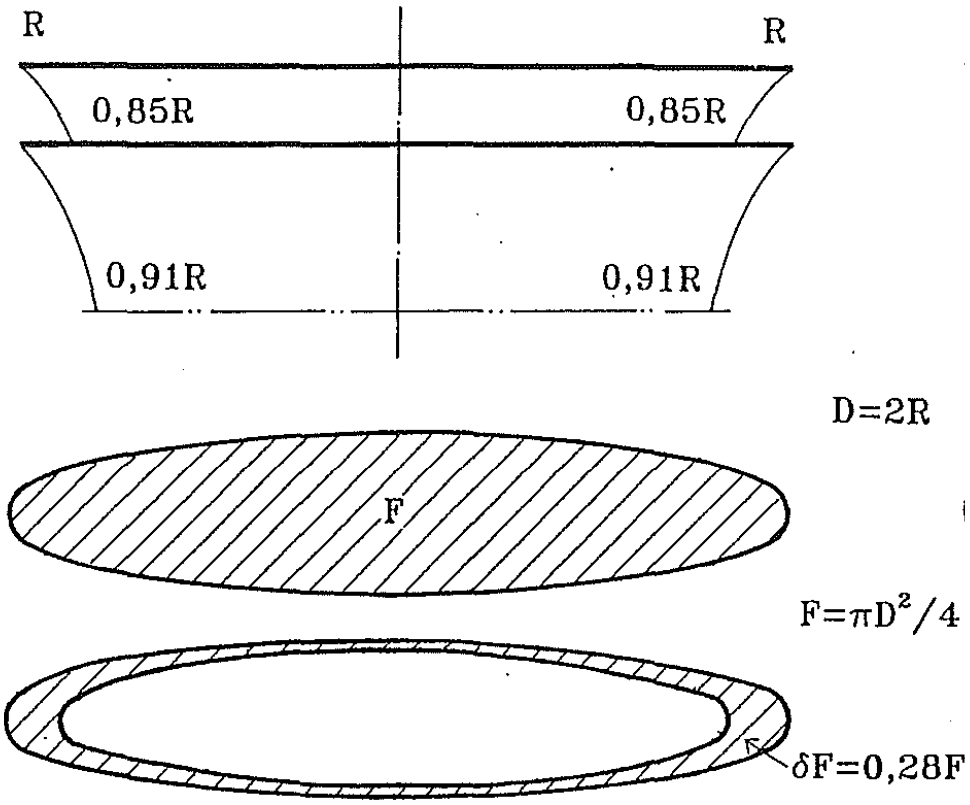

Figure 1.3: Flow model of coaxial rotorcraft (from Ref. 18).; The active area footprints of the rotors (portrayed beneath the rotors) consists of the area of one rotor plus the additional area of the lower rotor outside of the upper rotor wake.

Wake contraction ratios were determined from experimental tip vortex visualization of a coaxial Kamov Ka-32 helicopter operating in hover. It was found that the upper rotor's wake had contracted to 85% of the rotor radius (as shown in Fig. 1.3). Therefore the area lying outside the upper rotor's wake was 28% of lower rotor's area, giving the combined coaxial system a total effective area of $A = 1.28\pi R^2$. This method relies on experimental or other data to determine the contraction ratio at each operating condition and for each helicopter configuration.

More recently, Rand et al. [19,20] presented a momentum theory based method that modeled both rotors in a climb based on the other rotor's inflow, as shown in Fig. 1.4. The outboard section of the lower rotor however would not experience climb. The "equivalent climb" on each rotor is modulated by several interference coefficients calculated from experiments and free wake analysis. This analysis was unique in that it allowed for dissimilar rotors in terms of rotational speed and radius. This model was compared against vortex methods, CFD methods, and experimental results and was found to capture global behavior such as power very accurately, even though its inflow predictions, particularly at the blade tips, were inaccurate.

1.2.2 Inflow modeling in unsteady conditions

The theories presented so far have been "static" or "quasi-static" inflow theories, depending on their implementation. Changes in the aerodynamics and dynamics of the rotor provide either instantaneous changes (quasi-static) or provide no change (static) to the inflow velocity. As first shown by Carpenter and

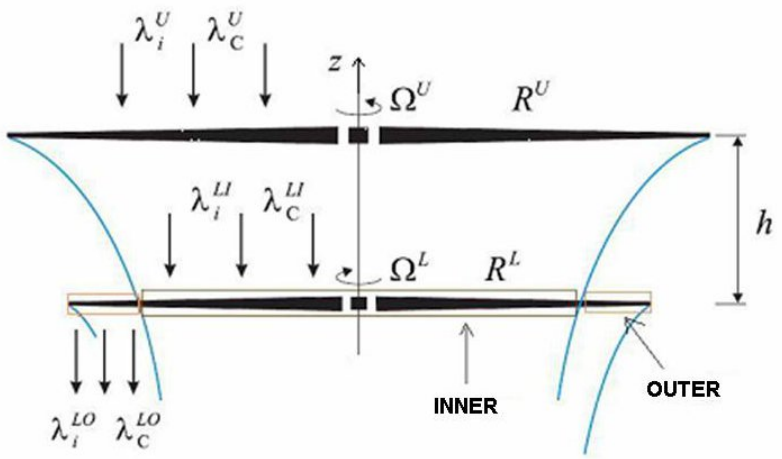

Figure 1.4: Flow model of coaxial rotorcraft (from Ref. 19). Each rotor is subjected to a climb based on the other rotor's inflow

Friedovich [21], this is not the case, for it takes time for inflow changes to build up in response to control inputs. These models are therefore not accurate for modeling unsteady conditions of the rotor.

Mathematical models of inflow dynamics typically are either in Ordinary Differential Equation (ODE) or Partial Differential Equation (PDE) form.

1.2.2.1 Inflow Models in ODE Form

State-space models of inflow are quite useful in predicting the inflow behavior. Although a small number of free wake state-space models have been proposed [22–24], most state-space inflow models are based on the closed-form acceleration-potential solution of the fluid dynamics equations over a disk. For a single main rotor, the most popular state-space model is the Pitt-Peters "dynamic inflow" [25, 26] which

gives the uniform inflow across the rotor disk as the solution of a system of ODEs:

$$\tilde{v}_i(\tilde{r},\psi) = \lambda_0 + \lambda_{1s}\tilde{r}\sin\psi + \lambda_{1c}\tilde{r}\cos\psi \tag{1.9}$$

$$[M]\{\}\begin{Bmatrix} \overset{*}{\lambda}_0 \\ \overset{*}{\lambda}_{1s} \\ \overset{*}{\lambda}_{1c} \end{Bmatrix} + [L]^{-1}\begin{Bmatrix} \lambda_0 \\ \lambda_{1s} \\ \lambda_{1c} \end{Bmatrix} = \begin{Bmatrix} C_T \\ -C_L \\ -C_M \end{Bmatrix} \tag{1.10}$$

where the $[M]$ and $[L]$ are defined as a function of the three components of velocity in the rotor coordinates and the momentum-theory nondimensional induced velocity.

This model has a few important assumptions. First it is an acceleration potential solution over an actuator disk, therefore implying an infinite number of blades. The shed vorticity effects are therefore assumed to be spread out over the disk. for flight dynamics purposes, a finite number of blades must be used, therefore the procedure of discretizing the disk inflow is required.

The theory has two model forms, a non-linear form and a linearized form. The non-linear model is completely non-linear in its thrust to average inflow relationship, however the moment to harmonic inflow relationships are linearized. Therefore the model is only valid for small perturbations in aerodynamic moment (pitch or roll), and it will not give the correct nonlinear responses to roll-moment perturbations that occur at zero thrust [27]. The linearized model is a perturbation model which assumes small perturbations about a given steady solution for all three states and inputs.

The Peters-He "finite-state wake" [28, 29], and their numerous subsequent developments, further developed the potential flow theory by expanding the inflow at the disk in terms of modal functions, adding higher harmonic as well as radial variations to the inflow distribution. The modal function is truncated to a finite number of states. It has been shown that with enough states the solution exhibit the shed wake effects seen in Theodorsen's theory and Loewy's theory, as well as the tip-loss effects predicted by Prandtl-Goldstein tip loss approximation.

The Pitt-Peters model and Peters-He finite-state wake models both do not account for inflow dynamics due to dynamic motions of the disk, either from blade dynamics or from hub rotational velocities (though it does account for hub translational velocities). Also neither theory is capable of properly predicting inflow dynamics for a rotor disk operating in vortex ring state, though they are able to predict the autorotational boundary for the vortex ring state. The theory recognizes the vortex ring state operating condition as having no physically realizable steady solution due to a negative eigenvalue in the inflow system [27].

Despite these theoretical limitations, the Pitt-Peters model and the Peters-He finite state wake are computationally very efficient and produce good results for many flight conditions for single rotor aircraft, or aircraft with multiple rotors which are configured in such a way to not cause excessive interference. These models are not suitable, however, for coaxial rotorcraft, as the solution to potential flow theory is more complicated when two rotors are taken into account.

In recent years, Prasad and Peters et al. have presented numerous papers attempting to extend the well-behaved Peters-He model to the much more compli-

cated coaxial rotor. Prasad et al. [30] extends two methods for single main rotor prediction to the coaxial rotor in hover. The first is the Peters-He dynamic inflow model. This paper uses two pressure fields superimposed to create a dual actuator disk representation. The second method used a Galerkin weighted residuals approach based on that shown in Morillo and Peters [31], extended to a coaxial rotor. The upper rotor's wake interaction with the lower rotor's inflow did not allow for the assumption of a rigid wake, therefore a wake contraction method was developed through incompressible flow equations and used for model correlations. These models were only tested against steady inflow experiments from Ref. 32, and so it is unclear how well this model captures dynamic interferences between rotors.

Nowak et al. [33] further extends this model to forward flight. This paper establishes the active-receiving rotor concept, which allows for the solution of off-disk inflows by relating the pressure from an active rotor to the induced inflow at a receiving rotor. The active-receiving rotor model has the Peters-He model form, but with different coefficient matrices. The equations for the active-receiving $[L]$ and $[M]$ matrices are not available in closed form, but must be computed numerically from time integration. Lookup tables of $[L]$ and $[M]$ matrices can be generated for each inflow skew angle. These models are compared with experimental data from the Harrington rotor wind tunnel tests and numerical results from a Free Vortex Method (FVM), but only in steady conditions.

Xin et al. [34] presented a theory which was based on the theory of active-receiving rotors. In this study, empirical expressions for induced velocity caused by a rotor at the location of the other rotor were produced. This off-rotor model used

Pitt-Peters form as given by Eq.(1.10), but the inputs would be the aerodynamic loading on one rotor, and the outputs would be the downwash at the other rotor. The induced velocity on a rotor would then be the summation of the self induced velocity calculated by a Pitt-Peters model (unmodified from single main rotor theory), and this additional velocity coming from the off-rotor expressions. The $[L]$ matrix was fit to steady results from a High fidelity free vortex wake model, and the $[M]$ matrix was calculated from the downwash gradient. The model is validated only against steady hub loads from flight test data for a coaxial rotor helicopter with a pusher propeller.

Yong-Boon et al. [35] expanded further on the finite state Active-Receiving Rotor Inflow Model (now called ARRIM). This paper pointed out that this theory cannot capture the complex aerodynamic interactions between upper and lower rotors in forward flight. This is because the theory assumes that each rotor has a prescribed cylindrical wake geometry, when in fact higher fidelity simulations (in this case, VVPM) show that the wake geometries are quite distorted. The rotors mutual interference effects therefore had to be quantified using frequency domain system identification of a high-fidelity free wake model. This method produced corrections to ARRIM influence coefficient matrix to align the wake skew better, by better capturing wake distortions due to rotor-to-rotor flow interactions.

The following year, Yong-Boon et al. [36,37] compared two new models which involve velocity potential superposition and pressure potential superposition, respectively. With the velocity potential superposition approach, upper rotor pressure perturbations at the lower rotor are assumed to be better captured than with the

pressure potential superposition approach. This is due to the existence of a time delay in the response for the velocity potential superposition approach, which the pressure potential superposition method is lacking. But the velocity potential superposition approach comes at the cost of requiring the calculation of the adjoint velocity states, which must be computed by backward integration in time, because the adjoint inflow equation is unstable. The pressure potential superposition is more readily usable because its form allows for forward in time integration, but it is considered less accurate because of the missing time delays. Therefore this work suggests using frequency domain identification on the velocity potential superposition method and applying corrections to the pressure potential superposition method. In this way, the pressure potential superposition model is able to capture the correct inflow phase response at the lower rotor for different values of upper rotor thrust coefficient. This pressure potential solution still requires integration in time for the off-rotor influence coefficient matrices, or lookup tables.

Juhasz et al. [20] presents a comparison between three different methods for aerodynamic prediction of coaxial rotorcraft, a blade element momentum theory approach, a free vortex wake approach, and a computational fluid dynamic approach. In particular, the BEMT method was very similar to the "equivalent climb" of Ref. 19. Each rotor was allowed to exist in a climb state due to a partial amount of the other rotor's inflow. These three models were validated against wind tunnel model test data from Ref. 32, though only for steady conditions. It was found that for particular details like inflow distributions the free-vortex wake methods and CFD methods tended to match the experimental data within about 10%. For

overall global quantities, such as power, BEMT often more accurately predicted the experimental result than the higher fidelity methods did.

The BEMT model from Ref. 20 was not explicitly valid in unsteady conditions but also was only exercised in steady conditions. In Ref. 38, this model was extended to allow for inflow dynamics. Instead of the inflow being modeled on each rotor by momentum theory, the inflow is instead modeled on each rotor separately by Peters-He inflow models. The interference climb velocities, as identified in Ref. 20, remain the same in form. They are allowed to change dynamically however when the inflow changes on the other rotor. This applies a sort of dynamic interference between the two rotors, at least for average inflow and thrust excitations. There is no delay added in the response between the rotors which will be shown to be an impactful part of the coaxial dynamics. Also this model does not have interference in the lateral or longitudinal inflow direction which will also be shown through free wake simulation responses. Nevertheless, this model represents the state of the art in coaxial rotor dynamic inflow modeling before this current dissertation's work.

1.2.2.2 Coaxial Inflow Models in PDE Form

Free-vortex theories have been used for coaxial rotorcraft modeling are are valid for unsteady conditions. Saito and Azuma [39] presented one such theory which used local momentum theory with modified prescribed wake, and also extended the model to work in forward flight. Andrew [40] presented a vortex/momentum/blade-element approach which modeled the tip vortex as a prescribed or relaxed vortex

as shown in Fig. 1.5. Both were compared and were found to agree well with experimental performance data in steady conditions.

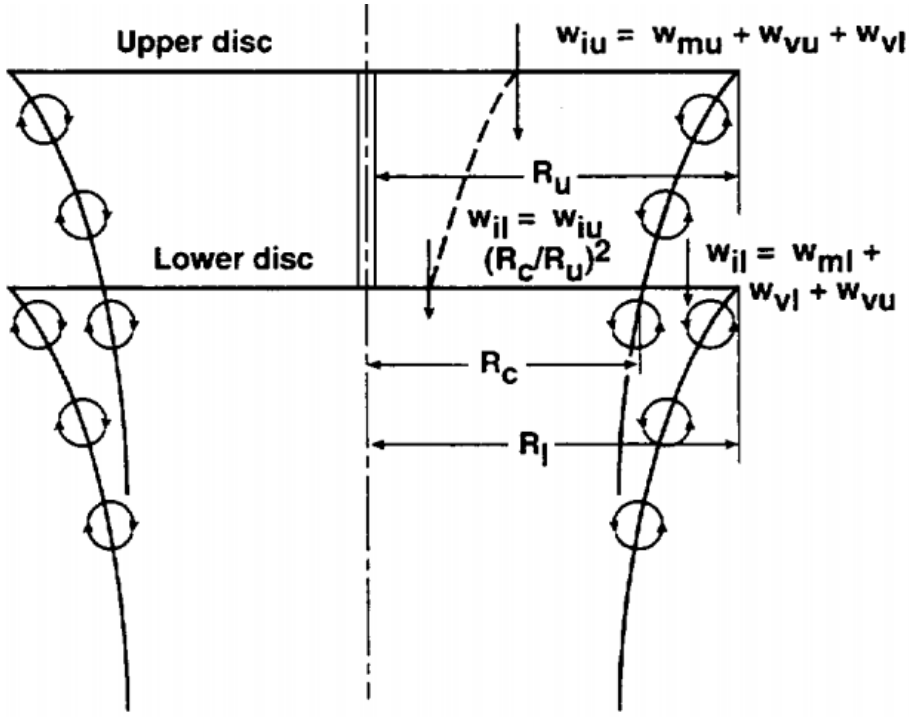

Figure 1.5: Flow model of coaxial rotorcraft (from Ref. 40).

Time accurate free-vortex wakes have also been used to model coaxial inflow systems. These include Refs. 41–47. These operate by modeling the wake as a set of discretized vortex filaments that are allowed to convect freely under the influence of the other vortex. The vortices start and trail from the blades and their strengths are generally set by the circulation generated on the blades. These models can model interactions between the two sets of wakes, coming from each rotor. Vortex-vortex and blade vortex intersections are typically very difficult to model and depend greatly on the model of the vortex core, which is typically calibrated carefully with wind tunnel data.

Coaxial inflow were modeled with Vorticity Transport Model (VTM) by Kim and Brown [48]. VTM is based on a time-dependent computational solution of the vorticity-velocity form of the Navier-Stokes equations on a Cartesian adaptive-grid system that encloses the rotorcraft. A convection algorithm used in the VTM helps preserve the vortical structures in the flow from being lost due to numerical dissipation. The adaptive-grid system evolves the wake by generating computational cells only where the vorticity is present. Extension of this model to coaxial is straightforward because each additional blade simply acts as an additional source of trailed and shed vorticity. This model was validated against steady measurements for Refs.8, 9.

Viscous Vortex Particle Method (VVPM) is used for coaxial modeling by Rajmonhan, Zhao and He [49] and by Singh and Friedmann [50]. VVPM directly solves the vorticity–velocity form of the incompressible Navier–Stokes equations in the Lagrangian formulation without the requirement of grid generation. A hybrid CFD method calculates the viscous flow near the blades and a nondissipating rotor wake over large distances. This method was validated against steady experimental data from McAlister and Tung [32] and from Cameron et al. [51].

Lastly, coaxial rotor flows have been calculated with varying degrees of complexity with Computation Fluid Dynamics (CFD) in Refs. 52–57. These method are all validated, only in steady conditions, with experimental data from either Ref. 8, 51,or 32, and only present results for steady conditions.

1.2.3 Experimental Validation of Inflow Dynamic Models

The above methods for coaxial rotors contain inflow dynamics because of their mathematical formulation, however have not been validated as such. The lack of validation for unsteady behavior is primarily due to the lack of available experimental data for coaxial dynamic maneuvers. There has, however, been validation of inflow dynamic models for single main rotor helicopters. These fall into two categories: indirect (e.g. through flap or aircraft response measurements) and direct (e.g. through unsteady flow visualization and measurement).

Indirect Approaches:

Inflow models have been extracted from flight and wind tunnel test data through their effects on flapping and damping stability derivatives rather than from wake flow measurements. These studies can be considered as indirect methods to extract and validate wake dynamic models.

Feik and Perrin [58] and Blackwell *et al.* [59] identified a portion of the Pitt-Peters dynamic inflow model [29] as part of a more detailed time-domain identification of a coupled rotor-fuselage linearized model of the Sikorsky Sea King helicopter in hover. A similar exercise was carried out by Houston [60] using a frequency domain system identification technique on hover flight test data of a Puma helicopter. The set of identified variables included an axial inflow derivative term, which was found to be about 60% larger than its predicted value. The discrepancy was attributed to unmodeled dynamics.

In a later study, Houston and Thomson [61] extracted the three components of the inflow [29] from blade flapping measurements of an autogyro in trimmed forward flight. Good agreement between theory and experiment was found for the uniform and longitudinal inflow components. A less satisfactory agreement for the lateral component was attributed to interactional aerodynamic effects specific to that particular configuration.

Coupled SH-2G coning/inflow dynamics based on the Pitt-Peters model have been analytically derived and included in the model structure of higher-order rotorcraft model [62, 63]. The final identified model agreed well with flight data and captured the key aircraft body dynamics very well.

The Sikorsky Bearingless Main Rotor (SBMR) system parameters were also extracted from frequency sweeps on the full scale rotor performed in a wind tunnel at two different forward flight conditions [64]. The identification showed that an accurate model of the on-axis rotor response could be extracted as based on the Pitt-Peters dynamic inflow model. Emphasis in this work was placed in correctly predicting the rotor off-axis response by including an aerodynamic phase lag and wake distortion effects due to rotor flapping.

Direct Approaches:

Carpenter and Freidovich [21] were the first to demonstrate inflow dynamics directly for single main rotors. The experiments they performed directly measured dynamic changes in inflow by measuring the change in drag on small balsa wood paddles mounted on a horizontal bar 2 feet below the rotor blades, immersed in the

rotor wake. The changes in inflow were produced by different swashplate collective ramps. They compared these experimental results with an analytical model.

A few of the ODE and PDE inflow models previously discussed are validated (for single main rotors) with these experiments. The Peters-He model was compared to this experimental data in Ref. 28. The comparison showed that the model gave good correlation with the experiment. Because this comparison was performed with the single radial function, zeroth harmonic version of the Peters-He model, it is equivalent to, and therefore validates, the Pitt-Peters model also. Free-vortex methods were compared against these experiments by Bhagwat and Leishman [65, 66]. They showed that the free wake method could accurately predict the time responses of the mean inflow due to the ramps in collective

The Carpenter and Freidovich experiments demonstrate the inflow dynamics but they are limited by the amount of time and energy spent exciting the full range of frequencies. Indeed a ramp response will excite all frequencies however a majority of the excitation energy will be at low frequency and measurements must be incredibly precise in order to accurately capture the dynamics at a any higher frequencies. This is difficult as typically the inflow measurements are not extremely accurate. Alternatively, a better way to excite inflow dynamics at known frequencies is to drive the rotor with sinusoidal swashplate inputs, at those frequencies.

Ellenrieder and Brinson [67, 68] presented the one study in literature that focused on extracting inflow dynamics through actual inflow measurements from sinusoidal forcing. A hingeless four-bladed 1.54 meter diameter rotor was placed in a wind tunnel and instrumented with hot wire anemometry probes mounted directly

below the rotor plane. The rotor had a swashplate that could actuate collective and cyclic controls at up to 50 Hz. The blades were instrumented with strain gauges to measure deflections of the blades, and the rotor shaft had a shaft encoder to measure azimuthal position of each blade.

The spanwise and azimuthwise inflow distribution, as well as flap angles, were measured for a series of single-frequency collective and cyclic swashplate excitations at frequencies of up to 1.5/rev. They presented partial inflow and flapping frequency responses. No models were fit to the frequency responses, but they were compared with analytical rotor models which used Pitt-Peters model for inflow dynamics. The dynamic response of the inflow was found to be highly complex, with significant variations with radius, distance from the rotor plane and frequency of excitation, because of the effects of both wake geometry and shed vorticity.

Bhagwat et al. [66] used these experimental results to validate the dynamics of a free wake model for a single main rotor helicopter (UH-60). They created localized (i.e. at a given radial and azimuthal location) inflow frequency responses to swashplate controls using the same method as in the experiments. A subset of the comparisons between experiment and the free wake model are shown in in Fig. 1.6.

This experimental data and free wake model predictions were obtained by oscillating a rotor control (in Fig. 1.6 case, collective pitch) in a sinusoidal manner at a constant frequency for each frequency point along the x axis. The induced velocity at the given location was then measured, and this output generally held to a sinusoidal shape at the same frequency as the input. The ratio between the input sine wave's amplitude to the output sine wave's amplitude is given as the

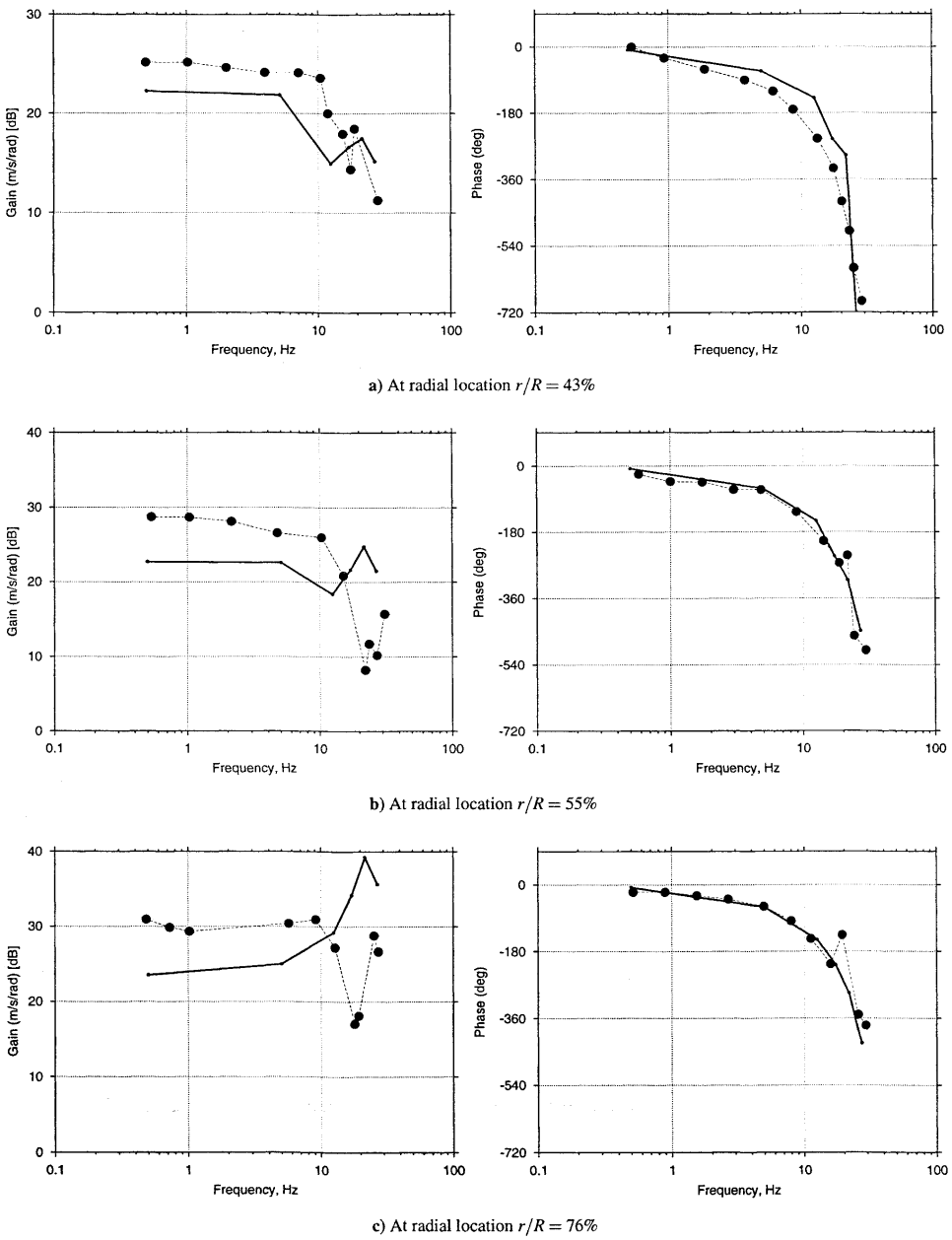

Figure 1.6: Validation of the MFW model (from Ref. 66).; magnitude (left) and phase (right) of induced velocity frequency response to cyclic excitation of collective pitch, at various blade radial locations. Solid symbols: experimental measurements from Ref. 68; solid lines are free wake model predictions. Results are for hover

magnitude (expressed in decibels, shown in the first column of Fig. 1.6), and the phase difference between the input's sine wave and the output's sine wave is the phase (expressed in degrees, shown in the second column of Fig. 1.6). Fig. 1.6 shows that free wake model tends to predict the correct phase fairly accurately and the magnitude within about 6 decibels (a factor of about two).

It should be noted that the measurements of Ref. 68 are incomplete, and do not allow a full validation of theoretical models. For example, aerodynamic loads (i.e. not including inertial loads) were not measured. Also the trimmed total rotor thrust was not measured, but rather estimated based on a simulation model. No other experiments exist that excite a rotor at given frequencies and record rotor aerodynamic loading as well as inflow.

No inflow dynamic measurements are currently available for coaxial rotors. The free wake model was only validated for coaxial rotors with static experimental data [42].

1.2.4 Extraction of time-domain aerodynamic models from frequency-domain data

There is an extensive literature on the extraction of low order, state-space aerodynamic models from frequency domain data for unsteady *airfoil* aerodynamics and aeroelasticity. Notable references include the pioneering work by Vepa [69], who introduced the technique of extracting approximate transfer functions from simple harmonic oscillation data. The method was applied to Theodorsen's function ($C(\omega)$)

to produce Padé approximants. Padé approximants approximate a known function of frequency as a transfer function in the form:

$$C(\omega) \simeq \frac{N(j\omega)}{D(j\omega)} \tag{1.11}$$

where N and D are polynomials of *equal* degrees:

$$N(j\omega) = (j\omega)^n + a_1(j\omega)^{n-1} + \ldots + a_n$$

$$D(j\omega) = (j\omega)^n + b_1(j\omega)^{n-1} + \ldots + b_n$$

The Padé approximant used in Ref. 69 was 4th over 4th order, i.e. $n = 4$ in Eq.(1.11). The difference between the actual value of $C(\omega)$ and the Padé approximant was minimized through a least squares technique. Results showed that the Padé approximant could predict the real and imaginary values of the Theodore function better than previous approximation methods.

Edwards *et al.* [70] applied the methodology to a generalized Theodorsen function for unsteady loads due to arbitrary airfoil motion in incompressible flow. A first order Padé approximant was used and the resulting states were augmented onto the airfoil sectional equations of motions. Root Loci of the aeroelastic modes were produced and the approximation technique gave good agreement with exact calculations for values of the airfoil aerodynamic flap, torsion, and plunge modes near the imaginary axis.

Venkatesan and Friedmann [71] applied the methodology to Loewy's function for rotorcraft shed wake effects. However, they used an approximate transfer function with more complex zeros and poles (not necessarily constrained to the same degree) and showed that the method could capture the real and imaginary parts

of Loewy's function in the frequency domain much more accurately than a $n = 5$ Padé approximant. In much more recent developments, the methodology has been applied to CFD-based airfoil calculations [72], once again showing that the reduced order models could match the high fidelity simulations of lift, drag and moment during dynamic oscillations of the airfoil.

Also notable is the ONERA dynamic stall model, initially formulated by Tran and Petot [73], consisting of a system of ordinary differential equations, the coefficients of which are extracted from oscillating airfoil tests. All these references can be considered as studying shed wake effects, whereas the present work addresses primarily trailed wake effects. This distinction is not completely rigorous because there may be overlaps both in methodology and in focus, but it can be conceptually useful.

There are also studies that have recently identified inflow dynamic models of the full rotor wake. Gennaretti et al. [74] used frequency domain system identification to identify the inflow dynamics of a single main rotor helicopter. The procedure was performed on a high fidelity Boundary Element Method (BEM) tool which solves the solution of the boundary integral equation formulation for the velocity potential field around rotors in arbitrary motion. Frequency responses were identified frequency by frequency using sinusoidal inputs to the aerodynamic solver. State-space models for the inflow were obtained through a rational-matrix approximation algorithm. The first set of state-space matrices were allowed to take on whatever form was required to best approximate the inflow responses, as opposed to fixing the states to known quantities and following the form established by Eq.(1.10).

The second set of state-space models constrained the form to the Pitt-Peters form. Refs. 75, 76 extends the methodology to higher harmonics of inflow, and presents both hover and forward flight results for a single main rotor.

Gennaretti et al. [77, 78] expanded the analysis to coaxial rotorcraft inflow dynamics. The procedure was essentially the same. Two different models were created. The $\lambda - q$ model created high order models relating the inflow dynamics to the hub, controls and flap perturbations. The $\lambda - f$ model was also higher order, relating the inflow dynamics to the aerodynamic loading on the rotors. The $\lambda - f$ model was not unique as it was dependent on the type of perturbation of the helicopter that was used to create the aerodynamic loading (i.e. a perturbation in controls, blade flap, or hub velocities)

He et al. [79] presented a similar identification from a VVPM model for both single main rotor and coaxial rotor. The rotor was subjected to continuous frequency sweep as opposed to harmonic oscillations at individual frequencies. Instead of perturbing the controls of the rotor, the blade circulation was directly prescribed therefore allowing sweeps in only one of the aerodynamic load terms at a time. The model that was found was in Peters-He form, but only for the first 3 states. The single main rotor results were compared to the Peters-He model coefficients to validate the methodology. The coaxial rotor was modeled by calculating inflow expansion coefficients on the other rotor, along with proper time delays, which affected the total inflow on each rotor. Results showed that the identified state-space models could capture the results of the full VVPM model well in the desired frequency range.

Keller et al. [80] used system identification on the CHARM free wake model to identify dynamic inflow for both single main rotors and coaxial rotors. In this study, the frequency sweep was also directly applied to the blade circulation function. The identified responses for the single main rotor were fit with a model in Pitt-Peters form. Additional models were created with an augmented number of states to capture the wake distortion effects caused by perturbations of the rotor tip path plane [81, 82]. The method was then utilized on a coaxial rotor to capture a model of just the vertical axis (λ_0 response to C_T on both rotors) interference response. For both the single main rotor and the coaxial rotor, they showed that the identified model could capture key inflow dynamics. The augmented model containing more states and wake distortion effects were able to better capture the responses than the first-order Pitt-Peters like models.

1.2.5 Flight Dynamics and Control of Coaxial Rotorcraft

Studies into coaxial flight dynamics and control roughly fall into two categories in terms of the models used for flight dynamic analysis. The first category either uses the real aircraft in flight test to optimize the control parameters for better handling qualities, or identifies state-space models from test flight data using time domain or frequency domain system identification and uses those model to optimize the control system. The second category instead uses analytically derived models. Due to a lack of state-space inflow models, these either do not model inflow dynamics

and instead use either steady state or quasi-steady assumptions for the inflow, or ignores inflow altogether.

Sweet [11] performed an analysis of the stability of the de Lackner HZ-1 Aerocycle, which was a coaxial rotor that a pilot would stand on and lean in a direction to produce control moments. Pitching moment and static stability derivatives with respect to angle of attack, velocity, and tipspeed were produced at different advance ratios using wind tunnel measurements. The stability derivatives were compared against analytical models which assume steady state longitudinal inflow. It was concluded that the available control power of the pilot would only allow the aircraft to reach 17 knots because of the stabilizing pitch moment in forward flight.

Ruddell [83] published a report on the Sikorsky XH-59 ABC Helicopter which included an investigation into the stability and control of the helicopter. The stability augmentation system (SAS) for the aircraft was tuned during flight test and the resulting aircraft was given Cooper-Harper ratings for handling qualities. The poles of the aircraft were determined, including the hover dynamic stability and the Dutch-roll mode. These results were not compared with any analytical results however.

Bourtsev et al. [84–86] discussed the flight dynamics and maneuverability of Kamov coaxial helicopters. They described the equations of motion and the methodology to identify parameters from flight data. Various maneuverability metrics were explored and time histories for maneuvers were compared with calculated quantities. It was concluded that the helicopter (particularly the Ka-50) could maneuver within operational limits and within special aerobatic limitations.

Ferguson and Thomson [87] completed a study of compound rotorcraft including coaxial rotorcraft with pusher propellers. The author noted that, as of then, there were no coaxial dynamic inflow models and elected to use Peters-He isolated rotor models. This work explored the roll, pitch, Dutch roll, and phugoid modes of the helicopter configurations. Wu et al. [88] analyzed a mid-scale UAV (rotor diameter of 3 meters) for stability and control. A inflow model is used which is an extension of momentum theory capturing interference between the rotors by using downwash interference terms. The study calculated perturbation models through linearized analysis and investigated the aircraft stability derivatives. Eigenvalue analysis was performed to explore the aircraft poles, and maneuvers were tested on a test platform to identify and confirm some parameters from flight test.

The dynamics and controllability of the Sikorsky X2 Technology Demonstrator was explored in depth by Fegely et al. [38]. This work presents a validation of two different coaxial compound helicopter flight dynamics models by correlation with the Sikorsky X2 flight test data. This study is perhaps the only study that uses inflow models that have dynamic interferences. The first flight dynamics model uses the analytical models from Refs. 30, 33. The flight dynamics model used the previously described "equivalent climb" dynamic inflow model. Both models showed good agreement with flight data for steady-state, as well as for dynamic frequency responses. The analytical models of the coupled rotor and fuselage were then modified by frequency domain identifications from flight data, thereby increasing fidelity. The aircraft responses were then explored and the broken-loop and closed-loop behavior of the Sikorsky X2 with its controller were analyzed, which matched well

with flight data. There is likely more work done in respect to the dynamics and control of the Sikorsky X2, the S-97 Raider [6], and the SB>1 Defiant, but it is not available in open literature.

Very recently, Chang et al. [89] presented a fairly extensive handling qualities evaluation of the AVX Joint-Multi-Role Coaxial Compound Helicopter. A real-time full flight simulation model was developed in FLIGHTLAB. The rotor wake was modeled using the Peters-He's finite state dynamic wake model augmented with the viscous Vortex Particle Method. Mutual aerodynamic interference modeling of the coaxial rotor was calibrated with the Viscous Vortex Particle Method. It is not clear whether the mutual interference terms are dynamic in behavior or whether they are static/quasi-steady. The model was exercised for various piloted simulation tests on different mission task elements which were given handling quality ratings based on the Cooper-Harper scale, as prescribed by ADS-33E [90]. The model was also assessed by calculating various handling qualities quantities such as bandwidths, phase delays, natural frequencies and other quantities prescribed in ADS-33E.

Lastly there are a large number of studies into coaxial flight dynamics and control are for small UAV models [91–94]. Though quite different in scale from full-size coaxial rotorcraft, the studies still typically try to account for the effects of rotor inflow mutual interference through modeling or through direct identification. However dynamic interference between the rotors was not considered; the interference was considered quasi-steady at best.

Common among these flight dynamics and control studies for coaxial rotorcraft, is that the low order *analytical* flight dynamics models necessary for the com-

putation of handling qualities assessments and the design of flight control systems are not yet available. In particular, they are missing low order, computationally efficient models of the rotor wake dynamics in ODE form required for linearized analysis. These studies instead resort to simplified assumptions and modifications of single main rotor dynamic inflow theory or they identify the aircraft dynamics from flight test data so that the inflow effects are already contained within the responses. The dynamics of a coaxial wake are coupled between the rotors and are further complicated by intersections of vortices with other vortices and also with the blades of the other rotor. The inflow dynamics have profound effects on the handling of the rotorcraft and must be accurately modeled. There are simulations that capture these effects but they are higher order partial differential equations that must be marched in time and are slow to compute. Most importantly, they are not in ODE form, and therefore not suitable for linearized analysis. This work will delve into the methodology to transform these higher order methods into low order models suitable for flight mechanics analysis.

1.2.6 Publications from Present Research

Portions of the research described in this dissertation have already appeared in the literature. They are briefly included in this review to highlight their key contributions to what has been a rapidly expanding field of research.

The first results have been presented in Ref. [95], which focused on the extraction of a state-space inflow dynamic model for an isolated single main rotor, using

frequency domain system identification applied to the results of a free wake analysis. Reference [95] was the result of collaborative work, which included a second methodology, primarily developed by Rand and Khromov. Whereas the present research is based on input-output relations obtained simultaneously over an entire range of frequencies of interest, the second methodology was based on a frequency-by-frequency fit of a semi-analytical solution, followed by an averaging of the coefficients of the state-space model over the range of frequencies of interest. Reference [95] was the first example in the literature of the extraction of a model of rotor wake dynamics in state-space, ODE form, from refined aerodynamic models not in ODE form.

Reference [96] extended the methodology to coaxial rotor configurations in hover. Additionally, the coaxial ODE wake model was coupled with a full aircraft simulation model, and full-aircraft results were presented for the hover response to pilot inputs both in the time and in the frequency domains. All of these were the first results of their kind in the literature.

Finally, Ref. [97] extended the methodology to forward flight, showed results for a coaxial-pusher rotorcraft with a model-following flight control system, and assessed the consequences of using the simplified inflow model of Ref. [38] on the controller performance. These were the first closed loop results discussed in the literature for a coaxial rotorcraft where the inflow model is identified from a higher fidelity simulation and properly captures aerodynamic mutual interference.

1.3 Objectives of Dissertation

The primary motivation for the current research is the lack of fundamental understanding of the flight dynamics and control behavior of coaxial rotorcraft configurations. In particular, the aerodynamic interactions between rotors have been shown to make it difficult to model the handling qualities characteristics in certain flight conditions. This difficulty arises from the fact that simple momentum theory models do not accurately predict the correct dynamic behavior of the wake; yet these simple theories, in ODE form, are the only theories that can be used for classical control theory analysis. Furthermore, computational efficiency is required for real-time piloted simulation and certain model-following controller architectures. With this in mind, this dissertation has the following objectives:

1. To develop a methodology to extract simple, accurate, and computationally efficient aerodynamic models in state-space, ODE form, from any detailed aerodynamic model not in state-space form, such as CFD-based models, or free vortex wake-based rotor inflow models. The methodology is based on frequency domain systems identification, is very general, and has wide applicability.

2. To demonstrate this methodology by applying it to the extraction of a state-space model of wake dynamics for a coaxial rotor configuration, starting from a time-accurate, free vortex wake model, formulated as a set of PDEs. Single main rotor configurations will be considered first for validation purposes, as

state-space models are already available for this simpler configuration. Coaxial rotors, for which such models do not exist, will be considered next.

3. To study the fundamental flight dynamic behavior of a coaxial compound rotorcraft configuration with a pusher propeller, by including the state-space inflow model into a full nonlinear flight dynamic simulation, and analyzing trim, poles, and time- and frequency-domain results.

4. To study the effects of the sophistication of rotor inflow modeling on the design and performance of flight control systems, by designing an optimized model-following flight control system for the coaxial-pusher configuration using two inflow models of different complexity, and comparing open- and closed-loop performance of the aircraft.

1.4 Outline of Thesis

Chap. 2 describes the mathematical model used for helicopter simulations. This model consists of the rotorcraft flight dynamics code, HeliUM, as well as the free-vortex wake method code, MFW. Also described are the mathematical forms of inflow models extracted in this dissertation.

In Chap. 3, the basic methodology of frequency domain system identification is reviewed. This methodology is general and applies to more than just the given coaxial inflow case. It is traditionally used to develop dynamic models of aircraft from flight test data or wind tunnel data. In this case we use it in a novel way to identify linear ODE models from outputs of simulations that are not in ODE

form. This procedure starts with frequency sweep perturbations of the inputs of the simulation. These time histories are converted into frequency responses in the frequency domain. These frequency responses are fit with appropriate optimized state-space models that capture the dynamics of the simulation. The models are then exercised in the time domain with various simulated inputs to show that the models correctly predict an approximation of the output behavior.

In Chap. 4, the system identification methodology is applied to extracting state-space inflow models of a UH-60 like helicopter from a free wake simulation and compared against classical state-space methods for predicting rotor inflow. The procedure is repeated for off-rotor locations such as the tail or a wing under the hub, and is then used to identify rotor inflow models in forward flight. Lastly, an extension of the procedure is used to identify the effects of tip-path path plane motion on the inflow dynamics.

In Chap. 5, the extension of this methodology to the identification of a state-space inflow model of a coaxial rotorcraft configuration in hover is discussed. This includes extending the state-space model of inflow to include both rotors, as well as couplings between the two rotors. The model is tested in the time domain to verify its accuracy.

In Chap. 6, a higher order form for coaxial rotor inflow is proposed which better captures the behavior of the inflow predicted by the free wake model than the first order state-space model form Chap. 5. This second order methodology is first used to identify a better state-space model for hover and is then used to capture the complex inflow behavior of a coaxial rotorcraft with propeller cruising in forward

flight at a speed of 200 knots and with a slightly tilted back rotor angle of attack of about two degrees. This methodology accurately captures the dynamics of the inflow in both cases, and is tested in the time domain to ensure correct predictions.

In Chap. 7, the identified state-space inflow models of the previous chapters are inserted back into the full flight dynamics simulation, and compared with classical theories and flight test data (for single main rotor). Full aircraft models are identified through linearized analysis, and key aircraft responses are compared. Lastly, an explicit model-following controller is designed for full aircraft models using a momentum-based theory inflow model and the higher order inflow model identified from MFW in hover. Differences in the controller design and resulting handling qualities of the aircraft under the controllers highlight the differences that determining the correct model can have in flight control design.

Chapter 8 provides a summary and the conclusions to this thesis, as well as recommendations for future work.

Chapter 2: Rotorcraft Mathematical Modeling

2.1 Overview

This chapter first presents the mathematical model used to simulate rotorcraft flight dynamics. The first section summarizes all the main features of the aircraft simulation model except for the rotor wake. The second section focuses on the rotor wake modeling and describes five models: (i) The Maryland free wake model used to extract the state-space model; (ii) The Pitt-Peters and Peters-He dynamic inflow models, used for single main rotor validations; and (iii) three simplified coaxial rotor inflow theories, used in the subsequent chapters of this dissertation.

2.2 Flight Dynamic Simulation Model

To analyze the effect of inflow dynamics on the full aircraft response, the full nonlinear flight dynamics simulation, HeliUM, was used. The mathematical model in HeliUM has been described in detail in Ref. 98, and only its main features will be summarized here.

The computational kernel of HeliUM consists of a system of nonlinear ODEs in the implicit form:

$$f(\dot{\boldsymbol{x}}, \boldsymbol{x}, \boldsymbol{u}, t) = 0 \tag{2.1}$$

where $\boldsymbol{x}$ is a vector of states, $\boldsymbol{u}$ is a vector of controls, and t is time. This ODE kernel should ideally comprise the entire mathematical model of the rotorcraft. The current state of the art is such that mathematical models not in state-space form are needed for adequate accuracy in several type of problems. One such example is free wake models of rotor inflow. Models not in state-space form cannot be linearized numerically, and also need to be properly coupled with state-space models in time marching simulations. The coupling of the free wake to the rest of the ODE kernel is schematically shown in Fig 2.1. The wake is placed in the portion marked "NonODE blocks". This computational structure is conceptually valid for all CFD-based models.

The ODE kernel is composed of the following basic elements: (i) Euler rigid-body equations of motion for the entire aircraft; (ii) A set of rotor equations of motion, for a user-defined number of rotors of arbitrary location and orientation on the aircraft, and with an arbitrary number of blades; (iii) and inflow dynamics equations if a state-space model of inflow is used.

The analysis is based on a "quasi-multibody" formulation, with fully numerical kinematics, flexible bodies arranged with an open-chain, tree-like topology, floating and co-rotational reference frames, but no algebraic equations of constraints. All flexible portions of the aircraft are modeled as beams. The beam model is based

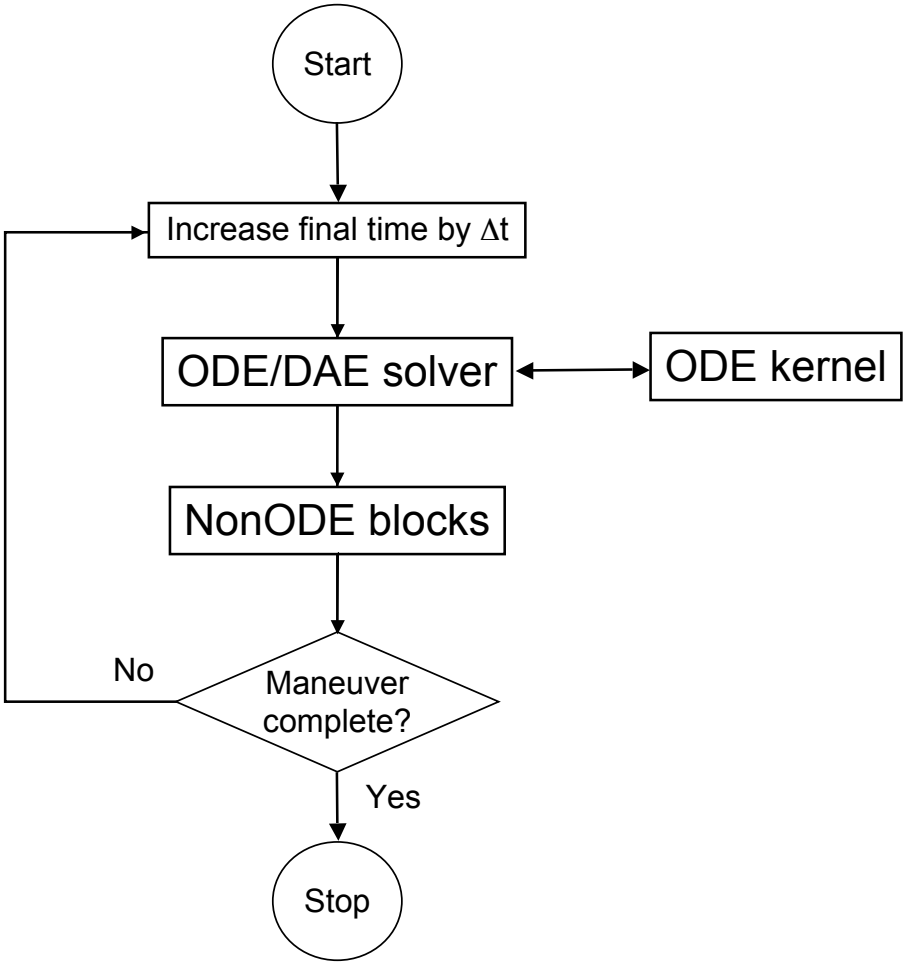

Figure 2.1: Flow chart for time marching maneuver simulations [98]

on that of Rosen and Friedmann [99], which is comparable to the classical model of Hodges and Dowell [100]. The actual model used is a modification that does not require the use of ordering schemes [101], and remains valid for elastic deformations beyond what are generally denoted as "moderately large". the three components of beam theory, namely, the force-stress relations, the stress-strain relations, and the strain displacement relations are implemented individually and combined numerically at solution time (the complete expressions can be found in Ref. 101)

The rotor equations compute coupled flap-lag-torsion beam theory, using a finite element discretization, and a modal coordinate transformations, which transform the governing partial differential equations of the blades into ordinary differential equations. The generalized displacement and velocity coordinates of the blade modes are then included in the state vector and can be solved for. Blade inertial forces are computed using the beam theory described above. Blade aerodynamics are caluclated with blade element theory, and are quasi-steady, with look-up tables for lift, drag and pitching moment coefficients as a function of Mach number and incidence angle, and radial flow drag corrections [102]. The inflow model is used to calculate the induced velocity on the airfoil, which modifies the perpendicular component of airfoil velocity U_P [12], and also the tangential component U_T when the inflow model provides an induced velocity component in that direction (such as free-wake models).

The non-linear equations of motion of the fuselage are formulated in the body fixed coordinate system with the assumption that the aircraft body is rigid. Aerodynamic look-up tables are available to provide aerodynamic forces and moments produced by the user-defined fuselage and/or empennages (depends on configuration). Additional rotors, such as tail rotors or pusher-propellers, can be modeled as Bailey momentum theory type rotors [131]. The equations of motion for the body include the force and moment equilibrium equations as well as the kinematic relationship between the aircraft body rates and the Euler rates.

2.2.1 Numerical Solution Methods

Three types of solutions to the equations of motion are available in the flight dynamics simulation, which correspond directly to the three types of analysis defined in Chap. 1. They are: (i) trim (steady-state analysis), (ii) time marching response (transient analysis), and (iii) full aircraft perturbation models (linearized analysis). The calculation of a steady state equilibrium condition, or trim, is formulated as a system of nonlinear algebraic equations, and does not require that the mathematical model be in ODE form. In particular, free wake or CFD-type calculation of rotor inflow can be used directly. All trim calculations for the fully coupled aircraft results were performed using the free wake in its original, finite difference-based formulation. HeliUM provides the MFW with the blade motion, including flapping and pitching, and the MFW returns predictions of inflow at the Gaussian quadrature points on the blade. The time marching response to pilot inputs is formulated as the solution of a system of ODEs, but portions of the models not in ODE form, such as MFW, can be used (see Ref. 98 for details concerning the coupling of these portions). For trim and time marching, the aircraft body equations of motion can be removed to create a "wind-tunnel" condition in which the shaft is held in a fixed position. In Chapters 3 through 6 , for the identification of perturbation inflow models, this wind-tunnel condition will be used. This must be done because the identification procedure requires a time-marching solution in which the helicopter states do not diverge. Helicopters are, however, almost always unstable without feedback from either a pilot or control system. Using the wind-tunnel mode ensures that the time-

marching solutions stay within the vicinity of trim. Only in chapter 7 will the Euler rigid-body equations of motion for the entire aircraft be included, with more details given accordingly. The third type of solution, i.e., linearized analysis, performs the extraction of a linearized model in state-space form, as detailed in Section 1.1.3, so long as the equations are described in ordinary differential form (i.e. not with MFW).

2.2.2 Rotor Inflow Modeling

Several options are available in HeliUM for the modeling of inflow across the rotor disk. The primary option for single main rotor helicopter is the Peters-He finite state wake model [26]. This implementation allows the user to set the number of inflow modes and harmonics that will be used. In its 3 state form, the equations simplify to the Pitt-Peters model [25]. For a generic rotor configuration (single main rotor, coaxial rotor, tilt rotor, tandem, etc.) the Maryland Free Wake (MFW) model is available. Specifically for coaxial configurations, there are three momentum theory based dynamic models used at various times in this dissertation. Lastly, the identified state-space inflow model that this dissertation focuses on defining can be utilized.

2.2.2.1 Maryland Free-Vortex Wake Model

The Maryland Freewake model is a time-accurate free-vortex wake method (FVM) model [103] based on the equation of vorticity transport [104]. Each blade

is modeled as a distribution of vortex singularities (bound vortices) in the flow field using the Weissinger-L lifting surface model [105]. The wake from each rotor blade consists of a vortex sheet and a concentrated tip vortex. In the present work, the near wake is assumed to be rigid and fixed to the blade. The near wake is truncated at 30° behind each blade, and is coupled by means of a circulation-preserving boundary condition to the far wake consisting of a single rolled-up tip vortices trailing from each blade. These trailed tip vortices are modeled as a set of connected discretized vortex filaments, with positions defined by Lagrangian markers that are connected by straight-line segments. These connected filaments approximate the otherwise curved vortex filaments; see Fig. 2.2. These markers are free to convect to force-free locations under the influence of the local velocity field. The motion of each Lagrangian marker is defined by the governing equation of motion for a fluid particle:

$$\frac{d\boldsymbol{r}}{dt} = \boldsymbol{V}(\boldsymbol{r}) \tag{2.2}$$

The velocity field $\boldsymbol{V}$ is the combination of the freestream velocity and the velocity induced by sources of vorticity, i.e. the bound vortex on each blade, the near wake of each blade, and the far wake of each blade. The induced velocity at any location due to one vortex element is computed by application of the Biot-Savart law which can be written as [12]:

$$\boldsymbol{V}_i = \frac{\Gamma}{4\pi} \int_\ell \frac{d\boldsymbol{\ell} \times \boldsymbol{r} v}{|\tilde{r}|^3} \tag{2.3}$$

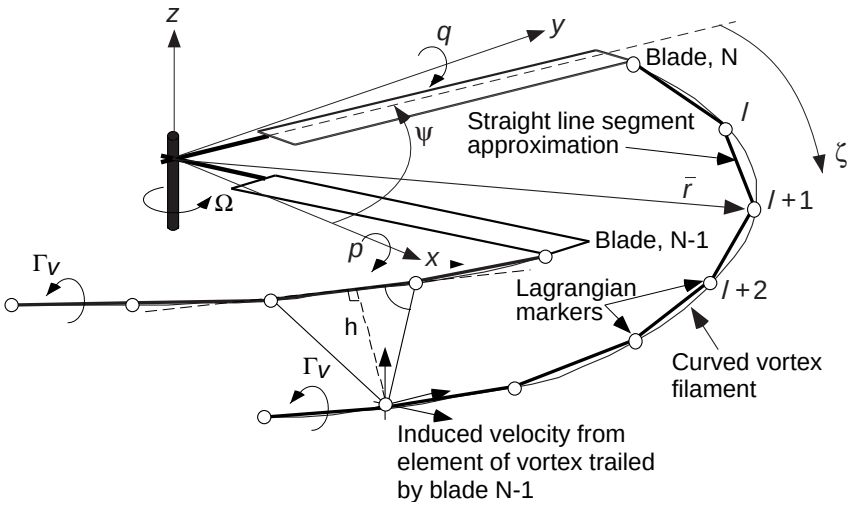

Figure 2.2: Schematic showing the Lagrangian markers used to represent the rotor wake [106].

where Γ is the circulation and $\tilde{r}$ is the distance of the point from the vortex line element $\boldsymbol{\ell}$. The total induced velocity at a location is therefore calculated by numerically integrating the induced velocity contribution from each vortex element over the entire flow field.

The motion of the trailed tip vortex filaments is obtained by solving the governing equation (Eq.(2.2)) using a time-accurate, two-step backward, predictor-corrector scheme (PC2B) that was developed by Bhagwat and Leishman [65]. This scheme results in a prediction of the induced velocity field that is second-order accurate [106]. As such, the model is not in state-space form and a linearized dynamic wake model cannot be extracted numerically by perturbing states and controls. Therefore, while trim calculations and time marching simulations can be performed with the MFW, linearized analyses cannot.

The MFW results in this work were obtained using tip trailed vortex filaments discretized with straight segments of length $\Delta\psi = 10°$, with the length of each filament equal to six rotor revolutions or 2160°. Shed vorticity was neglected. Blade dynamics do affect the MFW model, primarily by affecting the location first Lagrangian Marker of the tip vortex. For this purpose, the tip location of the flexible blades are inserted from HeliUM. The flap rates also affect the bound circulation strength and therefore the near wake strength.

There is no requirement that the point used for calculation of induced velocity be at any particular location, and so this equation can be used to compute the induced velocity at any point on and off the rotor.

2.2.2.2 Isolated Rotor Model

The simplest model is the "Isolated Rotor" model. In this model, each rotor is modeled as an isolated single main rotor using Pitt-Peters inflow models. The rotors operate without any input or change from the other rotor. If the rotors were sufficiently spaced (as in many rotor radii away) this model would likely be accurate, as influence from a vortex decays as a function of the distance cubed, making far off vortices have very little effect. This model is often used (as in Ref. 38) in high speed forward flight, and likewise will only be used in forward flight for this dissertation. The assumption here is that the wake is swept backwards away from the rotor quickly at high speeds and therefore has little influence on the other rotor, or even on itself.

The inflow dynamics are instead dominated by the rotor's few vortex segments that are still in the vicinity of the rotor disk.

2.2.2.3 Climbing Rotor Model

The "Climbing Lower Rotor" theory is based on Ref. 38, and will be used for comparisons to MFW responses in hover in Chap. 6. In hover, the assumption that the wake is swept away from the rotors is not valid, therefore some form of interference must be utilized. The Climbing Lower Rotor theory first models each rotor as an isolated single main rotor using Pitt-Peters model. It then places only the lower rotor in a climb equal to the upper rotor's *trimmed* average inflow.

In the special case of hover, with pure axial climb velocity μ_c, the $[L]^{-1}$ matrix from the Pitt-Peters model (Eq.(1.10)) can be written as:

$$[L]^{-1} = \begin{bmatrix} 2\lambda_m - 2\mu_c & 0 & 0 \\ 0 & \lambda_m - \mu_c/2 & 0 \\ 0 & 0 & \lambda_m - \mu_c/2 \end{bmatrix} \tag{2.4}$$

where λ_m is the solution to the momentum theory equation:

$$\lambda_m(\lambda_m - \mu_c) = C_T/2 \tag{2.5}$$

Therefore when the lower rotor is placed in a climb, the $[L]^{-1}$ matrix is changed according to Eq.(2.4) and Eq.(2.5). No other term in the Pitt-Peters model changes and so it is solved in the typical fashion. However, for aerodynamic loads calculations, the total downwash at a given radial and azimuthal station on the lower rotor

is now:

$$\tilde{v}_i^L(\tilde{r},\psi) = \underline{\mu_c^L} + \lambda_0 + \lambda_{1s}\tilde{r}\sin\psi + \lambda_{1c}\tilde{r}\cos\psi \tag{2.6}$$

Unlike most of the static models, this model assumes that the upper rotor's *vena contracta* has not yet contracted because the rotors are so closely spaced. Therefore the climb acts upon the whole lower rotor. This model has interference from the upper to lower rotor in a static sense, but not in a dynamic sense. The climb velocity of the lower rotor does not change with perturbations to the upper rotor inflow. It should be noted that this is not the intended usage for the Peters-He model, but rather an ad-hoc assumption that has been made for comparison. This work does not suggest that this model is in any way valid, but rather uses this model to make a point; that simplified assumptions will not necessarily work for coaxials.

2.2.2.4 Dynamic Climb Model

The third model used in this dissertation, named the "Dynamic Climb" model, more accurately follows Ref. 38 and uses the reference's dynamic interference terms for each rotor. A schematic of this inflow model is shown in Fig. 2.3.

The rotor disks of the coaxial are shown in the figure as the two horizontal black lines connected by the thicker black vertical line which represents the shaft. This model assumes that the *vena contracta* does not contract by the time it impinges the second rotor. It does, of course, contract by a small amount, but due to the close rotor spacing this contraction is considered negligible.

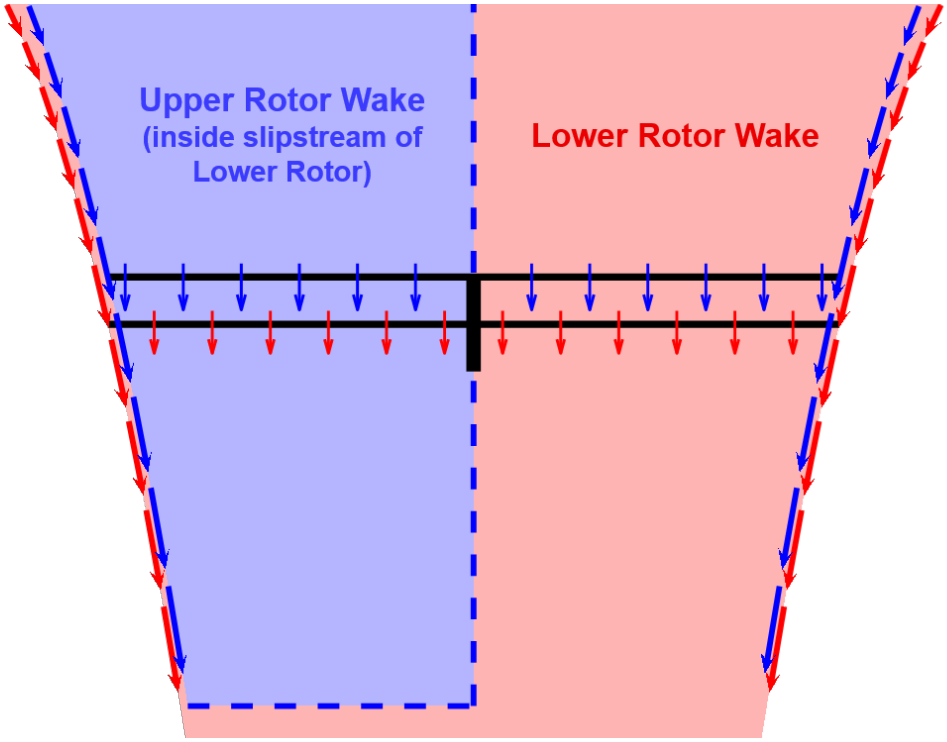

Figure 2.3: Schematic showing the Dynamic Climb coaxial rotor wake.

This model implements each rotor separately as a 3 state Pitt-Peters inflow model, as shown in Eq.(1.10. Furthermore, this model uses standard analytical values (of a single main rotor) for wake distortion and curvature to modify the inflow to account for tip-path plane perturbations (this will be explained further in Sec. 2.2.2.5). The Dynamic Climb model assumes that each rotor is in a climb equal to a percentage of the other rotor's average induced inflow. This means that unlike the climbing lower rotor theory, both rotors affect each other in this model. The climb velocities for the upper rotor and lower rotor are given as:

$$\mu_c^U = 0.86 * \lambda_0^L$$
$$\mu_c^L = 1.13 * \lambda_0^U \tag{2.7}$$

These climb velocities affect the $[L]$ matrix in the Pitt-Peters model for each rotor, according to Eqs.(2.4) and (2.5). The Pitt-Peters models for both rotors then calculate the self induced velocity for each rotor separately. Finally, the total induced inflow on each rotor be the Peters-He finite state wake inflow *plus* the climb velocity produced by the other rotor. Therefore the downwash equations (Eq.(1.9)) for the upper and lower rotors at a given radial and azimuthal station are:

$$\tilde{v}_i^U(\tilde{r},\psi) = \underline{\mu_c^U} + \lambda_0^U + \lambda_{1s}^U \tilde{r}\sin\psi + \lambda_{1c}^U \tilde{r}\cos\psi \tag{2.8}$$

$$\tilde{v}_i^L(\tilde{r},\psi) = \underline{\mu_c^L} + \lambda_0^L + \lambda_{1s}^L \tilde{r}\sin\psi + \lambda_{1c}^L \tilde{r}\cos\psi \tag{2.9}$$

This model will be called the "Dynamic Climb" model in this dissertation. Whereas the climbing lower rotor theory used the *trimmed* average inflow to define the climb, this theory allows the climb velocity to change in time. As each rotors average inflow changes in time, the climb velocities associated with each rotor changes instantaneously, according to Eq.(2.7). Therefore the $[L]$ matrix of a rotor, and consequently the derivative the rotors average inflow, is dependent on the average inflow of the other rotor. Therefore this model couples the rotors dynamically and changes the poles of the inflow system. The dynamic coupling only extends, however, to the average inflow. Changes in inflow harmonics on one rotor do not cause changes in inflow on the other rotor.

This method is easily implemented into existing flight dynamic simulations for single main rotors because it only uses the Pitt-Peters dynamic inflow equations applied to a climb (or may use the equivalent 3 state Peters-He finite state model

if necessary, which are typically already available in the simulation. Ref. 38 shows that this approach has been shown to work well for steady analysis, being capable of matching flight test results of measured hub moments and trim rotor controls, across a full range of flight speeds (0-240 kts, but at each velocity, there are new percentages in Eq.(2.7)). Ref. 38 also demonstrates the accuracy of this model in a dynamic sense. They show a comparison between frequency responses of flight data and the model. The responses shown are roll and pitch rate of the aircraft to pilot cyclic stick, at hover, 180 kts and 200 kts. Generally the frequency responses captured the flight data well, however there were several differences which required updates of the physical parameters of the model to better match the flight data.

2.2.2.5 Identified State-space Models

This section presents the structure of the inflow mode to be used in the identification study. The single rotor case is discussed first, followed by the extension to coaxial rotors.

Single Main Rotor Model Structure

Following the original work of Pitt and Peters [25], the inflow is written as

$$\tilde{v}_i(\tilde{r},\psi) = \tilde{v}_{\text{trim}}(\tilde{r},\psi) + \lambda_0 + \lambda_{1s}\tilde{r}\sin\psi + \lambda_{1c}\tilde{r}\cos\psi \tag{2.10}$$

where $\tilde{v}_{\text{trim}}(\tilde{r},\psi)$ is the induced velocity of the trim state. Note that within this work, the above inflow distribution is defined as the one that occurs when a blade is located at the specific location over the disc. The analysis does not determine the

inflow at disc locations where a blade is not present. Also the inflow coefficients λ in Eq.(2.10) are considered to be perturbations from trim. Therefore each should be considered to actually be $\Delta\lambda$, with the Δ dropped for convenience.

The induced velocity perturbation states λ_0, λ_{1s} and λ_{1c} are related to the perturbations of the rotor thrust, and roll and pitch moments (ΔC_T, ΔC_L and ΔC_M) by an ODE in the same form as the Pitt-Peters model (Eq.(1.10). For clarity, the matrix $[\bar{L}]$ will be defined as equivalent to $[L]^{-1}$. For hover, the matrices in the Pitt-Peters model take on a diagonal form:

$$\begin{bmatrix} M_{11} & 0 & 0 \\ 0 & M_{22} & 0 \\ 0 & 0 & M_{33} \end{bmatrix} \begin{Bmatrix} \overset{*}{\lambda}_0 \\ \overset{*}{\lambda}_{1s} \\ \overset{*}{\lambda}_{1c} \end{Bmatrix} + \begin{bmatrix} \bar{L}_{11} & 0 & 0 \\ 0 & \bar{L}_{22} & 0 \\ 0 & 0 & \bar{L}_{33} \end{bmatrix} \begin{Bmatrix} \lambda_0 \\ \lambda_{1s} \\ \lambda_{1c} \end{Bmatrix} = \begin{Bmatrix} \Delta C_T \\ \Delta C_L \\ \Delta C_M \end{Bmatrix} \tag{2.11}$$

In forward flight the longitudinal inflow λ_{1c} and average inflow λ_0 coefficients are coupled in the Pitt-Peters model (lateral inflow λ_{1s} remains uncoupled). Therefore the matrices take on a different form, with two extra terms added to the $[\bar{L}]$ matrix:

$$\begin{bmatrix} M_{11} & 0 & 0 \\ 0 & M_{22} & 0 \\ 0 & 0 & M_{33} \end{bmatrix} \begin{Bmatrix} \overset{*}{\lambda}_0 \\ \overset{*}{\lambda}_{1s} \\ \overset{*}{\lambda}_{1c} \end{Bmatrix} + \begin{bmatrix} \bar{L}_{11} & 0 & \bar{L}_{13} \\ 0 & \bar{L}_{22} & 0 \\ \bar{L}_{31} & 0 & \bar{L}_{33} \end{bmatrix} \begin{Bmatrix} \lambda_0 \\ \lambda_{1s} \\ \lambda_{1c} \end{Bmatrix} = \begin{Bmatrix} \Delta C_T \\ \Delta C_L \\ \Delta C_M \end{Bmatrix} \tag{2.12}$$

Higher order dynamics that are not capable of being captured commonly occur in the free wake data. In particular, there is often a higher phase roll-off than can not be captured by the above systems of equations. These phase roll-offs are well captured with the addition of a time delay between the forcing and the inflow response. Therefore, for some identifications in this dissertation, the right hand side of the above equations is modified to delay the forcing:

$$\cdots = \left\{ \begin{array}{c} \Delta C_T \\ \Delta C_L \\ \Delta C_M \end{array} \right\} \left(t - \left[\begin{array}{ccc} \tau_{11} & 0 & \tau_{13}{}^{*} \\ 0 & \tau_{22} & 0 \\ \tau_{31}{}^{*} & 0 & \tau_{33} \end{array} \right] \right) \tag{2.13}$$

* Forward flight only

The time delay matrix τ is written this way for conciseness, however its meaning requires further clarification. For example, consider Eq.(2.13) with the modification that all of the elements in $[M]$,$[\bar{L}]$, and $[\tau]$ are non-zero:

$$[M] \left\{ \begin{array}{c} \overset{*}{\lambda}_0 \\ \overset{*}{\lambda}_{1s} \\ \overset{*}{\lambda}_{1c} \end{array} \right\} + \left[\bar{L}\right] \left\{ \begin{array}{c} \lambda_0 \\ \lambda_{1s} \\ \lambda_{1c} \end{array} \right\} = \left\{ \begin{array}{c} \Delta C_T \\ \Delta C_L \\ \Delta C_M \end{array} \right\} \left(t - \left[\begin{array}{ccc} \tau_{11} & \tau_{12} & \tau_{13} \\ \tau_{21} & \tau_{22} & \tau_{23} \\ \tau_{31} & \tau_{32} & \tau_{33} \end{array} \right] \right) \tag{2.14}$$

The time delay matrix always has the dimensions: number of states (inflow coefficients) by number of inputs (aerodynamic forcing coefficients). If each column has each of its parameters equivalent to each other, i.e., $\tau_{11} = \tau_{21} = \tau_{31}$, $\tau_{12} = \tau_{22} = \tau_{32}$, and $\tau_{13} = \tau_{23} = \tau_{33}$, then a given input is always delayed by the same amount, and the time delay can be written more simply as:

$$[M] \left\{ \begin{array}{c} \overset{*}{\lambda}_0 \\ \overset{*}{\lambda}_{1s} \\ \overset{*}{\lambda}_{1c} \end{array} \right\} + \left[\bar{L}\right] \left\{ \begin{array}{c} \lambda_0 \\ \lambda_{1s} \\ \lambda_{1c} \end{array} \right\} = \left\{ \begin{array}{c} \Delta C_T(t - \tau_{11}) \\ \Delta C_L(t - \tau_{22}) \\ \Delta C_M(t - \tau_{33}) \end{array} \right\} \tag{2.15}$$

However if the column parameters are not equivalent, the time delay matrix form actually describes that the forcing term should be delayed a different amount of time depending on which inflow coefficient is being calculated. This means that the

system of equations needs to be solved once fully for each inflow coefficient, using only the time delays from the given row of the $[\tau]$ matrix. For the example shown in Eq.(2.14), the equations would need to be solved three times, for each of the three states, i.e.,

$$\begin{cases} \text{for } \lambda_0: \quad [M]\begin{Bmatrix} \overset{*}{\lambda}_0 \\ \overset{*}{\underline{\lambda}}_{1s} \\ \overset{*}{\underline{\lambda}}_{1c} \end{Bmatrix} + \left[\bar{L}\right]\begin{Bmatrix} \lambda_0 \\ \underline{\lambda_{1s}} \\ \underline{\lambda_{1c}} \end{Bmatrix} = \begin{Bmatrix} \Delta C_T(t-\tau_{11}) \\ \Delta C_L(t-\tau_{12}) \\ \Delta C_M(t-\tau_{13}) \end{Bmatrix} \\ \text{for } \lambda_{1s}: \quad [M]\begin{Bmatrix} \overset{*}{\underline{\lambda}}_0 \\ \overset{*}{\lambda}_{1s} \\ \overset{*}{\underline{\lambda}}_{1c} \end{Bmatrix} + \left[\bar{L}\right]\begin{Bmatrix} \underline{\lambda_0} \\ \lambda_{1s} \\ \underline{\lambda_{1c}} \end{Bmatrix} = \begin{Bmatrix} \Delta C_T(t-\tau_{21}) \\ \Delta C_L(t-\tau_{22}) \\ \Delta C_M(t-\tau_{23}) \end{Bmatrix} \\ \text{for } \lambda_{1c}: \quad [M]\begin{Bmatrix} \overset{*}{\underline{\lambda}}_0 \\ \overset{*}{\underline{\lambda}}_{1s} \\ \overset{*}{\lambda}_{1c} \end{Bmatrix} + \left[\bar{L}\right]\begin{Bmatrix} \underline{\lambda_0} \\ \underline{\lambda_{1s}} \\ \lambda_{1c} \end{Bmatrix} = \begin{Bmatrix} \Delta C_T(t-\tau_{31}) \\ \Delta C_L(t-\tau_{32}) \\ \Delta C_M(t-\tau_{33}) \end{Bmatrix} \end{cases} \tag{2.16}$$

The other inflow coefficients that are calculated, which are underlined in Eq.(2.16), are incorrectly delayed and therefore are only used for the numerical calculation of the ODE system.

The τ matrix is written in the form shown in Eq.(2.14) not only for conciseness but also for the method in which it is more often utilized. ODEs with time delays can not be directly solved by a generic ODE solver, and specifically require a Delay

Differential Equation (DDE) solver. To avoid this complication, the state-space equations need to be converted into a different form. Eq.(2.14) can be transformed with the Laplace transform:

$$\left[\frac{\boldsymbol{\lambda}(s)}{\mathbf{C}(s)}\right] = \left[[M]\, s + \left[\bar{L}\right]\right]^{-1} \circ \underbrace{\exp^{*}\left(-[\tau]\, s\right)}_{[\tau(s)]} \tag{2.17}$$

where $\exp^{*}$ is element-by-element scalar exponential

The second half of Eq.(2.17) is the time delay transfer function matrix $[\tau(s)]$. Padé approximations are then used to convert the time delay transfer function matrix $[\tau(s)]$ into the approximate time delay transfer function matrix $[\hat{\tau}(s)]$ [107]. The . Each element of the time delay transfer function matrix is written as:

$$\tau_{ij}(s) = e^{-\tau_{ij}s} = \frac{e^{-\tau_{ij}s/2}}{e^{\tau_{ij}s/2}} \approx \frac{1 - \tau s/2 + \tau^2 s^2/12\ldots}{1 + \tau s/2 + \tau^2 s^2/12\ldots} = \hat{\tau}_{ij}(s) \tag{2.18}$$

The Padé approximant is truncated to the first order term or the second order term, depending on the length of the time delay. Larger time delays require the second order term to ensure that the error in the approximation is small. The approximate time delay transfer function matrix, $[\hat{\tau}(s)]$, can now be used to modify the state-space model written in transfer function form:

$$\left[\frac{\boldsymbol{\lambda}(s)}{\mathbf{C}(s)}\right]_{TDA} = \frac{\boldsymbol{\lambda}(s)}{\mathbf{C}(s)} \circ [\hat{\tau}(s)] \tag{2.19}$$

(where the "TDA" subscript indicates "Time Delays Absorbed"). The new transfer function, with the time delays absorbed, can then be converted back to state-space form through state-space minimal realization [108]. The new state-space form will have added states that correspond to the poles and zeros of the

time delays. The number of added states will often be quite large, but the systems themselves are typically still computationally inexpensive.

As will be shown, the definition of the inflow is different from the classical ones of the original work of Pitt and Peters [25], and they are explicit functions of time while their definition does not contain any integrations over the disc.

The basic assumptions behind the above formulation are as follows: (i) the above systems of equations are linear, and therefore, periodic excitation of the right hand side forcing vector at a single frequency, ω, yields a response of λ_0, λ_{1s}, and λ_{1c} in the same frequency; (ii) the $[3 \times 3]$ matrices $[M]$ and $\left[\bar{L}\right]$ are constants and not functions of ω.

Definition of the States

Because the dynamic inflow model is based on the assumption of a solid disk [25, 109], some care in the definition of the states is necessary when extracting the model from a theory that considers a finite number of blades. The baseline definition from Ref. 25 describes the inflow distribution over the rotor disk as uniform with azimuthal variation:

$$\lambda(\psi, \tilde{r}) = \lambda_0 + \lambda_{1s}\tilde{r}\sin\psi + \lambda_{1c}\, r\cos\psi \tag{2.20}$$

while the inflow coefficients are described as an integration over the rotor disk:

$$\lambda_0 = \frac{1}{\pi}\int\int \lambda\, dA \tag{2.21}$$

which is generally decomposed into integrations over the azimuth angle $\psi = \Omega t$ and the nondimensional spanwise coordinate r where $dA = \tilde{r} \cdot d\tilde{r} \cdot d\psi$. When using an

aerodynamic theory that models individual blades, this definition is not appropriate for a state, because it requires not only information at the current time, but also at all other times required to compute the azimuth integral: e.g., over the previous rotor revolution. Therefore, the following definition is used in the present study:

$$\lambda_0(t) = \frac{1}{N_b} \sum_{n=1}^{N_b} \int_0^1 \lambda(n, \tilde{r})\, d\tilde{r} \tag{2.22}$$

Where $\lambda(n, \tilde{r})$ indicates the induced inflow on the n-th blade at the radial location $\tilde{r}$ at the given point in time. With this definition, which simply reinterprets the concept of Eq.(2.21) of an integral over one rotor revolution, λ_0 can be rigorously used as a state. The λ_{1c} and λ_{1s} harmonics are similarly defined.

The slightly different roles of time t and blade azimuth ψ also need to be kept in mind. Consider for example the definition of λ_{1c} (λ_c in [25]):

$$\lambda_{1c} = \frac{4}{\pi} \int \int \lambda\, r \cos\psi\, dA \tag{2.23}$$

then transform the integral and indicate explicitly the dependency on time:

$$\lambda_{1c}(t) = \frac{4}{\pi} \int_0^{2\pi} \int_0^1 \lambda(t; \psi, \tilde{r})\, \tilde{r} \cos\psi\, \tilde{r} d\tilde{r}\, d\psi \tag{2.24}$$

For a solution over a disk, r and ψ both play the role of spatial variables (the integral could have just as well been decomposed according to $dA = dx\, dy$ using Cartesian coordinates), and t and $\psi = \Omega t$ are interchangeable. For a solution with individual blades, *ψ and t are not interchangeable*. For example, the λ_{1c} time response to a given input depends on the initial location of the blades around the azimuth, whereas, if the rotor is considered as a solid disk, it does not. Therefore, it may be

conceptually useful to write the definition of λ_{1c} as:

$$\lambda_{1c}(t) = \frac{6}{N_b} \sum_{n=1}^{N_b} \int_0^1 \lambda(n, \tilde{r}) \tilde{r} \cos \psi_n \, d\tilde{r} \tag{2.25}$$

where ψ_n is the azimuth angle of the n-th blade at time t. Similarly, the definition of λ_{1s} will be written as:

$$\lambda_{1s}(t) = \frac{6}{N_b} \sum_{n=1}^{N_b} \int_0^1 \lambda(n, \tilde{r}) \tilde{r} \sin \psi_n \, d\tilde{r} \tag{2.26}$$

Wake Curvature and Distortion for Single Main Rotors

The Pitt-Peters inflow model, in its basic form, Eq.(2.12), is not capable of capturing the effects of wake distortion due to body angular rates and rotor flapping. Asa a consequence, when used in a flight dynamic simulation, magnitude, and often even sign, of the off-axis response to pilot inputs were often inconsistent with the flight test data [110–112]. Keller et al. [81, 82] proposed that perturbations to the tip path plane due to angular rates and blade flapping cause the wake to curve and distort in shape. For example, Fig. 2.4, from Ref. 82, shows schematically how the wake distorts in response to a pitch rate input. This effects the longitudinal inflow (lateral inflow for roll rate). Also, in the theory, pitch rate q is considered equivalent to negative longitudinal flap rate $-\overset{*}{\beta}_{1c}$, and roll rate p is considered equivalent to negative lateral flap rate $-\overset{*}{\beta}_{1s}$, in the sense that they produce the same tip path plane motion, and therefore the same wake distortion. This would be rigorously true for a teetering rotor, and it is reasonably close to true for other rotor types as long as the flap hinge offset (or equivalent hinge offset for hingeless rotors) is small.

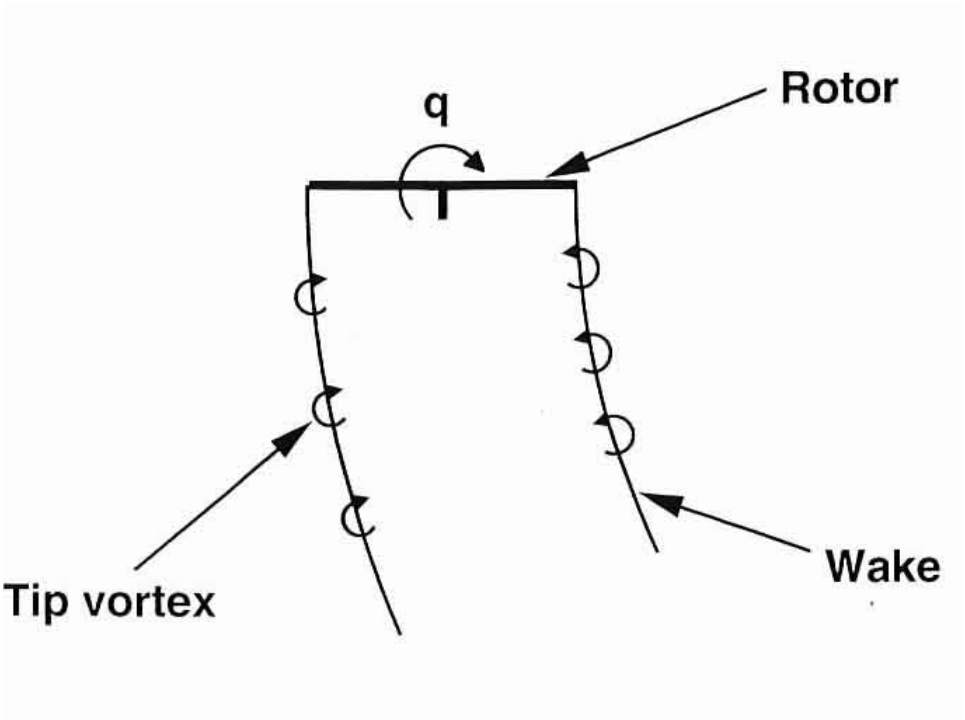

Figure 2.4: Wake distortion in response to a pitch rate input (from Ref. 82).

A modification to the Pitt-Peters models for inflow was proposed in Ref. 81. The equations were originally written as:

$$\tau_i \hat{v}_c' + \hat{v}_c = -K_L C_M + K_T \mu_x + K_R \left(\Delta q/\Omega + a_1'\right) \tag{2.27}$$

$$\tau_i \hat{v}' s + \hat{v}_s = -K_L C_L + K_T \mu_y + K_R \left(\Delta p/\Omega + b_1'\right)$$

where:

$$-K_L = \frac{-1}{\bar{v}_0} = L_{22} = L_{33}$$

$$\tau_i = M_{22} L_{22} = M_{33} L_{33}$$

$$a_1' = -\overset{*}{\beta}_{1c}$$

$$b_1' = -\overset{*}{\beta}_{1s}$$

These equations can be rewritten as:

$$[M]\,[L]\begin{Bmatrix} \overset{*}{\lambda}_0 \\ \overset{*}{\lambda}_{1s} \\ \overset{*}{\lambda}_{1c} \end{Bmatrix} + \begin{Bmatrix} \lambda_0 \\ \lambda_{1s} \\ \lambda_{1c} \end{Bmatrix} = [L]\begin{Bmatrix} \Delta C_T \\ \Delta C_L \\ \Delta C_M \end{Bmatrix} + \begin{Bmatrix} 0 \\ K_T\mu_y + K_R\left\{\dfrac{\Delta p}{\Omega} - \overset{*}{\beta}_{1s}\right\} \\ K_T\mu_x + K_R\left\{\dfrac{\Delta q}{\Omega} - \overset{*}{\beta}_{1c}\right\} \end{Bmatrix} \tag{2.28}$$

or equivalently:

$$[M]\begin{Bmatrix} \overset{*}{\lambda}_0 \\ \overset{*}{\lambda}_{1s} \\ \overset{*}{\lambda}_{1c} \end{Bmatrix} + [L]^{-1}\begin{Bmatrix} \lambda_0 \\ \lambda_{1s} \\ \lambda_{1c} \end{Bmatrix} = \begin{Bmatrix} \Delta C_T \\ \Delta C_L \\ \Delta C_M \end{Bmatrix} + [L]^{-1}\begin{Bmatrix} 0 \\ K_T\mu_y + K_R\left\{\dfrac{\Delta p}{\Omega} - \Delta\,\overset{*}{\beta}_{1s}\right\} \\ K_T\mu_x + K_R\left\{\dfrac{\Delta q}{\Omega} - \Delta\,\overset{*}{\beta}_{1c}\right\} \end{Bmatrix} \tag{2.29}$$

The equations show that p, q, $\overset{*}{\beta}_{1s}$ and $\overset{*}{\beta}_{1c}$ act as additional inputs. Since there are no changes to the $[M]$ and $[L]$ matrices, there are no additional poles added to the system. Roll, pitch, and flap rates can be described as producing an *equivalent* aerodynamic moment to the rotor, which is given as the rate multiplied by the gain shown above. Also note that the translational velocity components along the x and y rotor axes have a similar effect on the inflow and are described by the K_T terms. This will not be further explored or identified in this dissertation, but the procedure would be similar.

Reference 82 derived an analytical solution for the value of K_R using potential flow theory, which was found to be $K_R = 1.5$. Experimentally, they identified (using frequency domain system identification) K_R from a hovering UH-60 helicopter to be $K_R = 3.0$. They also noted that Ref. 113 identified from flight test data a differently formulated parameter that was equivalent to $K_R = 2.2$. There clearly is some variance in the value of K_R, which might vary depending on the rotor.

However, its ability to capture correctly the off-axis response makes it an important parameter to include in the identification.

Six State Coaxial Rotor Inflow Model

For the coaxial rotor induced inflow, the model can be written as a linearized extension of the Pitt-Peters model, i.e.,

$$\begin{bmatrix} M_{11} & 0 & 0 & M_{14} & 0 & 0 \\ 0 & M_{22} & 0 & 0 & M_{25} & 0 \\ 0 & 0 & M_{33} & 0 & 0 & M_{36} \\ M_{41} & 0 & 0 & M_{44} & 0 & 0 \\ 0 & M_{51} & 0 & 0 & M_{55} & 0 \\ 0 & 0 & M_{61} & 0 & 0 & M_{66} \end{bmatrix} \begin{Bmatrix} \overset{*}{\lambda}{}_0^U \\ \overset{*}{\lambda}{}_{1s}^U \\ \overset{*}{\lambda}{}_{1c}^U \\ \overset{*}{\lambda}{}_0^L \\ \overset{*}{\lambda}{}_{1s}^L \\ \overset{*}{\lambda}{}_{1c}^L \end{Bmatrix} + \begin{bmatrix} \bar{L}_{11} & 0 & 0 & \bar{L}_{14} & 0 & 0 \\ 0 & \bar{L}_{22} & 0 & 0 & \bar{L}_{25} & 0 \\ 0 & 0 & \bar{L}_{33} & 0 & 0 & \bar{L}_{36} \\ \bar{L}_{41} & 0 & 0 & \bar{L}_{44} & 0 & 0 \\ 0 & \bar{L}_{51} & 0 & 0 & \bar{L}_{55} & 0 \\ 0 & 0 & \bar{L}_{61} & 0 & 0 & \bar{L}_{66} \end{bmatrix} \begin{Bmatrix} \lambda_0^U \\ \lambda_{1s}^U \\ \lambda_{1c}^U \\ \lambda_0^L \\ \lambda_{1s}^L \\ \lambda_{1c}^L \end{Bmatrix}$$

$$\cdots = \begin{Bmatrix} \Delta C_T^U \\ \Delta C_L^U \\ \Delta C_M^U \\ \Delta C_T^L \\ \Delta C_L^L \\ \Delta C_M^L \end{Bmatrix} \left(t - \begin{bmatrix} \tau_{11} & 0 & 0 & \tau_{14} & 0 & 0 \\ 0 & \tau_{22} & 0 & 0 & \tau_{25} & 0 \\ 0 & 0 & \tau_{33} & 0 & 0 & \tau_{36} \\ \tau_{41} & 0 & 0 & \tau_{44} & 0 & 0 \\ 0 & \tau_{51} & 0 & 0 & \tau_{55} & 0 \\ 0 & 0 & \tau_{61} & 0 & 0 & \tau_{66} \end{bmatrix} \right) \tag{2.30}$$

$\boldsymbol{\lambda}$ and the aerodynamic loading vector C_T now both have 6 coefficients, 3 per rotor. Upper and lower rotor coefficients are now labeled with a "U" and "L" superscripts respectively. There are now twice as many swashplate controls, i.e., $\boldsymbol{\theta} = \begin{bmatrix} \theta_0^U & \theta_{1S}^U & \theta_{1C}^U & \theta_0^L & \theta_{1S}^L & \theta_{1C}^L \end{bmatrix}^\intercal$. Although these controls are usually linked in coaxial rotor helicopters, they will be treated as individual controls in this study.

Therefore the $[M]$ and $[L]^{-1}$ in Eq.(2.30) are now 6 by 6 constant (for a given flight condition) matrices that define the inflow model, and will be extracted using frequency domain system identification methods, and $[\tau]$ is a 6 by 6 matrix of time delays that approximates the higher order dynamics not explicitly included in the model. The Δ prefixes on the states and inputs are dropped throughout for brevity, except when explicitly necessary.

Twelve State Coaxial Rotor Inflow Model

If six inflow states is not enough to accurately capture the dynamic behavior over a broad frequency range, then more states can be added. In the previous models there was no distinction between the inflow states and the inflow coefficients; they were equivalent. In terms of classical control theory, this means that the output matrix is the identity matrix. More states can be included without adding more inflow coefficients. One choice could be to assume that each of the six coaxial inflow coefficients consists of two states, summed together to make the whole coefficient, i.e.,

$$\underbrace{\begin{Bmatrix} \lambda_0^U \\ \lambda_{1S}^U \\ \lambda_{1C}^U \\ \lambda_0^L \\ \lambda_{1S}^L \\ \lambda_{1C}^L \end{Bmatrix}}_{\boldsymbol{\lambda}} = \underbrace{\begin{Bmatrix} \lambda_{0N}^U \\ \lambda_{1SN}^U \\ \lambda_{1CN}^U \\ \lambda_{0N}^L \\ \lambda_{1SN}^L \\ \lambda_{1CN}^L \end{Bmatrix}}_{\boldsymbol{\lambda_N}} + \underbrace{\begin{Bmatrix} \lambda_{0F}^U \\ \lambda_{1SF}^U \\ \lambda_{1CF}^U \\ \lambda_{0F}^L \\ \lambda_{1SF}^L \\ \lambda_{1CF}^L \end{Bmatrix}}_{\boldsymbol{\lambda_F}} \tag{2.31}$$

The two states are labeled with "N" and "F" added to the original subscripts. Note that Eq.(2.31) can be rewritten as:

$$\underbrace{\begin{Bmatrix} \lambda_0^U \\ \lambda_{1S}^U \\ \lambda_{1C}^U \\ \lambda_0^L \\ \lambda_{1S}^L \\ \lambda_{1C}^L \end{Bmatrix}}_{\boldsymbol{\lambda}} = \begin{bmatrix} 1 & 1 & 0 & 0 & 0 & 0 & 0 & 0 & 0 & 0 & 0 & 0 \\ 0 & 0 & 1 & 1 & 0 & 0 & 0 & 0 & 0 & 0 & 0 & 0 \\ 0 & 0 & 0 & 0 & 1 & 1 & 0 & 0 & 0 & 0 & 0 & 0 \\ 0 & 0 & 0 & 0 & 0 & 0 & 1 & 1 & 0 & 0 & 0 & 0 \\ 0 & 0 & 0 & 0 & 0 & 0 & 0 & 0 & 1 & 1 & 0 & 0 \\ 0 & 0 & 0 & 0 & 0 & 0 & 0 & 0 & 0 & 0 & 1 & 1 \end{bmatrix} \underbrace{\begin{Bmatrix} \lambda_{0N}^U \\ \lambda_{0F}^U \\ \lambda_{1SN}^U \\ \lambda_{1SF}^U \\ \lambda_{1CN}^U \\ \lambda_{1CF}^U \\ \lambda_{0N}^L \\ \lambda_{0F}^L \\ \lambda_{1SN}^L \\ \lambda_{1SF}^L \\ \lambda_{1CN}^L \\ \lambda_{1CF}^L \end{Bmatrix}}_{\boldsymbol{\lambda_{NF}}} \tag{2.32}$$

The new set of states can all be contained in the new state vector, labeled as $\boldsymbol{\lambda_{NF}}$. The output matrix is no longer the identity matrix but is instead the block diagonal matrix shown in Eq.(2.32). With this inflow output equation the inflow state equations can be written as:

$$[M]\begin{Bmatrix} \overset{*}{\lambda}{}^{U}_{0N} \\ \overset{*}{\lambda}{}^{U}_{0F} \\ \overset{*}{\lambda}{}^{U}_{1SN} \\ \overset{*}{\lambda}{}^{U}_{1SF} \\ \overset{*}{\lambda}{}^{U}_{1CN} \\ \overset{*}{\lambda}{}^{U}_{1CF} \\ \overset{*}{\lambda}{}^{L}_{0N} \\ \overset{*}{\lambda}{}^{L}_{0F} \\ \overset{*}{\lambda}{}^{L}_{1SN} \\ \overset{*}{\lambda}{}^{L}_{1SF} \\ \overset{*}{\lambda}{}^{L}_{1CN} \\ \overset{*}{\lambda}{}^{L}_{1CF} \end{Bmatrix} + \left[L^{-1}\right]\begin{Bmatrix} \lambda^{U}_{0N} \\ \lambda^{U}_{0F} \\ \lambda^{U}_{1SN} \\ \lambda^{U}_{1SF} \\ \lambda^{U}_{1CN} \\ \lambda^{U}_{1CF} \\ \lambda^{L}_{0N} \\ \lambda^{L}_{0F} \\ \lambda^{L}_{1SN} \\ \lambda^{L}_{1SF} \\ \lambda^{L}_{1CN} \\ \lambda^{L}_{1CF} \end{Bmatrix} = [B]\begin{Bmatrix} \Delta C^{U}_{T} \\ \Delta C^{U}_{L} \\ \Delta C^{U}_{M} \\ \Delta C^{L}_{T} \\ \Delta C^{L}_{L} \\ \Delta C^{L}_{M} \end{Bmatrix} \tag{2.33}$$

The $[M]$ and $[L]^{-1}$ matrices would then both be 12x12 matrices. In the 6 state coaxial inflow system, it was assumed that the form of the terms in the matrices would mirror the Pitt-Peters form, and many of the terms are assumed to be zero. But in this case, with larger matrices, the forms would need to be determined. The equation also has a $[B]$ matrix now which is required in order to make the dimensions compatible with the input vector. This $[B]$ matrix would therefore need to be 12x6 and its form would also need to be determined. Another way of writing this system involves making the following substitutions:

$$[G] = [M]^{-1}[B] \qquad \& \qquad [F] = -[M]^{-1}[L]^{-1} \tag{2.34}$$

Then the inflow state equations can be written as:

$$\begin{Bmatrix} \overset{*}{\lambda}{}^{U}_{0N} \\ \overset{*}{\lambda}{}^{U}_{0F} \\ \overset{*}{\lambda}{}^{U}_{1SN} \\ \overset{*}{\lambda}{}^{U}_{1SF} \\ \overset{*}{\lambda}{}^{U}_{1CN} \\ \overset{*}{\lambda}{}^{U}_{1CF} \\ \overset{*}{\lambda}{}^{L}_{0N} \\ \overset{*}{\lambda}{}^{L}_{0F} \\ \overset{*}{\lambda}{}^{L}_{1SN} \\ \overset{*}{\lambda}{}^{L}_{1SF} \\ \overset{*}{\lambda}{}^{L}_{1CN} \\ \overset{*}{\lambda}{}^{L}_{1CF} \end{Bmatrix} = [F] \begin{Bmatrix} \lambda^{U}_{0N} \\ \lambda^{U}_{0F} \\ \lambda^{U}_{1SN} \\ \lambda^{U}_{1SF} \\ \lambda^{U}_{1CN} \\ \lambda^{U}_{1CF} \\ \lambda^{L}_{0N} \\ \lambda^{L}_{0F} \\ \lambda^{L}_{1SN} \\ \lambda^{L}_{1SF} \\ \lambda^{L}_{1CN} \\ \lambda^{L}_{1CF} \end{Bmatrix} + [G] \begin{Bmatrix} \Delta C^{U}_{T} \\ \Delta C^{U}_{L} \\ \Delta C^{U}_{M} \\ \Delta C^{L}_{T} \\ \Delta C^{L}_{L} \\ \Delta C^{L}_{M} \end{Bmatrix} \tag{2.35}$$

In this case, the $[F]$ matrix would be 12x12 and the $[G]$ matrix would be 12x6. Since the forms of the terms inside the matrices are unknown for either way that the equations are written, Eq.(2.35) offers the advantage that there are less unknown matrix terms.

Coaxial Rotor Inflow Model with Wake Distortion

One further extensions would be to include the wake distortion effects in this 12 state coaxial inflow model. As shown by Eq.(2.29), the flap rates (or equivalent body angular rates) can be considered as additional inputs to the inflow model. Eq.(2.29) could be rewritten so that both the aerodynamic forcing and flap rates appear in the same input vector. So this will be done with the coaxial system. The new inputs will be placed in the input vector nearest to the aerodynamic forging term to which they are most similar. So the lateral flap rates will be after the roll

moments and the longitudinal flap rates will be after the longitudinal moments. The resulting state equation is:

$$\begin{Bmatrix} \overset{*}{\lambda}{}^{U}_{0N} \\ \overset{*}{\lambda}{}^{U}_{0F} \\ \overset{*}{\lambda}{}^{U}_{1SN} \\ \overset{*}{\lambda}{}^{U}_{1SF} \\ \overset{*}{\lambda}{}^{U}_{1CN} \\ \overset{*}{\lambda}{}^{U}_{1CF} \\ \overset{*}{\lambda}{}^{L}_{0N} \\ \overset{*}{\lambda}{}^{L}_{0F} \\ \overset{*}{\lambda}{}^{L}_{1SN} \\ \overset{*}{\lambda}{}^{L}_{1SF} \\ \overset{*}{\lambda}{}^{L}_{1CN} \\ \overset{*}{\lambda}{}^{L}_{1CF} \end{Bmatrix} = [F] \begin{Bmatrix} \lambda^{U}_{0N} \\ \lambda^{U}_{0F} \\ \lambda^{U}_{1SN} \\ \lambda^{U}_{1SF} \\ \lambda^{U}_{1CN} \\ \lambda^{U}_{1CF} \\ \lambda^{L}_{0N} \\ \lambda^{L}_{0F} \\ \lambda^{L}_{1SN} \\ \lambda^{L}_{1SF} \\ \lambda^{L}_{1CN} \\ \lambda^{L}_{1CF} \end{Bmatrix} + [G] \underbrace{\begin{Bmatrix} \Delta C^{U}_{T} \\ \Delta C^{U}_{L} \\ \Delta \overset{*}{\beta}{}^{U}_{1S} \\ \Delta C^{U}_{M} \\ \Delta \overset{*}{\beta}{}^{U}_{1C} \\ \Delta C^{L}_{T} \\ \Delta C^{L}_{L} \\ \Delta \overset{*}{\beta}{}^{L}_{1S} \\ \Delta C^{L}_{M} \\ \Delta \overset{*}{\beta}{}^{L}_{1C} \end{Bmatrix}}_{C_\beta} \tag{2.36}$$

The $[G]$ matrix must now be 12x10 to make the dimensions compatible. Therefore the form of the matrix needs to be further determined. This will be explored in Chap. 6. Lastly, note that though the equations only explicitly write $\overset{*}{\beta}$ terms, they are also meant to implicitly include the body angular rates, as this form keeps the assumption that the body angular rates and the flap rates are equivalent.

2.2.3 Off-Rotor Inflow Modeling

Free vortex wake models must be able to calculate the induced velocity at arbitrary locations of the flow field, because that velocity is needed to define the motion of the blade vortices. This can also be used to compute the velocity induced by the rotor wake at any other points of interest, e.g., on the horizontal tail or on a wing under the hub.

It should be noted that an accurate calculation of the induced velocity at an empennage is difficult, due to the complexity of the flow field, which includes the interaction of the rotor wake vortices with the fuselage, the effects of the empennage on the bound and trailed vorticity, and the role of other configuration dependent elements, such as jet exhaust, tail rotors, and pusher propellers [12]. The models used in this study capture only some of the relevant physics, and do so in an approximate way. On the other hand, these models are adequate for the development and the illustration of the methodologies to extract state-space inflow models, because they are sophisticated and have mathematical characteristics representative of more advanced aerodynamic theories.

A state-space model can be made with either the rotor aerodynamic loading or the rotor induced velocity as inputs, and off-rotor induced velocities as output. This might look very similar to Eq.(2.13), such as:

$$\begin{bmatrix} M_{11} & M_{12} & M_{13} \\ M_{21} & M_{22} & M_{23} \\ M_{31} & M_{32} & M_{33} \end{bmatrix} \begin{Bmatrix} \overset{*}{\lambda}_0 \\ \overset{*}{\lambda}_{1s} \\ \overset{*}{\lambda}_{1c} \end{Bmatrix} + \begin{bmatrix} \bar{L}_{11} & \bar{L}_{12} & \bar{L}_{13} \\ \bar{L}_{21} & \bar{L}_{22} & \bar{L}_{23} \\ \bar{L}_{31} & \bar{L}_{32} & \bar{L}_{33} \end{bmatrix} \begin{Bmatrix} \lambda_0 \\ \lambda_{1s} \\ \lambda_{1c} \end{Bmatrix} \tag{2.37}$$

$$\cdots = \begin{Bmatrix} \Delta C_T \\ \Delta C_L \\ \Delta C_M \end{Bmatrix} \left(t - \begin{bmatrix} \tau_{11} & \tau_{11} & \tau_{13} \\ \tau_{11} & \tau_{22} & \tau_{11} \\ \tau_{31} & \tau_{11} & \tau_{33} \end{bmatrix} \right) \tag{2.38}$$

where $\bar{v}_x$, $\bar{v}_y$, and $\bar{v}_z$ are the components of the velocity at a point, or the average velocity across a surface or volume, normalized by main rotor tipspeed. Each of the 3x3 matrices here contain 9 unknown quantities, with little known about whether certain values should be considered zero/negligible or not. Determination of the form would therefore be part of the identification.

Depending on the location of interest, an even simpler approach is possibly, that is, to express the induced velocity at that location as simply an output equation, i.e., as a linear combination of rotor inflow states, with the possible addition of a time delay, and no additional states. This approximation may be sufficiently accurate for flight dynamics applications, because in this case the spatial details of the flow field tend to be relatively unimportant. Furthermore, the induced velocity model can be extracted using only the low frequency portion, between 1 to 5 rad/s, of the frequency response, because for flight dynamics purposes, this is the region of interest.

In the present study, output equation models were developed for average induced velocity along the 1/4 chord line of the horizontal tail. Although only the component of the main rotor inflow normal to the rotor disk is used, all three components of the induced velocity at the tail are considered. Therefore, the three induced

velocity components are defined by the following model:

$$\begin{Bmatrix} \bar{v}_x \\ \bar{v}_y \\ \bar{v}_z \end{Bmatrix} = \begin{bmatrix} K_{0x} & K_{1cx} & K_{1sx} \\ K_{0y} & K_{1cy} & K_{1sy} \\ K_{0z} & K_{1cz} & K_{1sz} \end{bmatrix} \begin{Bmatrix} \lambda_0(t-\tau_0) \\ \lambda_{1c}(t-\tau_{1C}) \\ \lambda_{1s}(t-\tau_{1S}) \end{Bmatrix} \tag{2.39}$$

where $\bar{v}_x, \bar{v}_y$, and $\bar{v}_z$ are the average induced velocity components at the 1/4 chord of the horizontal tail, non-dimensionalized by tip-speed, and the λ terms are the inflow harmonics at the rotor disks, and the notation $\lambda_0(t-\tau_0)$ denotes the value of λ_0 delayed by τ_0 seconds. The 9 constants K and the 3 delays τ in Eq.(2.39) are the unknowns of the model which needs to be identified.

A similar model was produced for the induced velocity at the wing under the hub. In this case, a similar spread of points as for the horizontal tail were calculated in order to still get an average, but they were located below the rotor. The form used for wing induced velocity was different, using up to nine time delays:

$$\begin{Bmatrix} \bar{v}_x \\ \bar{v}_y \\ \bar{v}_z \end{Bmatrix} = \begin{bmatrix} K_{0x} & K_{1cx} & K_{1sx} \\ K_{0y} & K_{1cy} & K_{1sy} \\ K_{0z} & K_{1cz} & K_{1sz} \end{bmatrix} \circ \begin{bmatrix} t-\tau_{0x} & t-\tau_{1cx} & t-\tau_{1sx} \\ t-\tau_{0y} & t-\tau_{1cy} & t-\tau_{1sy} \\ t-\tau_{0z} & t-\tau_{1cz} & t-\tau_{1sz} \end{bmatrix} \begin{Bmatrix} \lambda_0 \\ \lambda_{1c} \\ \lambda_{1s} \end{Bmatrix} \tag{2.40}$$

where $\bar{v}_x, \bar{v}_y$, and $\bar{v}_z$ are the average induced velocity components at the 1/4 chord of the wing under the hub, non-dimensionalized by tip-speed, and the λ terms are the inflow harmonics at the rotor disks. The unknowns of the model which need to be identified are the gains K and the time delays τ. As an illustration of the

notation of Eq.(2.40), consider the expansion of the $\bar{v}_x$ induced velocity component:

$$\bar{v}_x = K_{0x}\lambda_0(t - \tau_{0x}) + K_{1cx}\lambda_{1c}(t - \tau_{1cx}) + K_{1sx}\lambda_{1s}(t - \tau_{1sx})$$

These models can then be directly used in flight dynamic simulations, when state-space models are available to predict the average, lateral, and longitudinal inflow. Time delays must be handled similarly to the way described in the previous section.

Chapter 3: System Identification Methodology

3.1 Overview

This chapter presents the basics of frequency domain system identification of state space models for perturbation dynamics. This methodology is a well-vetted approach used frequently on flight data or wind tunnel data [63]. This dissertation takes the novel approach of applying the methodology to a free-vortex wake simulation to identify state-space models of the inflow. This method will be utilized for a few different applications, including single main rotor inflow, off-rotor inflow, coaxial rotor inflow and higher order coaxial rotor inflow. This chapter will present the basics of system identification that will be common among all of these applications.

3.2 Non-parametric Identification

The first step to frequency domain identification uses inputs in the form of frequency sweeps to excite the dynamics over a broad frequency range, allowing for identification to identify frequency responses using a single time history. This procedure can be performed as a flight, wind tunnel, or simulation.

The procedure must first start from a position of equilibrium or trim. For flight tests, this simply means allowing the pilot to trim the aircraft. A simulation must be marched forward in time until equilibrium is achieved for all the states. With simulations such the MFW, the wake geometry must converge to a periodic solution which is steady in the non-rotating frame. Next, a frequency-sweep [63] is applied to the inputs in the input vector u. Each input in u is individually exercised in the manner shown in Fig. 3.1.

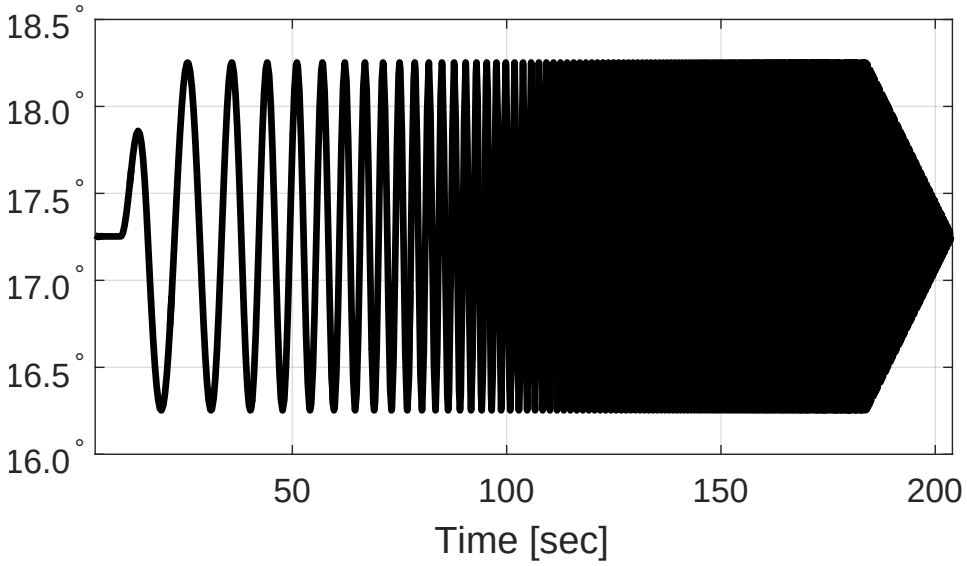

Figure 3.1: Representative frequency-sweep input.

This frequency sweep input starts at the trim value and then starts to cycle in a sinusoidal manner. The initial frequency of the sweep is set by the desired lower bound. The identification will only accurately capture dynamics that occur above this lower bound. For flight dynamics purposes, this is often set around 1 rad/sec. Anything below this bound is generally not important to handling qualities and is

easily corrected for by pilot inputs. The frequency of the input slowly increases until it reaches an upper bound. For flight dynamics and handling qualities applications, this bound is typically set between 10 to 30 rad/sec. Fig. 3.1 shows a representative input used in the present study. A representative output is shown in Fig. 3.2.

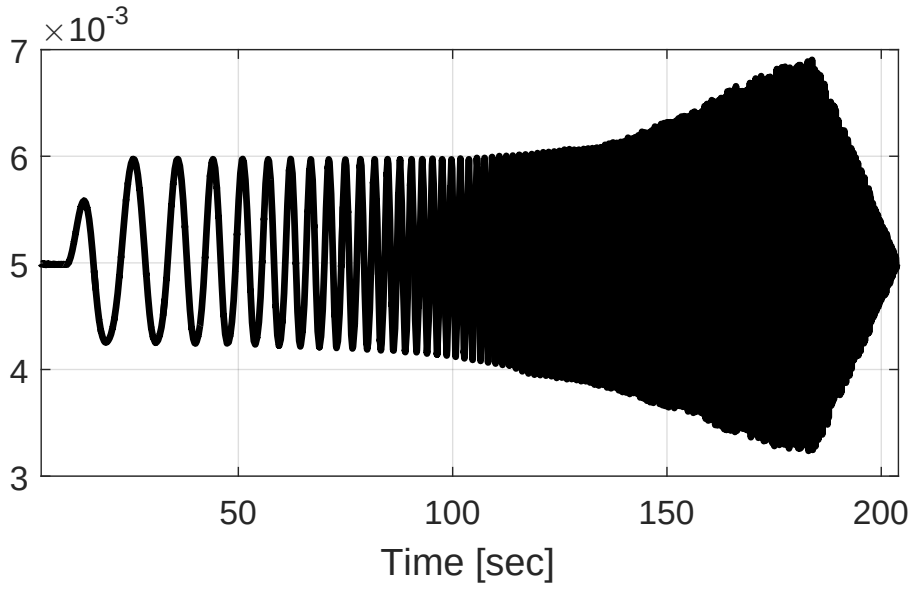

Figure 3.2: Representative output of a frequency sweep

The time histories are processed through Fourier transforms and subsequent manipulations to transform the data into the frequency domain. The system identification code CIFER [63] is used in this dissertation to process the time histories from the frequency sweeps, though any other similarly implemented code could be used to perform the procedure. First, a *non-parametric* model is identified. Here, model input-output behavior is characterized by frequency response curves (Bode plots) and there is no assumed model structure. The Fourier transform for a signal

$x(t)$ can be written as a *finite* Fourier transform:

$$X(f,T) = \int_0^T x(t)e^{-2\pi i f t}dt \iff x(t) = 0 \begin{cases} t \leq 0 \\ \\ t \geq T \end{cases} \tag{3.1}$$

where f is any real number, and corresponds to new independent variable of the Fourier transform; the frequency (in hertz, as written). The if and only if conditional in Eq.(3.1) requires that the signal starts from zero and returns to zero (or trim) as is shown in both of the representative signals (Figs 3.1 and 3.2). Signals are not measured continuously, but rather as a sequence of discrete time points at a certain sample rate. Therefore the finite Fourier Transform must be written as a *discrete* Fourier transform (DFT) for the finite set of N sampled data points [114]:

$$X(f_k) = X\left(\frac{k}{N\Delta t}\right) = \Delta t \sum_{n=0}^{N-1} x(n\Delta t)e^{(-2\pi i k n)/N} \tag{3.2}$$

where k *and* $n = 0, 1, 2, \ldots, N-1$. Δt is the time increment of the sampled data. $X(f_k)$ are the Fourier coefficients at the discrete frequency points f_k. The DFT is computed numerically through a special implementation of the fast Fourier transform (FFT), specifically the chirp z-transform [115], to reduce computational cost. The FFT produces estimates of the power spectral densities, which are defined as:

$$\hat{G}_{AB} = \frac{2}{T}\left[\overline{A(f)^{\intercal}}B(f)\right] \tag{3.3}$$

The input auto-spectrum ($\hat{G}_{\boldsymbol{uu}}$ where $\boldsymbol{u}$ are inputs), the output auto-spectrum ($\hat{G}_{\boldsymbol{yy}}$ where $\boldsymbol{y}$ are outputs), and the cross-spectrum ($\hat{G}_{\boldsymbol{uy}}$ where $\boldsymbol{u}$ are inputs and $\boldsymbol{y}$ are outputs) are produced. The FFT is performed multiple times on each time history data set, each time with a different spectral window that is sized in length so that

it captures certain frequency ranges optimally. This results in several different estimates of the spectral densities, which are more or less accurate at certain frequencies based on the window size used. An optimization based composite-windowing procedure then combines the various results from the different window sizes to achieve a single smooth estimate of the spectral densities [63, 116, 117].

The spectral density results can then be used to calculate the frequency response from input to output at each frequency response. For a single-output-single-input (SISO) system, the relationship can be described as the ratio between the cross-spectrum and the input auto-spectrum :

$$\frac{y(s)}{u(s)} = \hat{H}_{uy}(\omega) = \frac{\hat{G}_{uy}(\omega)}{\hat{G}_{uu}(\omega)} \tag{3.4}$$

Along with the frequency response curves, response coherence is also generated. Coherence of a SISO frequency response is defined as:

$$\gamma^2_{uy}(\omega) = \frac{|\hat{G}_{uy}(\omega)|^2}{|\hat{G}_{uu}(\omega)||\hat{G}_{yy}(\omega)|} \tag{3.5}$$

and it can be interpreted a direct measure of the linearity between the input and output. Responses with high coherence are linear, have a high signal-to-noise ratio, and are not excited by secondary inputs.

3.3 Parametric identification : State-space

Next, a *parametric* model is fitted to the frequency response curves, with an assumed model structure, in state-space form:

$$\dot{\boldsymbol{x}} = [A]\boldsymbol{x} + [B]u \tag{3.6}$$

$$\boldsymbol{y} = [C]\boldsymbol{x} \tag{3.7}$$

where the state-vector is $\boldsymbol{x}$ (of size N_x), the input vector is u (of size N_u), and the output vector is $\boldsymbol{y}$ (of size N_y).

This basic structure is often modified by the addition of a time delay matrix to account for unmodeled higher order dynamics:

$$\dot{\boldsymbol{x}} = [A]\boldsymbol{x} + [B]\boldsymbol{u}(t - [\tau]) \tag{3.8}$$

$$\boldsymbol{y} = [C]\boldsymbol{x} \tag{3.9}$$

where $[\tau]$ is the time delay matrix, which functions as described in the single main rotor model structure part of Sec. 2.2.2.5. These equations are also sometimes modified to be in another form:

$$[M]\dot{\boldsymbol{x}} + [\bar{L}]\boldsymbol{x} = \boldsymbol{u}(t - [\tau]) \tag{3.10}$$

$$\boldsymbol{y} = [C]\boldsymbol{x} \tag{3.11}$$

First, note if $[B]$ is square (which requires $\boldsymbol{u}$ to be the same length as $\boldsymbol{x}$) and invertible, then the following can be stated as equivalent:

$$[B]^{-1} = [M] \qquad and \qquad -[B]^{-1}[A] = [\bar{L}] \tag{3.12}$$

In the present study, The $[C]$ matrix in the output equations will typically be the identity matrix therefore making the outputs identical to the states and restricting the number of states to the number of outputs. The C matrix can also be a larger matrix allowing for more states than outputs, as will be shown in Chap. 6. However the values in the matrix are still assumed and are not identified.

The A and B matrices, or equivalently the M and $\bar{L}$ matrices in the inflow models, contain the parameters that need to be identified. These are referred to as "free variables" or "free parameters". These parameters can be collected in the vector $\boldsymbol{\Theta}$. Not all the values in matrices are free parameters. Many are assumed to be zero and sometimes a parameter can be assumed to have a constant value. Some parameters are known to be equivalent to other terms and therefore can be constrained to the value or a function of another free variable. This often happens when there is some known physical mechanism for symmetry in the system. Additional details will be provided in subsequent chapters.

The free variables in this state-space model are optimized for a best fit to the non-parametric frequency responses. The state space model can be represented as an complex-valued matrix T in the frequency domain. The various non-parametric frequency responses can also be grouped in a frequency response matrix labeled $\hat{T}_c$. The model accuracy is measured by a cost function, J, which is a direct measure

of phase and magnitude differences between the model and the non-parametric frequency responses. The cost function for an individual transfer function fit used in the present study is defined as [63]:

$$J = \frac{20}{n_\omega} \sum_{n=1}^{n_\omega} W_{\gamma_{uy}} \left[W_g (|\hat{T}_c(\omega_n)| - |T(\omega_n)|)^2 + W_g (\angle \hat{T}_c(\omega_n) - \angle T(\omega_n))^2 \right] \tag{3.13}$$

where the three weighting values are defined, respectively, as:

$$W_{\gamma_{uy}} = \left[1.58 \left(1 - e^{-\gamma_{uy}(\omega_n)^2} \right) \right]^2, \qquad W_g = 1, \qquad W_p = \pi/180 \tag{3.14}$$

Only the first weight is a function of the calculated coherence at the frequency ω_n. The ω_n are a set of frequency points along the frequency range that are equally spaced on the log-frequency scale. This ensure that the minimum cost corresponds to the function that produces the best fit when displayed on the Bode plot. When there are multiple frequency responses to be fit with a single state-space model, an average cost J_{ave} is used as the optimization metric, though most often, the individual costs are still listed, as it is important to check that no particular cost is too high. For this cost function, the standard guideline [63] is that $J_{ave} < 50$ indicates an excellent fit, $J_{ave} < 100$ indicates a good fit, and $J_{ave} < 200$ are considered acceptable for some individual transfer function (e.g. off-axis responses for rotorcraft flight dynamics problems).

Parameters $\mathbf{\Theta}$ within the state-space model are further analyzed by their normalized Cramer-Rao bounds $\overline{CR}$ and normalized insensitivity values $\overline{I}$. The normalized insensitivity of a parameter is a measure of its overall effect on the cost

function, and is defined for the i-th parameter as [63]:

$$\overline{I}_i = \left| \frac{1/\sqrt{\left[\frac{\partial^2 J_{sum}}{\partial \mathbf{\Theta} \partial \mathbf{\Theta}^\intercal}\right]_{ii}}}{\Theta_i} \right| \times 100\% \tag{3.15}$$

where J_{sum} is the summation of the individual costs. The Cramer-Rao value is a measure of a parameter's correlation with other parameters in the model structure, and is defined as [63]:

$$\overline{CR}_i = \left| \frac{2\sqrt{\left[\left[\frac{\partial^2 J_{sum}}{\partial \mathbf{\Theta} \partial \mathbf{\Theta}^\intercal}\right]^{-1}\right]_{ii}}}{\Theta_i} \right| \times 100\% \tag{3.16}$$

Parameters with low insensitivity ($< 10\%$) and low Cramer-Rao bounds ($< 20\%$) are well identified and important to an accurate model and are retained. Parameters with high Cramer-Rao and insensitivity values are unreliable and therefore are eliminated from the model structure as long as they do not incur a large loss of accuracy [63]. Removing these terms typically means fixing them to zero, though it can also be achieved by constraining their value to another term. Upon removal and subsequent re-optimization, the cost may increase slightly ($\Delta J_{ave} \approx 1$ to 2) but the resulting simpler system is more desirable [63]. If removal incurs a large cost penalty, then other ways of reducing the system should be explored, or the current insensitivities and Cramer-Rao bounds should be accepted as is.

3.3.1 Correlation Problem

The procedure laid out in the previous section assumes that one input can be swept independently of the other inputs. The other inputs are held constant while only one input is swept with the frequency sweep. However, sometimes the desired state-space system has inputs that are not truly simulation inputs. For example, classical inflow systems relate inflow to the aerodynamic loading on the rotor, however both of these are actually outputs of the simulation, while the true inputs are the swashplate controls. Another example is on a real aircraft when there are redundant flight controls and a flight control system that converts the the pilot inputs into a different set of actuator inputs. In these cases the actual inputs would be the swashplate controls or the pilot controls. These are fully governable in the sense that they can be forced to any value desired and are not a product or outcome of the simulation or physical system. These actual inputs can be referred to as controls, and labeled $\boldsymbol{\theta}$.

The inputs that are really outputs, which can be referred to as "input-outputs", are not necessarily fully governable in the sense that it is difficult to force them to take on a desired value in time because they are truly an outcome of the simulation or system. It can be very difficult to only excite one of the input-outputs while keeping all the remaining input-outputs at their trim values. And often the input-outputs will be intensely coupled and it is not trivial to separate the contributions of each input-output to each output. In this case, the input-outputs to the model are said to be *correlated*. An example of this correlation is shown in Fig. 3.3. A

single frequency sweep on a control of the simulation produces the two input-outputs shown in the figure. The two input-outputs cycle at the same frequency as the actual input and so are correlated in time. Given only these two time histories, as well as an output caused by these combined input-outputs, it would be impossible to tell which of the inputs actually caused the output. This means that the time histories are multiple-input-multiple-output (MIMO) and must be handled differently than SISO identifications.

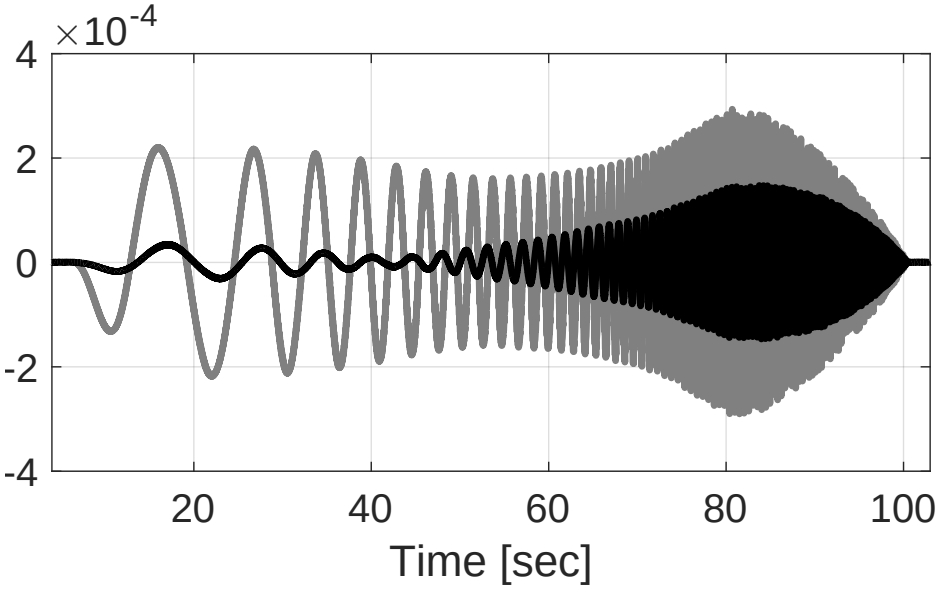

Figure 3.3: Example of two correlated input-output time histories from a frequency sweep.

3.3.2 MIMO system identification

To identify a system with multiple inputs, the inputs be independent and uncorrelated 63. Because input-outputs are driven by the same physical input, they are highly, if not completely correlated. A simple example demonstrates why this

is a problem. Assume first that a system has two inputs and two outputs but the system is not coupled, meaning that input A affects only output A and input B affects only output B. This type of system can be referred to as *diagonal*. This can be written in transfer function form as shown in Eq.(3.17):

$$y_A(s) = \frac{y_A(s)}{u_A(s)} * u_A(s) \tag{3.17}$$

$$\underbrace{y_B(s)}_{\text{Outputs}} = \underbrace{\frac{y_B(s)}{u_B(s)}}_{\text{Transfer Fcns.}} * \underbrace{u_B(s)}_{\text{Inputs}} \tag{3.18}$$

If the equations are really written this way, then system identification would really just be two separate SISO identifications. A single time history gives values for the two inputs in time and values for two outputs in time. Based on the given form, it would be assumed that input A only affects output A, and input B only affects output B. However, in most cases, it is not known whether a system is diagonal. Input B may have some effect on output A, and input A might have some effect on output B. Even if the equations are dominated by the diagonal terms it is still important to account for the influence of the off-diagonal terms and not assume that they are negligible.

If there are extra non-diagonal terms, the Eq.(3.18) could take the form shown in Eq.(3.19):

$$\underbrace{y_B(s)}_{\text{Outputs}} = \underbrace{\frac{y_B(s)}{u_B(s)}}_{\substack{\text{On-axis} \\ \text{Transfer Fcns.}}} * \underbrace{u_B(s)}_{\substack{\text{On-axis} \\ \text{Inputs}}} + \underbrace{\frac{y_B(s)}{u_A(s)}}_{\substack{\text{Off-axis} \\ \text{Transfer Fcns.}}} * \underbrace{u_A(s)}_{\substack{\text{Off-axis} \\ \text{Inputs}}} \tag{3.19}$$

If this were written in terms of spectral densities:

$$\begin{Bmatrix} G_{u_B y_B(\omega)} \\ G_{u_A y_B(\omega)} \end{Bmatrix} = \underbrace{\begin{bmatrix} G_{u_B u_B}(\omega) & G_{u_B u_A}(\omega) \\ G_{u_A u_B}(\omega) & G_{u_A u_A}(\omega) \end{bmatrix}}_{\text{Input Auto-Spectrum Matrix}} \begin{Bmatrix} \frac{y_B(s)}{u_B(s)} \\ \frac{y_B(s)}{u_A(s)} \end{Bmatrix} \tag{3.20}$$

Therefore, the solution for the frequency responses require the Input Auto-Spectrum matrix to be inverted. This matrix is not invertible when the cross-control coherence is one or close to one. Cross control coherence is a measure of how linear the relationship is between the controls, just as regular coherence measures the linear relationship between input and output, and is therefore the direct measure of correlation.

High cross-control coherence means that the other control can be largely predicted through a linear relationship if the first control is known. Perfect cross-control coherence means that the two controls are perfectly correlated and the relationship can be quantified perfectly with a linear system (i.e. bode plot, transfer function or state-space model). Therefore, identifications can not be performed when the inputs are correlated. Three separate methods have been assessed to try to remove or negate the effects of correlation. They consist of cross-feeds, decorrelation through noise, and the Joint-Input-Output Method.

3.3.3 Cross-feed Method

One approach is to use a combination of the actual inputs or controls to remove or at least minimize one of the input-outputs so that it can be considered negligible. This reduces Eq.(3.20) so that there is only one input on the right hand

side of the equation, and the problem is well-posed for a single time history. A proper combination of actual inputs can achieve responses that are dominated by a single input-output. This is done by utilizing a cross-feed, i.e., by injecting as input a proper *combination* of both θ_A and θ_B into the simulation. The cross-feed transfer function for Eq.(3.18) would seek to minimize the off-axis transfer function part as typically that would be the easiest to remove since it is already the smaller contribution. For Eq.(3.18), this means trying to minimize the size of u_A. The cross-feed which determines the combination as a function of the frequency of excitation, is the solution $K(s)$ to the following:

$$\frac{u_A(s)}{\theta_B(s)} + K(s)\frac{u_A(s)}{\theta_A(s)} = 0 \tag{3.21a}$$

$$K(s) = -\frac{u_A/\theta_B(s)}{u_A/\theta_A(s)} = -\frac{\theta_A}{\theta_B}(s) \tag{3.21b}$$

$K(s)$ describes in the frequency domain how much θ_A should be used when θ_B is used, so that only (or at least primarily) u_B is produced. More accurately, it describes the precise amplitude ratio and phasing ratio between the two actual inputs.

The required frequency responses to compute this cross-feed are $u_B/\theta_A(s)$ and $u_B/\theta_B(s)$ so they must be produced first. Frequency sweep inputs of θ_A only, and of θ_B only, are applied separately to the simulation, and the time histories of u_A and u_B due to each input are obtained. Because the actual inputs are able to be independently excited, these responses can be computed as SISO identifications. The *non-parametric* frequency responses of the off-axis input u_B to each of the two actual inputs are computed. CIFER can then perform frequency response arithmetic to calculate the *non-parametric* cross-feed frequency response, as in Eq.(3.4). The

NAVFIT utility in CIFER is then used to fit a *parametric* transfer function to the cross-feed frequency response. The output cross-feed θ_A time history is then determined by simulating $K(s)$ with a θ_B frequency input, using an ODE solving algorithm such as LSIM from the Control System Toolbox for MATLAB.

The combined input of the θ_B frequency sweep and the θ_A cross-feed to the simulation wake will provide primarily the on-axis input-output u_B and a substantially reduced off-axis input-output u_A. Figure 3.4 gives an example of a frequency sweep and cross-feed that would produce only the on-axis input-output from Fig. 3.3. The gray line represents the actual frequency response part and the black line shows the amount of off-axis control that must be added to cancel the off-axis input-output. The resulting outputs with the cross-feed are shown in Fig. 3.5, which shows that the off-axis response black line response is at least an order of magnitude lower than the on-axis gray line response at all frequencies. With most of the off-axis input-output (black line) canceled, the system has essentially one input and can be analyzed using the SISO method shown earlier.

The downsides to such a method are apparent. First, any error in the cross-feed results in a solution that does not have the off-axis input-output fully canceled out. This is shown in Figure 3.5 where at the higher frequency range the off-axis input-output is not quite zero, and is in fact just barely small enough to safely ignore. This error can be caused by several things.

First, if the relationship between actual inputs and input-outputs are not quite linear, then the crossfeed will only cancel the linear portion of the off-axis input-output. Next the cross-feed relies on low order polynomial fits to capture the full

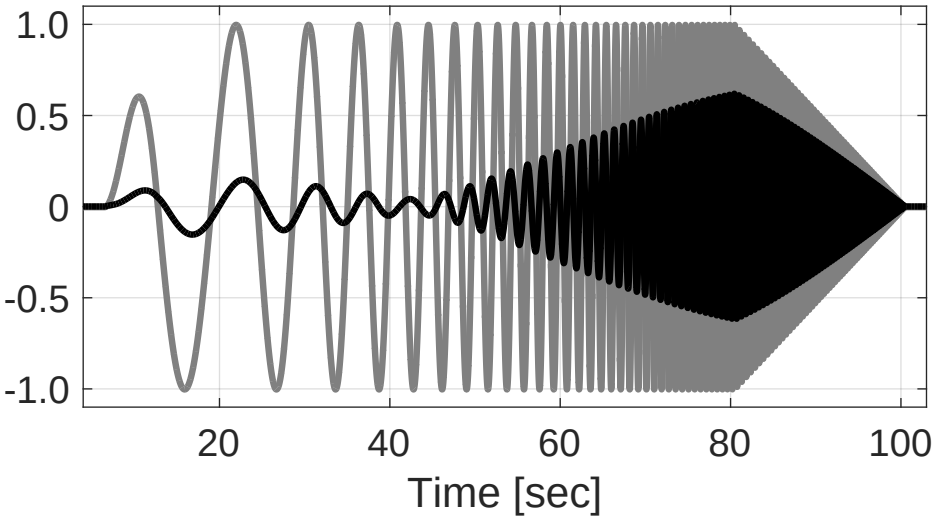

Figure 3.4: Actual input time histories for cross-feed. Gray line shows frequency sweep, black line shows cross-feed

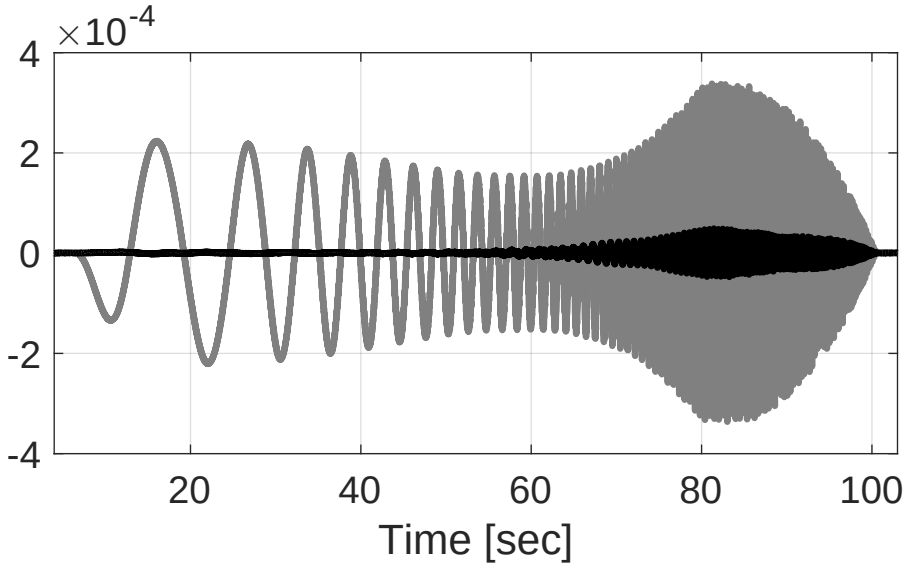

Figure 3.5: Input-output time histories with cross-feed. Gray line shows primary on-axis response, black line shows mostly canceled off-axis response

frequency response calculated by Eq.(3.21b). Differences between the low order fit and the actual frequency response will make the cancellation imperfect. Hand-

tweaking the cross-feed can help cancel more off-axis input-output, but it is a tedious process that requires extensive insight and intuition into the form of the cross-feed transfer function.

Even if the cross-feed does work, it is still a long two-step process. The identification must first run frequency sweeps without cross-feeds, and then run frequency sweeps with cross-feeds, resulting in twice as many simulation runs. The last disadvantage is that the formula stated in Eq.(3.21b) is for two correlated controls. A similar derivation for three controls proves to be much more complicated. The cross-feed becomes a cross-feed matrix, requiring more than one transfer function to be fit. The size of the matrix grows by $(n-1)^2$ where n is the number of controls. Even at 3 correlated controls, the complexity of the cross-feeds can make errors compound and it becomes very difficult to get the correct answer.

The main benefit of this method is that it is much easier to see that the method produced the correct result. If the cross-feed is in anyway incorrect, it will be quite obvious from the resulting time history that the off-axis input-output was not canceled properly. The cancellation of the off-axis input-output is not obscured behind a mathematical procedure but takes place in a physical sense (or directly in simulation). On the other hand, if the off-axis input-output is fully canceled, the cross-feed is assuredly correct, but also the accuracy of the cross-feed is not really important as long as the desired affect was achieved.

3.3.4 Decorrelation Through Noise

The contaminating effects of partially correlated inputs can be removed so long as they are not highly or fully correlated [63]. As shown in Eq.(3.20), conditioned frequency responses can be achieved by inverting the input auto-spectrum matrix and multiplying it by the cross-spectrum vector. But this methodology relies upon the inputs being only partially correlated, so that the input auto-spectrum matrix is invertible and not ill-conditioned. For the case of correlated simulation input-outputs, this means that the input-outputs must be made to be only partially correlated

The correlation between input-outputs can be reduced into partial correlation with proper insertion of noise into the controls. Noise, when fed into the controls, lowers the correlation between the input-outputs. When the cross-control coherence is low enough ($\gamma_{uu}^2 < 0.5$), inversion of the spectral matrices can be achieved, and Eq.(3.20) can be solved. The downside to this method is that the addition of noise will decrease the coherence of the identification. Special care must be taken to keep the signal to noise ratio high enough to allow inversion of the cross-spectrum matrices, but low enough so that it does not drastically affect the coherence.

To achieve this, Gaussian noise is generated, but then shaped by a shaping function so that the shape of its peak to peak amplitude curve is roughly the same as the peak to peak amplitude curve for the frequency sweep shown in figure 3.1. Then the noise is scaled down by roughly the ratio between the on-axis input-outputs and the off-axis input-outputs. This signal is then fed into the *off-axis* controls during

a frequency sweep so that they produce primarily changes in the off-axis input-outputs, giving them the noise of the control and therefore decorrelating them from the other input-outputs.

An example of a frequency sweep with noise input into the controls is shown in Figure 3.6. The normal frequency sweep is inserted into the main control, shown by the black line, and a noisy input is inserted into the off-axis control, shown by the gray line. This produces the input-outputs that are shown in Figure 3.7. These input-outputs are no longer correlated because the noise primarily feeds into the off-axis input-output, making the two input-outputs no longer linear dependent on each-other in time.

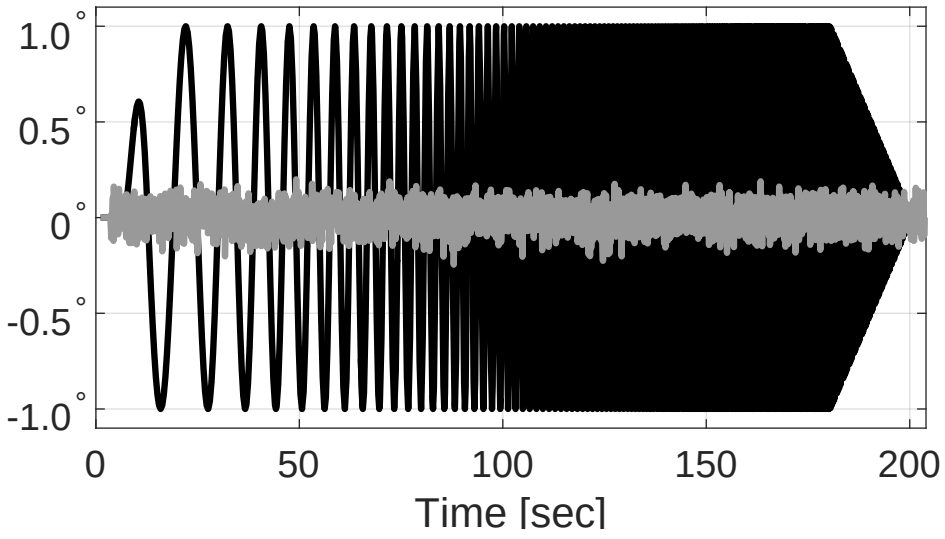

Figure 3.6: Sample control time histories for decorrelation through noise.

The shaping function and the scaling ratio must be tuned and adjusted. The noise level should be no higher than necessary to achieve inversion of the spectral matrix because any excess noise tends to degrade the coherence. But noise that

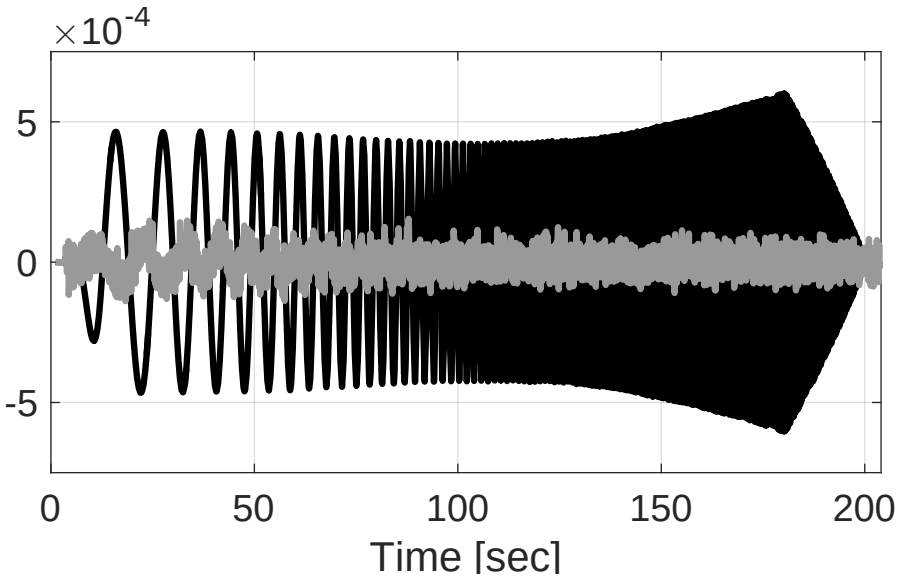

Figure 3.7: Sample input-output time histories for decorrelation through noise.

is too low will cause the inversion of the input auto-spectrum to break down due to ill-conditioning. So a few iterations are most often necessary to find an optimal balance. This means that this method can often be quite expensive in terms of computational loads and manual input. Also if the inputs are correlated enough, it becomes almost impossible to remove enough correlation without reducing the coherence to below acceptable levels.

3.3.5 Joint-Input Output Method

For this work, the issue of correlation is solved not with cross-feeds or noise inputs, but rather through transfer function manipulation similar to the methodology shown in Ref. 74, 118. The first step of the Joint-Input Output method is to obtain a series of Single-Input Multiple-Output (SIMO) frequency responses of the outputs *and* the input-outputs to the true simulation inputs or controls. SIMO identification

can proceed simply as multiple separate SISO identifications governed by Eq.(3.4). This can be performed now because the user has full authority over the controls. They are kept decoupled by activating one at a time with the frequency sweep input, while the other controls are held at their trim value. Each of the control frequency sweeps produces a non-parametric frequency responses for each of the outputs and also a non-parametric frequency responses for each of the input-outputs.

When the responses of the controls are grouped in matrix form, two transfer function matrices are generated. The matrix $\left[\frac{\boldsymbol{y}(s)}{\boldsymbol{\theta}(s)}\right]$ describes the output responses to the control inputs. The element in the i-th row and j-th column is the response of the i-th component of the output vector $\boldsymbol{y}$ to a frequency response input of the j-th component of the control vector $\boldsymbol{\theta}$ with all other controls held at their respective trim values (the notation that implies the division between two vectors is not mathematically rigorous, and is used only for clarity). The matrix $\left[\frac{\boldsymbol{u}(s)}{\boldsymbol{\theta}(s)}\right]$ describes the input-output responses to the control inputs. Note that each element of the two response matrices is generally a function of frequency, therefore in practice the two matrices are three-dimensional, with frequency as the third dimension.

The desired frequency responses of outputs to input-outputs can then be found by numerical inversion and multiplication at each individual frequency:

$$\left[\frac{\boldsymbol{y}(s)}{\boldsymbol{u}(s)}\right] = \left[\frac{\boldsymbol{y}(s)}{\boldsymbol{\theta}(s)}\right] \times \left[\frac{\boldsymbol{u}(s)}{\boldsymbol{\theta}(s)}\right]^{-1} \tag{3.22}$$

For each frequency response in the $[\boldsymbol{y}(s)/\boldsymbol{\theta}(s)]$ and $[\boldsymbol{u}(s)/\boldsymbol{\theta}(s)]$ matrices the coherence is also calculated. However, there is not a straightforward way to calculate the exact coherence of frequency responses obtained from the arithmetics

of Eq.(3.22). But from an analysis of the coherence of the individual frequency responses that go into the calculation of $\boldsymbol{y}(s)/\boldsymbol{u}(s)$, it is possible to calculate a weighted average coherence, based on the following considerations.

1. The coherence from input to output is equal to the coherence from output to input. The coherence matrix of the inverse of a frequency response matrix must remain the same as that of the original matrix. For this method, this establishes:

$$Coh\left(\left[\frac{\boldsymbol{u}(s)}{\boldsymbol{\theta}(s)}\right]^{-1}_{i,j}\right) = Coh\left(\left[\frac{\boldsymbol{u}(s)}{\boldsymbol{\theta}(s)}\right]_{i,j}\right)$$

2. When two SISO frequency responses are multiplied, the total coherence is roughly equal to the smaller coherence of the two components. So this is used to approximate:

$$Coh\left(\left[\frac{\boldsymbol{y}(s)}{\boldsymbol{\theta}(s)}\right]_{i,j} \times \left[\frac{\boldsymbol{u}(s)}{[\boldsymbol{\theta}(s)}\right]^{-1}_{j,i}\right) \approx \min\left\{Coh\left(\left[\frac{\boldsymbol{y}(s)}{\boldsymbol{\theta}(s)}\right]_{i,j}\right),\ Coh\left(\left[\frac{\boldsymbol{u}(s)}{\boldsymbol{\theta}(s)}\right]^{-1}_{j,i}\right)\right\}$$

3. The level of coherence is unimportant if the product of two frequency responses produces a very small magnitude output, relative to the other contributing parts. Conversely, if the product of two frequency responses produces a relatively large magnitude output, then its contribution to the overall coherence is higher. This suggests that a magnitude weight based summation would be appropriate.

A singular index of the $[\boldsymbol{y}(s)/\boldsymbol{u}(s)]$ matrix is calculated by:

$$\left[\frac{\boldsymbol{y}(s)}{\boldsymbol{u}(s)}\right]_{i,j} = \sum_{k=1}^{n\boldsymbol{\theta}} \left[\frac{\boldsymbol{y}(s)}{\boldsymbol{\theta}(s)}\right]_{i,k} \times \left[\frac{\boldsymbol{u}(s)}{\boldsymbol{\theta}(s)}\right]_{k,j}^{-1} \tag{3.23}$$

This broken down equation more clearly shows that $n\boldsymbol{\theta}$ (number of controls) transfer function multiplications are summed to give a value for a given index in the $\boldsymbol{y}(s)/\boldsymbol{u}(s)$ matrix. Magnitude based weights are defined as:

$$W_{i,j}(n) = \frac{\left|\left[\frac{\boldsymbol{y}(s)}{\boldsymbol{\theta}(s)}\right]_{i,n} \times \left[\frac{\boldsymbol{u}(s)}{\boldsymbol{\theta}(s)}\right]_{n,i}^{-1}\right|}{\left|\left[\frac{\boldsymbol{y}(s)}{\boldsymbol{u}(s)}\right]_{i,j}\right|} \tag{3.24}$$

The coherence is then approximately equal to the average weighted coherence:

$$Coh\left(\left[\frac{\boldsymbol{y}(s)}{\boldsymbol{u}(s)}\right]_{i,j}\right) \approx \sum_{n=1}^{n\theta} \left(W_{i,j}(n) \times \min\left\{ Coh\left(\left[\frac{\boldsymbol{y}(s)}{\boldsymbol{\theta}(s)}\right]_{i,n}\right),\ Coh\left(\left[\frac{\boldsymbol{u}(s)}{\boldsymbol{\theta}(s)}\right]_{n,i}\right)\right\}\right) \tag{3.25}$$

With the responses and coherence of $\boldsymbol{y}(s)/\boldsymbol{u}(s)$ solved at each frequency, the procedure can continue with state-space model identification as described above.

The first advantage of this method are that it works with only one set of frequency sweeps. The frequency sweeps are run on each of the independent controls and once this set is complete, the final responses can be calculated. There is no need for manual changes in the frequency sweep parameters, and no need for repetitive iterations on the sweeps. This method is rather robust in terms of getting results versus the other two methods. Therefore this method is much more capable of being automated, or of being used by a researcher without system identification background.

There are some limitations inherent in this method. From Eq.(3.22), it can be seen that the $\left[\frac{\boldsymbol{u}(s)}{\boldsymbol{\theta}(s)}\right]$ matrix must be invertible at each frequency point. In practice this is not difficult to do unless one of the frequency sweeps either does nothing or is a linearly combination of other frequency sweeps. However this limitation of invertibility does enforce that the matrix must be square. A pseudo-inverse may be acceptable if there are more controls ($\boldsymbol{\theta}$) than input-outputs terms ($\boldsymbol{u}$), but it will not work if there are more input-outputs than controls. So this method does require one independent sweep per input-output term.

The second disadvantage is that if there low coherence results between the controls and either the input-outputs or the outputs, it is necessary to establish when the data will be neglected as unreliable. If the responses have low magnitude (20 dB lower than on-axis responses) and low coherence then they can be safely neglected. But large responses that have low coherence likely should not be neglected and the resulting coherence formulation given by Eq.(3.25) will give a low coherence. This does not necessarily indicate the linearity of the response anymore but may simply indicate the reliability of the frequency response. For example the coherence between $\boldsymbol{u}$ and $\boldsymbol{y}$ may be perfect (because it is linear), but if $\boldsymbol{\theta}$ to $\boldsymbol{u}$ or $\boldsymbol{\theta}$ to $\boldsymbol{y}$ has low coherence (because they are non-linear), then the result will not show that perfect coherence.

3.3.6 Time Domain Verification

The identified state-space models should be validated in the time domain. One way to perform this is using another CIFER utility, VERIFY, which performs time-domain verification. A new set of controls, different from the frequency sweeps used in the identification, is applied to the simulation or real life system to get new time histories of the outputs $\boldsymbol{y}$ and the input-outputs $\Delta\boldsymbol{u}$. The new time histories of $\Delta\boldsymbol{u}$ are then used as inputs to a linear simulation based on the state-space system previously identified, calculating the corresponding outputs $\boldsymbol{y}$. These can be directly compared with the simulation or real systems time histories to ensure adequate agreement [63].

3.4 Summary

The chapter presents the basics of frequency domain system identification methodology, and also some of the developments necessary for application to high-fidelity aerodynamic numerical models. The methodology presented in the chapter is very general, and can be used with many types of aerodynamic prediction model or even other prediction models not related to aerodynamics. It is also well vetted for identifying input-output relationships from test flight data and other real life systems.

Indeed the only real restrictions on the methodology are:

1. The simulation or system must have a set of independent controls that can be excited separately in order to excite the dynamics of the system.

2. The simulation or system must have a set of measurable outputs, and if applicable, a measurable set of input-outputs, though certainly the procedure works just fine if the desired responses are from controls to outputs.

3. Physical insight is useful but is not wholly necessary. Knowing which outputs are caused by which inputs can be useful in the initial set-up of the state-space formulation, and in deciding what quantities may be input-outputs versus outputs.

4. The dynamics of the system, between desired inputs and outputs, should be at least mostly linear. This is not a failing of the methodology though as the procedure will indicate the lack of linearity in the first step. It is just an obvious corollary that a linear system can not fit a non-linear system. This is the same as stating that a straight line can not be fit to a parabola. However this procedure will still try produce the best *approximate* linear model, just as linear least squares will still find the best linear fit through a parabola.

As a consequence, it should be possible to extract accurate inflow dynamic models from high fidelity aerodynamic models that incorporate effects not easily captured by momentum theory-based models, such as aerodynamic interference, or stall effects. The methodology can also be applied to extract state-space models of the inflow at points away from the rotor disk, such as fuselage and empennage. Lastly, this methodology will readily extend to multi-rotor configurations where

inflow impingement from one rotor onto another may be prevalent. This will allow for the identification of coaxial state-space inflow models and investigation into its inflow and vehicle dynamics.

Chapter 4: Single Main Rotor Inflow System Identification

4.1 Overview

The single main rotor helicopter is a well-known configuration that has been studied in detail. In particular, the inflow dynamics have been studied and derived analytically through momentum and potential flow theory, chiefly by the Pitt-Peters model [25] and its subsequent extensions. These methods have been shown to well capture the dynamics that the inflow adds to the full dynamics of a rotorcraft. It provides a good theoretical basis for the form of inflow dynamics that should be contained within free vortex wakes and higher fidelity aerodynamic models. It also provides a vetted model that can be compared against new models identified directly from the higher fidelity simulations, in absence of better experimental data. So it makes sense to begin establishing the frequency domain system identification procedure for inflow on a single main rotor. This chapter identifies state space inflow models from a free-vortex wake simulation of a UH-60-like helicopter with characteristics defined from Ref. [119]. The models are identified in various flight regimes and are compared with the models predicted by Pitt-Peters [25]. Extensions are also shown to demonstrate the ability for the same methodology to predict the

inflow off of the rotor disk, at other locations where aerodynamic interference may be important, like at the fuselage or the tail.

4.2 Rotor Inflow Model Identification

Inflow models for a single main rotor are identified in the form given by Eq.(2.11) for hover and Eq.(2.12) for forward flight. The models are extracted using frequency domain system identification, as described in Chap. 3, applied to the inflow time histories generated by the MFW. For this identification, the rotor shaft is held fixed, as if in a wind-tunnel, to avoid divergence in the time histories due to aircraft dynamics. For the initial identification, the blade dynamics, i.e. flap, lag, and torsion degrees of freedom, are held rigid to avoid the effects of wake distortion described in Sec. 2.2.2.5. First, the wake is marched forward in time until moment trim is achieved, the wake geometry has converged to a periodic solution, and the desired value of ΔC_T has been reached with a trim value of collective pitch θ_0. Next, a frequency-sweep [63] input of collective pitch θ_0, similar to that shown in Fig. 3.1, is applied to the trimmed rotor, and the corresponding time histories of ΔC_T, ΔC_L, and ΔC_M and inflow harmonics λ_0, λ_{1c}, and λ_{1s} are calculated. A representative time history of a thrust coefficient C_T to a sweeps of collective input θ_0 is shown in fig. 4.1. The inflow response to the same sweep is shown in Fig. 4.2. The frequency sweep is then repeated on the other swashplate controls, θ_{1S} and θ_{1c}, and once again the time histories of the inflow components λ_0, λ_{1c}, and λ_{1s} and of the aerodynamic loading ΔC_T, ΔC_L, and ΔC_M are computed. However it should be noted that, in

hover, axial symmetry of the rotor makes the $\lambda_{1c}(s)/\Delta C_M(s)$ response identical to the $\lambda_{1s}(s)/\Delta C_L(s)$, so only one frequency sweep is actually required.

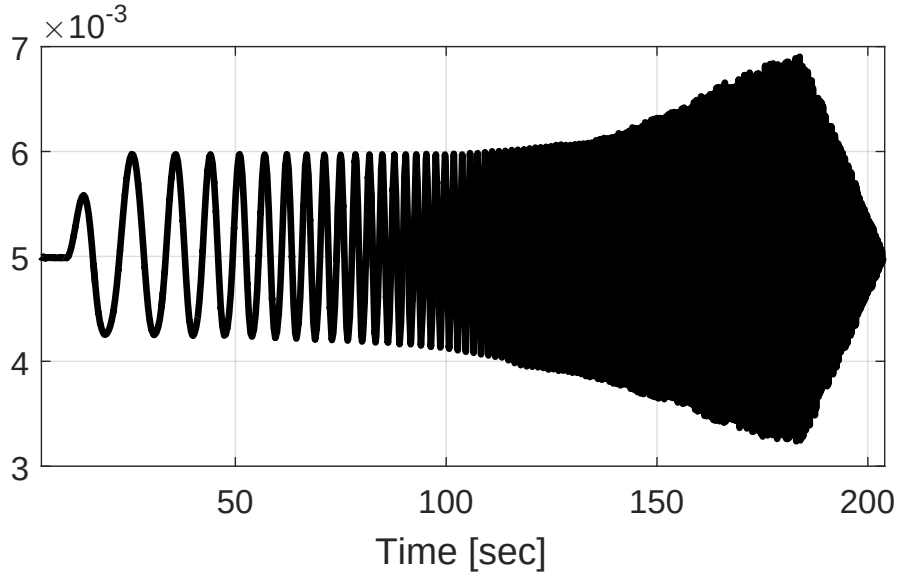

Figure 4.1: Representative thrust coefficient C_T response to a frequency sweep of collective θ_0.

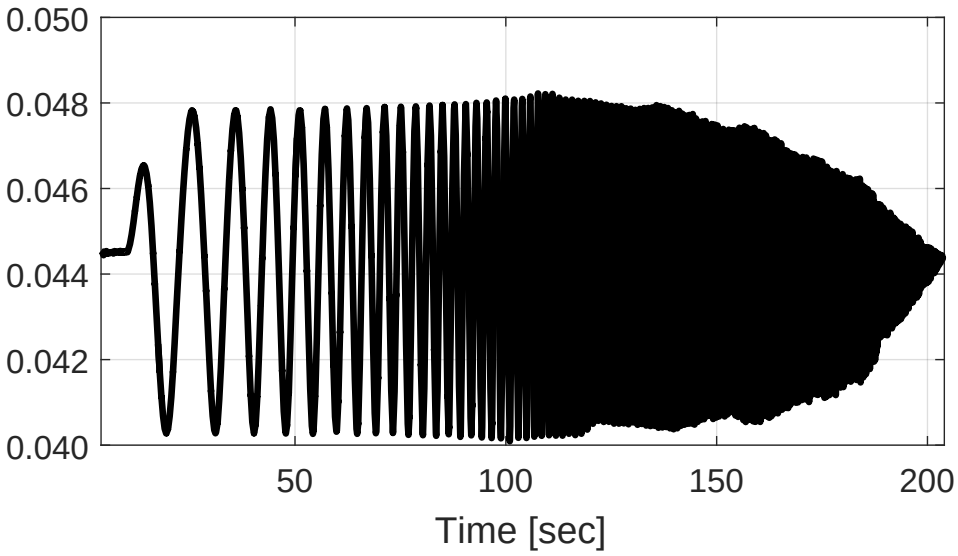

Figure 4.2: λ_0 response for a frequency sweep of θ_0.

Once the thrust and moment coefficients and inflow harmonics are obtained from the wake calculation, they become, respectively, the input-outputs and outputs for the subsequent system identification procedure. The Joint Input-Output method described in Sec. 3.3.5 is used to solve the correlation problem, which is important in the hover case particularly because the aerodynamic moments are correlated. Equation (3.22) of the Joint-Input Output method becomes:

$$\left[\frac{\boldsymbol{\lambda}(s)}{\Delta\mathbf{C}(s)}\right] = \left[\frac{\boldsymbol{\lambda}(s)}{\boldsymbol{\theta}(s)}\right] \times \left[\frac{\Delta\mathbf{C}(s)}{\boldsymbol{\theta}(s)}\right]^{-1} \tag{4.1}$$

Where the $\boldsymbol{\lambda}$ vector contains $[\lambda_0 \;\; \lambda_{1S} \;\; \lambda_{1C}]^\intercal$, the aerodynamic loading vector $\Delta\mathbf{C}$ contains $[\Delta C_T \;\; \Delta C_L \;\; \Delta C_M]^\intercal$, and the swashplate control vector $\boldsymbol{\theta}$ contains $[\theta_0 \;\; \theta_{1S} \;\; \theta_{1C}]^\intercal$.

Next, a *parametric* state-space model is fit to the frequency response curves. The form for hover is taken from Eq.(2.11), with time delays added as shown in Eq.(2.15), such that the final form is:

$$\begin{bmatrix} M_{11} & 0 & 0 \\ 0 & M_{22} & 0 \\ 0 & 0 & M_{33} \end{bmatrix} \begin{pmatrix} \overset{*}{\lambda}_0 \\ \overset{*}{\lambda}_{1s} \\ \overset{*}{\lambda}_{1c} \end{pmatrix} + \begin{bmatrix} \bar{L}_{11} & 0 & 0 \\ 0 & \bar{L}_{22} & 0 \\ 0 & 0 & \bar{L}_{33} \end{bmatrix} \begin{pmatrix} \lambda_0 \\ \lambda_{1s} \\ \lambda_{1c} \end{pmatrix} = \begin{pmatrix} \Delta C_T(t-\tau_{11}) \\ \Delta C_L(t-\tau_{22}) \\ \Delta C_M(t-\tau_{33}) \end{pmatrix} \tag{4.2}$$

Because the responses of λ_{1c} to ΔC_M and λ_{1s} are ΔC_L are equivalent in hover due to axial symmetry, it is also helpful to constrain $M_{33} = M_{22}$, $\bar{L}_{33} = \bar{L}_{22}$, and $\tau_{33} = \tau_{22}$. This leaves six free variables in this state-space model which are optimized for the best fit with the non-parametric frequency responses: M_{11}, M_{22}, $\bar{L}_{11}$, $\bar{L}_{22}$, τ_{11}, andτ_{22}.

For forward flight, the form originates from Eq.(2.12), with time delays added as shown in Eq.(2.13), such that the final form is:

$$\begin{bmatrix} M_{11} & 0 & 0 \\ 0 & M_{22} & 0 \\ 0 & 0 & M_{33} \end{bmatrix} \begin{Bmatrix} \overset{*}{\lambda}_0 \\ \overset{*}{\lambda}_{1s} \\ \overset{*}{\lambda}_{1c} \end{Bmatrix} + \begin{bmatrix} \bar{L}_{11} & 0 & \bar{L}_{13} \\ 0 & \bar{L}_{22} & 0 \\ \bar{L}_{31} & 0 & \bar{L}_{33} \end{bmatrix} \begin{Bmatrix} \lambda_0 \\ \lambda_{1s} \\ \lambda_{1c} \end{Bmatrix} = \cdots$$
$$\begin{Bmatrix} \Delta C_T \\ \Delta C_L \\ \Delta C_M \end{Bmatrix} \left(t - \begin{bmatrix} \tau_{11} & 0 & \tau_{13} \\ 0 & \tau_{22} & 0 \\ \tau_{31} & 0 & \tau_{33} \end{bmatrix} \right) \tag{4.3}$$

In Pitt-Peters model the M_{22} and M_{33} are equal, even in forward flight, so this constraint will be preserved for the identified state space forward flight model. Eq.(4.3) uses two additional time delays, τ_{13} and τ_{31}. Compared with the hover case, two additional frequency responses must be fit with this model to complete the identification. They are the response of average inflow λ_0 to pitch moment input ΔC_M and the response of longitudinal inflow λ_{1c} to thrust input ΔC_T. Like all previous frequency responses, these responses will be produced using the Joint Input-Output method described in Sec 3.3.5. For the forward flight case, 12 independent parameters will have to be identified: M_{11}, M_{22}, $\bar{L}_{11}$, $\bar{L}_{22}$, $\bar{L}_{33}$, $\bar{L}_{13}$, $\bar{L}_{31}$, τ_{11}, τ_{22}, τ_{33}, τ_{13}, andτ_{31}.

4.2.1 Time Domain Verification

The state-space models identified as described in the previous sections is verified in the time-domain using a set of swashplate controls, different from those used in the identification. VERIFY then uses the time histories of $\Delta\mathbf{C}$ as inputs to a linear simulation based on the state-space system previously identified, calculating the corresponding outputs $\Delta\boldsymbol{\lambda}$. These can added to their respective trim values and then directly compared with the MFW time histories of inflow to ensure that the identified inflow model sufficiently matches the free wake.

4.3 Hover

4.3.1 Frequency Responses and State-space Modeling

The methodology was applied to a single main rotorcraft in hover, whose configuration is described in Appendix B.

4.3.1.1 Collective Degree of Freedom

The first results are limited to the collective degree of freedom. The inflow equation is simply:

$$M_{11}\overset{*}{\lambda}_0 + \bar{L}_{11}\lambda_0 = \Delta C_T \tag{4.4}$$

Figure 4.3 compares four $\lambda_0(s)/\Delta C_T(s)$ frequency responses. The first response is computed using the Pitt-Peters dynamic inflow model [25]. The second is computed using the same model incorporated into the full flight dynamic simulation

HeliUM [98], such that the actual input is the swashplate collective θ_0, and the thrust coefficient C_T is obtained as part of the calculations, with blade flapping motion included. The third response is the inflow non-parametric frequency response identified from the MFW. The fourth response is an inflow non-parametric frequency response identified, using the same procedure, in Ref. [95] with a different free-wake method model, RAPiD Free Wake model (RFW). All responses are in good agreement at low frequency ($\omega < 4 - 6$ rad/sec), where the high-order free wake models reduce to a simple first-order behavior. Above $\omega > 5$ rad/sec, both the RFW and the MFW show some additional phase lag.

Fig. 4.4 compares the $\lambda_0(s)/\Delta C_T(s)$ non-parametric frequency response identified from MFW and the $\lambda_0(s)/\Delta C_T(s)$ frequency response obtained from the state-space inflow model of Eq.(4.2) extracted through identification. The agreement is good, and in particular that is identified from the free wake simulation is presented in . The state-space model matches well with its associated frequency responses and the pole roll off near 6 rad/sec is well captured. The cost of the identification for the model is $J < 40$, indicating an excellent match between in the frequency domain.

Table 4.1 lists coefficients of the identified state-space model identified from MFW. The coefficients are compared to Pitt-Peters coefficients, and also with two sets of parameters identified through frequency domain system identification from HeliUM with Pitt-Peters incorporated, and from RFW. The transfer functions of the various state-space models are compared in Fig. 4.5. The Cramer-Rao ($CR_i < 6\%$) and insensitivity ($I_i < 3\%$) values are very low, indicating high confidence in, and low correlation between, the parameter values [63].

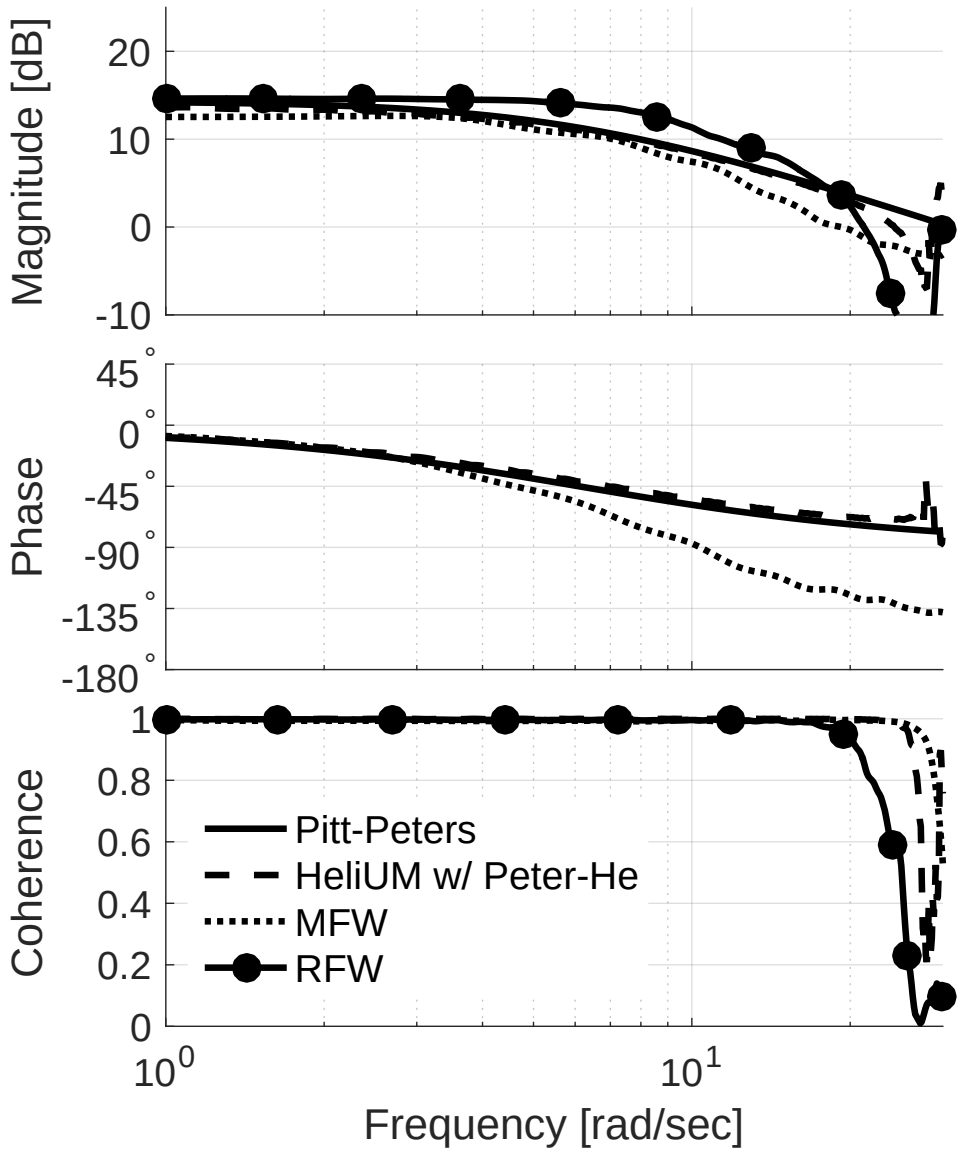

Figure 4.3: Non-parametric average inflow λ_0 response to thrust coefficient ΔC_T input.

4.3.1.2 Cyclic Degree of Freedom

For the identification of the response to cyclic inputs, the starting point used was a *Peters-He* model, 10 states and 3 harmonics. The controls were subjected to frequency sweeps the Joint-Input Output method was used to find the λ_{1c} to ΔC_M

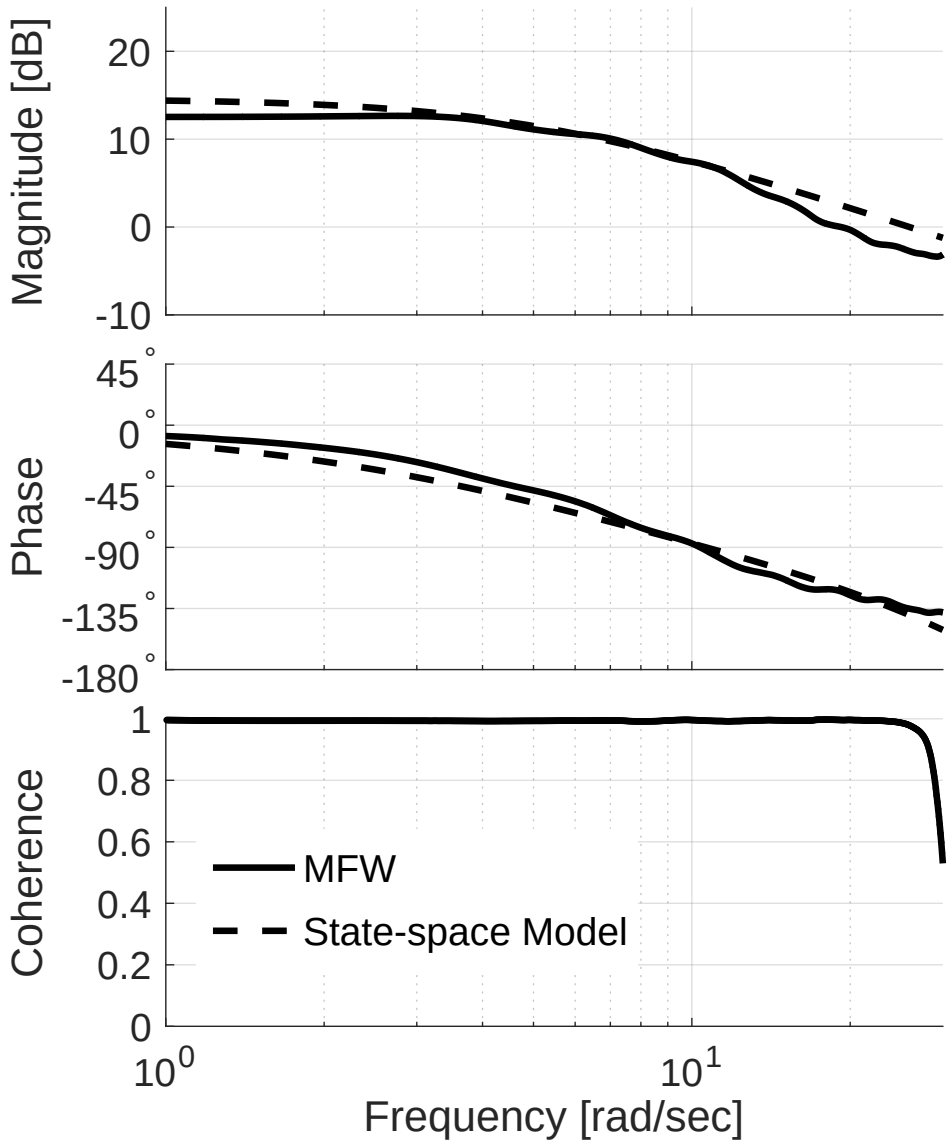

Figure 4.4: inflow λ_0 response to thrust coefficient ΔC_T input: Full MFW vs. identified state-space model

frequency response. This is also shown in Fig. 4.6, with the line labeled HeliUM w/ Peters-He. A comparison with the first-order Pitt-Peters model, also shown in the figure, indicates that the additional states are not necessarily in this frequency range, as the wake still has essentially a first order behavior. The following first

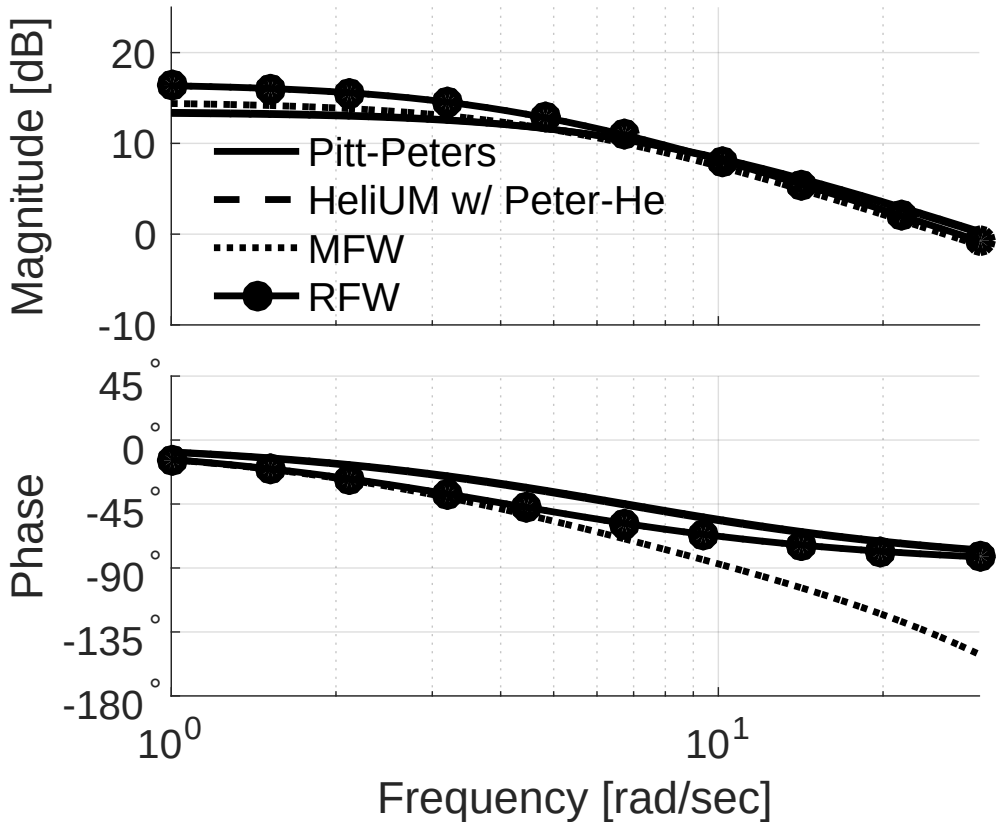

Figure 4.5: Inflow λ_0 response to thrust coefficient ΔC_T input: Comparison of different state-space models.

order transfer function (fit from 1-30 rad/sec):

$$\frac{\lambda_{1c}}{\Delta C_M} = \frac{-262.38}{(10.6201)} \tag{4.5}$$

is therefore sufficiently accurate. Fig. 4.6 shows two more curves. The first, labeled as "MFW", is the frequency response from the full, nonlinear MFW. This is the frequency response that will be used to extract the linearized state-space inflow model. The second is similar but obtained from the RFW.

The frequency response from the MFW was fit with a state space model of the form of Eq.(4.2). The results are shown in Fig. 4.7. The coefficients of the

Table 4.1: Comparison of inflow coefficients in the vertical axis obtained using frequency sweeps.

Model	M_{11}/Ω_0	$\bar{L}_{11}$	τ_{11}
identified from MFW	0.0379	0.187	.0408
Pitt-Peters (Ref. 25)	0.0314	0.214	none
Pitt-Peters identified (including blade flapping)	0.0321	0.211	none
identified from RFW	0.0360	0.148	n/a

identified model are shown in Table 4.2, together with those of the Pitt-Peters model, the 10-state Peters-He identified model, and the model identified form the RFW. Good agreement between all the identified models and the Pitt-Peters model is shown. However, there is a considerable 2nd order shape apparent in MFW and RFW magnitude curves. At low frequency the slopes are not flat like the Pitt-Peters models, but rather has a positive slope. This is better fit with a low frequency zero and two mid frequency poles, hence a second order transfer function. Two poles also allow for the phase to change by more than 90 degrees as the two free-wake models do (compared to the dynamic inflow models which stop at -90 degrees). However a first order model still fits the frequency response data fairly well, as long as time delays are included.

The transfer function (or state-space model with parameters from Table 4.2) representations are all compared in Fig. 4.8. The small discrepancies in the $\bar{L}_{22}$

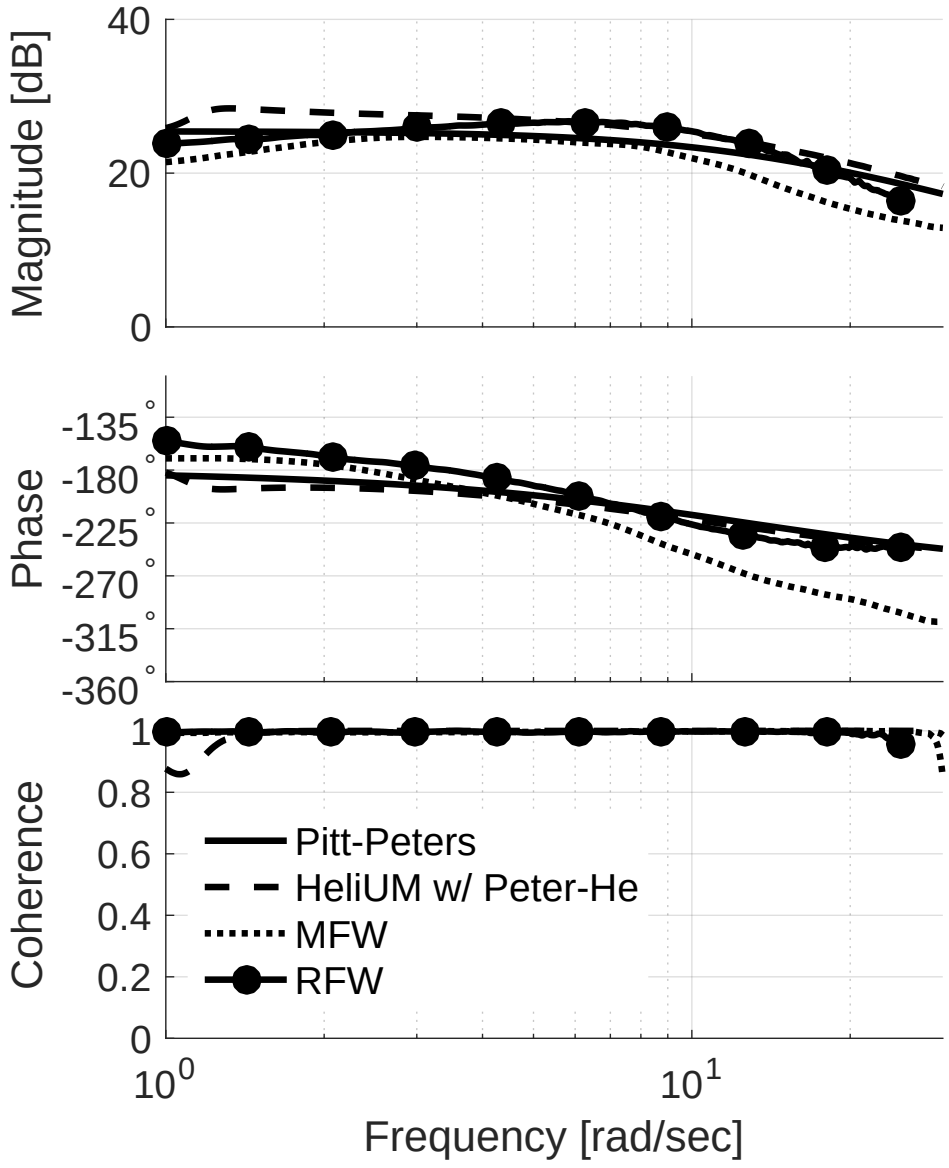

Figure 4.6: Non-parametric λ_{1c} frequency response to ΔC_M.

values in Table 4.2 are a result of steady-state differences in Fig. 4.6. These steady-state differences are made more apparent in Fig. 4.8.

Note that, because this is an isolated rotor model, with no fuselage, tail rotor, or any other feature that could otherwise make the response non-symmetric, the

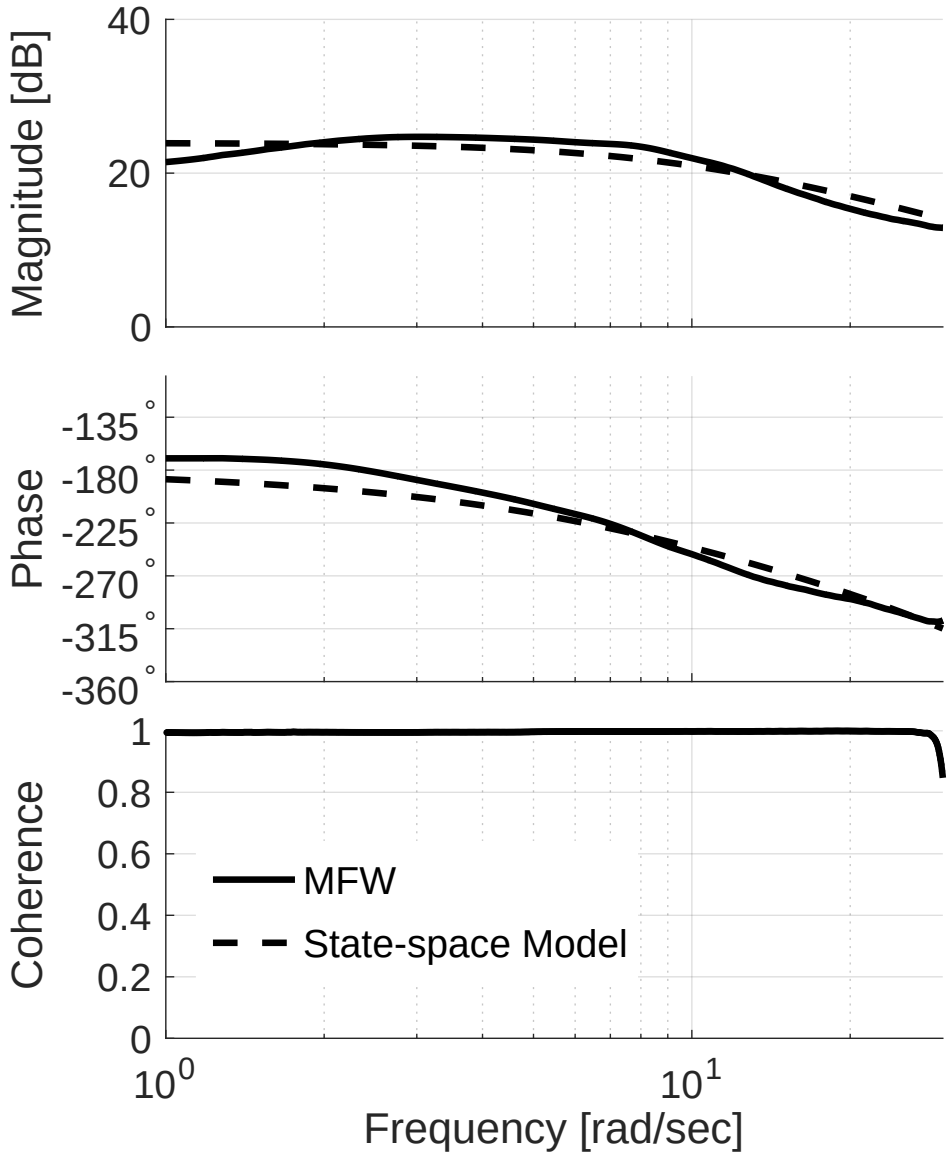

Figure 4.7: Non-parametric vs Parametric (State-space Model) λ_{1c} frequency response to ΔC_M.

response of the λ_{1s} to ΔC_L is identical to the response of λ_{1c} to ΔC_M and $M_{22} = M_{33}$ and $\bar{L}_{22} = \bar{L}_{33}$

Table 4.2: Comparison of cyclic inflow coefficients (diagonal terms only) obtained using frequency sweeps.

Model	M_{22}/Ω_0	$\bar{L}_{22}$	τ_{22}
Pitt-Peters (Ref. 25)	-0.0042	-0.0534	none
HeliUM: 10 state Peters-He	-0.0038	-0.0405	none
MFW	-.0063	-.0636	0.0369
RFW (Rigid)	-0.0043	-0.0651	n/a

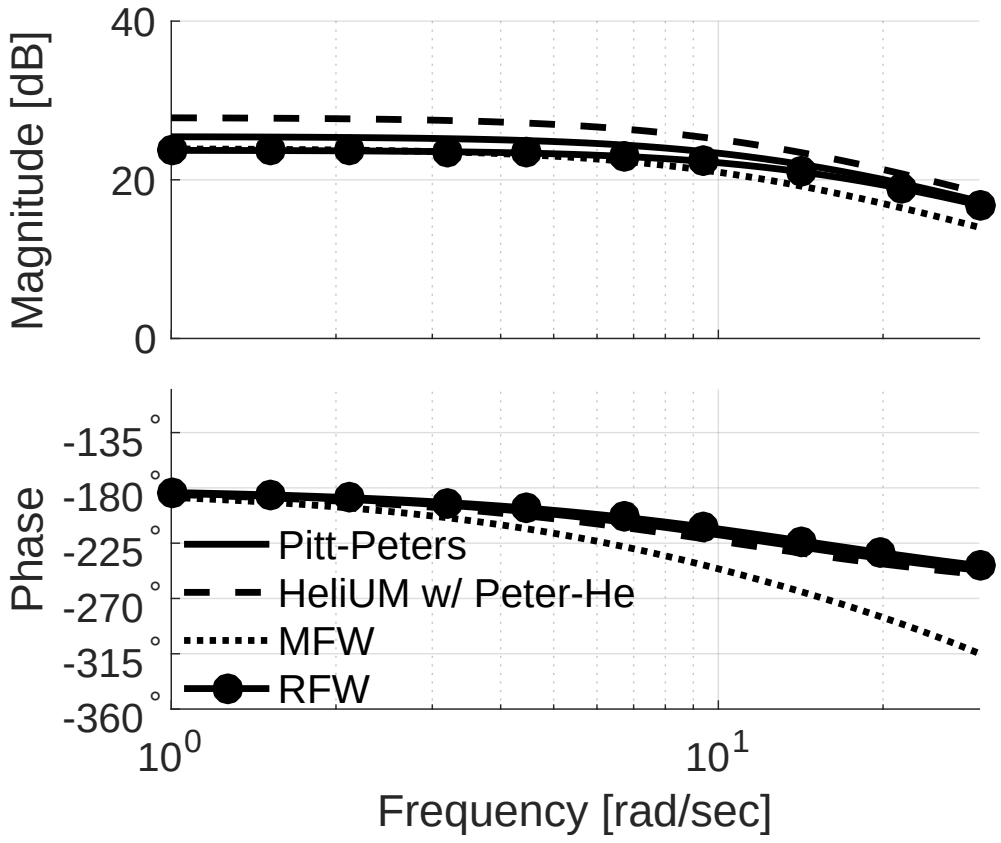

Figure 4.8: Comparison of different state-space model of λ_{1c} response to ΔC_M.

4.3.2 Time Verification

The state-space inflow model obtained from system identification was verified in the time domain by using inputs different from those used for the identification. In this case a doublet-like perturbation, shown in Fig. 4.9, was input into the swash-plate. The time histories of the corresponding aerodynamic loading ΔC_T, ΔC_L, and ΔC_M and inflow coefficients λ_0, λ_{1c}, and λ_{1s} were computed using the full, nonlinear MFW. The inflow coefficients were compared with those predicted by the identified state-space model.

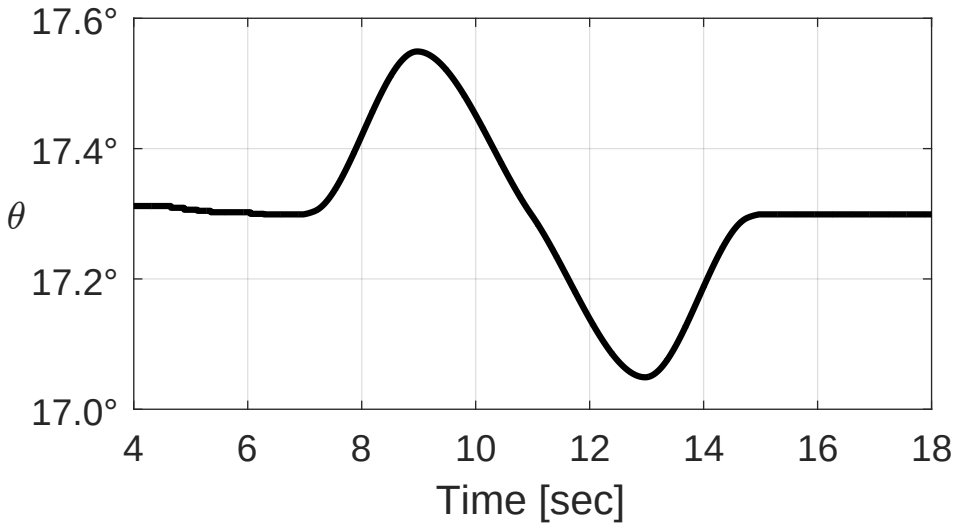

Figure 4.9: Representative doublet maneuver used for time verification.

Figure 4.10 shows the aerodynamic thrust C_T and average inflow λ_0 from doublet of collective θ_0. The top plot shows the thrust coefficient C_T corresponding to the θ_0 doublet, computed using the MFW. The perturbation (from trim) thrust

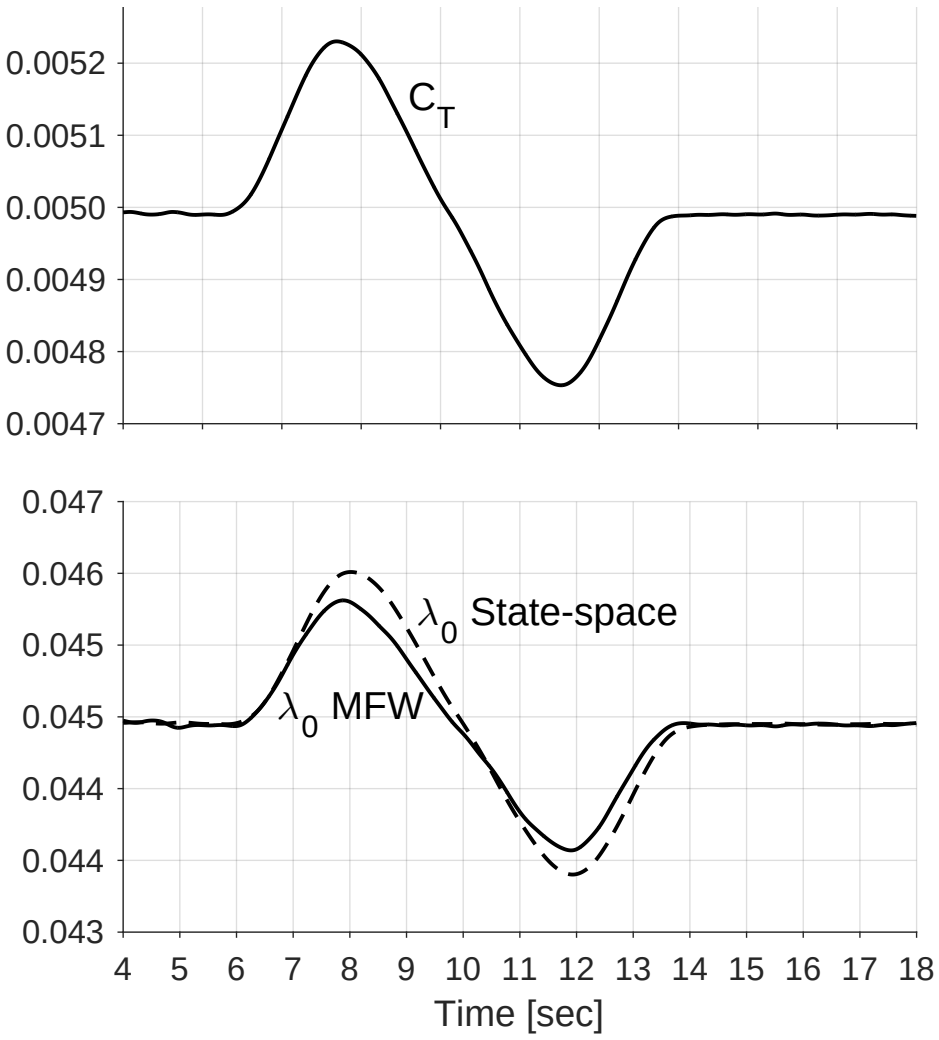

Figure 4.10: Time-domain verification of state-space model for average inflow given a doublet in C_T. Dashed line indicates state-space prediction; solid line indicates MFW actual data.

ΔC_T is then used as input to the identified state-space inflow model. The output of the identified state-space model is perturbation inflow $\Delta\lambda_0$, which is added to trim average inflow to obtain total average inflow λ_0. The bottom plot shows a comparison of the average inflow λ_0 response of the MFW (solid line) and the identified state-space model (dashed line). There is generally good agreement between the two

responses. The mismatch is caused by the fact that the model does not capture the whole frequency range perfectly, because the dynamics are not precisely first order, as shown in Fig. 4.4.

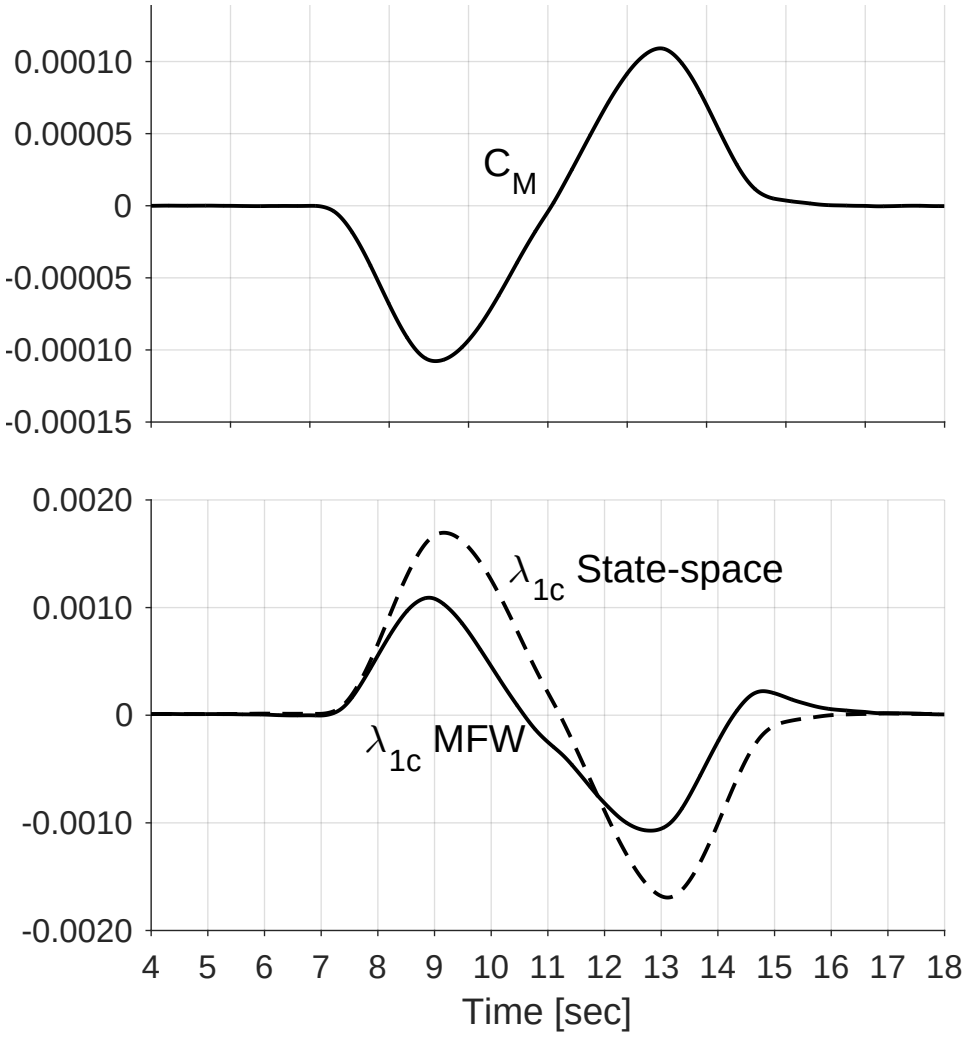

Figure 4.11: Time-domain verification of state-space model for longitudinal inflow given a doublet in C_M. Dashed line indicates state-space prediction; solid line indicates MFW actual data.

Similarly, Fig. 4.11 shows the aerodynamic pitching moment C_M and longitudinal inflow λ_{1c} from doublet of cyclic θ_{1c}. The top plot shows the pitching moment

C_M corresponding to the θ_{1c} doublet, computed using the MFW. The perturbation pitch moment ΔC_M is then used as input to the identified state-space inflow model. The output of the identified state-space model is perturbation inflow $\Delta\lambda_{1c}$, which is added to trim longitudinal inflow to obtain total longitudinal inflow λ_{1c}. The bottom plot shows a comparison of the total longitudinal inflow λ_{1c} response of the MFW (solid line) and the identified state-space model (dashed line). There is generally good agreement between the two responses. The mismatch is caused by the fact that the model does not capture the whole frequency range perfectly, because the dynamics are not precisely first order, as shown in Fig. 4.4. There is more disagreement between the MFW and the identified state-space model as compared to the λ_0-C_T time verification. This is directly related to the error shown in Fig. 4.7, which is larger than for the average inflow frequency response. The model still does capture the correct sign and most of the magnitude and phasing of the response.

4.4 Forward Flight Results

Inflow models were identified at two advance ratios, $\mu = 0.1$ and $\mu = 0.2$.

4.4.1 Frequency Responses and State-space Modeling

4.4.1.1 Advance Ratio $\mu = 0.1$

The λ_0 response to aerodynamic thrust C_T at $\mu = 0.1$ is shown in Figure 4.12. The solid line shows the MFW data, and the dashed line the best state-space model fit. The match of the model is excellent, and the time delays help capture the higher

order dynamics shown by the extended phase roll-off (te phase of a rigorously first order model would have been asymptotic to $-90°$).

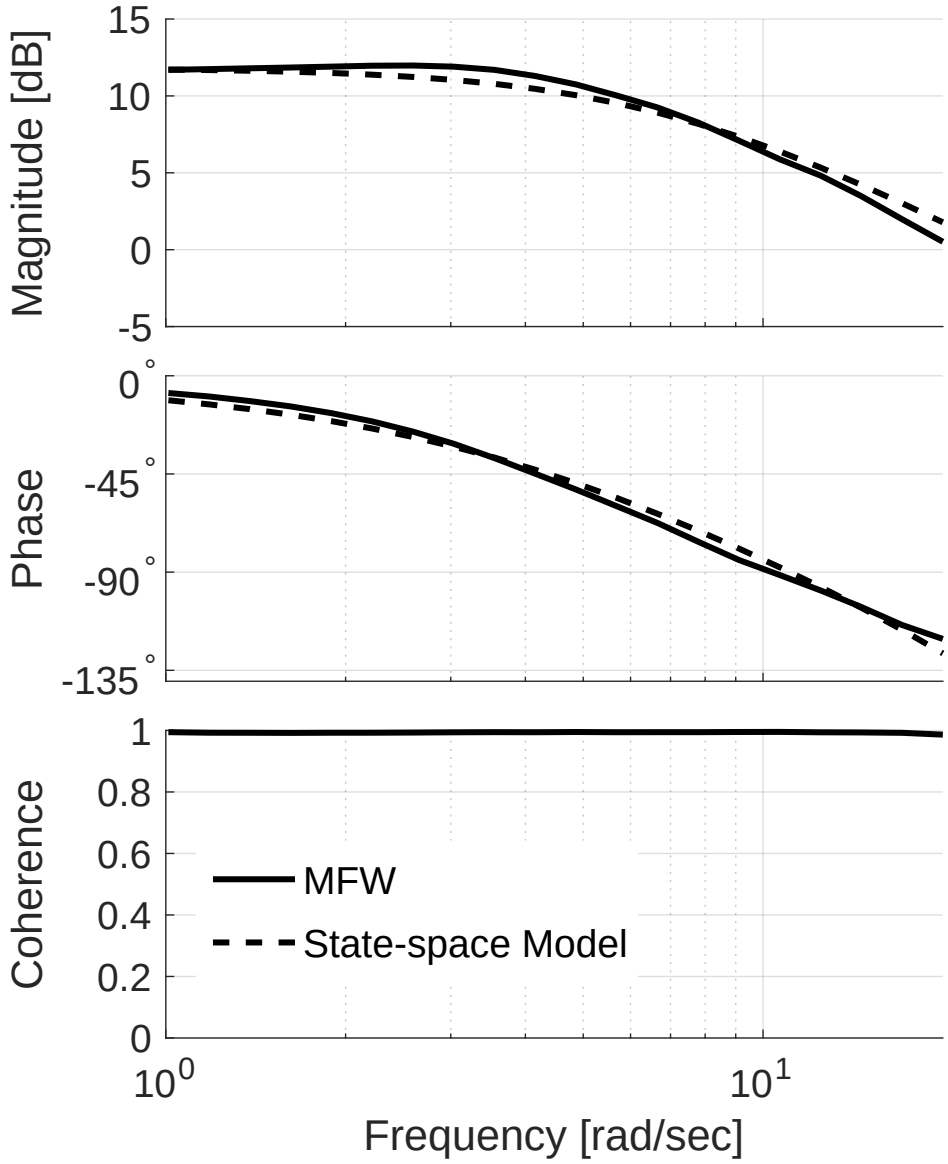

Figure 4.12: Inflow λ_0 frequency response to C_T at $\mu = 0.1$. Cost of the fit is 12.2.

Figure 4.13 shows the response of lateral inflow λ_{1s} to roll moment C_L. The solid line shows the MFW data, and the dashed line showing the state-space model fit. The magnitude of this response is flatter at low frequency than hover (shown in

Fig. 4.7). This indicates that a single pole with no zeros will capture the magnitude curve well. The phase curve can then be corrected by addition of a time delay. The result is that a first order system, with only one pole, but with a time delay, captures much better captures the response shape, and produces a very accurate fit.

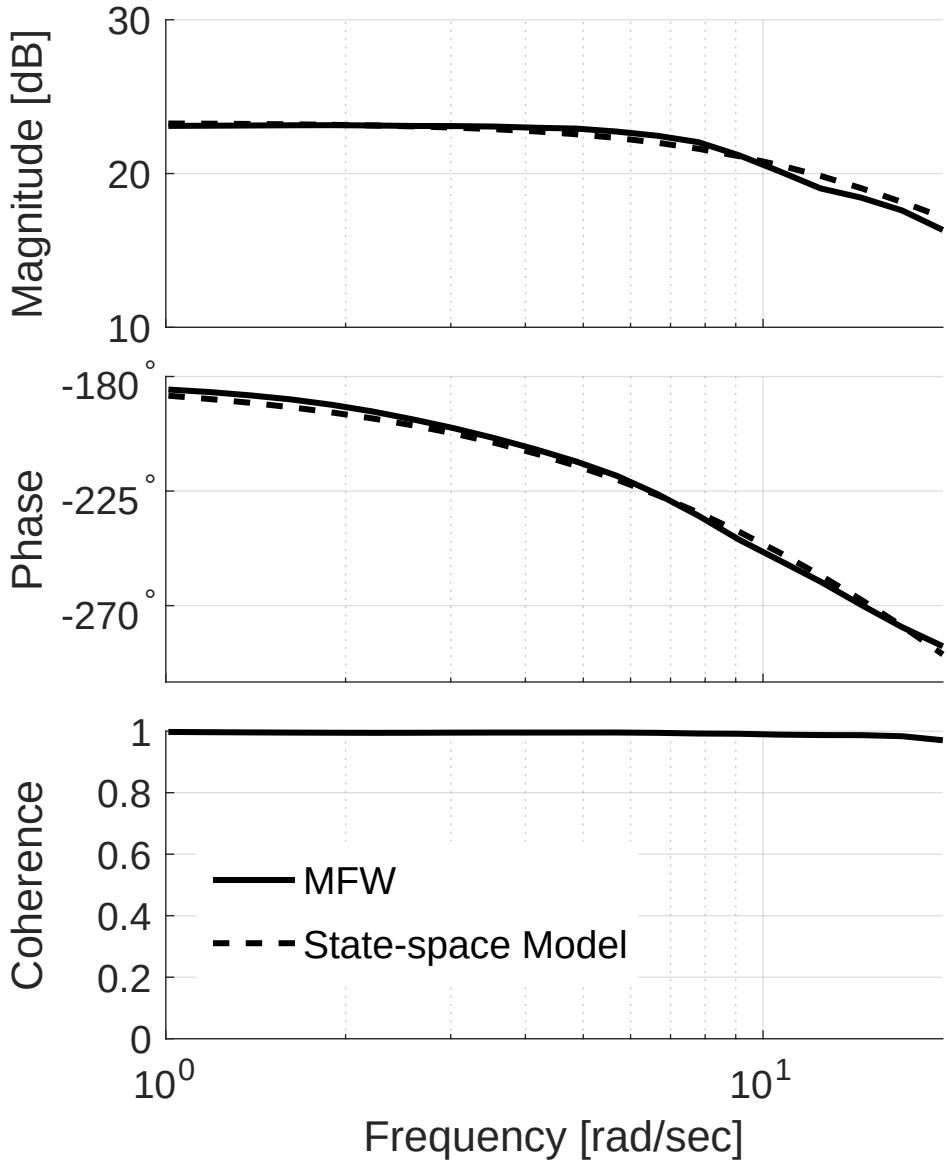

Figure 4.13: Inflow λ_{1s} frequency response to C_L at $\mu = 0.1$. Cost of the fit is 4.9.

The last primary response at $\mu = 0.1$ is the longitudinal inflow λ_{1c} response to input pitch moment C_M, shown in Fig. 4.14. The magnitude of this response is not flat at low frequency, but rather rises, peaks at around 6 rad/sec, and then falls off. This behavior is similar to that shown in Fig. 4.7, which was noted to have a better potential fit with a second order system; particularly with a zero at low frequency and two stable poles in the middle frequency range. The forward flight state-space model does indeed include these for this response. The transfer function, corresponding to the dashed line in Fig. 4.14, is:

$$\frac{\lambda_{1c}}{C_M} = \frac{-165.72(5.94)}{(7.06)(13.35)} \tag{4.6}$$

The zero, however, is not separated far enough from the poles to really make magnitude slope change apparent, as it is mostly canceled by the pole at 7.06 rad/sec. However the optimization finds this to be the optimal fit to the state-space model because it keeps the cost of the other responses low, particularly C_M to λ_0. Nevertheless the given fit is exceptable in terms of capturing the response.

The first off-axis response in forward flight, shown in this section, is the λ_{1c} response to thrust C_T, shown in Fig. 4.15. This frequency response has a change in slope in the middle frequency range more indicative of 2 poles, but is nevertheless captured reasonably well with a single pole and a time delay, as shown by a cost of $J = 80$.

The second off-axis response of interest, i.e. the response of average inflow λ_0 to pitching moment C_M, is shown in Figure 4.15. The response to C_M contributes less towards average inflow λ_0 than the primary responses does, but it still needs to

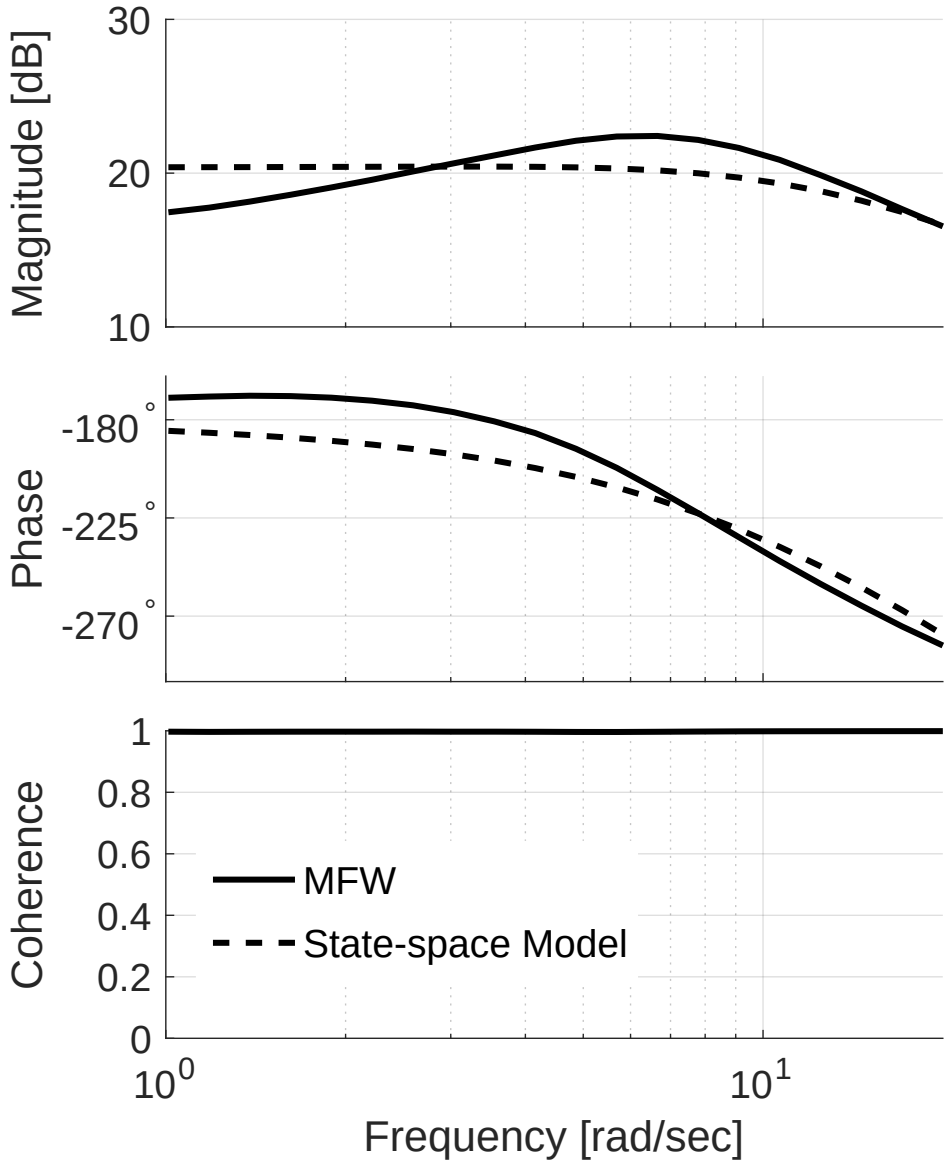

Figure 4.14: Inflow λ_{1c} frequency response to C_M at $\mu = 0.1$. Cost of the fit is 120.1

be retained to maintain the overall accuracy of the identification. However the cost of this state-space fit is not as important due to low magnitude of the response.

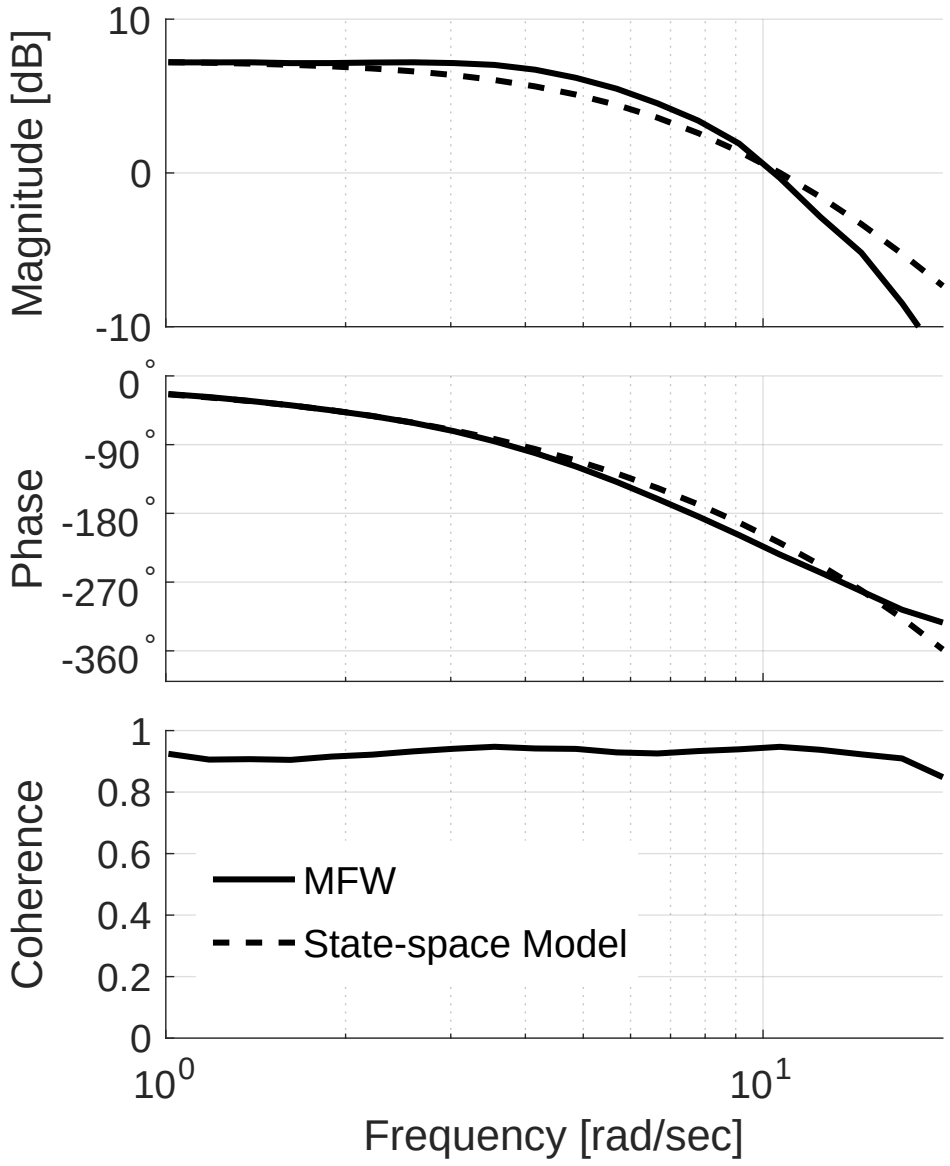

Figure 4.15: Inflow λ_{1c} frequency response to C_T at $\mu = 0.1$. Cost of the fit is 80.5

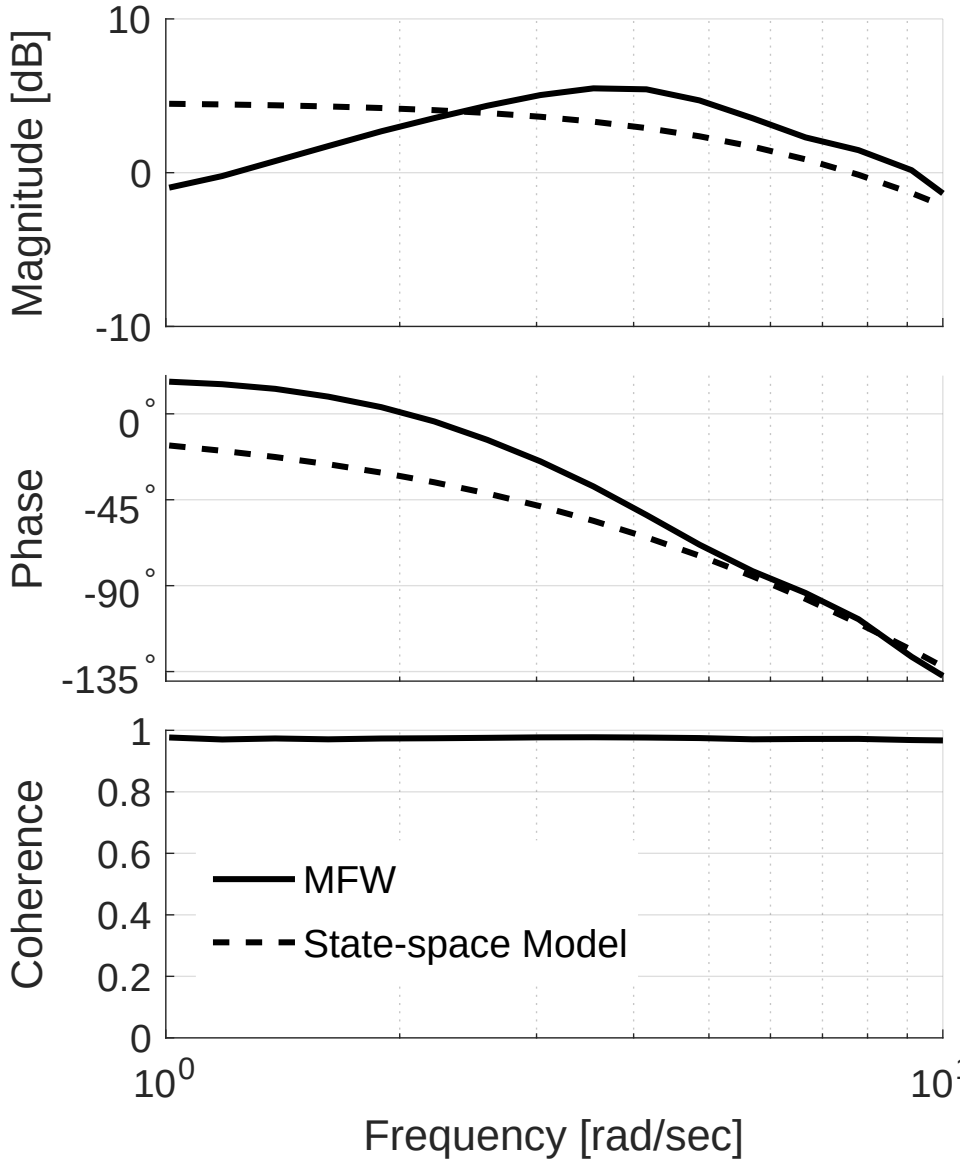

Figure 4.16: Inflow λ_0 frequency response to C_M at $\mu = 0.1$. Cost of the fit is 259.4

The full system in state space form for the $\mu = 0.1$ case is given by:

$$\begin{bmatrix} .0394 & 0 & 0 \\ 0 & -0.00603 & 0 \\ 0 & 0 & -0.00603 \end{bmatrix} \begin{Bmatrix} \overset{*}{\lambda}_0 \\ \overset{*}{\lambda}_{1s} \\ \overset{*}{\lambda}_{1c} \end{Bmatrix} + \begin{bmatrix} 0.234 & 0 & 0.038 \\ 0 & -0.0685 & 0 \\ 0.0521 & 0 & -0.0873 \end{bmatrix} \begin{Bmatrix} \lambda_0 \\ \lambda_{1s} \\ \lambda_{1c} \end{Bmatrix}$$
$$= \begin{Bmatrix} \Delta C_T \\ \Delta C_L \\ \Delta C_M \end{Bmatrix} \left(t - \begin{bmatrix} t - 0.047 & 0 & t - 0.071 \\ 0 & t - 0.043 & 0 \\ t - 0.20 & 0 & t - 0.039 \end{bmatrix} \right) \tag{4.7}$$

4.4.1.2 Advance Ratio $\mu = 0.2$

The λ_0 response to aerodynamic thrust ΔC_T at $\mu = 0.2$ is shown in Fig. 4.17. The solid line shows the actual MFW data, and the dashed line the best state-space model fit to the data. As for the $\mu = 0.1$ case the match of the model, as a first order system and a time delay, is excellent.

The lateral inflow λ_{1s} response to input roll moment ΔC_L is shown in Fig. 4.18. The magnitude of this response is flat at low frequency and so a first order system with one pole and a time delay produces an accurate fit.

The last primary response is the longitudinal inflow λ_{1c} response to input pitch moment ΔC_M, shown in Figure 4.19. As for the $\mu = 0.1$ case, the magnitude of this response has a shape that is well fit by a second order system with two poles and a zero. However, compared with the $\mu = 0.1$ case, this response has a little less

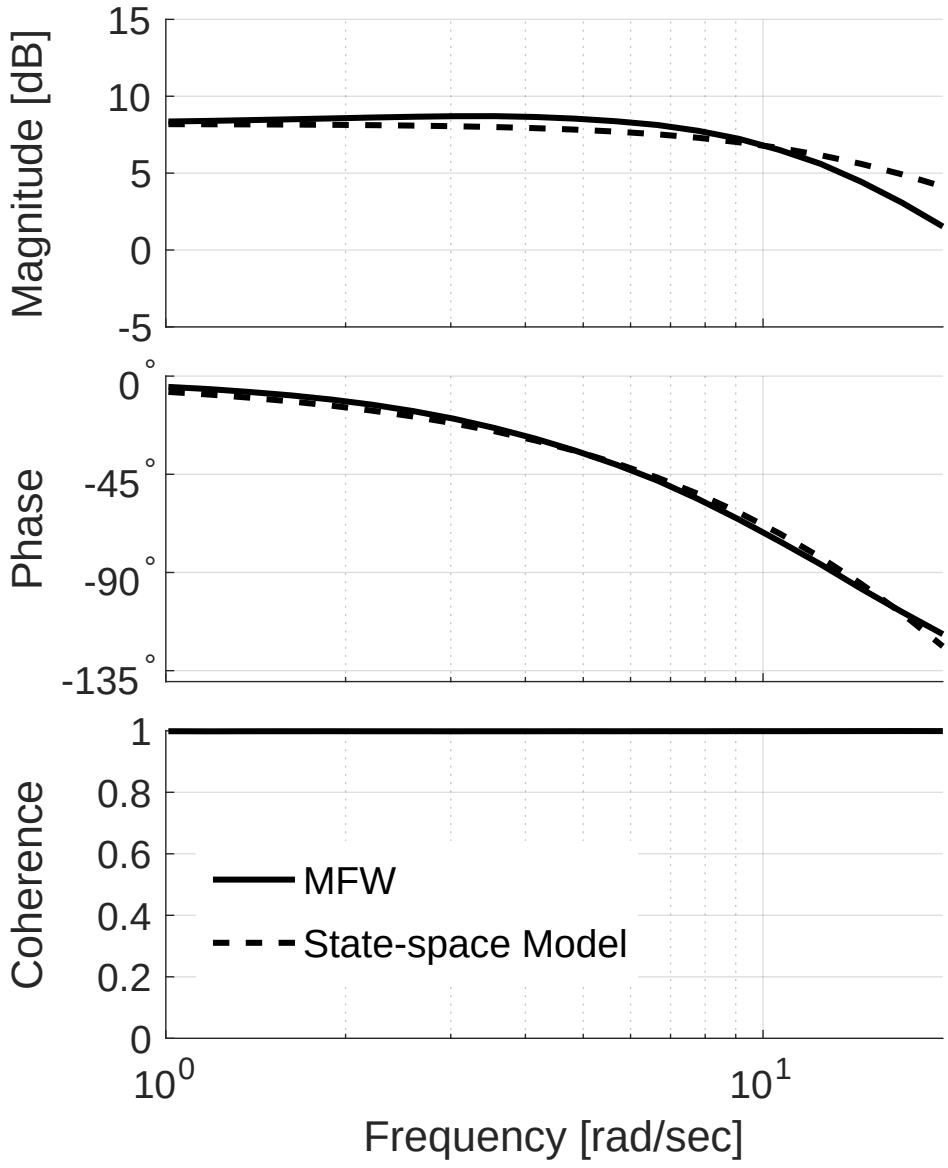

Figure 4.17: Inflow λ_0 frequency response to ΔC_T at $\mu = 0.2$. Cost of the fit is 18.1.

variation leading to the first order system fitting slightly better than in the $\mu = 0.1$ case.

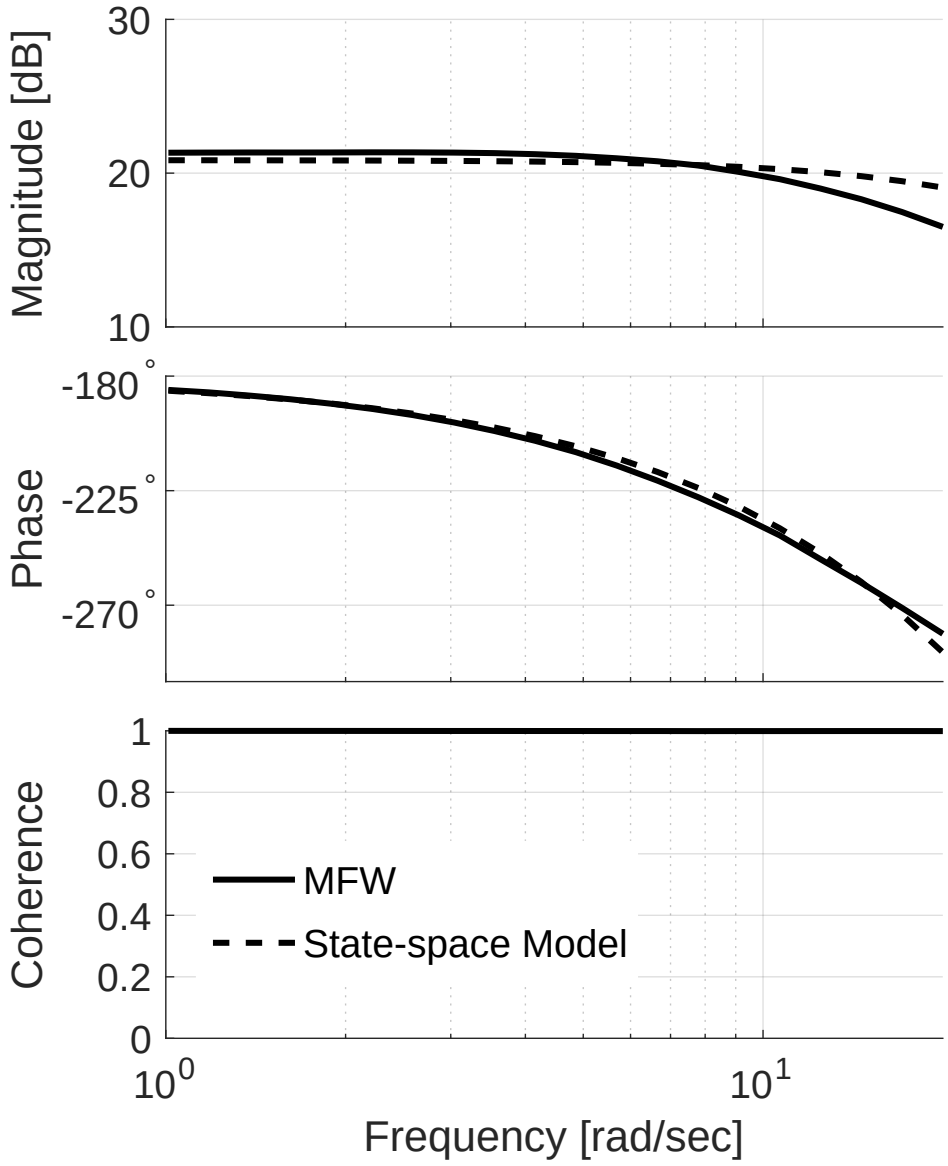

Figure 4.18: Inflow λ_{1s} frequency response to ΔC_L at $\mu = 0.2$. Cost of the fit is 19.7.

The response of longitudinal inflow λ_{1C} to thrust ΔC_T is shown in Fig. 4.20. This frequency response is captured accurately with a single pole and a time delay, as shown by the cost of 20.

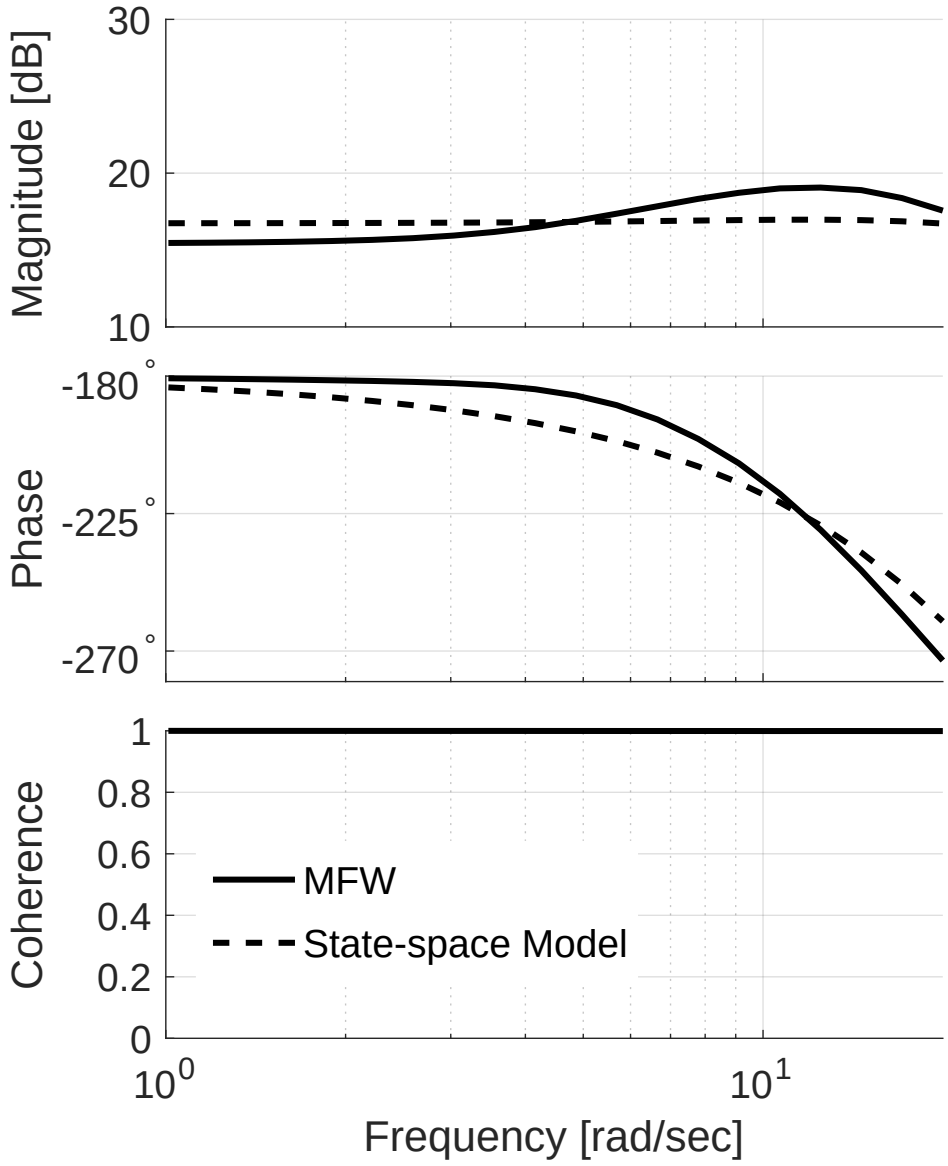

Figure 4.19: Inflow λ_{1c} frequency response to ΔC_M at $\mu = 0.2$. Cost of the fit is 55.5

The small off-axis λ_0 response to C_M is shown in Figure 4.21. As with the $\mu = 0.1$ case, the response is very small. Therefore the significantly worse fit, indicated by a value of the cost function $J = 1447$, does not affect the accuracy of the state-space model significantly. This means that the this frequency response can

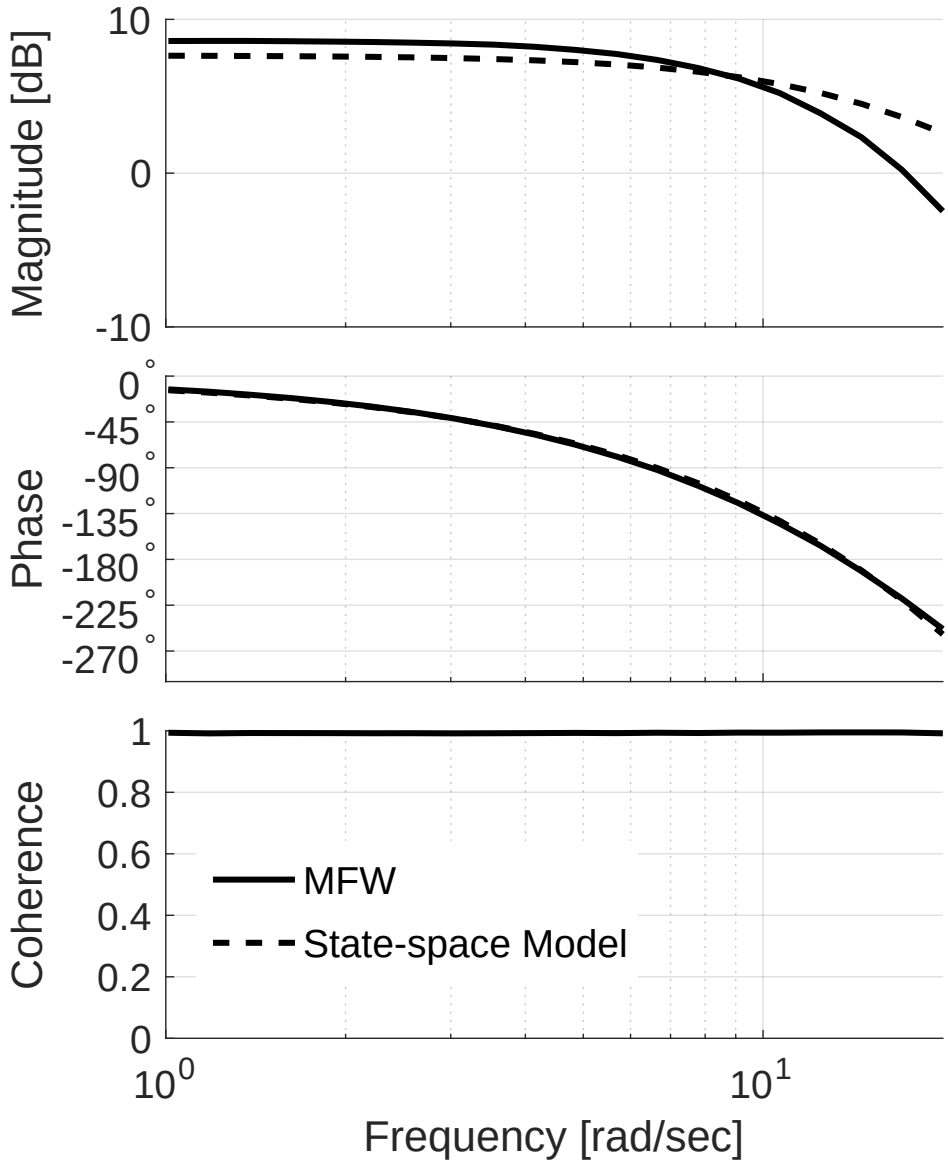

Figure 4.20: Inflow λ_{1c} frequency response to ΔC_T at $\mu = 0.2$. Cost of the fit is 55.5

likely be removed from the optimization for the state-space model. However, this would require changing the form in Eq.(4.3), specifically setting $\bar{L}_{31}$ and τ_{13} to zero. This is not explored in this work because a form equivalent to Pitt-Peters model was desired.

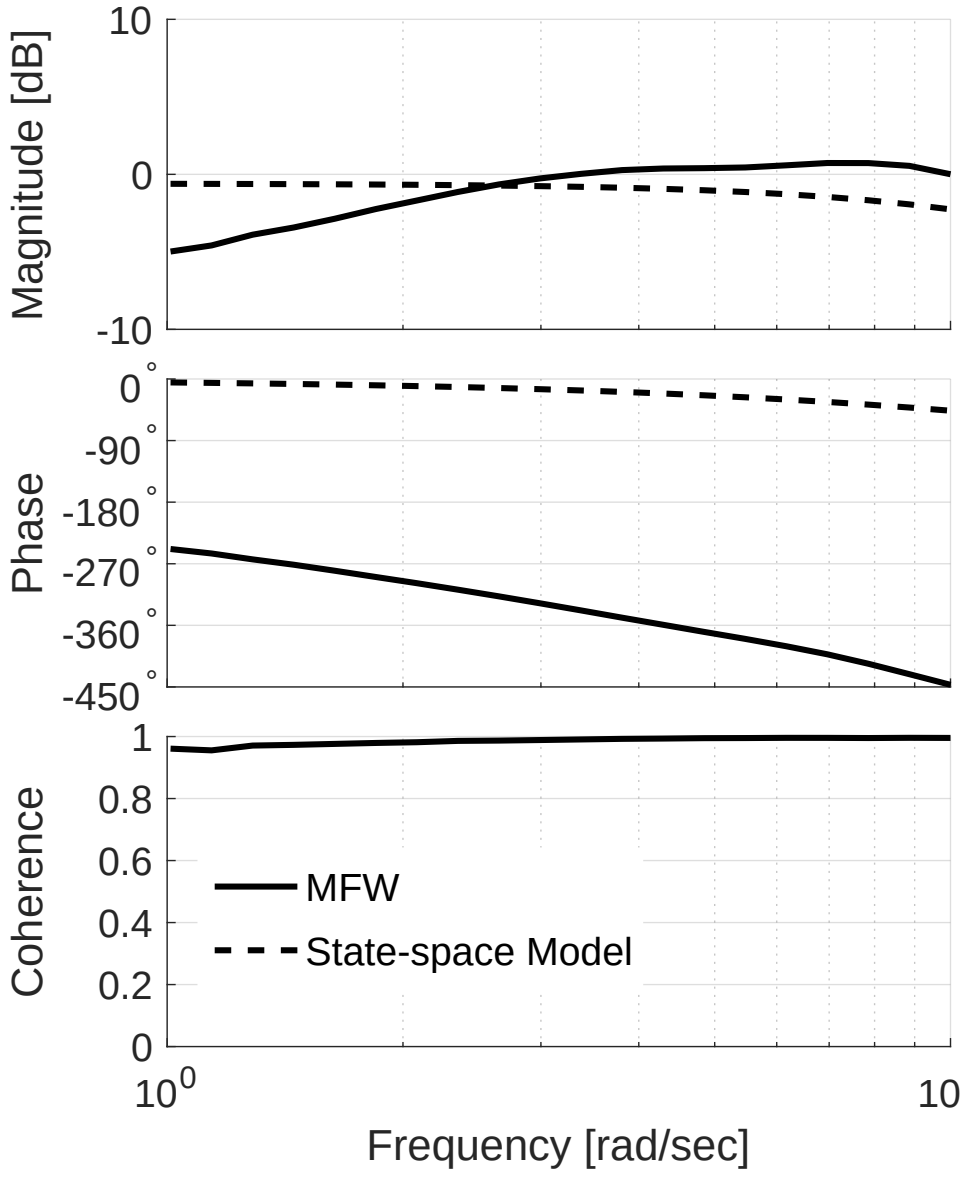

Figure 4.21: Non-parametric vs Parametric (State-space (S.S.) Model) λ_0 frequency response to C_M at $\mu = 0.2$. Cost of the fit is 1447

The full system in state space form for the $\mu = 0.2$ case is given by:

$$\begin{bmatrix} .0254 & 0 & 0 \\ 0 & -0.00323 & 0 \\ 0 & 0 & -0.00323 \end{bmatrix} \begin{pmatrix} \overset{*}{\lambda}_0 \\ \overset{*}{\lambda}_{1s} \\ \overset{*}{\lambda}_{1c} \end{pmatrix}$$

$$+ \begin{bmatrix} 0.345 & 0 & 0.047 \\ 0 & -0.09 & 0 \\ 0.121 & 0 & -0.129 \end{bmatrix} \begin{pmatrix} \lambda_0 \\ \lambda_{1s} \\ \lambda_{1C} \end{pmatrix}$$

$$= \begin{bmatrix} t - 0.062 & 0 & t - 0.00 \\ 0 & t - 0.057 & 0 \\ t - 0.15 & 0 & t - 0.05 \end{bmatrix} \begin{pmatrix} \Delta C_T \\ \Delta C_L \\ \Delta C_M \end{pmatrix} \tag{4.8}$$

4.4.2 Time Domain Verification

4.4.2.1 Advance Ratio $\mu = 0.1$

The time domain verification of the state-space model of Eq.(4.7) consists of three doublets , of collective, lateral and longitudinal cyclic pitch, respectively. The first doublet of collective pitch $\Delta\theta_0 = 0.25^\circ$ excites all three aerodynamic inputs, ΔC_T, ΔC_L, and ΔC_M, which in turn produce all three outputs, λ_0, λ_{1s}, and λ_{1c}. Inputs and corresponding on-axis outputs are shown in Figs. 4.22, 4.23 and 4.24, respectively.

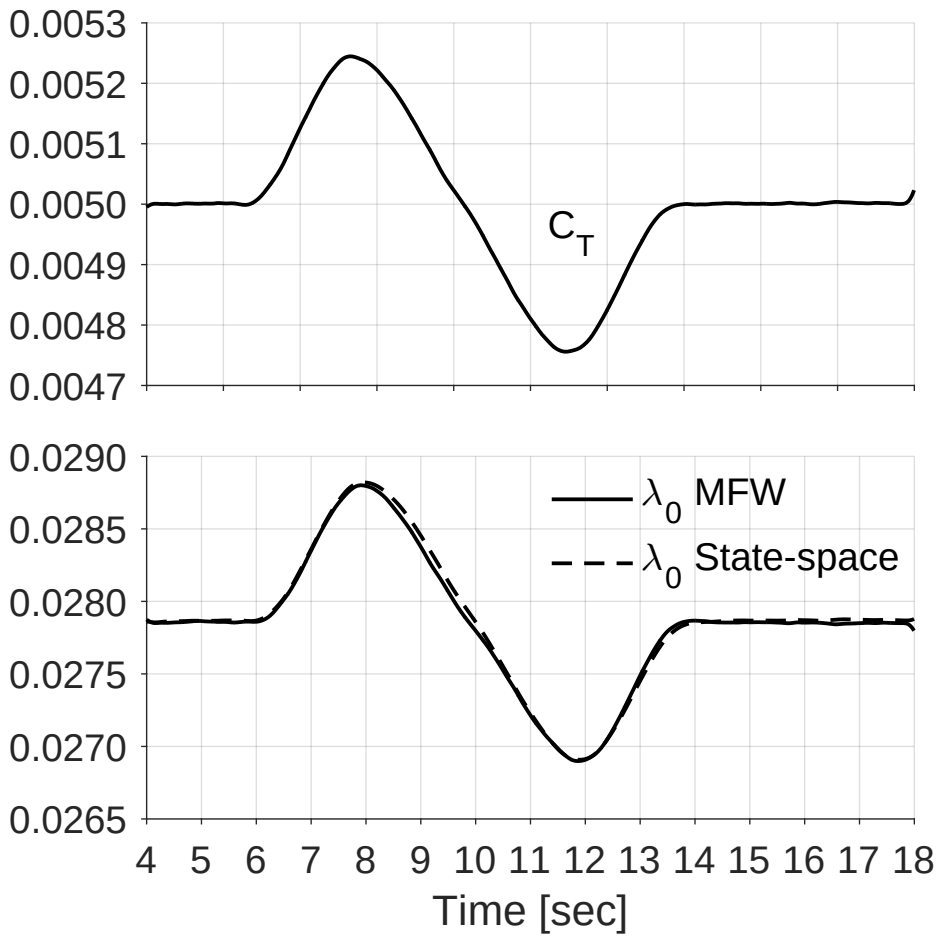

Figure 4.22: Time domain verification of inflow model, Eq.(4.7); solid line: MFW, dashed line: Eq.(4.7). Input: doublet of magnitude $\theta_0 = 0.25°$, $\mu = 0.1$.

The match for the λ_0 response to the three aerodynamic inputs, ΔC_T, ΔC_L, and ΔC_M, Fig. 4.22, is excellent. The state space system slightly over predicts the lateral inflow λ_{1s} response to the three aerodynamic inputs, Fig. 4.23, compared with the MFW prediction. The agreement is again very good for the longitudinal inflow λ_{1c} response to the three aerodynamic inputs, Fig. 4.24. Because the primary

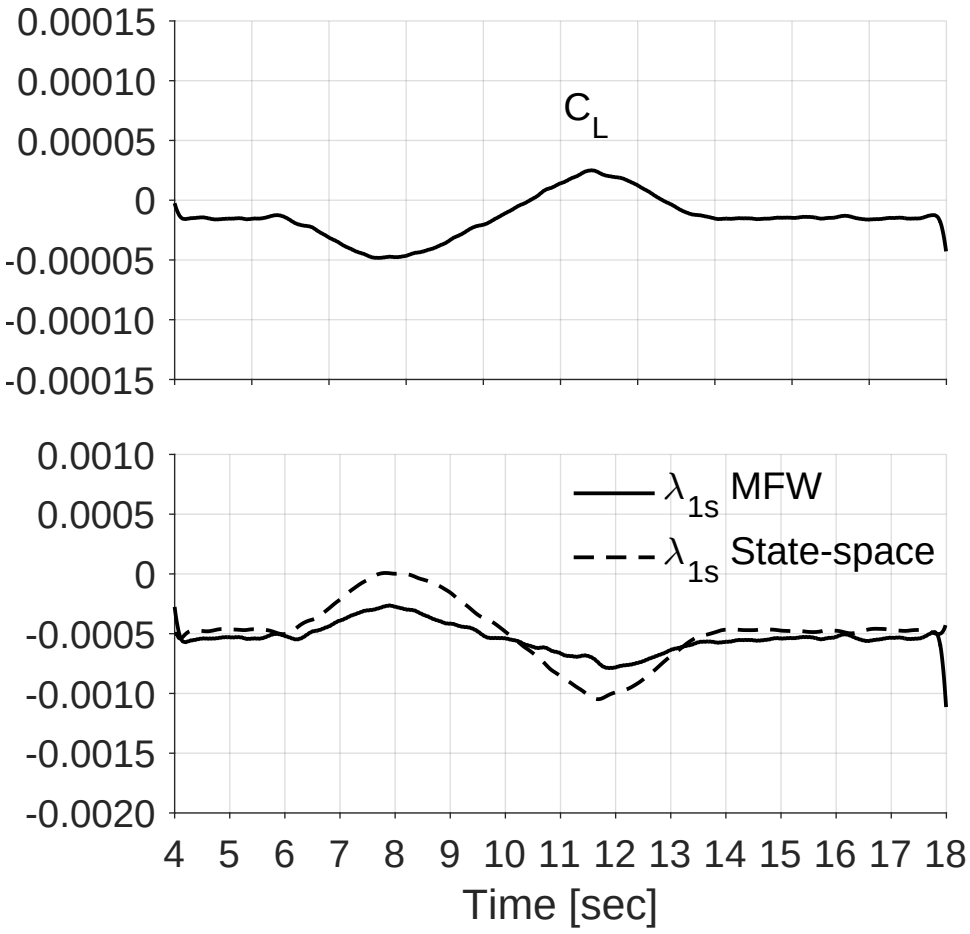

Figure 4.23: Time domain verification of inflow model, Eq.(4.7); solid line: MFW, dashed line: Eq.(4.7). Input: doublet of magnitude $\theta_0 = 0.25°$, $\mu = 0.1$.

responses to collective are C_T and λ_0, longitudinal and lateral inflow components are smaller secondary effects.

The second verification is a doublet of lateral cyclic $\Delta\theta_{1s}$ of magnitude 0.25 degrees. This maneuver produces a mostly decoupled response with just roll moment ΔC_L. Therefore the primary inflow output is lateral inflow λ_{1s}, as is shown in Fig. 4.25. The agreement with MFW predictions is excellent. The θ_{1s} doublet

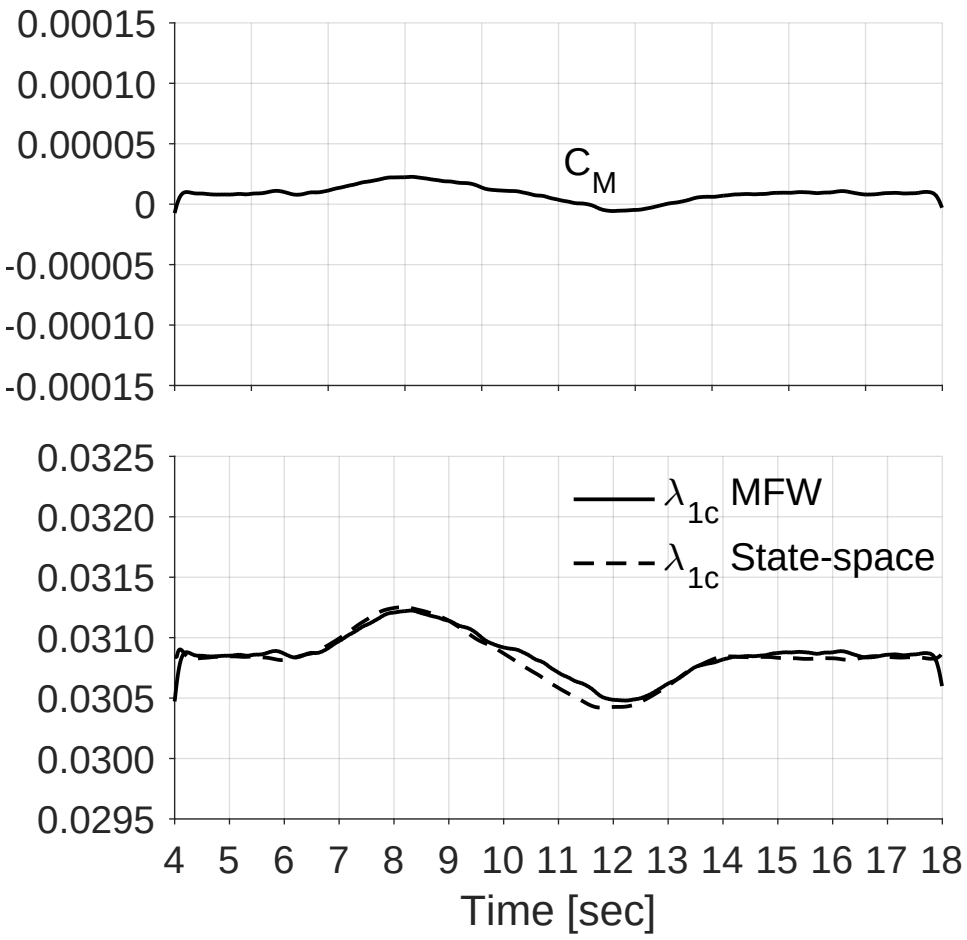

Figure 4.24: Time domain verification of inflow model, Eq.(4.7); solid line: MFW, dashed line: Eq.(4.7). Input: doublet of magnitude $\Delta\theta_0 = 0.25°$, $\mu = 0.1$.

generates very small ΔC_T and ΔC_M, therefore the corresponding time histories are not shown.

The third and final verification maneuver is a doublet of longitudinal cyclic $\Delta\theta_{1c}$ of magnitude 0.25 degrees. This maneuver produces mostly pitch moment ΔC_M. Therefore the primary inflow output is longitudinal inflow λ_{1c}, shown in Fig. 4.26. Longitudinal inflow is overpredicted, compared with the MFW. This is

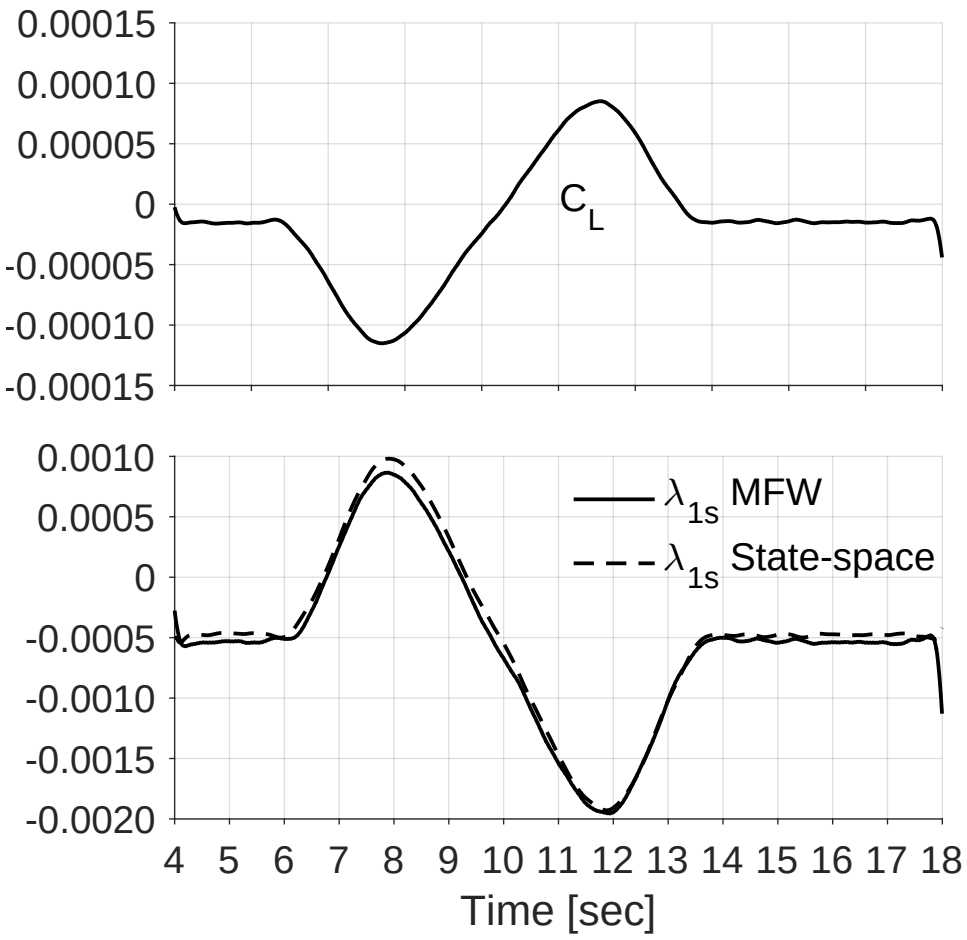

Figure 4.25: Time domain verification of inflow model, Eq.(4.7); solid line: MFW, dashed line: Eq.(4.7). Input: doublet of magnitude $\Delta\theta_0 = 0.25°$, $\mu = 0.1$.

caused by the larger error in the state-space fit (shown in Fig. 4.14). The $\Delta\theta_{1c}$ doublet generates very small C_T, as shown in Fig. 4.27, but through the couplings of Eq.(4.3), some λ_0 is generated, also shown in Fig. 4.27. λ_0 is underpredicted and but also small in magnitude, as is predicted by Fig. 4.16 .

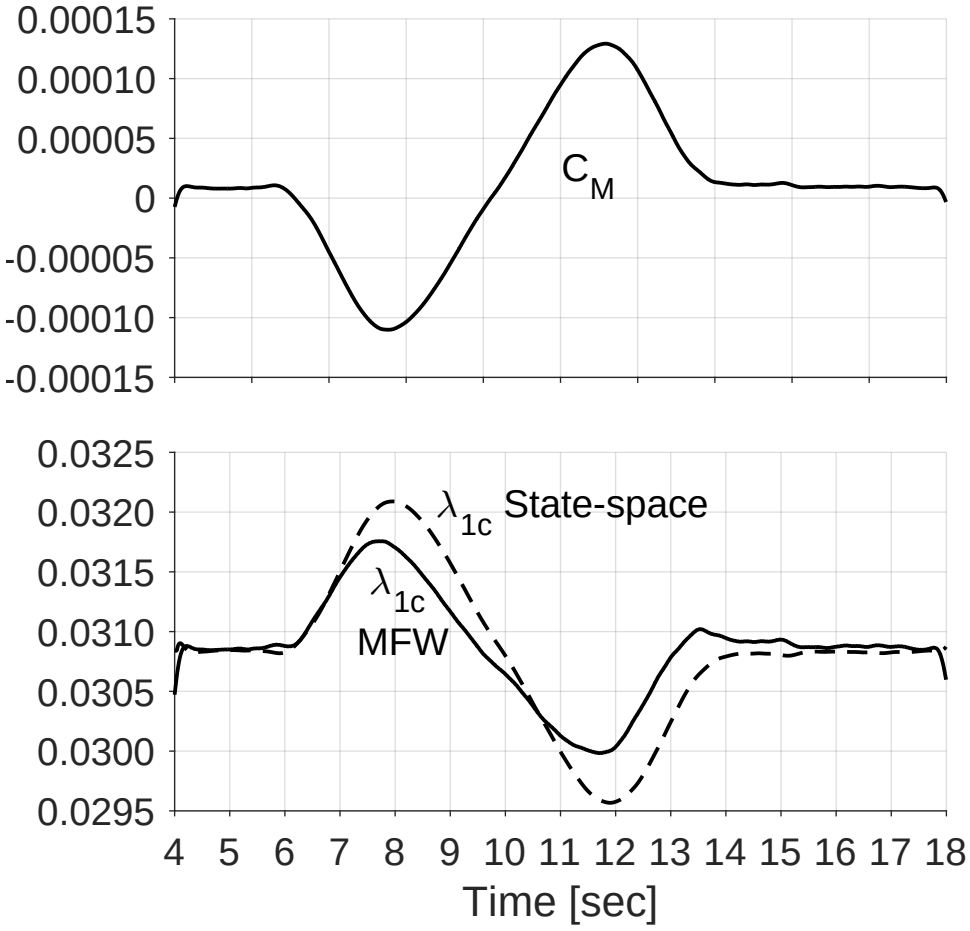

Figure 4.26: Time domain verification of inflow model, Eq.(4.7); solid line: MFW, dashed line: Eq.(4.7). Input: doublet of magnitude $\Delta\theta_{1c} = 0.25°$, $\mu = 0.1$.

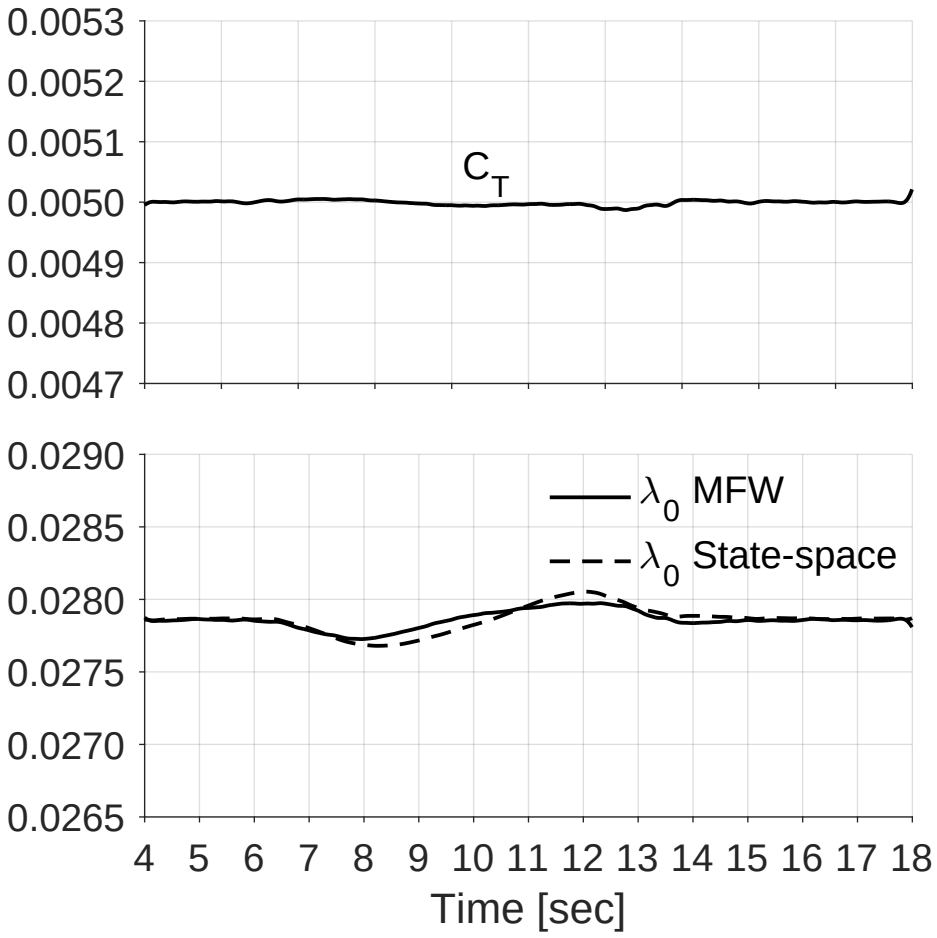

Figure 4.27: Time domain verification of inflow model, Eq.(4.7); solid line: MFW, dashed line: Eq.(4.7). Input: doublet of magnitude $\Delta\theta_{1c} = 0.25°$, $\mu = 0.1$.

4.4.2.2 Advance Ratio $\mu = 0.2$

The time domain verification of the $\mu = 0.2$ state-space model of Eq.(4.8) consists of three doublets , of collective, lateral and longitudinal cyclic pitch, respectively. The first doublet of collective pitch $\Delta\theta_0 = 0.25°$ excites all three aerodynamic inputs, ΔC_T,ΔC_L, and ΔC_M, which in turn produce all three outputs, λ_0, λ_{1s}, and

λ_{1c}. Inputs and corresponding on-axis outputs are shown in Figs. 4.28, 4.29 and 4.30, respectively.

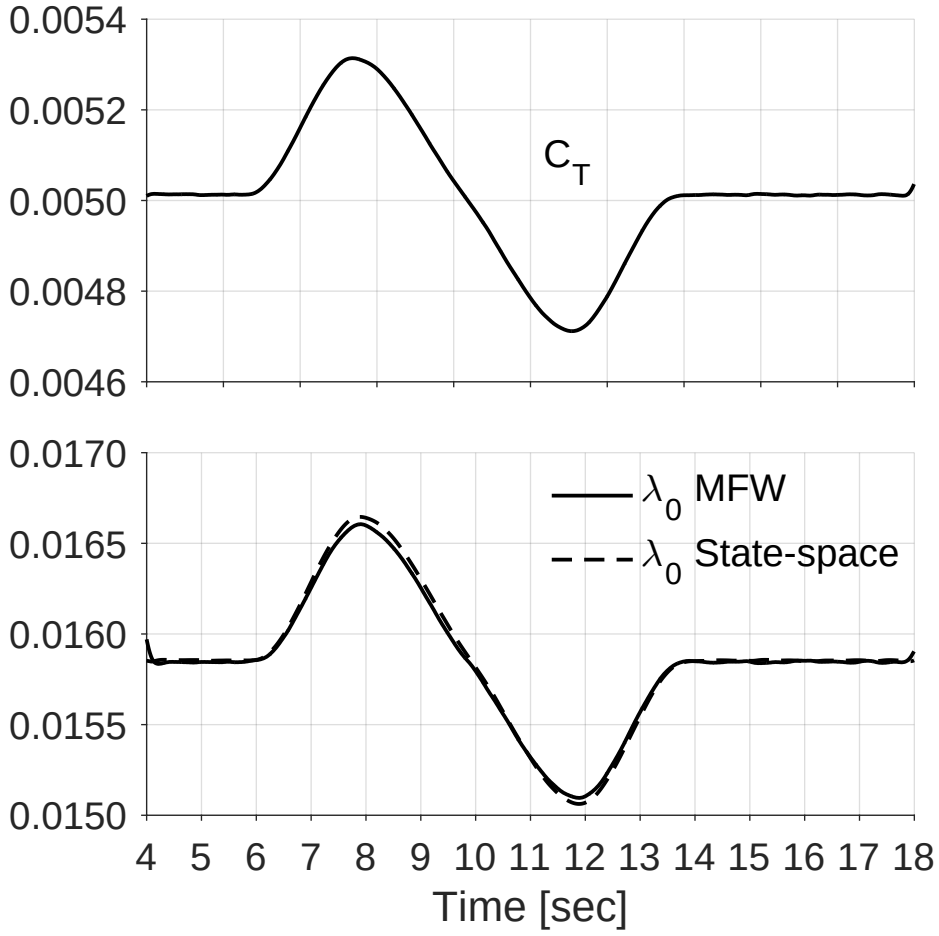

Figure 4.28: Time domain verification of inflow model, Eq.(4.8); solid line: MFW, dashed line: Eq.(4.8). Input: doublet of magnitude $\Delta\theta_0 = 0.25°$, $\mu = 0.2$.

The match for the λ_0 response to the three aerodynamic inputs, ΔC_T,ΔC_L, and ΔC_M, Fig. 4.28, is excellent. As in the $\mu = 0.1$ case, the state space system slightly over predicts the lateral inflow λ_{1s} response to the three aerodynamic inputs, Fig. 4.29, compared with the MFW prediction. The agreement is again very good

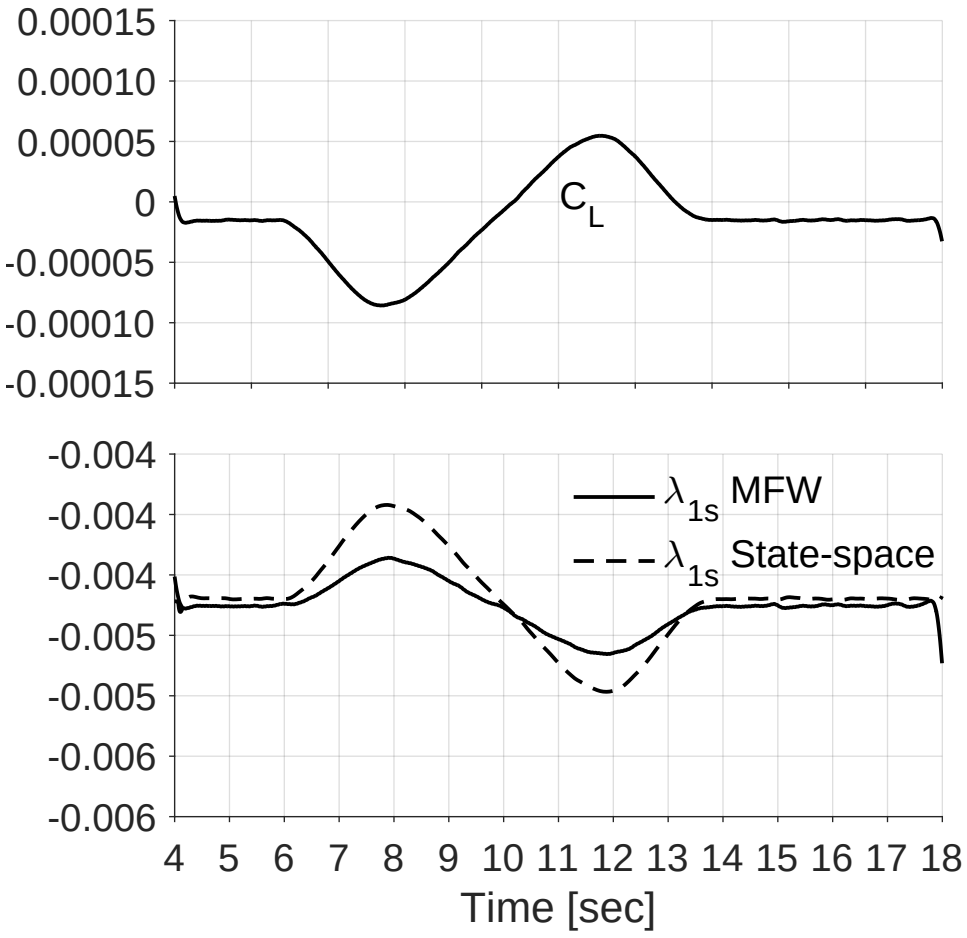

Figure 4.29: Time domain verification of inflow model, Eq.(4.8); solid line: MFW, dashed line: Eq.(4.8). Input: doublet of magnitude $\Delta\theta_0 = 0.25°$, $\mu = 0.2$.

for the longitudinal inflow λ_{1c} response to the three aerodynamic inputs, Fig. 4.30. Because the primary responses to collective are C_T and λ_0, longitudinal and lateral inflow components are smaller secondary effects.

The second verification is a doublet of lateral cyclic $\Delta\theta_{1s}$ of magnitude 0.25 degrees. This maneuver produces a mostly decoupled response with just roll moment ΔC_L. Therefore the primary inflow output is lateral inflow λ_{1s}, as is shown in Fig. 4.31. The agreement with MFW predictions is excellent. The θ_{1s} doublet

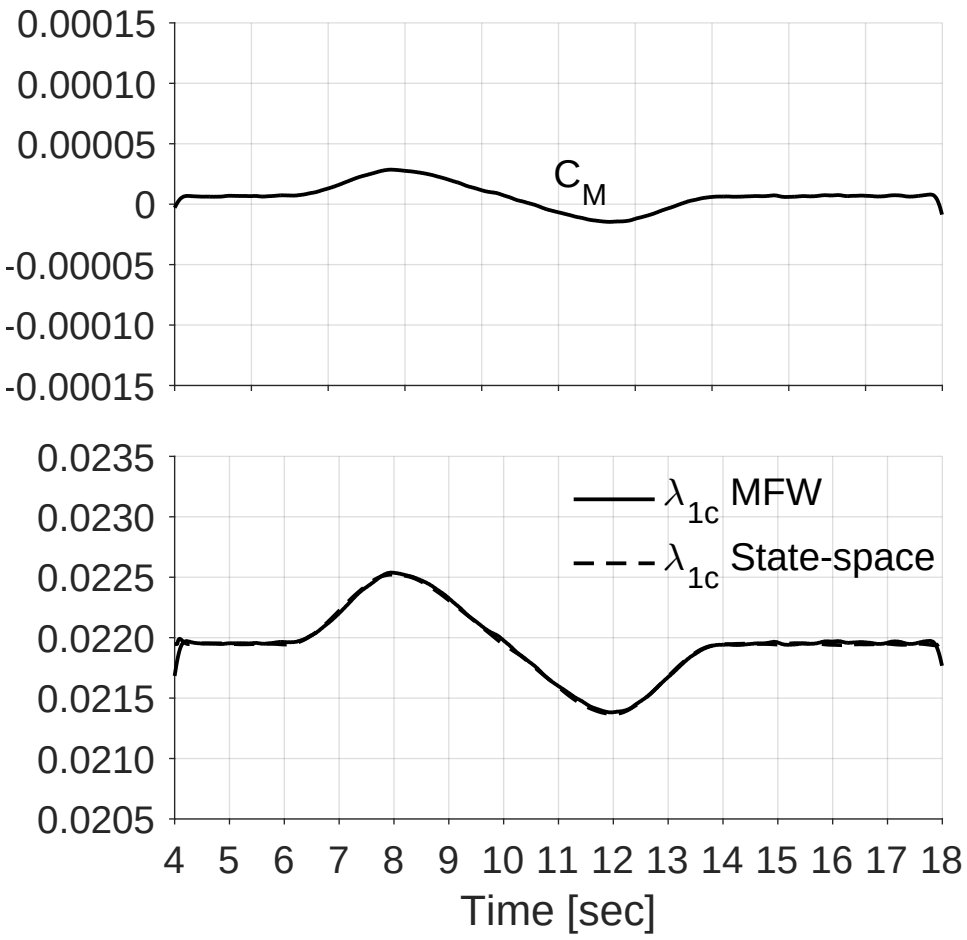

Figure 4.30: Time domain verification of inflow model, Eq.(4.8); solid line: MFW, dashed line: Eq.(4.8). Input: doublet of magnitude $\Delta\theta_0 = 0.25°$, $\mu = 0.2$.

generates very small ΔC_T and ΔC_M, therefore the corresponding time histories are not shown.

The third and final verification maneuver is a doublet of longitudinal cyclic $\Delta\theta_{1c}$ of magnitude 0.25 degrees. This maneuver produces mostly pitch moment ΔC_M. Therefore the primary inflow output is longitudinal inflow λ_{1c}, shown in Fig. 4.26. Longitudinal inflow is overpredicted, compared with the MFW. This is

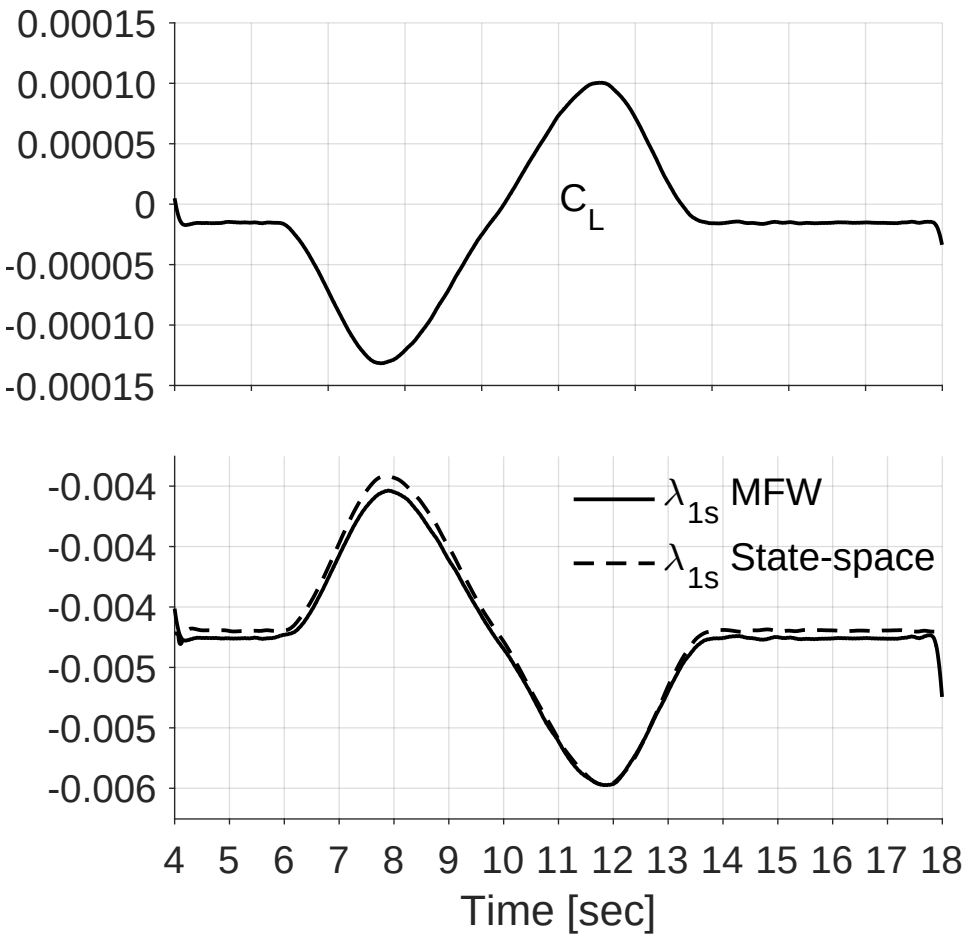

Figure 4.31: Time domain verification of inflow model, Eq.(4.8); solid line: MFW, dashed line: Eq.(4.8). Input: doublet of magnitude $\Delta\theta_{1s} = 0.25°$, $\mu = 0.2$.

caused by the larger error in the state-space fit (shown in Fig. 4.14). The $\Delta\theta_{1c}$ doublet generates very small C_T, as shown in Fig. 4.27, but through the couplings of Eq.(4.3), some λ_0 is generated, also shown in Fig. 4.27. λ_0 is underpredicted and but also small in magnitude, as is predicted by Fig. 4.21. The $\Delta\theta_{1c}$ doublet generates very small C_L, therefore, the corresponding time histories are not shown.

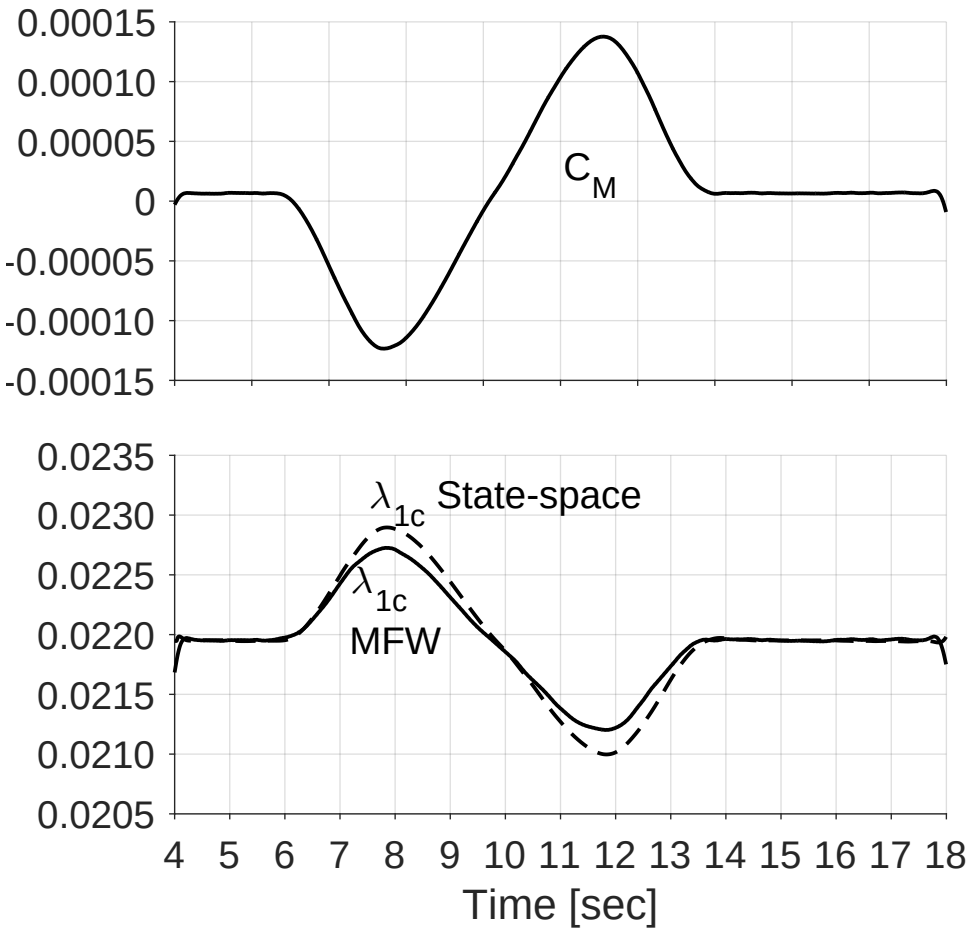

Figure 4.32: Time domain verification of inflow model, Eq.(4.8); solid line: MFW, dashed line: Eq.(4.8). Input: doublet of magnitude $\Delta\theta_{1c} = 0.25°$, $\mu = 0.2$.

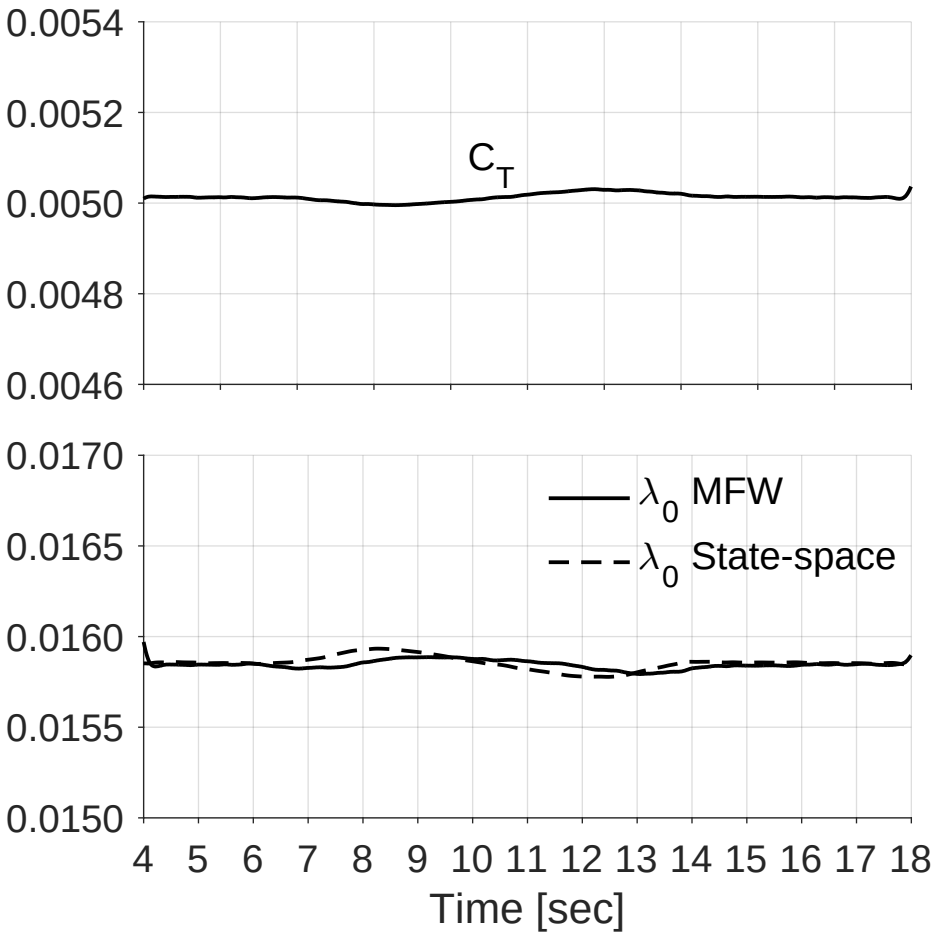

Figure 4.33: Time domain verification of inflow model, Eq.(4.8); solid line: MFW, dashed line: Eq.(4.8). Input: doublet of magnitude $\Delta\theta_{1c} = 0.25°$, $\mu = 0.2$.

4.5 Comparisons with the Perturbation Pitt-Peters Model

This section compares the three models identified for hover, $\mu = 0.1$, and $\mu = 0.2$ with the perturbation version of the Pitt-Peters model [25,26]. Figure 4.34 shows the three parameters on the diagonal of the M matrix as a function of advance ratio.

In the Pitt-Peters model, the M matrix is not a function of advance ratio. The identification methodology used in this study does not enforce this constraint (though the constraint that $M_{22} = M_{33}$ is the same as in the Pitt-Peters model). The parameters are fairly similar in value between the two models across the range of flight speeds. The average of the identified M_{11} values is 0.0354 or 12% larger than Pitt-Peters model. The average of the identified M_{22} and M_{33} values is -0.0052 or 20% larger (more negative) than the Pitt-Peters model.

Figure 4.35 shows the three parameters on the diagonal of the $\bar{L}$ matrix. The parameters from each model show very similar trends and values. The values on the diagonal, for the model identified from the MFW, tend to be slightly larger (on average, around 20-30%) than those of the Pitt-Peters model.

Finally, Fig. 4.36 shows the remaining two parameters not on the diagonal of the $\bar{L}$ matrix, i.e. $\bar{L}_{13}$ and $\bar{L}_{31}$. Both parameters are set to zero at hover in both models. The parameter $\bar{L}_{13}$ remains very small for the identified model, whereas it increases to about 0.17 at $\mu = 0.2$ for the Pitt-Peters model. The values of the parameter $\bar{L}_{31}$ for the two models are generally close with a maximum difference of about 20

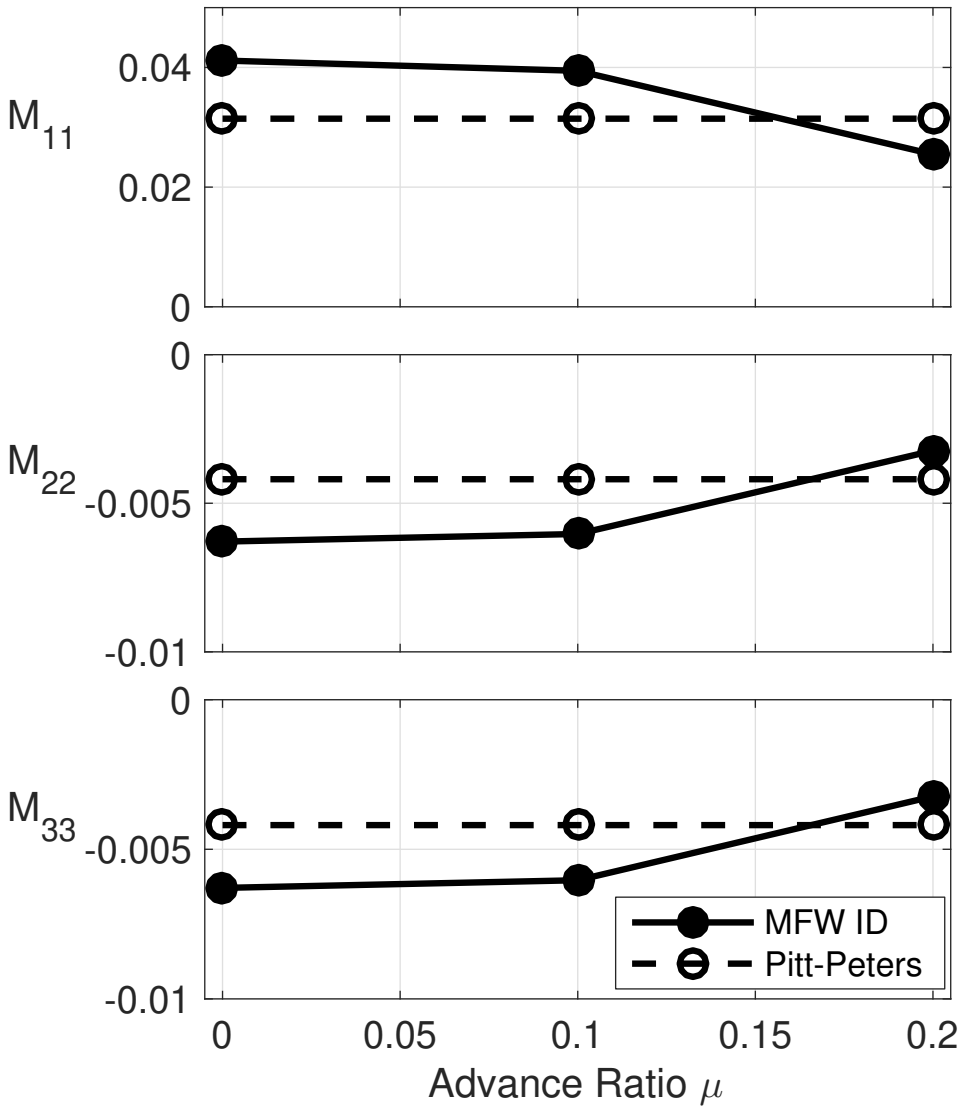

Figure 4.34: M matrix parameters varying with speed and compared between MFW identified model and Pitt-Peters dynamic inflow model.

In the absence of experimental results, the reasonably good agreement with the widely used Pitt-Peters model gives confidence that the identification methodology developed in this study is suitable for the extraction of low order, state-space rotor inflow models.

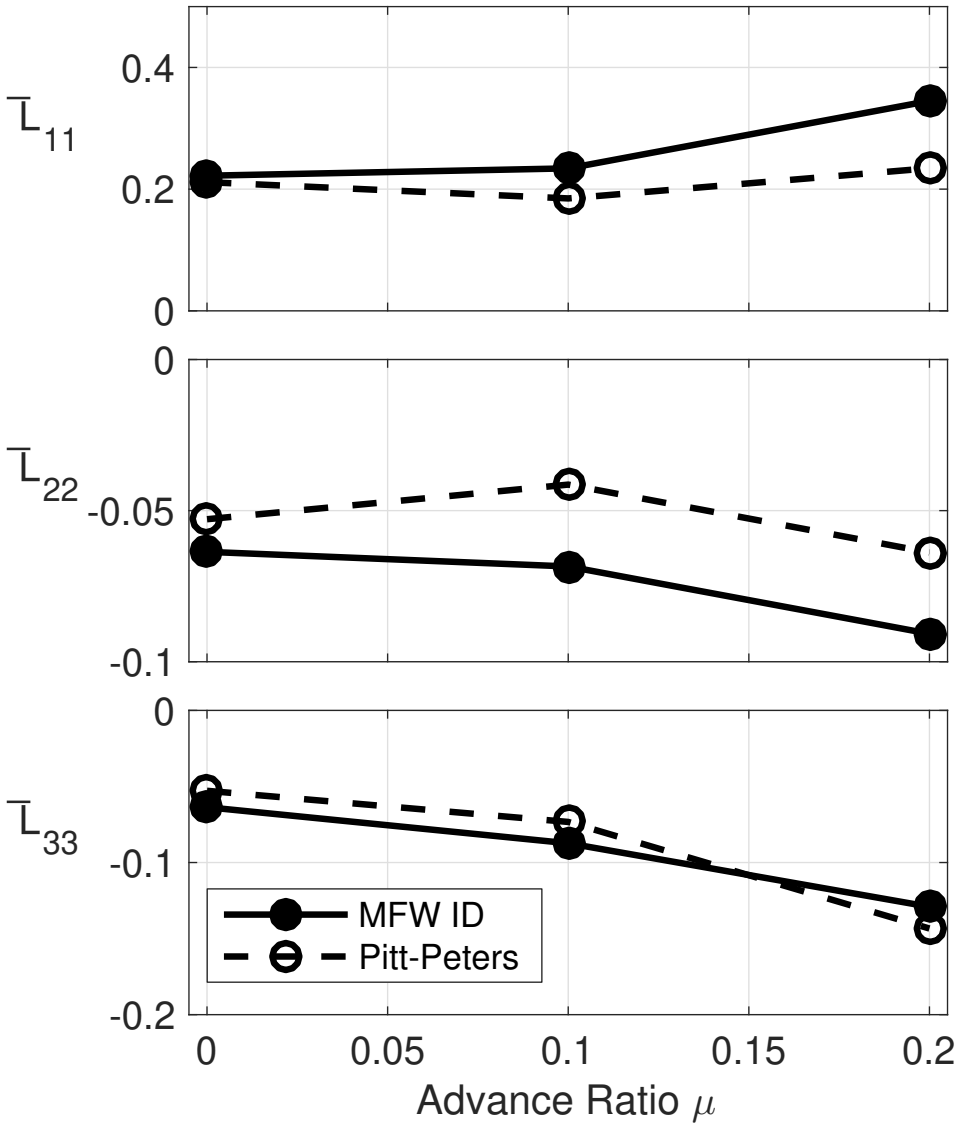

Figure 4.35: Diagonal terms of the $\bar{L}$ matrix varying with speed and compared between MFW identified model and Pitt-Peters dynamic inflow model.

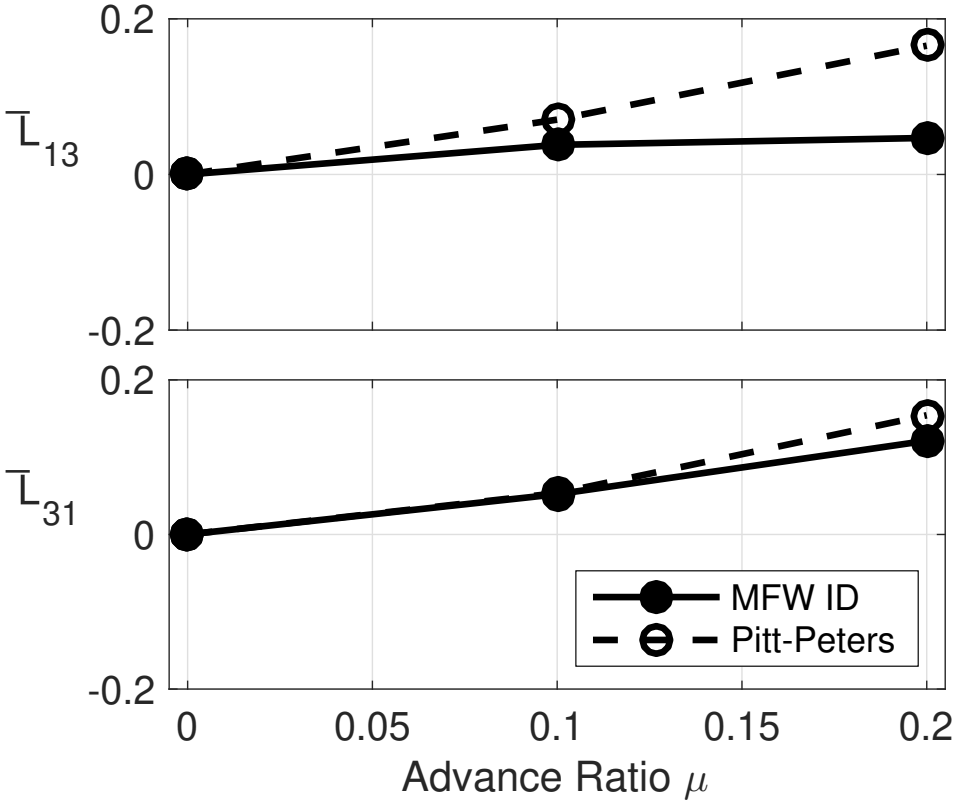

Figure 4.36: Off-diagonal terms of the $\bar{L}$ matrix varying with speed and compared between MFW identified model and Pitt-Peters dynamic inflow model.

4.6 Off-Rotor Inflow Models

Using the MFW model, frequency responses can be computed from the rotor's induced inflow components λ_0, λ_{1c}, and λ_{1s} to the induced velocities $\bar{v}_x$, $\bar{v}_y$ and $\bar{v}_z$ at any location off-rotor. The procedure is the same, with the exception that the inputs and outputs are different. This system can then be fit with a full state-space model as with the inflow model.

The non-parametric frequency response matrix of interest is now $\left[\frac{\bar{\boldsymbol{v}}(s)}{\boldsymbol{\lambda}(s)}\right]$ and, similarly to Eq.(3.22), it is calculated by the Joint Input-Output method:

$$\left[\frac{\bar{\boldsymbol{v}}(s)}{\boldsymbol{\lambda}(s)}\right] = \left[\frac{\bar{\boldsymbol{v}}(s)}{\boldsymbol{\theta}(s)}\right] \times \left[\frac{\boldsymbol{\lambda}(s)}{\boldsymbol{\theta}(s)}\right]^{-1} \tag{4.9}$$

Output equation models in the forms given by either Eqs.(2.39) or (2.40) are fit to each frequency response. The induced velocity model can be fit using only the frequency portions, e.g. between 1 to 5 rad/sec, of the frequency responses, because for flight dynamics purposes, this is the region of interest.

4.6.1 Horizontal Tail Results

The methodology described to identify output-equation off-rotor induced velocity was performed on the MFW to come up with the relationship between $\boldsymbol{\lambda}$ and $\bar{v}_x$, $\bar{v}_y$ and $\bar{v}_z$ for a single main rotor in hover. For the tail inflow model, the average of the seven points across the 1/4 chord line was used. The output equation for the

induced velocities was determined to be:

$$\begin{Bmatrix} \bar{v}_x \\ \bar{v}_y \\ \bar{v}_z \end{Bmatrix} = \begin{bmatrix} -0.2892 & -0.3108 & 0.0532 \\ -0.142 & -0.1353 & 0.3407 \\ 0.3148 & 0.5361 & -0.1104 \end{bmatrix} \begin{Bmatrix} \lambda_0(t-0.06225) \\ \lambda_{1c}(t-0.2115) \\ \lambda_{1s}(t-0.6929) \end{Bmatrix}$$

Figure 4.37 shows the time-domain verification. This was performed using a ramp input, and time histories calculated from the state-space model are compared to the actual output of the MFW. The time-domain verification shows that the system responds well in the long term, but has some initial higher frequency discrepancies. The error here is attributable to the fact that the velocities have been approximated to be a linear combination of the inflow coefficients, and the responses were only fit at low frequency. However, the simple output-only model appears to give adequate results.

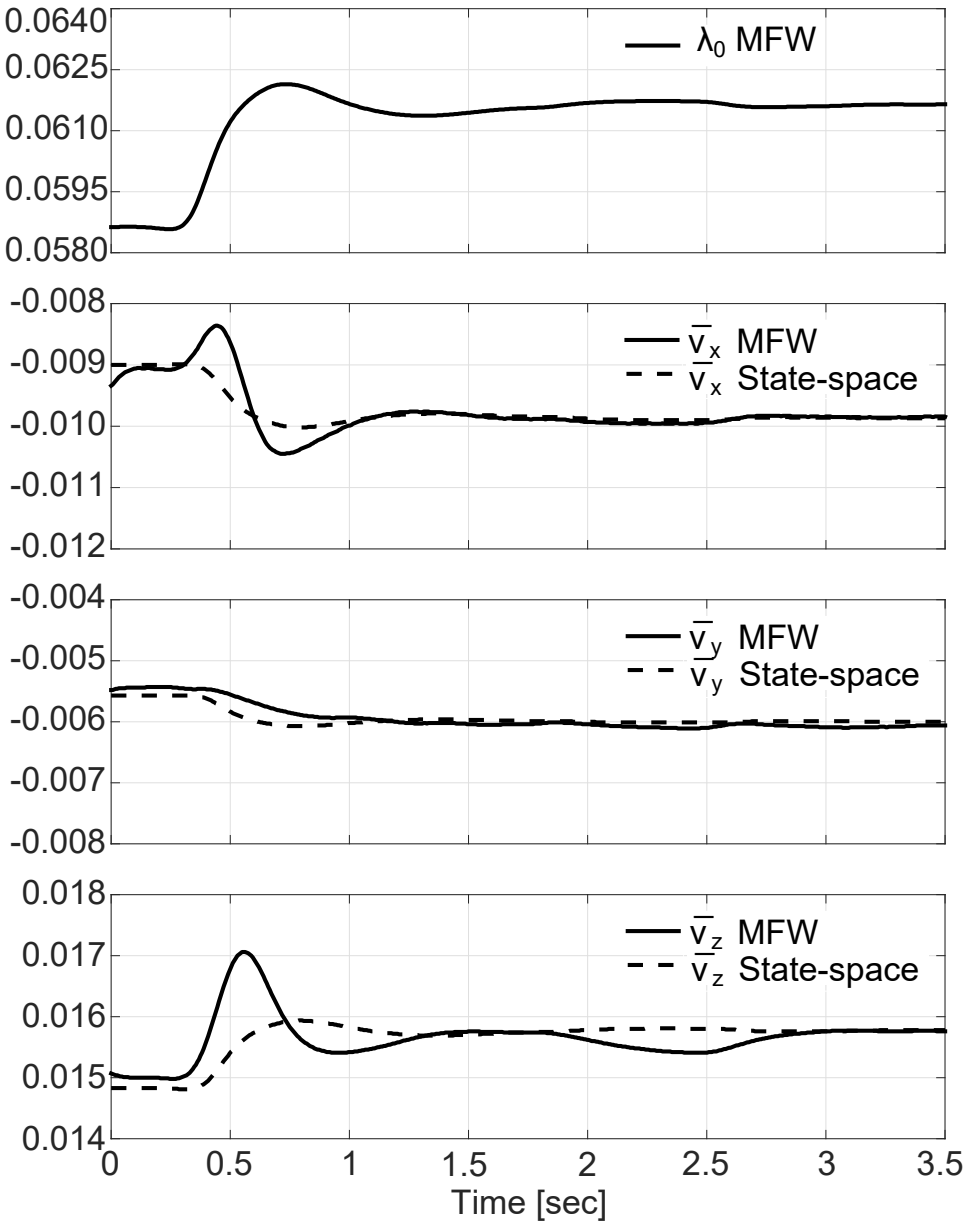

Figure 4.37: Time-domain verification of induced velocity model at the horizontal tail; input is a ramp in θ_0.

4.6.2 Wing Under Hub Results

The output equation for the wing under the hub, fit to the form defined by Eq.(2.40), is:

$$\begin{Bmatrix} \bar{v}_x \\ \bar{v}_y \\ \bar{v}_z \end{Bmatrix} = \begin{bmatrix} 0.0221 & -0.7496 & -0.2117 \\ 0 & 0.207 & -0.766 \\ -1.366 & 0.02861 & 0 \end{bmatrix} \circ \begin{bmatrix} t-0.2149 & t-0.541 & t-0.3795 \\ t-0 & t-0.4452 & t-0.5327 \\ t-0.07075 & t-0.154 & t-0 \end{bmatrix} \times \begin{Bmatrix} \lambda_0 \\ \lambda_{1c} \\ \lambda_{1s} \end{Bmatrix} \tag{4.10}$$

The time-domain verification of these output equations is shown by Fig. 4.38. A doublet input of θ_0 is used, and the time histories from the identified output equation model are compared to those of the MFW. For this case, a perturbation in λ_0 only produces a significant perturbation in $\bar{v}_z$. The output equation-based model provides a very good fit.

4.7 Wake Curvature and Distortion Identification

To extract the K_R in hover with frequency domain system identification the following procedure was used. First, since the flap rates are now part of the inputs to the inflow model, the response of λ_{1S} to $\overset{*}{\beta}_{1s}$ and λ_{1C} to $\overset{*}{\beta}_{1c}$ must be identified. Besides the set of frequency sweeps on all the pilot controls, $\boldsymbol{\theta}$, with the flapping

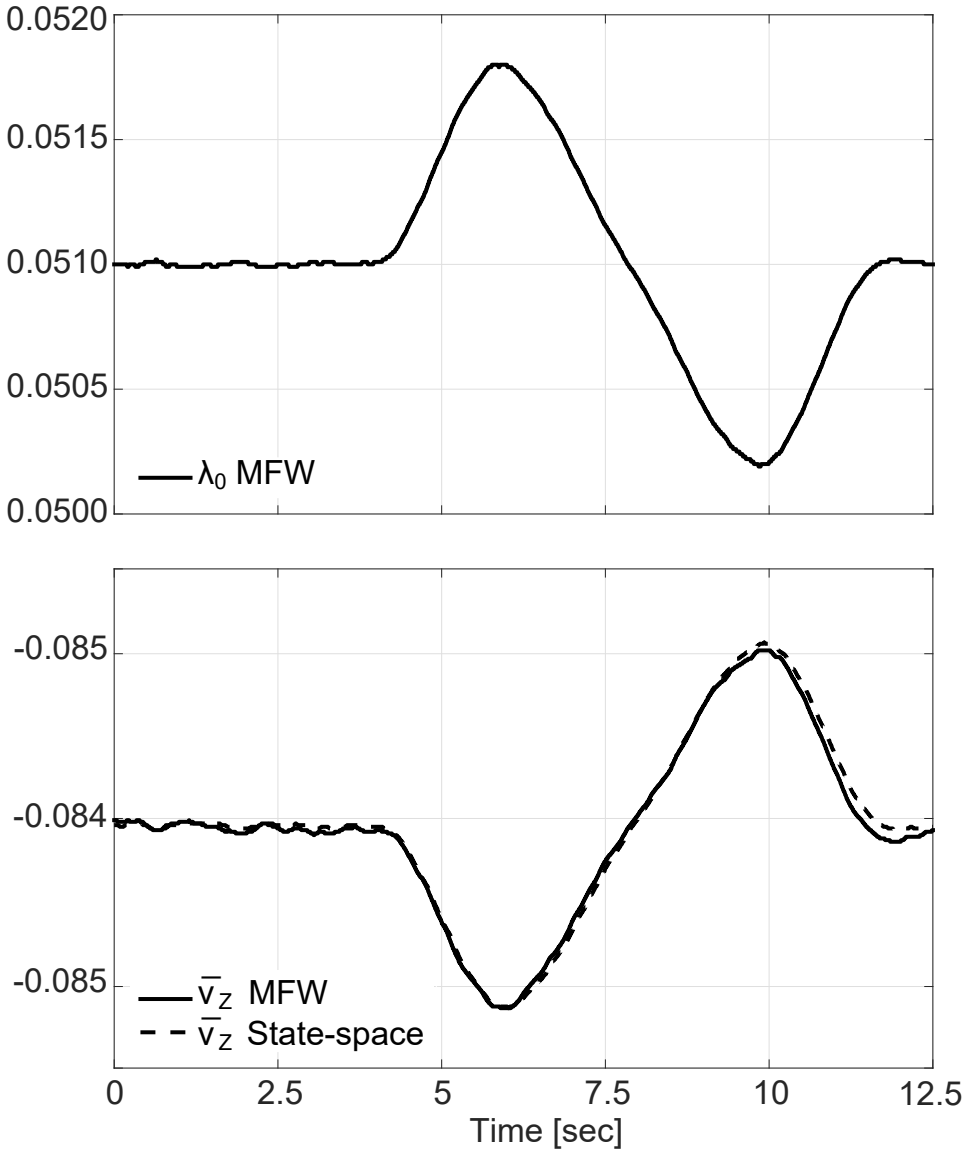

Figure 4.38: Time-domain verification of off-rotor fuselage induced velocity given a doublet in λ_0 (compared with MFW)

set to zero, an additional set of frequency sweeps are performed with the same inputs except that flapping is free to flap. This second set of frequency sweeps will be denoted as the responses to the input $\boldsymbol{\theta}_\beta$. The flap rates can be grouped into the vector $\overset{*}{\boldsymbol{\beta}} = \left\{ \begin{array}{cc} \overset{*}{\beta}_{1s} & \overset{*}{\beta}_{1c} \end{array} \right\}$. With both sets of frequency sweeps, the frequency

responses of $\mathbf{C}$, $\overset{*}{\boldsymbol{\beta}}$, and $\boldsymbol{\lambda}$ to $\left\{ \begin{array}{cc} \boldsymbol{\theta} & \boldsymbol{\theta}_\beta \end{array} \right\}$ can all be found in non-parametric form. The Joint-Input Output method of Sec. 3.3.5 can then be modified to show that the following relationship exists:

$$\left[\begin{array}{cc} \dfrac{\boldsymbol{\lambda}(s)}{\Delta \mathbf{C}(s)} & \dfrac{\boldsymbol{\lambda}(s)}{\Delta \overset{*}{\boldsymbol{\beta}}(s)} \end{array} \right] = \left[\begin{array}{cc} \dfrac{\boldsymbol{\lambda}(s)}{\boldsymbol{\theta}(s)} & \dfrac{\boldsymbol{\lambda}(s)}{\boldsymbol{\theta}_\beta(s)} \end{array} \right] \left[\begin{array}{cc} \dfrac{\Delta \mathbf{C}(s)}{\boldsymbol{\theta}(s)} & \dfrac{\Delta \mathbf{C}(s)}{\boldsymbol{\theta}_\beta(s)} \\ 0 & \dfrac{\Delta \overset{*}{\boldsymbol{\beta}}(s)}{\boldsymbol{\theta}_\beta(s)} \end{array} \right]^{-1} \tag{4.11}$$

The desired frequency responses for the identification $\lambda(s)/\Delta C(s)$ and $\lambda(s)/\Delta \dot{\beta}(s)$ can then be found numerically at each frequency point using Eq.(4.11).

To calculate K_R, take the second row of Eq.(2.29) and write it as (removing the terms K_T and p/Ω):

$$M_{22} \overset{*}{\lambda}_{1s} + L_{22}^{-1} \lambda_{1s} = \Delta C_L + L_{22}^{-1} K_R \left(-\Delta \overset{*}{\beta}_{1s} \right) \tag{4.12}$$

and take Laplace Transform:

$$\lambda_{1s}(s) = \frac{1}{\left(M_{22} s + L_{22}^{-1}\right)} \Delta C_L(s) + \frac{-L_{22}^{-1} K_R}{\left(M_{22} s + L_{22}^{-1}\right)} \Delta \overset{*}{\beta}_{1s}(s) \tag{4.13}$$

In the frequency domain the inflow equation can also be written as:

$$\lambda_{1s}(s) = \frac{\lambda_{1s}(s)}{\Delta C_L(s)} \Delta C_L(s) + \frac{\lambda_{1s}(s)}{\Delta \overset{*}{\beta}_{1s}(s)} \Delta \overset{*}{\beta}_{1s}(s) \tag{4.14}$$

Therefore:

$$\frac{\lambda_{1s}(s)}{\Delta C_L(s)} = \frac{1}{\left(M_{22} s + L_{22}^{-1}\right)} \tag{4.15}$$

$$\frac{\lambda_{1s}(s)}{\Delta \overset{*}{\beta}_{1s}(s)} = \frac{-L_{22}^{-1} K_R}{\left(M_{22} s + L_{22}^{-1}\right)} \tag{4.16}$$

Substituting Eq.(4.15) into Eq.(4.16) gives:

$$\frac{\lambda_{1s}(s)}{\Delta \overset{*}{\beta}_{1s}(s)} = \frac{\lambda_{1s}(s)}{\Delta C_L(s)} \left(-L_{22}^{-1} K_R \right) \tag{4.17}$$

Rearrange to solve for K_R:

$$K_R = -L_{22} \frac{\frac{\lambda_{1s}(s)}{\overset{*}{\Delta\beta}_{1s}(s)}}{\frac{\lambda_{1s}(s)}{\Delta C_L(s)}} \tag{4.18}$$

For the value of L_{22}, one can use the value form the identification with no flapping. Alternatively, the Pitt-Peters value can be used, which, for a hovering rotor case, is $L_{22} = -1/V_T = -1/\sqrt{C_T/2}$. Finally, this gives the expression:

$$K_R = \frac{1}{\sqrt{C_T/2}} \frac{\frac{\lambda_{1s}(s)}{\overset{*}{\Delta\beta}_{1s}(s)}}{\frac{\lambda_{1s}(s)}{\Delta C_L(s)}} \tag{4.19}$$

Note that although K_R is written as a constant, it is generally a function of frequency.

Inflow responses to flapping and roll moment were calculated and manipulated using Eq.(4.19) to arrive at K_R as a function of frequency. This identified response was also fit with a value constant with frequency to determine the best constant K_R. Figure 4.39 shows the calculated response, along with the best constant K_R value ($K_R = 1.44$) and the analytical solution from Ref. 82 ($K_R = 1.5$).

Therefore, the results indicate that K_R is not constant, but rather a function of frequency. This means that the amount of equivalent moment that flapping produces is also a function of frequency, with an average value that turns out to be very close to that predicted by analytical solutions based on potential flow theory [82]. However, the results shown here suggest that the dynamics of the wake, and the effect of rotor dynamics on the wake, are more complex than a simplified theory can predict.

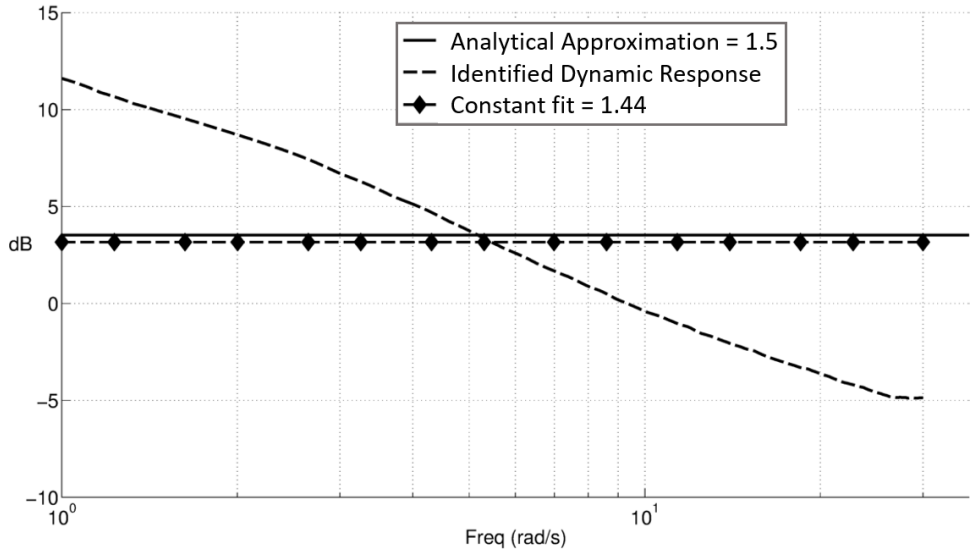

Figure 4.39: Comparison of identified K_R frequency response with analytical solution. Only magnitude shown.

4.8 Summary

The chapter presents a methodology for utilizing advanced high-fidelity aerodynamic numerical models to create a first order dynamic-inflow-type of formulation for the benefit of advanced helicopter flight dynamics applications. The extraction of the low-order, state space inflow dynamic models is accomplished using frequency domain system identification techniques described in Chap. 3.

This chapter presents results from the high-fidelity aerodynamic tool, the Maryland free wake model (MFW), and compares against the results provided by a similar procedure using the RAPiD wake model (RFW) . Both models were used in the time domain and their outputs were carefully processed under various assumptions to identify the dynamic-inflow-type system of equations.

The method developed and implemented on the free-wake wake model, uses frequency sweeps to excite the entire frequency range of interest. System identification is possible using a single time history. For the MFW, sweeps are injected through blade pitch changes and the resulting aerodynamic thrust and inflow variations are used in the identification process.

For the vertical C_T only excitation, the two free wake models produced very similar results. Both free wake models correctly produced first-order types of inflow responses to thrust inputs that compare well to the Pitt-Peters dynamic inflow model. There was a slightly increasing phase roll off (i.e. effective lag) in the frequency response of both free wake models above approximately 5 rad/sec.

For the cyclic inputs, the MFW and RFW models yield similar behavior to the dynamic inflow models. The MFW model does require time delays to model uncaptured higher order dynamics. For both the MFW and RFW models, a significant 2nd order behavior shows up in the magnitude curves.

The identification procedure was next used to identify Pitt-Peters-like inflow systems in forward flight. These models well captured the dynamics of the MFW simulation and showed how the dynamics change with flight condition.

The method was then used to approximately predict the inflow of any point off of the rotor. For a more accurate representation, a full state-space model could be determined for the off-rotor point using the same method as for the rotor inflow state space model. The method employed here, instead, was to compute off-rotor inflow as a linear combination of the on-rotor inflow states. This has the advantage of not needing extra states, however this advantage may be negated by the need

for additional states arising from the Padé approximations to the time delays. The time-domain verification results show that the approximation is reasonably accurate.

Lastly, the identification method was demonstrated for identification of wake curvature and distortion effects. An extension of the Joint-Input Output method was shown to identify inflow responses to flapping rates (or any tip-path plane perturbations). The model structure required manipulation to allow for the results to be shown in the form of K_R which is comparable with literature. The results show that these effects do indeed exist in MFW however they likely are a more complicated function of frequency that is not captured simply by a gain.

Chapter 5: Coaxial Rotorcraft Inflow System Identification

5.1 Overview

This chapter extends the methodology described in chapters 2-4 to a coaxial rotor. This chapter identifies a state space inflow model from a free-vortex wake simulation of a coaxial helicopter in hover, whose configuration is described in Appendix B. The general features of the state-space model have been described in Sec. 2.2.2.5. The present chapter will describe the details of the structure of the model and of the identification process. As for the single main rotor case, frequency responses of the inflow to the components of the aerodynamic rotor loads will be extracted as best fits. The model will then be verified in the time domain.

5.2 Frequency Response Generation

As with the single main rotor case, the shaft is held fixed and flap dynamics are held rigid. The MFW is first marched forward in time until moment trim has been achieved, the wake geometry has converged to a periodic solution, and the desired input values of total thrust coefficient, as well as torque balance, have been reached. Next, frequency sweep "chirp" inputs, shown in Fig. 3.1, of all controls

in $\boldsymbol{\theta}$ are applied, one control at a time, and the corresponding time histories of the perturbation inflow state vector $\Delta\boldsymbol{\lambda}$ and the perturbation aerodynamic load vector $\Delta\mathbf{C}$ are calculated. Therefore, $\Delta\boldsymbol{\lambda}$ and $\Delta\mathbf{C}$ are both outputs of the wake model, corresponding to the input $\boldsymbol{\theta}$. Since there are six swashplate controls in $\boldsymbol{\theta}$, the frequency sweep is repeated six times.

The vectors $\Delta\mathbf{C}$ and $\Delta\boldsymbol{\lambda}$ are also, respectively, the input and outputs for the system described by Eq.(2.30). This is the state-space system that is extracted from the wake responses. The frequency domain system identification tool CIFER® [63] is utilized to analyze the time histories. The Joint-Input Output method described in Sec. 3.3.5 is used to account for the correlation of the inputs $\Delta\mathbf{C}$. This is even more important for a coaxial rotorcraft as there are aerodynamic couplings between the two rotors and therefore the aerodynamic loading is almost always highly correlated. The other two methods (cross-feed and decorrelation through noise), presented in Secs. 3.3.3 and 3.3.4, are difficult to perform since the number of couplings is now much higher, therefore they were not used for the coaxial case.

The first step of the Joint-Input Output method is to obtain a series of Single-Input Multiple-Output (SIMO) frequency responses of inflow and aerodynamic loads to swashplate inputs. With a coaxial rotor, there are 6 swashplate control chirps (3 for the upper rotor and 3 for the lower rotor) each producing 12 non-parametric frequency responses; 6 describing the response of $\boldsymbol{\lambda}$ and 6 describing the response of $\mathbf{C}$, all to the given control. When the responses of all six controls are grouped in matrix form, two 6 by 6 transfer function matrices are generated, $\begin{bmatrix}\boldsymbol{\lambda}(s)\\ \overline{\boldsymbol{\theta}(s)}\end{bmatrix}$ and

$\left[\frac{\mathbf{C}(s)}{\boldsymbol{\theta}(s)}\right]$. With these matrices, the Joint Input-Output method can be performed to obtain $\left[\frac{\boldsymbol{\lambda}(s)}{\mathbf{C}(s)}\right]$ using Eq.(4.1). These three matrix transfer functions describe the same responses as the similar matrices do for the single main rotor case. These responses can be subdivided into "on-rotor" and "cross-rotor" responses as shown in Eq.(5.1):

$$\left\{\frac{\text{Output}}{\text{Input}}\right\} = \left[\begin{array}{c|c} \text{On-Rotor} & \text{Cross-Rotor} \\ \text{(Upper on Upper)} & \text{(Lower on Upper)} \\ \hline \text{Cross-Rotor} & \text{On-Rotor} \\ \text{(Upper on Lower)} & \text{(Lower on Lower)} \end{array}\right] \tag{5.1}$$

The upper right partition describes the effects of the lower rotor on the upper rotor, the lower left partition those of the upper rotor on the lower rotor. As distance between the two rotors goes to infinity, terms of the off-diagonal blocks go to zero, and the diagonal blocks converge to the corresponding single main rotor results. This was used as a test case to check the identification procedure.

5.3 State-Space Model Identification

In general, all of the responses $[\boldsymbol{\lambda}(s)/\mathbf{C}(s)]$ obtained from the free wake are nonzero and the three 6 by 6 matrices $[M]$, $[L]^{-1}$, and $[\tau]$ are fully populated, therefore a total of 108 parameters would need to be identified. Physical insight along with examination of the frequency responses obtained can be used to reduce

the number of free parameters and make the identification problem more tractable. The following assumptions and simplifications were used:

1. The 3-by-3 $[M]$ and $[L]^{-1}$ matrices in the Pitt-Peters dynamic inflow model are diagonal in hover, and this form was retained for the four 3-by-3 submatrices of the coaxial rotorcraft model. The same structure was also assumed for the matrix $[\tau]$

2. In hover, the rotor behavior in pitch is identical to that in roll but shifted by 90°. This allows to constrain selected values of the state space matrices to be identical.

3. If a frequency response had low coherence and small magnitude, it was excluded from the identification, on the assumption that it was mostly due to small non-linearities in the system. If response magnitudes were not small, but the coherences were low, the frequency responses would not be considered reliable and would have to be ignored even if potentially significant. However, no such situation occurred in the results of this chapter.

4. If the coherence was high but the magnitude was low, it was assumed that the response was negligible and the corresponding transfer function was set to zero.

5. The form of $[M]$, $[L]^{-1}$, and τ was assumed to correspond directly to the form of $[\boldsymbol{\lambda}(s)/\mathbf{C}(s)]$, in the sense that if the magnitude of the $\{i, j\}$ component of

$\boldsymbol{\lambda}(s)/\mathbf{C}(s)$ was below some preassigned threshold at all frequencies, then the $\{i, j\}$ component of the state space matrices would be set to zero.

Combining all these criteria, and after constraining the following parameters constrained to be identical:

$$m_{22} = m_{33} \quad m_{44} = m_{55} \quad m_{25} = m_{36} \quad m_{52} = m_{63}$$

$$l_{22} = l_{33} \qquad l_{44} = l_{55} \qquad l_{25} = l_{36} \qquad l_{52} = l_{63}$$

$$\tau_{22} = \tau_{33} \qquad \tau_{44} = \tau_{55} \qquad \tau_{25} = \tau_{36} \qquad \tau_{52} = \tau_{63}$$

the hover preliminary form of $[M]$ and $[L]^{-1}$ was found to be (only nonzero terms are shown):

$$[M] = \begin{bmatrix} m_{11} & & & m_{14} & & \\ & m_{22} & & & m_{25} & \\ & & m_{22} & & & m_{25} \\ m_{41} & & & m_{44} & & \\ & m_{52} & & & m_{55} & \\ & & m_{52} & & & m_{55} \end{bmatrix}$$

$$[L]^{-1} = \begin{bmatrix} l_{11} & & & l_{14} & & \\ & l_{22} & & & l_{25} & \\ & & l_{22} & & & l_{25} \\ l_{41} & & & l_{44} & & \\ & l_{52} & & & l_{55} & \\ & & l_{52} & & & l_{55} \end{bmatrix} \tag{5.2}$$

$$[\tau] = \begin{bmatrix} \tau_{11} & & & \tau_{14} & & \\ & \tau_{22} & & & \tau_{25} & \\ & & \tau_{22} & & & \tau_{25} \\ \tau_{41} & & & \tau_{44} & & \\ & \tau_{52} & & & \tau_{55} & \\ & & \tau_{52} & & & \tau_{55} \end{bmatrix}$$

In summary the following 24 parameters had to be identified: m_{11}, m_{22}, m_{14}, m_{25}, m_{41}, m_{52}, m_{44}, m_{55}, l_{11}, l_{22}, l_{14}, l_{25}, l_{41}, l_{52}, l_{44}, l_{55}, τ_{11}, τ_{22}, τ_{14}, τ_{25}, τ_{41}, τ_{52}, τ_{44}, and τ_{55}.

5.4 Results for Hover

The coaxial rotor, described in Appendix B, was trimmed in hover, with trim C_T for the upper and lower rotors are 0.0053 and 0.0043, respectively. Frequency responses were then generated.

5.4.1 Frequency Responses

This section presents hover frequency responses obtained using the full, nonlinear MFW, and the corresponding curve fits obtained using the identified state-space model. In all plots, unless specified other wise, the solid lines indicate the MFW frequency responses, the dashed lines the state-space model fits.

Figure 5.1 shows the upper and lower rotor average induced inflow λ_0 to a thrust perturbation C_T^U of the upper rotor. It is interesting to note that the inflow responses of the upper and lower rotor are approximately equal in magnitude over the full frequency range.

At the lowest frequency (1 rad/sec), the upper rotor response is slightly larger than the lower rotor response, whereas, in the middle frequency band, there is a larger λ_0^L response than λ_0^U response, before falling back below at high frequency. These responses have values of coherences very close to one across the whole fre-

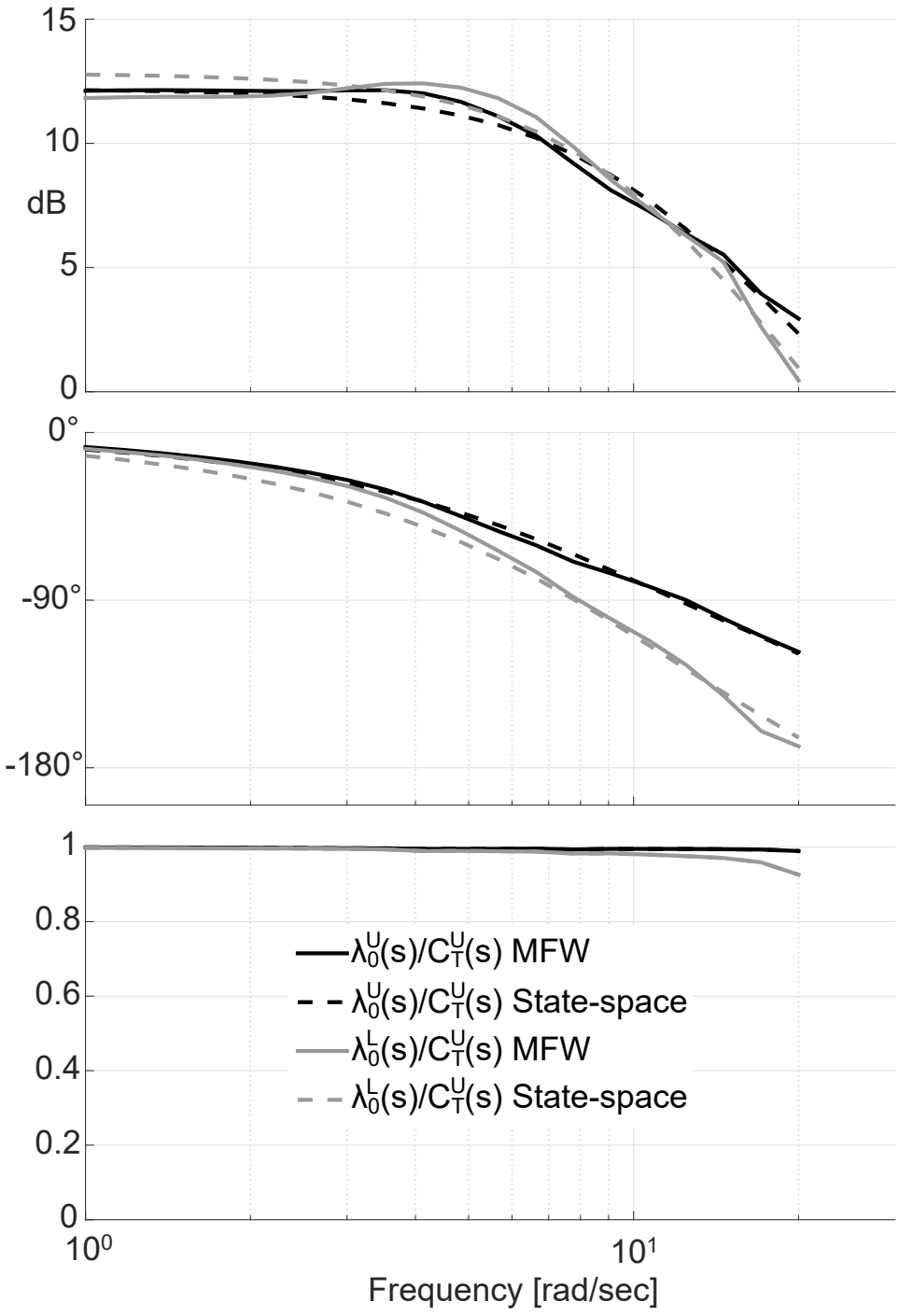

Figure 5.1: Responses of λ_0^U and λ_0^L to C_T^U; magnitude(top), phase(middle), and coherence(bottom)

quency range, as shown by the bottom plot in Fig. 5.1, which implies that the dynamics of the wake in these conditions are linear and time-invariant. In principle, a larger set of equations describing the inflow dynamics could be identified which would fit the magnitude and phase curves even better without being over-parameterized. However it was decided to keep the state space model in the first order form given by Eq.(5.2), with the idea of providing a straightforward extension to coaxial rotors of the well known dynamic inflow model, and to accept the small errors shown in the figures.

A second order inflow response would have provided a better fit, especially in the region of the apparent rise of the λ_0^L response at mid frequency. Because only a first order approximation is used, the optimization fits the system with a slightly higher gain at all frequencies to account for the higher magnitude in the middle frequencies.

The companion response, i.e. that of the *lower* rotor thrust C_T^L to λ_0^U and λ_0^L, is shown in Fig. 5.2.

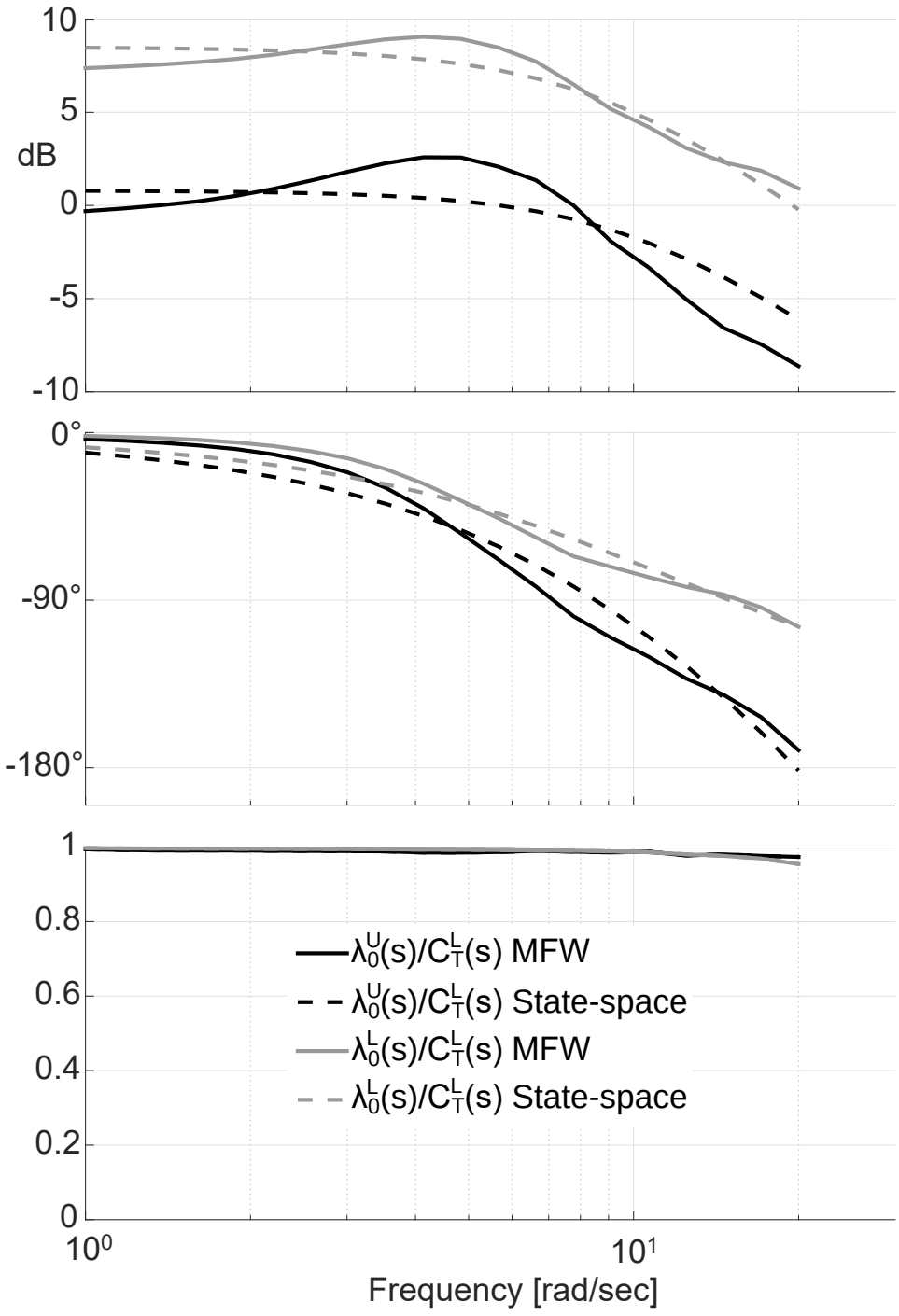

Figure 5.2: Responses of λ_0^U and λ_0^L to C_T^L showing MFW non-parametric model vs the state-space parametric model; magnitude(top), phase(middle), and coherence(bottom)

Relative to the effects of C_T^U perturbations, C_T^L perturbations have a much smaller effect on the inflows of both rotors. In particular, the lower rotor thrust C_T^L perturbations have very little effect on the upper rotor inflow λ_0^U. In fact, the upper rotor thrust perturbations C_T^U have a larger effect on the lower rotor inflow λ_0^L than lower rotor thrust C_T^L does over the entire frequency range (as was shown in Fig. 5.1). The MFW frequency responses shows a rather second order behavior and are not well modeled by the first order model structure assumed in this analysis. However, for the reasons previously mentioned a first-order dynamic inflow type form was retained even if probably not optimal.

Figure 5.3 shows the responses of the upper λ_{1C}^U and lower λ_{1C}^L longitudinal inflow to the upper rotor pitching moment C_M^U. Once again, the upper rotor effect on the lower rotor is roughly the same magnitude as effect on the upper rotor itself,confirming a strong coupling. Both of these responses require time delays to help fit the higher order unmodeled dynamics. The lower rotor requires a significantly larger time delay, because of the larger phase roll-off. Though not shown here, the equivalent responses of C_L^U to λ_{1S}^U and λ_{1S}^L are almost exactly the same, due to hover rotor symmetry. These responses again demonstrate that a first-order inflow model structure may not be adequate in capturing all the dynamics of a coupled coaxial rotor system.

In the same manner as the C_T^L responses, Fig. 5.4 shows a dissimilar effect on both rotors longitudinal induced inflow caused by pitching moments of the lower rotor, C_M^L. The response of λ_{1C}^L is much larger than the response of λ_{1C}^U, indicating relatively little upper rotor coupling for this flow condition. Also comparing the

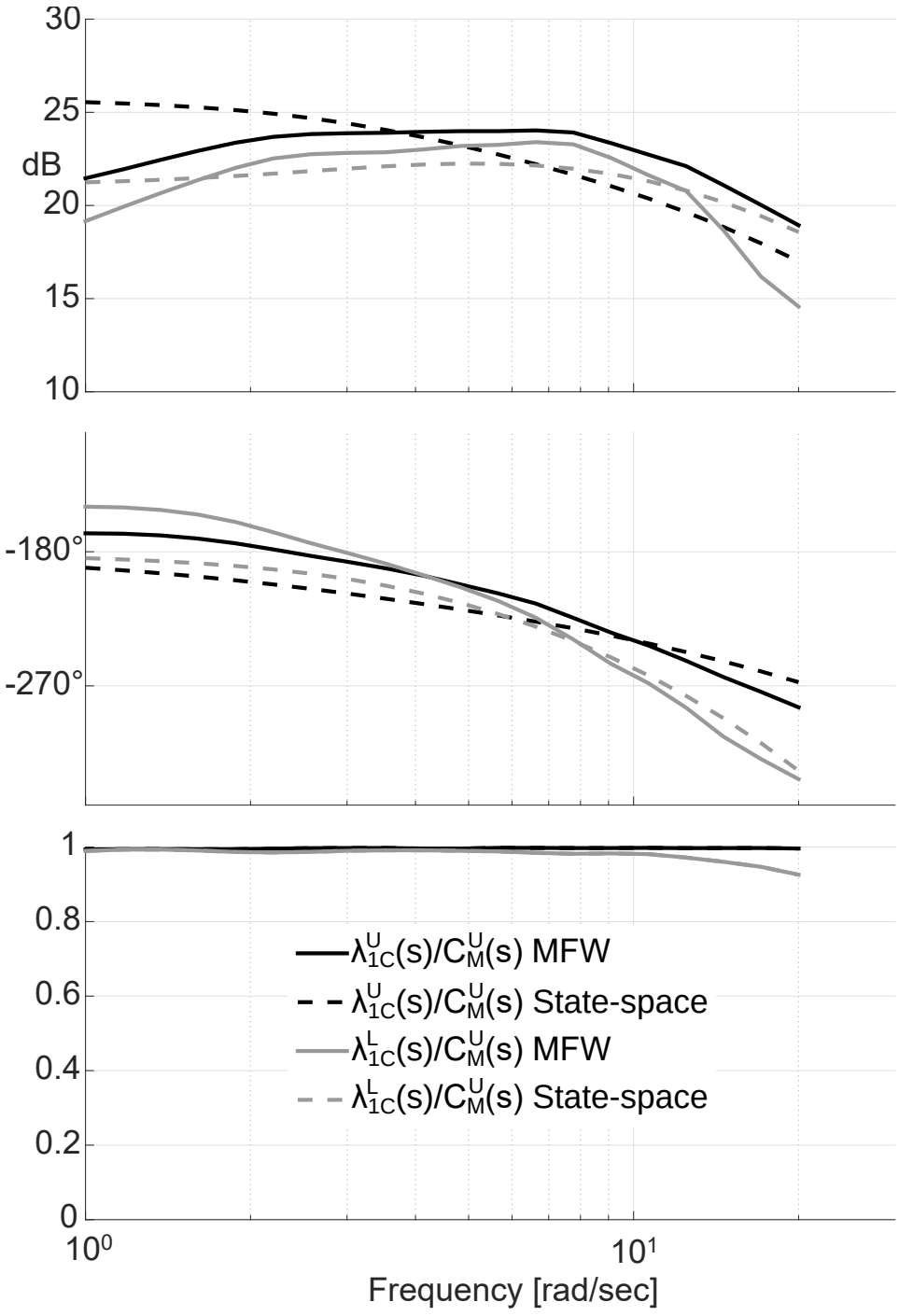

Figure 5.3: Responses of λ^U_{1C} and λ^L_{1C} to C^U_M showing MFW non-parametric model vs the state-space parametric model; magnitude(top), phase(middle), and coherence(bottom)

response of λ_{1C}^{L} of this figure with the same response on Fig. 5.3 shows that for the lower rotor, excitations from the upper rotor have a larger magnitude than excitations from the lower rotor itself.

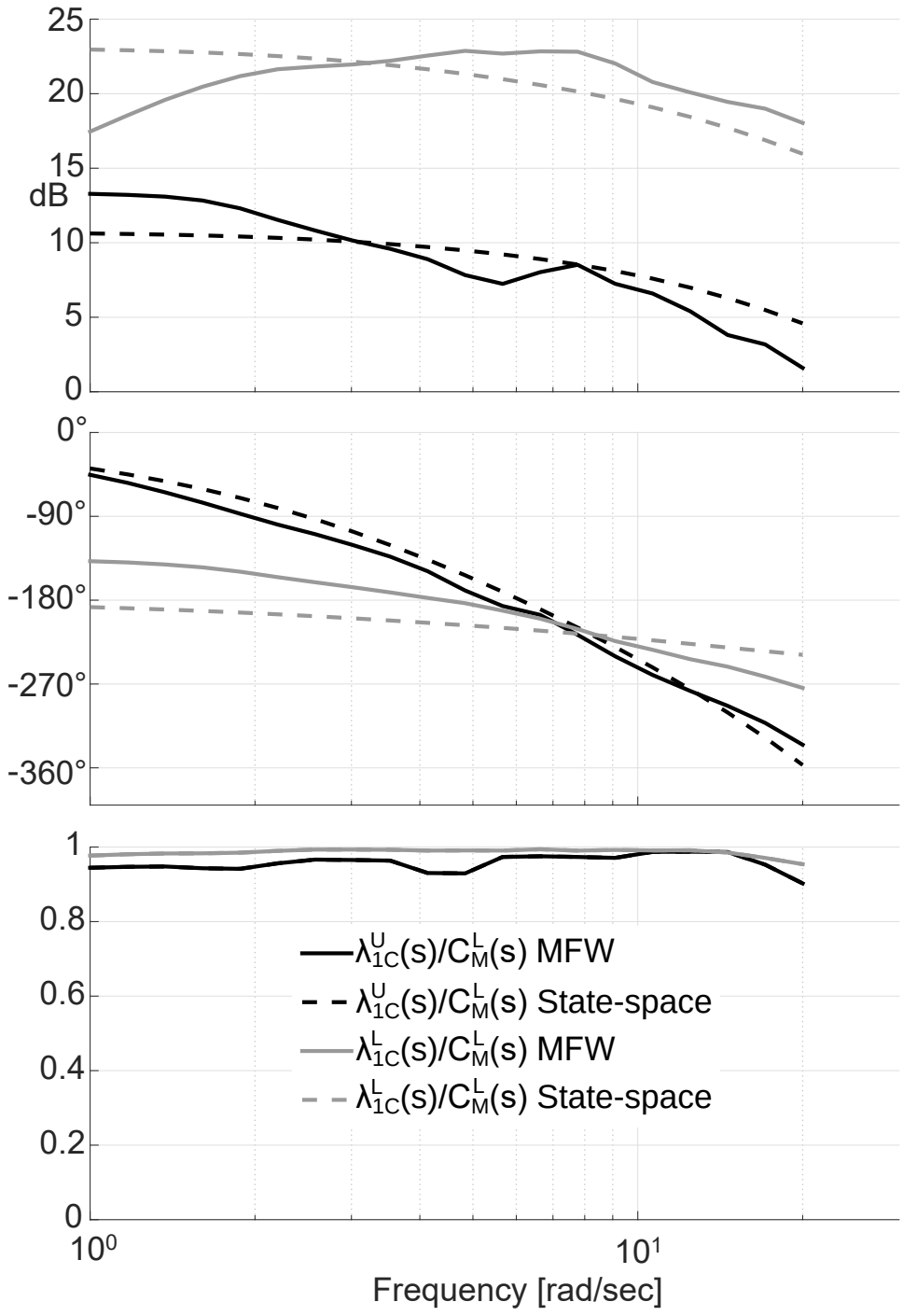

Figure 5.4: Responses of λ^U_{1C} and λ^L_{1C} to C^L_M showing MFW non-parametric model vs the state-space parametric model; magnitude(top), phase(middle), and coherence(bottom)

Table 5.1 summarizes the costs of all of the transfer function fits, as well as the average. Generally, costs below 200 are considered acceptable [63]. The majority of the responses are well represented by the low-order form of the model, with the collective on-axis having costs of $J < 50$, meaning an excellent fit is obtained. The

Table 5.1: Cost of state-space parameterizations

Response	Cost
$\lambda_0^U(s)/C_T^U(s)$	3.7
$\lambda_0^L(s)/C_T^U(s)$	17.2
$\lambda_{1C}^U(s)/C_M^U(s)$	204.0
$\lambda_{1C}^L(s)/C_M^U(s)$	178.1
$\lambda_{1S}^U(s)/C_L^U(s)$	204.1
$\lambda_{1S}^L(s)/C_L^U(s)$	177.7
$\lambda_0^U(s)/C_T^L(s)$	85.3
$\lambda_0^L(s)/C_T^L(s)$	28.8
$\lambda_{1C}^U(s)/C_M^L(s)$	115.8
$\lambda_{1C}^L(s)/C_M^L(s)$	463.6
$\lambda_{1S}^U(s)/C_L^L(s)$	115.1
$\lambda_{1S}^L(s)/C_L^L(s)$	462.5
Average Cost	171.3190

lower rotor on-axis moment response have the largest costs, meaning the form used may not be adequate for capturing the dynamics in the frequency range of the fit. As shown in Table 5.1, the cost of this state-space fit is rather high at 463.61, well above the recommended maximum amount of 200. In particular, the response has a large amount of error at low frequency in both phase and magnitude,which implies that, when these ODE systems are used in the simulation with slow maneuvers,

there will likely be more λ_{1C}^{L} created per unit of C_{M}^{L} and there will be a phase error of about 45 degrees, compared with the MFW predictions.

The identified state-space model is Eq(2.30) with:

$$[M] = \begin{bmatrix} 0.851 & 0 & 0 & -0.4664 & 0 & 0 \\ 0 & -0.243 & 0 & 0 & 0.06601 & 0 \\ 0 & 0 & -0.243 & 0 & 0 & 0.06601 \\ 0.674 & 0 & 0 & 1.0563 & 0 & 0 \\ 0 & 0.3349 & 0 & 0 & -0.27 & 0 \\ 0 & 0 & 0.3349 & 0 & 0 & -0.27 \end{bmatrix}$$

$$[L]^{-1} = \begin{bmatrix} 0.4418 & 0 & 0 & -0.182 & 0 & 0 \\ 0 & -0.0453 & 0 & 0 & -0.01089 & 0 \\ 0 & 0 & -0.0453 & 0 & 0 & -0.01089 \\ -0.7262 & 0 & 0 & 0.6748 & 0 & 0 \\ 0 & 0.03581 & 0 & 0 & -0.06139 & 0 \\ 0 & 0 & 0.03581 & 0 & 0 & -0.06139 \end{bmatrix}$$

$$[\tau] = \begin{bmatrix} 0.03373 & 0 & 0 & 0.09985 & 0 & 0 \\ 0 & 0.02264 & 0 & 0 & 0.1265 & 0 \\ 0 & 0 & 0.02264 & 0 & 0 & 0.1265 \\ 0 & 0 & 0 & 0.02631 & 0 & 0 \\ 0 & 0.08218 & 0 & 0 & 0 & 0 \\ 0 & 0 & 0.08218 & 0 & 0 & 0 \end{bmatrix} \tag{5.3}$$

5.4.2 Time-Domain Verification

The hover inflow model was validated in the time-domain using smooth doublet inputs. The first verification was with a doublet on symmetric collective θ_0^S which produced a similar looking doublet in both C_T^U and C_T^L. Figure 5.5 shows these thrust responses in the top plot. The middle and bottom plot show, respectively, the λ_0^L and λ_0^U responses from the identified state-space model, and are compared to the actual time histories produced by the full, nonlinear MFW. In general the agreement is good. The high frequency oscillation in the λ_0^L MFW response is caused by blade-vortex interaction caused when the lower rotor blades hit the upper rotor's wake. Most of the error of the state-space model can be directly attributed to the error in the fits shown in Figs. 5.1 and 5.2.

A doublet that excited the longitudinal inflow was also performed, with the results shown in Fig. 5.6. This doublet was performed on θ_{1C}^U creating doublets in both C_M^U and C_M^L. The corresponding time histories for λ_{1C}^U and λ_{1C}^L are shown in the middle and bottom plots, respectively. The error is slightly larger than for the collective doublet case, but the general trend is still well captured. The error is larger due to the larger difference between the identified state-space model and the MFW, previously pointed out in Figs. 5.3 and 5.4.

5.5 Summary

This chapter presents a frequency domain system identification methodology to extract a low order coaxial rotor inflow model in the form of a system of ODEs,

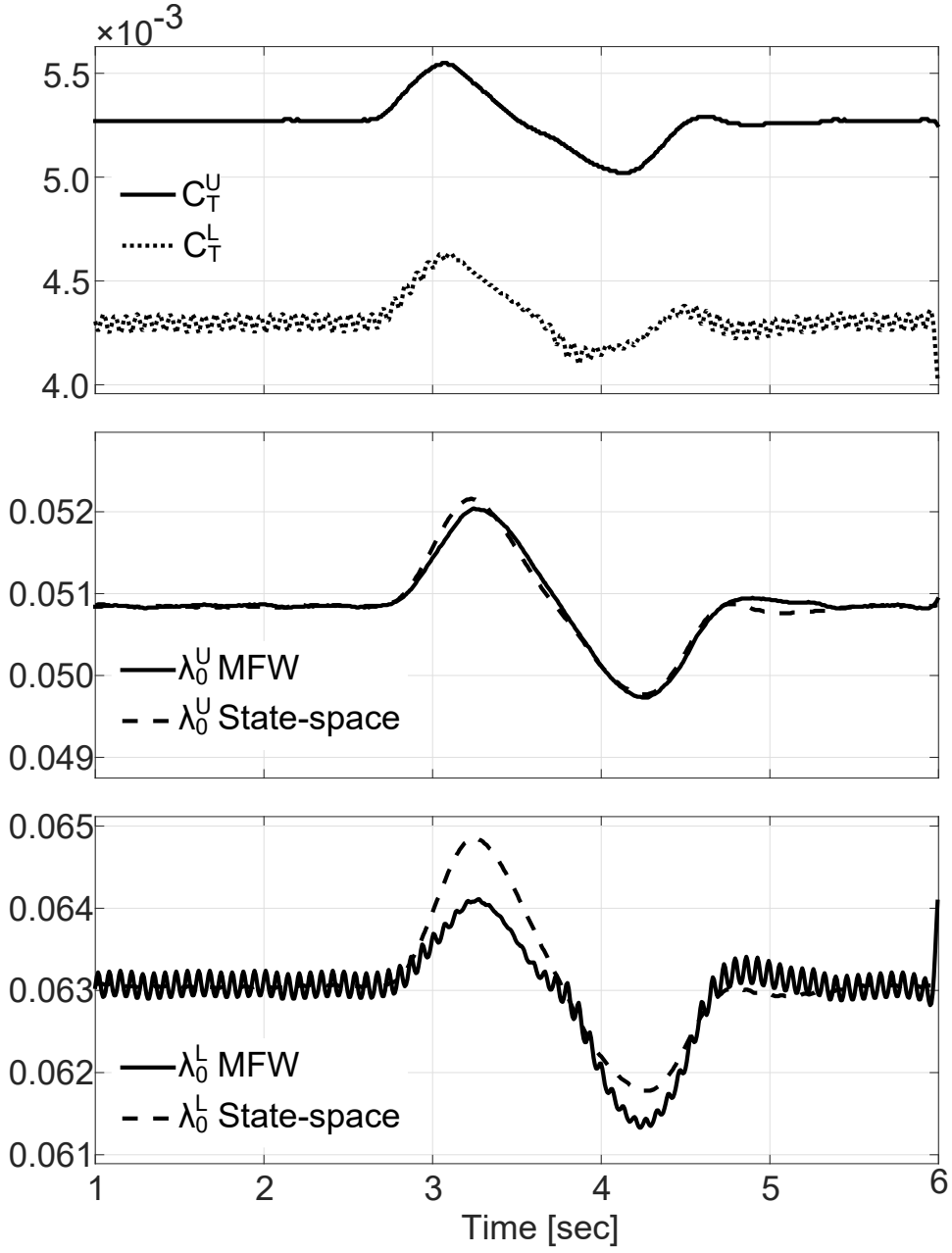

Figure 5.5: Time-domain verification of symmetric collective θ_0^S doublet, showing the thrust perturbations and the resulting time histories of λ_0^U and λ_0^L from the identified state-space model and the MFW

suitable for flight dynamics and control applications. The methodology is demon-

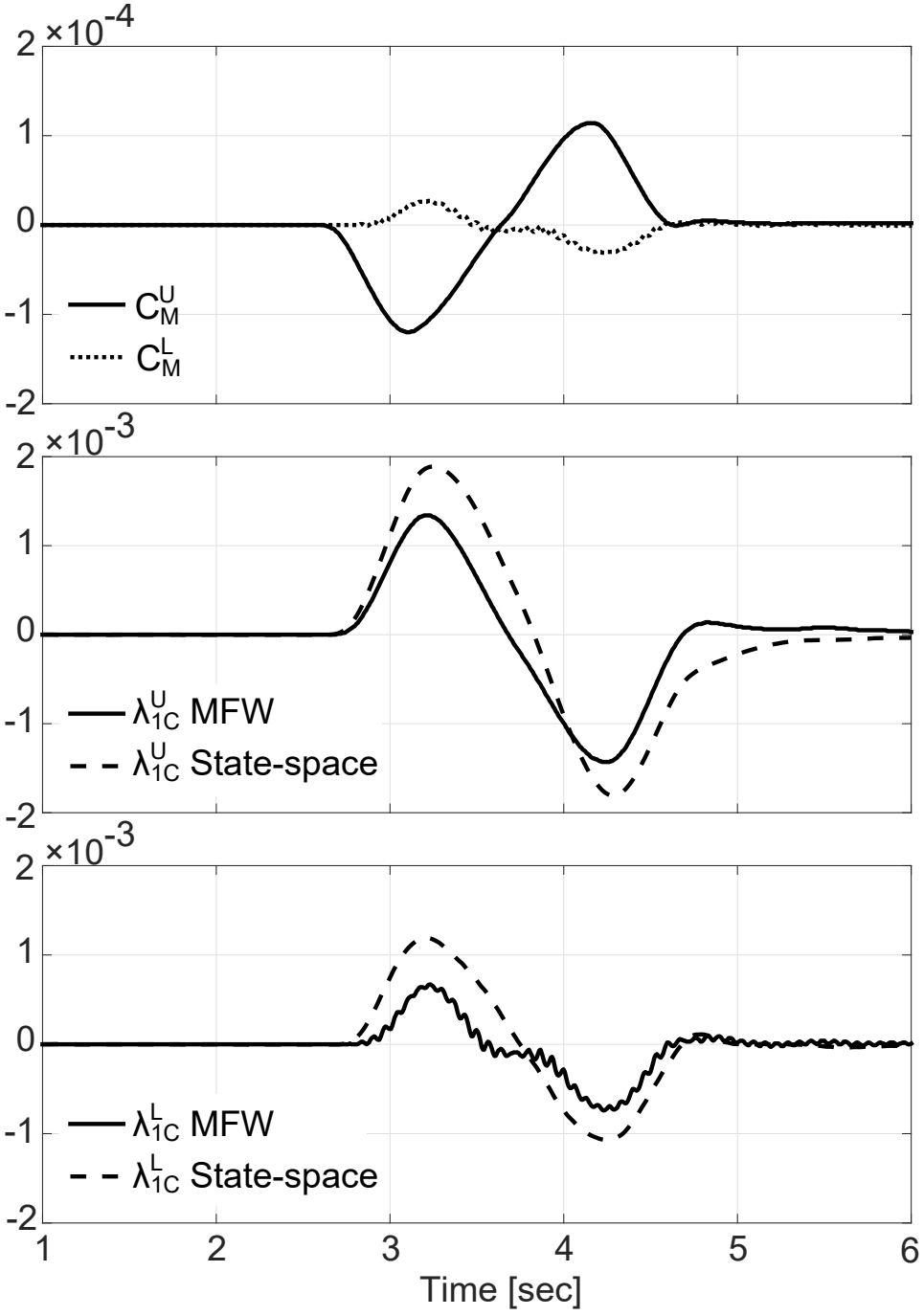

Figure 5.6: Time-domain verification of upper rotor longitudinal cyclic θ_{1C}^{U} doublet, showing the pitching moment perturbations and the resulting time histories of λ_{1C}^{U} and λ_{1C}^{L} from the identified state-space model and the MFW

strated using a free-vortex wake simulation, but it is applicable to a wide variety of advanced aerodynamic analyses, including CFD-based ones.

The wake dynamics describing the relationship from rotor loads to inflow were extracted as non-parametric frequency responses. These responses showed that this type of dynamics of the rotor wake is linear in the frequency range of interest in flight dynamics. Each non-parametric response had generally high coherence across that frequency range.

The non-parametric frequency responses were fit with a first order state-space model, which allows coupling and interference between the rotors. In general, the state space model fit well the collective responses, but mis-alignment was found in the lateral and longitudinal inflow responses when compared to the free-wake frequency responses. The state-space model of the inflow was written in first order form to provide a straightforward extension to coaxial rotors of the well known dynamic inflow model. However, it is possible that a higher order model could be created to better capture the shape of the non-parametric frequency responses. Even simple second order models for each of the given frequency responses would likely improve the accuracy of the identification. Higher order models come at the cost of model complexity and loss of insight into the physical meaning of the inflow states. In the first order model presented, the states are the inflow coefficients. There is an appeal in the simplicity of having the states be an exact quantity one can measure. Further analysis would need to be done to determine the physical meaning of any higher order states. For this reason, the first order model is used in this chapter, and higher order analysis is reserved for subsequent chapters.

Chapter 6: Higher Order Coaxial Rotorcraft Inflow System Identification

6.1 Overview

The previous chapter completed a preliminary study of the flight dynamics of coaxial configurations but the role of these inflow dynamic models in steady flight and maneuvers has not yet been studied in depth. Additionally, Chap. 5 did not take into account the effects of tip-path plane motion on the inflow. Refs. 81,82 show the need for modeling the effects of wake distortion caused by movement of the tip-path plane of single main rotor configurations, either through flap rates or through body motions. In particular, for single main rotors these effects are necessary to accurately predict the off-axis response of the aircraft. Wake distortion for the coaxial rotorcraft was shown to be required for on-axis agreement with flight test data [38]. The purpose of this chapter is to show an extension of the inflow model system identification methodology to include rotor flapping and wake distortion.

As part of this extension, the method will also be extended to a case with a coaxial rotor in forward flight. The identification of a low-order inflow model for a closely-spaced coaxial configuration in forward flight requires particular care

for several reasons. First, because the rotors are close, the aerodynamic couplings between them are strong, and in general it cannot be assumed that, even at high speed, there is no interference between the two wakes. Second, the physics of a coaxial configuration are such that significant correlation between inputs and outputs exists. Finally, it has been shown [80] that coupling between inflow states and wake curvature exists, and creates higher-order behavior in the inflow system. As a consequence, the size of the inflow model tends to grow, and the number of parameters to be identified becomes large.

The Higher order methodology used will be described in detail, including in particular the determination of the higher order model structure and the challenges posed by the significant size of the problem (of the order of one hundred parameters to be identified).

Lastly this chapter will evaluate these inflow model's effects on flight dynamics and control. This chapter will explore the key effects of rotor inflow and interference on the dynamics of a coaxial rotorcraft configurations, in comparison to an inflow model without dynamic rotor interference. This chapter will also demonstrate the design of explicit model-following feedback controllers, showing the effect of inflow dynamics, including rotor-rotor interference, on the controller parameters and resulting performance.

6.2 Higher Order State-Space Model

It has been shown that tip-path plane motion causes wake distortions that modify the dynamics of the wake [81], and that it is essential to include these effects to achieve the correct aircraft response [82]. The extension, proposed in Ref. 81, of the Pitt-Peters model to include the tip-path plane motion "K_R" wake distortion effects was shown in Eq.(2.29). The logical supposition is that these effects would persist in a coaxial rotorcraft, though they may be modified by the rotor-rotor interactions. A previous analysis of the performance and handling of the Sikorsky X2 Technology Demonstrator [38] did include the effects of K_R and was able to adequately match flight test data.

More recently, a second order approach to wake distortion effects was proposed [80] for a single main rotor which tries to interpret the wake distortion as phenomena arising from changes in the far-wake and near-wake separately. The idea is that the far-wake is mostly distorted by tip-path plane motion and the near wake is mostly distorted by the aerodynamic forcing. However there is still intense coupling between the two portions of the wake, and so this produces second order responses previously shown in this dissertation and also in Refs. 80 and 79. These references were all adequately fit with first-order systems with time delays, but appear to require a second order ODE to properly fit their shape, and possibly remove the need for a time delay.

The perception that a higher order model may be necessary is aligned with the single main rotor results shown in Chap. 4. The inflow responses often looked like

they needed a few more poles and zeros to accurately capture their values, though they were likely captured well enough with the lower order models. The results for K_R in Sec. 2.2.2.5 showed that the wake distortion inflow response that was higher order and required further dynamics (poles and zeros) to truly be captured by a model. The coaxial results in Chap. 5 truly demonstrated the need for a higher order model.

The new single main rotor form that was proposed in Ref. [80] takes the 3-state Pitt-Peters model and turns it into a 5-state model where each harmonic inflow state is replaced with two inflow states for that harmonic near and far portion. This form is shown in Eq.(6.1), which is just for the lateral harmonic inflow, but the form is identical for the longitudinal harmonic inflow.

$$\begin{Bmatrix} \dot{\Delta\lambda}_{1SN} \\ \dot{\Delta\lambda}_{1SF} \end{Bmatrix} = \begin{bmatrix} F_{11} & 0 \\ F_{21} & F_{22} \end{bmatrix} \begin{Bmatrix} \Delta\lambda_{1SN} \\ \Delta\lambda_{1SF} \end{Bmatrix} + \begin{bmatrix} G_{11} & G_{12} \\ 0 & G_{22} \end{bmatrix} \begin{Bmatrix} \Delta C_L \\ \Delta\dot{\beta}_{1S} \end{Bmatrix} \tag{6.1}$$

$$\Delta\lambda_{1S} = \Delta\lambda_{1SN} + \Delta\lambda_{1SF}$$

It was found that allowing the average inflow to also hold the same form provides much improved fit to the MFW data. Tip-path plane motion in the vertical direction was not considered as an "input" to the system, but the wake was allowed to distort due to the coupling with the near-wake. This is not an effect traditionally captured by "K_R" but wake contractions and expansions in the vertical direction are highly visible in the far-wake when experiencing thrust perturbations. This rounds out the full model for a single rotor to have 6 states; 3 near-wake and 3 far-wake.

6.2.1 Twelve State Coaxial Rotor Inflow Model for Hover

This six state form can be extended to a hovering coaxial rotor system in much the same way that the three state inflow system was extended to the coaxial rotor in Chap. 5. The F and G matrices will have the initial form of 4 single-rotor six-state models stacked in a 2x2 manner, resulting in 12x12 matrices, as shown in Eq.(6.3).

$$\begin{Bmatrix} \Delta\dot{\lambda}^U_{0N} \\ \Delta\dot{\lambda}^U_{0F} \\ \Delta\dot{\lambda}^U_{1SN} \\ \Delta\dot{\lambda}^U_{1SF} \\ \Delta\dot{\lambda}^U_{1CN} \\ \Delta\dot{\lambda}^U_{1CF} \\ \Delta\dot{\lambda}^L_{0N} \\ \Delta\dot{\lambda}^L_{0F} \\ \Delta\dot{\lambda}^L_{1SN} \\ \Delta\dot{\lambda}^L_{1SF} \\ \Delta\dot{\lambda}^L_{1CN} \\ \Delta\dot{\lambda}^L_{1CF} \end{Bmatrix} = [F] \underbrace{\begin{Bmatrix} \Delta\lambda^U_{0N} \\ \Delta\lambda^U_{0F} \\ \Delta\lambda^U_{1SN} \\ \Delta\lambda^U_{1SF} \\ \Delta\lambda^U_{1CN} \\ \Delta\lambda^U_{1CF} \\ \Delta\lambda^L_{0N} \\ \Delta\lambda^L_{0F} \\ \Delta\lambda^L_{1SN} \\ \Delta\lambda^L_{1SF} \\ \Delta\lambda^L_{1CN} \\ \Delta\lambda^L_{1CF} \end{Bmatrix}}_{\lambda_{NF}} + [G] \underbrace{\begin{Bmatrix} \Delta C^U_T \\ \Delta C^U_L \\ \Delta\dot{\beta}^U_{1S} \\ \Delta C^U_M \\ \Delta\dot{\beta}^U_{1C} \\ \Delta C^L_T \\ \Delta C^L_L \\ \Delta\dot{\beta}^L_{1S} \\ \Delta C^L_M \\ \Delta\dot{\beta}^L_{1C} \end{Bmatrix}}_{C_\beta} \tag{6.2}$$

$$\underbrace{\begin{Bmatrix} \Delta\lambda^U_0 \\ \Delta\lambda^U_{1S} \\ \Delta\lambda^U_{1C} \\ \Delta\lambda^L_0 \\ \Delta\lambda^L_{1S} \\ \Delta\lambda^L_{1C} \end{Bmatrix}}_{\lambda} = \underbrace{\begin{Bmatrix} \Delta\lambda^U_{0N} \\ \Delta\lambda^U_{1SN} \\ \Delta\lambda^U_{1CN} \\ \Delta\lambda^L_{0N} \\ \Delta\lambda^L_{1SN} \\ \Delta\lambda^L_{1CN} \end{Bmatrix}}_{\lambda_N} + \underbrace{\begin{Bmatrix} \Delta\lambda^U_{0F} \\ \Delta\lambda^U_{1SF} \\ \Delta\lambda^U_{1CF} \\ \Delta\lambda^L_{0F} \\ \Delta\lambda^L_{1SF} \\ \Delta\lambda^L_{1CF} \end{Bmatrix}}_{\lambda_F}$$

$$F = \begin{bmatrix} \blacksquare & 0 & 0 & 0 & 0 & 0 & \blacksquare & 0 & 0 & 0 & 0 & 0 \\ \blacksquare & \blacksquare & 0 & 0 & 0 & 0 & \blacksquare & \blacksquare & 0 & 0 & 0 & 0 \\ 0 & 0 & \blacksquare & 0 & 0 & 0 & 0 & 0 & \blacksquare & 0 & 0 & 0 \\ 0 & 0 & \blacksquare & \blacksquare & 0 & 0 & 0 & 0 & \blacksquare & \blacksquare & 0 & 0 \\ 0 & 0 & 0 & 0 & \blacksquare & 0 & 0 & 0 & 0 & 0 & \blacksquare & 0 \\ 0 & 0 & 0 & 0 & \blacksquare & \blacksquare & 0 & 0 & 0 & 0 & \blacksquare & \blacksquare \\ \blacksquare & 0 & 0 & 0 & 0 & 0 & \blacksquare & 0 & 0 & 0 & 0 & 0 \\ \blacksquare & \blacksquare & 0 & 0 & 0 & 0 & \blacksquare & \blacksquare & 0 & 0 & 0 & 0 \\ 0 & 0 & \blacksquare & 0 & 0 & 0 & 0 & 0 & \blacksquare & 0 & 0 & 0 \\ 0 & 0 & \blacksquare & \blacksquare & 0 & 0 & 0 & 0 & \blacksquare & \blacksquare & 0 & 0 \\ 0 & 0 & 0 & 0 & \blacksquare & 0 & 0 & 0 & 0 & 0 & \blacksquare & 0 \\ 0 & 0 & 0 & 0 & \blacksquare & \blacksquare & 0 & 0 & 0 & 0 & \blacksquare & \blacksquare \end{bmatrix}$$

$$G = \begin{bmatrix} \blacksquare & 0 & 0 & 0 & 0 & \blacksquare & 0 & 0 & 0 & 0 \\ 0 & 0 & 0 & 0 & 0 & \blacksquare & 0 & 0 & 0 & 0 \\ 0 & \blacksquare & \blacksquare & 0 & 0 & 0 & \blacksquare & \blacksquare & 0 & 0 \\ 0 & 0 & \blacksquare & 0 & 0 & 0 & 0 & \blacksquare & 0 & 0 \\ 0 & 0 & 0 & \blacksquare & \blacksquare & 0 & 0 & 0 & \blacksquare & \blacksquare \\ 0 & 0 & 0 & 0 & \blacksquare & 0 & 0 & 0 & 0 & \blacksquare \\ \blacksquare & 0 & 0 & 0 & 0 & \blacksquare & 0 & 0 & 0 & 0 \\ 0 & 0 & 0 & 0 & 0 & \blacksquare & 0 & 0 & 0 & 0 \\ 0 & \blacksquare & \blacksquare & 0 & 0 & 0 & \blacksquare & \blacksquare & 0 & 0 \\ 0 & 0 & \blacksquare & 0 & 0 & 0 & 0 & \blacksquare & 0 & 0 \\ 0 & 0 & 0 & \blacksquare & \blacksquare & 0 & 0 & 0 & \blacksquare & \blacksquare \\ 0 & 0 & 0 & 0 & \blacksquare & 0 & 0 & 0 & 0 & \blacksquare \end{bmatrix} \tag{6.3}$$

■ and ■ indicate upper and lower rotor (respectively) free parameters in system identification

6.2.2 Twelve State Coaxial Rotor Inflow Model for Forward Flight

Inflow Models were also derived for the case of forward flight at 200 knots,corresponding to an advance ratio of $\mu = 0.54$. The rotor had an angle of attack of $\alpha = 2°$. In

this trim condition, which is expected to be highly likely for high-speed flight of coaxial-pusher configurations, the free stream encounters the lower rotor first, and portions of the upper rotor may be immersed in the wake of the lower rotor. In this case, there is full coupling between all the aerodynamic inputs and the inflow outputs. For this case, all of the outputs respond to all of the inputs, creating a very coupled system. Separation by axis can no longer be assumed as it was for hover, and terms cannot be constrained to simplify the problem. Due to the difficulty of this identification, wake distortions due to tip-path plane motion is neglected. Every term in the 12 by 12 matrices of Eq.(2.35) is now potentially a free parameter to be identified. However, it was decided that the $[F]$ matrix would still be a combination of 6 blocks by 6 blocks, all of the form of the $[F]$ matrix shown in Eq.(6.1), at least initially. Therefore, the higher order form for the $[F]$ matrix in Eq.(6.2.1) was retained to capture the higher order behavior of the wake, which exist regardless of tip-path plane perturbations (the wake does experience distortions to its geometry even with only aerodynamic loading perturbations). The $[G]$ matrix initially has all free terms, but since the wake distortion due to tip-path plane motion is neglected, the flap rates are not included as inputs and the $[G]$ matrix only has six columns, corresponding to the six coaxial rotor aerodynamic loading terms.

Additional details on the structure of the model are provided by Eq.(6.7). The free parameters (blue and red squares indicate the upper and lower rotor parameters, respectively) are all obtained for the identification.

$$\begin{Bmatrix} \Delta\dot{\lambda}^{U}_{0N} \\ \Delta\dot{\lambda}^{U}_{0F} \\ \Delta\dot{\lambda}^{U}_{1SN} \\ \Delta\dot{\lambda}^{U}_{1SF} \\ \Delta\dot{\lambda}^{U}_{1CN} \\ \Delta\dot{\lambda}^{U}_{1CF} \\ \Delta\dot{\lambda}^{L}_{0N} \\ \Delta\dot{\lambda}^{L}_{0F} \\ \Delta\dot{\lambda}^{L}_{1SN} \\ \Delta\dot{\lambda}^{L}_{1SF} \\ \Delta\dot{\lambda}^{L}_{1CN} \\ \Delta\dot{\lambda}^{L}_{1CF} \end{Bmatrix} = [F] \underbrace{\begin{Bmatrix} \Delta\lambda^{U}_{0N} \\ \Delta\lambda^{U}_{0F} \\ \Delta\lambda^{U}_{1SN} \\ \Delta\lambda^{U}_{1SF} \\ \Delta\lambda^{U}_{1CN} \\ \Delta\lambda^{U}_{1CF} \\ \Delta\lambda^{L}_{0N} \\ \Delta\lambda^{L}_{0F} \\ \Delta\lambda^{L}_{1SN} \\ \Delta\lambda^{L}_{1SF} \\ \Delta\lambda^{L}_{1CN} \\ \Delta\lambda^{L}_{1CF} \end{Bmatrix}}_{\lambda_{NF}} + [G] \underbrace{\begin{Bmatrix} \Delta C^{U}_{T} \\ \Delta C^{U}_{L} \\ \Delta C^{U}_{M} \\ \Delta C^{L}_{T} \\ \Delta C^{L}_{L} \\ \Delta C^{L}_{M} \end{Bmatrix}}_{C} \tag{6.4}$$

$$\underbrace{\begin{Bmatrix} \Delta\lambda^{U}_{0} \\ \Delta\lambda^{U}_{1S} \\ \Delta\lambda^{U}_{1C} \\ \Delta\lambda^{L}_{0} \\ \Delta\lambda^{L}_{1S} \\ \Delta\lambda^{L}_{1C} \end{Bmatrix}}_{\lambda} = \underbrace{\begin{Bmatrix} \Delta\lambda^{U}_{0N} \\ \Delta\lambda^{U}_{1SN} \\ \Delta\lambda^{U}_{1CN} \\ \Delta\lambda^{L}_{0N} \\ \Delta\lambda^{L}_{1SN} \\ \Delta\lambda^{L}_{1CN} \end{Bmatrix}}_{\lambda_{N}} + \underbrace{\begin{Bmatrix} \Delta\lambda^{U}_{0F} \\ \Delta\lambda^{U}_{1SF} \\ \Delta\lambda^{U}_{1CF} \\ \Delta\lambda^{L}_{0F} \\ \Delta\lambda^{L}_{1SF} \\ \Delta\lambda^{L}_{1CF} \end{Bmatrix}}_{\lambda_{F}} \tag{6.5}$$

where:

$$F = \begin{bmatrix} \blacksquare & 0 & \blacksquare & 0 & \blacksquare & 0 & \blacksquare & 0 & \blacksquare & 0 & \blacksquare & 0 \\ \blacksquare & \blacksquare & \blacksquare & \blacksquare & \blacksquare & \blacksquare & \blacksquare & \blacksquare & \blacksquare & \blacksquare & \blacksquare & \blacksquare \\ \blacksquare & 0 & \blacksquare & 0 & \blacksquare & 0 & \blacksquare & 0 & \blacksquare & 0 & \blacksquare & 0 \\ \blacksquare & \blacksquare & \blacksquare & \blacksquare & \blacksquare & \blacksquare & \blacksquare & \blacksquare & \blacksquare & \blacksquare & \blacksquare & \blacksquare \\ \blacksquare & 0 & \blacksquare & 0 & \blacksquare & 0 & \blacksquare & 0 & \blacksquare & 0 & \blacksquare & 0 \\ \blacksquare & \blacksquare & \blacksquare & \blacksquare & \blacksquare & \blacksquare & \blacksquare & \blacksquare & \blacksquare & \blacksquare & \blacksquare & \blacksquare \\ \blacksquare & 0 & \blacksquare & 0 & \blacksquare & 0 & \blacksquare & 0 & \blacksquare & 0 & \blacksquare & 0 \\ \blacksquare & \blacksquare & \blacksquare & \blacksquare & \blacksquare & \blacksquare & \blacksquare & \blacksquare & \blacksquare & \blacksquare & \blacksquare & \blacksquare \\ \blacksquare & 0 & \blacksquare & 0 & \blacksquare & 0 & \blacksquare & 0 & \blacksquare & 0 & \blacksquare & 0 \\ \blacksquare & \blacksquare & \blacksquare & \blacksquare & \blacksquare & \blacksquare & \blacksquare & \blacksquare & \blacksquare & \blacksquare & \blacksquare & \blacksquare \end{bmatrix} \tag{6.6}$$

$$G = \begin{bmatrix} \blacksquare & \blacksquare & \blacksquare & \blacksquare & \blacksquare & \blacksquare \\ \blacksquare & \blacksquare & \blacksquare & \blacksquare & \blacksquare & \blacksquare \\ \blacksquare & \blacksquare & \blacksquare & \blacksquare & \blacksquare & \blacksquare \\ \blacksquare & \blacksquare & \blacksquare & \blacksquare & \blacksquare & \blacksquare \\ \blacksquare & \blacksquare & \blacksquare & \blacksquare & \blacksquare & \blacksquare \\ \blacksquare & \blacksquare & \blacksquare & \blacksquare & \blacksquare & \blacksquare \\ \blacksquare & \blacksquare & \blacksquare & \blacksquare & \blacksquare & \blacksquare \\ \blacksquare & \blacksquare & \blacksquare & \blacksquare & \blacksquare & \blacksquare \\ \blacksquare & \blacksquare & \blacksquare & \blacksquare & \blacksquare & \blacksquare \\ \blacksquare & \blacksquare & \blacksquare & \blacksquare & \blacksquare & \blacksquare \end{bmatrix} \tag{6.7}$$

■ and ■ indicate upper and lower rotor (respectively) free parameters in system identification

Eq.(6.2) and Eq.(6.5), for hover and forward flight, both have no time delays. In Chaps. 4 and 5, time delays were used to model approximately the higher order dynamics that could not be captured with the first order form. In particular, they helped capture the phase roll-off that made the error of the state space model quite high if the time delays were not included. The time delays needed to be converted

to ODEs using Padé approximations for the model to be rigorously in state-space form, and this changed the 6 state inflow equation into a system with 32 states. So with the form of Eq.(6.2), the complexity is actually reduced because there are no time delays, and therefore fewer states.

6.3 Frequency Response Generation

For forward flight, when wake distortion due to tip-path plane motion is neglected, the frequency response generation is performed the same as in Chap. 5. The tip-path plane effects are incorporated in the model for hover, however, so the inflow responses to blade flapping must be identified, as described in Sec. 4.7. The Joint Input Output method of Sec. 3.3.5 is used as shown in Eq.(4.11), with the one difference being that each vector is now twice the length, containing both an upper and lower rotor portion, as was done in Chap. 5. The parametric model is then found by assuming that the form of the system is as shown in Eq.(6.2), and determining the elements of the matrices $[F]$ and $[G]$ that best fit the non-parametric models, both $\lambda(s)/\Delta C(s)$ and $\lambda(s)/\Delta\dot{\beta}(s)$.

For a coaxial rotorcraft, it is important to note that flap-inflow coupling may look quite different than a single main rotor. In Ref. 81, wake curvature was the motivation behind the extended momentum theory, but in the coaxial case there is also added effect that rotor spacing is essentially changing with tip-path plane motion, and rotor-rotor interference therefore may fluctuate. Also there are really two sets of wake trailers, one for each rotor, with the upper rotor wake inside (most

of the time) the lower rotor wake. Tip-path plane motion of one rotor is therefore quite likely to distort the wake of the other rotor.

6.4 State Space Parameter Identification Challenges and Techniques

The new state space model forms present new challenges for the procedure of identifying the optimal values to fit the non-parametric frequency responses. Most complex optimization problems are not purely convex in nature and therefore do not have only a single optimal solution. Many problems have multiple local minima in addition to the global minima. As the number of design variable increases, the likelihood of additional minima is generally increased. State-space identification is no different [63]. The optimization algorithm often will get stuck in local minima, or in minima that don't satisfy certain requirements for an optimal solution. In past chapters, these concerns were mostly non-existent because the number of terms to identify was much smaller. However, the complexity of the number of additional terms in this chapter places a burden on the designer to satisfy multiple constraints for the optimal values chosen.

6.4.1 Stability requirements

The first requirement, which is that the state-space inflow model be stable, follows from physical considerations. First, if the full, nonlinear MFW simulation is unstable to perturbations in aerodynamic loading, then the inflow time histories would be diverging with perturbations of the aerodynamic loading. But this is not

seen in any of the frequency sweeps indicating that the state-space inflow system should always be stable. Secondly, time verification will not succeed if the system is unstable because the state-space inflow model will diverge and not match the MFW. So the state-space identification procedure needs to always identify a stable inflow state-space system. The simplest of stability is to compute eigenvalues of the inflow model and verify that the real parts are all less than zero.

There was no practical was to add a stability constraint in the software used in this study [63] to perform the identification. Therefore, the approach taken was to start with a stable solution and repeatedly check the stability of the state-space inflow model (through eigenvalue computation) throughout the optimization to ensure that the optimization does not lead to an unstable state-space model. This happens quite frequently, typically when parameters are added or removed from the model. In a highly coupled system like Eq.(eq:FFInflowDef), changes in parameters can very easily change the value of one or more of the twelve eigenvalues, so that they have negative values. When the solution does go unstable, the parameters are reverted to the last known stable solution.

6.4.2 Sensitivity and Cramer-Rao Bounds Requirements

State-space models in the form of Eq.(6.2) or Eq.(6.5) must be checked to ensure that they are not over-parameterized. This means that there are correlated or insensitive parameters in the matrices that are not necessary to describe the dynamics. Those parameters will have high Cramer-Rao bounds, Eq.(3.16), or high

insensitivities, Eq.(3.15). The free parameters in Eqs.(6.2) and (6.5) are those with which the optimization is started. The insensitivities and Cramer-Rao percentages must be scrutinized, as stated in Chap. 3. Parameters that are too insensitive ($\overline{I}_i > 10\%$) or have too high of Cramer-Rao bounds ($\overline{CR}_i > 20\%$) should be removed [63]. This has not changed from the previous identifications, it has just become much more common, given the complexity of these systems. As a result, the final optimizations will be shown to fix many of the parameters and set them to zero.

6.4.3 Initial Conditions

It is especially important to start with a good initial guess of the identification parameters for this very complex model structure. Choosing the initial condition can be a difficult process. One solution that tends to work is to first identify the first order system as shown in Chap. 5. With a first order system identified, the additional states of this chapter can then be added, with zeroes in their locations. At that point the system will still have the same cost and behavior because all of the second order terms are zero. The user can then fix the first order terms and allow the second order terms to optimize on their own. This produces a system that is a pretty good initial guess. It has an advantage that the states are "sorted" into first and second order states, and the user can easily turn off either part by manipulating the output matrix. This system can then be further optimized by freeing all of the parameters at once.

Another approach commonly recommended [63], is to first fit the primary responses and then subsequently add the remaining responses. In this case this could mean first fitting the two on-rotor portions of the matrices only using the on-rotor frequency responses and ignoring the mutual interference frequency responses. Once the two rotors are fit separately, the on-axis terms can be fixed and the remaining frequency responses added. The optimization will then provide a solution that fits the other frequency responses while hopefully not changing the on-axis responses too significantly. From this solution, often times, every parameter can be freed and the optimization will likely approach a well behaved solution. The key is that optimizing with less parameters involved first, allows the optimization to better navigate the non-linear equations, and keeps the routine from moving too far away from desirable solutions.

The above two approaches were combined to obtain the results for this chapter. For clarity, the notation $F\{i,j\}$ or $G\{i,j\}$ is used to denote the i-th row, j-th column element of either the $[F]$ or $[G]$ matrices. For both hover and forward flight, the initial model was produced using the following steps.

1. First, fit the on-rotor diagonal responses with first order terms only. This means only using the responses λ_0^U/C_T^U, λ_{1c}^U/C_M^U, λ_{1s}^U/C_L^U, λ_0^L/C_T^L, λ_{1c}^L/C_M^L, and λ_{1s}^L/C_L^L in the cost function. For hover, every parameter in Eq.(6.2) is fixed to zero *except* $F\{1,1\}$, $F\{3,3\}$, $F\{5,5\}$, $F\{7,7\}$, $F\{9,9\}$, $F\{11,11\}$, $G\{1,1\}$, $G\{3,2\}$, $G\{5,4\}$, $G\{7,6\}$, $G\{9,7\}$, and $G\{11,9\}$. For forward flight, every parameter in Eq.(6.5) is fixed to zero *except* $F\{1,1\}$, $F\{3,3\}$, $F\{5,5\}$,

$F\{7,7\}$, $F\{9,9\}$, $F\{11,11\}$, $G\{1,1\}$, $G\{3,2\}$, $G\{5,3\}$, $G\{7,4\}$, $G\{9,5\}$, and $G\{11,6\}$. This subset of the parameters is optimized to the subset of frequency responses. Ensure that the state-space system is stable. This may require some manual flipping of signs of some parameters.

2. Next, fix the parameters from step 1 to their optimized values, and free the first order off-rotor parameters $F\{1,7\}$, $F\{3,9\}$, $F\{5,11\}$, $F\{7,1\}$, $F\{9,3\}$, $F\{11,5\}$. Also, for hover, free $G\{1,6\}$, $G\{3,7\}$, $G\{5,9\}$, $G\{7,1\}$, $G\{9,2\}$, and $G\{11,4\}$. For forward flight, also free $G\{1,4\}$, $G\{3,5\}$, $G\{5,5\}$, $G\{7,1\}$, $G\{9,2\}$, and $G\{11,3\}$. Add in the off-rotor frequency responses: λ_0^U/C_T^L, λ_{1c}^U/C_M^L, λ_{1s}^U/C_L^L, λ_0^L/C_T^U, λ_{1c}^L/C_M^U, and λ_{1s}^L/C_L^U. Once again optimize parameters, and ensure stability.

3. Now free all the non-zero parameters from steps 1 and 2 and optimize together, while ensuring stability. This produces a state-space inflow model that is similar to that found in Chap. 5 for a hovering coaxial rotor.

4. For forward flight only, the extended couplings need to be added to this system. This is best done slowly, by repeating the following steps:

   (a) Fix all non-zero parameters

   (b) Choose an off-axis frequency response or pair of frequency responses to add, e.g. λ_0^U/C_M^L and λ_0^U/C_M^L.

   (c) Free the zero-valued (not yet used) parameters that should have a large impact on these responses. These are typically terms that have rows and

columns corresponding to the given inputs and outputs in the chosen responses. For the given example, this would be terms in the first row of both matrices. For the $[F]$ matrix, only odd columns are chosen, so $F\{1,3\}$, $F\{1,5\}$, $F\{1,9\}$, $F\{1,11\}$. In the $[G]$ matrix, free the given control of the pair, C_M^L, which corresponds to $G\{1,6\}$. Optimize this subset of parameters, and unsure stability.

(d) The parameters used in the previous step may not all be impactful on the given responses. The insensitivity of the parameters should be checked and parameters with very high insensitivities should be set back to a fixed value of zero. The guideline for insensitive parameters is that the insentivity of a parameter should not exceed $\overline{I}_i > 10\%$ [63], however for this procedure a much higher threshold is suggested, potentially even $\overline{I}_i > 100\%$. Highly insensitive parameters will be removed from the system later, but it is best to, for now, only remove parameters that seem to have essentially no impact. In the example, $F\{1,3\}$ may end up being very insensitive because it describes the affect of λ_{1s}^U on λ_0^U which is not very relevant to the already added frequency responses. Therefore it might be set back to zero and fixed. If this is done the free parameters should be re-optimized.

(e) Now all of the non-zero parameters (which have been used so far), or some subset that makes sense given the frequency responses that were added,

should be freed and re-optimized, while ensuring stability. Another check for really insensitive parameters may be useful again.

this will slowly build the matrices from the ground up, ensuring stability, and keeping some really insensitive parameters out of the system.

5. For hover only, the first order flap rate terms and frequency responses need to be added. First fix all non-zero parameters. Add in frequency responses $\lambda^U_{1s}/\overset{*}{\beta}{}^U_{1s}$, $\lambda^U_{1c}/\overset{*}{\beta}{}^U_{1c}$, $\lambda^U_{1s}/\overset{*}{\beta}{}^L_{1s}$, $\lambda^U_{1c}/\overset{*}{\beta}{}^L_{1c}$, $\lambda^L_{1s}/\overset{*}{\beta}{}^U_{1s}$, $\lambda^L_{1c}/\overset{*}{\beta}{}^U_{1c}$, $\lambda^L_{1s}/\overset{*}{\beta}{}^L_{1s}$, and $\lambda^L_{1c}/\overset{*}{\beta}{}^L_{1c}$. free the parameters $G\{3,3\}$, $G\{5,5\}$, $G\{7,8\}$, $G\{9,10\}$, $G\{3,8\}$, $G\{5,10\}$, $G\{9,3\}$, and $G\{11,5\}$. Optimize and ensure stability.

6. The system will now be a system in which half of the states do nothing, because the even rows should be all zeros. Therefore, it is still first order in the sense that there is one output for each state. For hover, it is likely that the remainder of the zero fixed parameters can be freed and optimized without leading the optimization to a local minima/unstable solution. For forward flight, there are likely too many remaining terms to all be added at once. Instead, a procedure similar to step 4 should be performed, to slowly add in the remaining terms. The only difference would be that, at this point, all of the frequency responses have been added, so step 4(b) would be skipped.

6.4.4 Model Reduction due to Insensitivity and Cramer-Rao Bounds

With a fully populated, or close to fully populated, matrices from Eq.(6.2) or Eq.(6.5), there are likely either insensitive parameters or parameters with high

Cramer-Rao bounds. In the single main rotor case, no parameters were ever removed because the system is already parameterized by so few variables. In the 12 state forward flight model, Eq.(6.7) shows 180 parameters. Nearly half of them need be removed in the result that will be shown.

The process for removing them is fairly straight-forward. The goal is for all parameters to achieve under 10% insensitivity and under 20% Cramer-Rao bound percentages. The highest insensitivities should be removed first. Every time a parameter is removed, the new solution should be converged and checked to ensure that the solution has stayed stable and the cost function has not risen too abruptly, not more than about 5%. Ref. 63 gives a guideline that a single frequency responses cost should not rise by more than 10 and the average cost should not rise more than 1-2. If either of these constraints fails, then the previous parameters should be restored and the next most insensitive parameter should be tried. Some experimentation may be needed to determine which parameter really is best to be removed. Once all the remaining free parameters are below 10% insensitivity, parameters with Cramer-Rao bound percentages above 20% should start to be removed, with the same deference to the stated constraints. If the insensitive parameters are becoming difficult to remove, the highest Cramer-Rao bound percentage could be removed instead. The procedure can be automated with great care and thoughtful logic. Figure 6.1 gives an outline of the algorithm that was used to complete the parameter reduction.

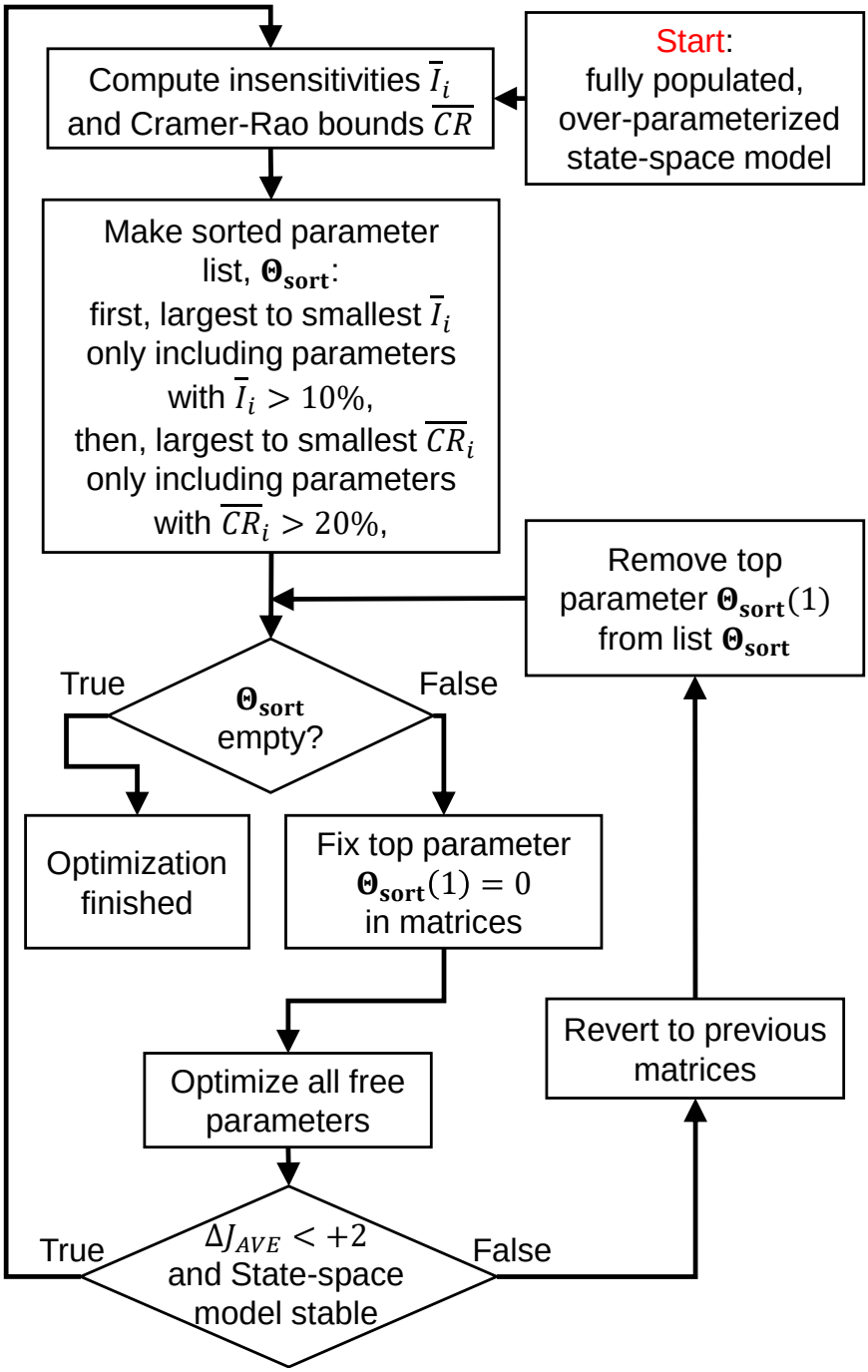

Figure 6.1: Flowchart of algorithm used for reducing parameters with high insensitivity or high Cramer-Rao bounds

6.5 Results for Hover Model

The coaxial rotor, described in Appendix B, was trimmed in hover, with trim C_T for the upper and lower rotors are 0.0053 and 0.0043, respectively. Frequency responses were then generated through frequency sweeps.

6.5.1 Frequency Responses

The frequency responses $\lambda(s)/C(s)$ for the coaxial configuration are shown in Figs 6.2 to 6.7. In all figures solid lines indicate the frequency responses obtained with the full, nonlinear MFW, the dashed lines those obtained with the identified state-space model.

Figures 6.2 and 6.3 show the responses of upper and lower rotor average inflow, λ_0^U and λ_0^L, to upper rotor and lower rotor thrust perturbations C_T^U and C_T^L, respectively. The costs J of the state-space models are listed on each figure and all indicate excellent fits.

The fit is generally very good for both sets of responses, giving confidence in the model structure used.

Figure 6.4 and 6.5 show the responses of lateral harmonic inflow λ_{1s} to upper rotor and lower rotor roll moment perturbations, C_L^U and C_L^L, respectively.

The upper rotor roll moment C_L^U responses, Fig 6.4, shows significant second-order attributes and provide excellent fits with the proposed form. The lower rotor roll moment C_L^L responses, Fig 6.5 also show some higher-order behavior but only fit adequately with the proposed form. The lower rotor lateral inflow λ_{1s}^L response

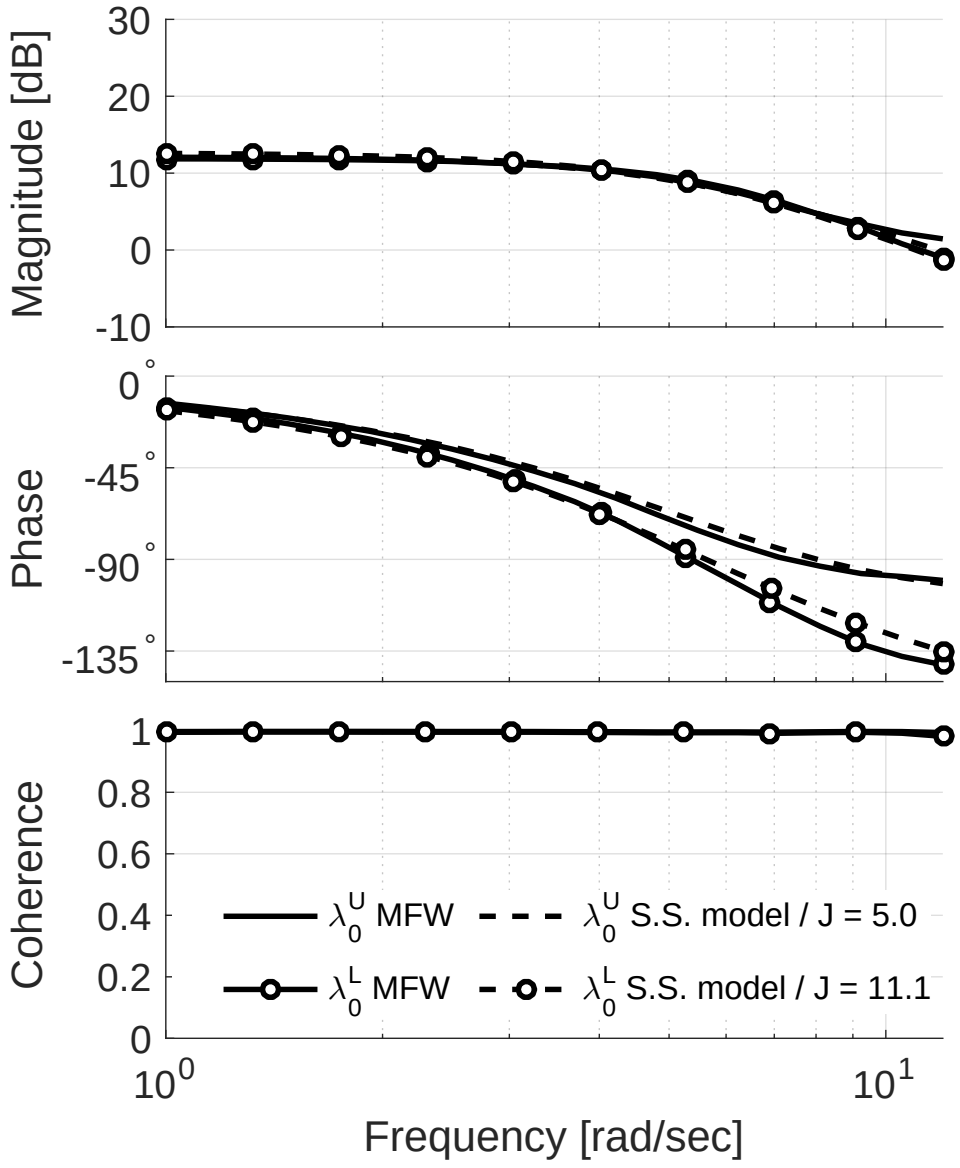

Figure 6.2: Average inflow response λ_0 to upper rotor thrust C_T^U for both rotors in hover. Trim C_T for the upper and lower rotors are 0.0052 and 0.0043, respectively. Solid line, MFW, dashed line, state-space model.

to lower rotor roll moment has a cost of 108.9 but it very similar in magnitude to the lower rotor lateral inflow λ_{1s}^L response to *upper* rotor roll moment C_L^U. It is important to note that the upper rotor effect on the lower rotor is nearly as important as lower rotor effect on itself, as shown by the similar magnitudes of the

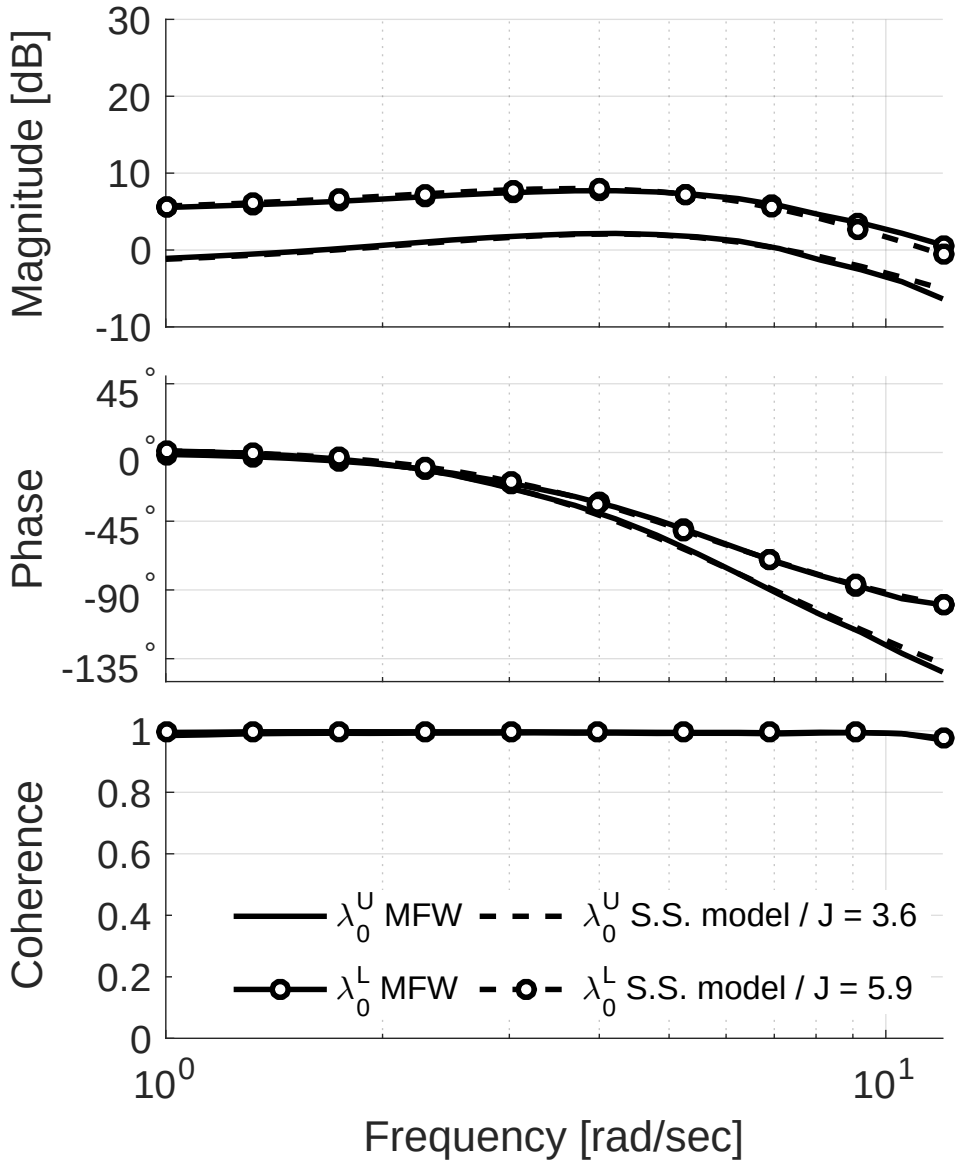

Figure 6.3: Inflow response of λ_0 on both rotors to lower rotor thrust C_T^L; Solid line, MFW, dashed line, state-space model.

responses. The model must capture both of these accurately, which it does. The upper rotor lateral inflow λ_{1s}^U response to lower rotor roll moment C_L^L has the highest cost of 158.6, but it is also the lowest in magnitude of any of the responses, so this high cost is deemed acceptable. Overall, the greatly improved cost functions for the

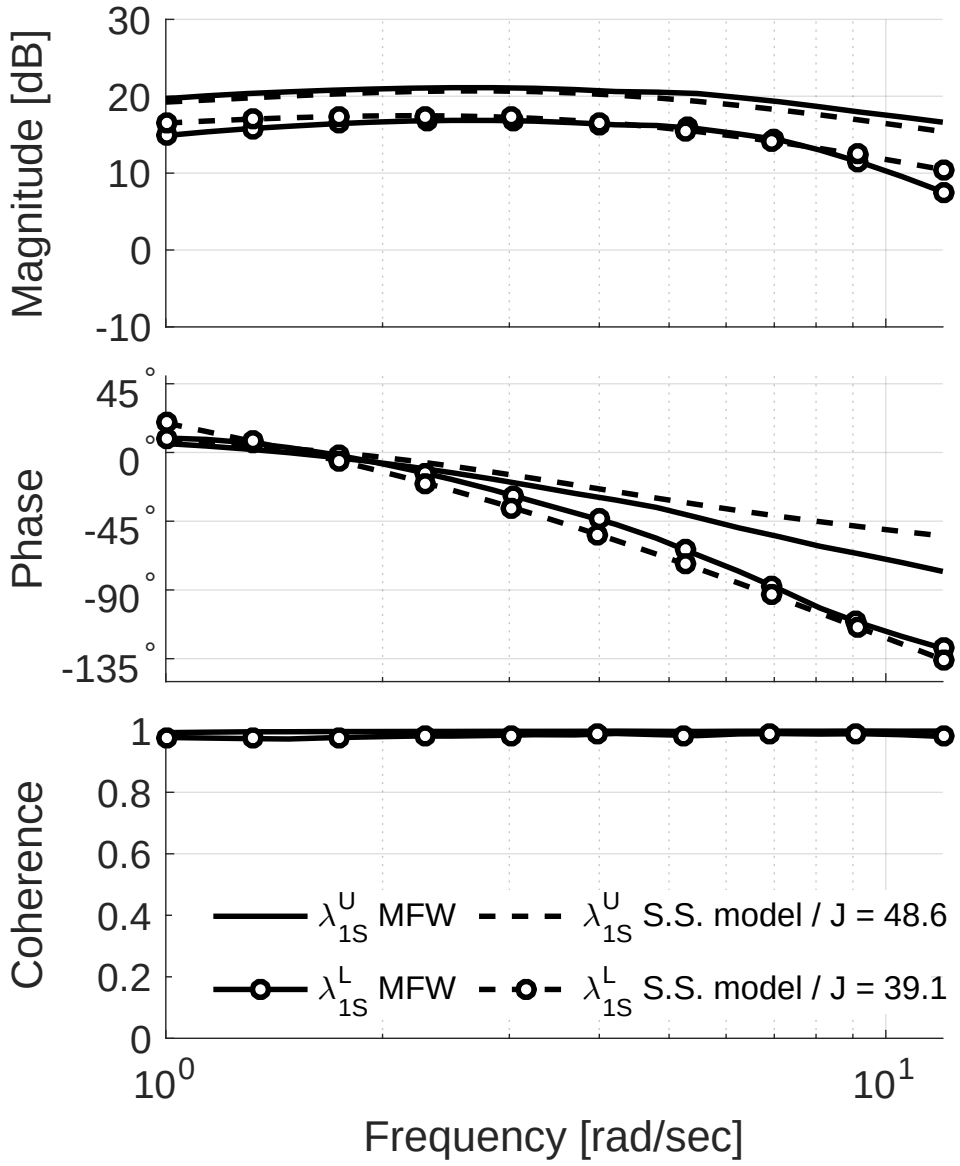

Figure 6.4: Inflow response of λ_{1S} on both rotors to upper rotor roll moment C_L^U; Solid line, MFW, dashed line, state-space model.

higher order inflow dynamics model validate this higher order structure. Table 6.1 compares the cost of the 12-state and the 6-state model from Chapter 5. In most individual frequency responses, the cost of the higher order fit decreased, indicating a better fit, and the overall average cost decreased by 55%.

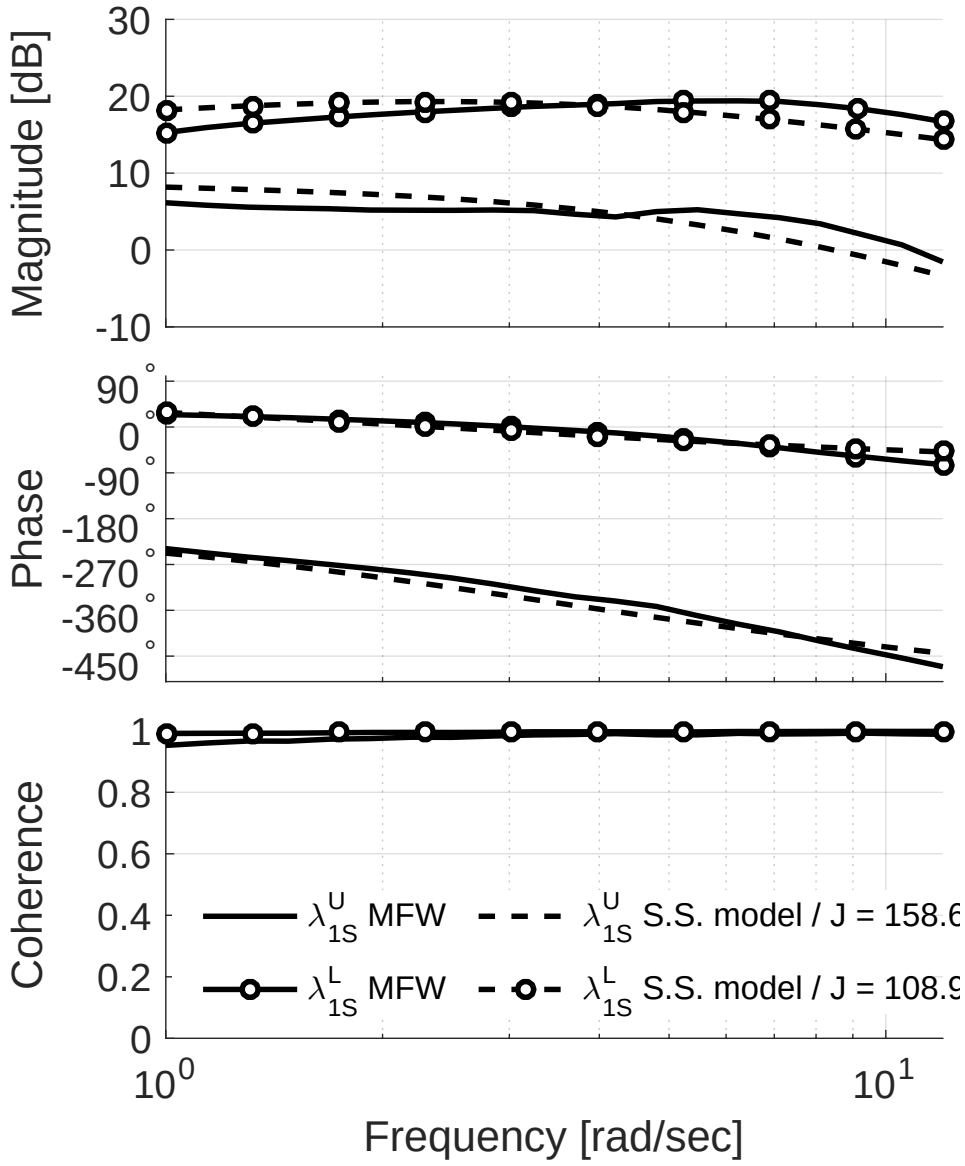

Figure 6.5: Inflow response of λ_{1S} on both rotors to lower rotor roll moment C_L^L; Solid line, MFW, dashed line, state-space model.

The $\lambda(s)/\dot{\beta}(s)$ type responses are shown next, which help determine the wake distortion effects. Figures 6.6 and 6.7 show the frequency response of both rotors lateral harmonic inflow λ_{1s} to the upper and lower rotor cyclic flapping rate, $\dot{\beta}^U_{1S}$ and $\dot{\beta}^L_{1S}$. The model structure is able to capture all the responses fairly well. There

Table 6.1: Cost J of 12 state model and 6 state model from Chap. 5

Response	J (6 state)	J (12 state)
$\lambda_0^U(s)/C_T^U(s)$	3.7	5.0
$\lambda_0^L(s)/C_T^U(s)$	17.2	11.1
$\lambda_{1C}^U(s)/C_M^U(s)$	204.0	48.6
$\lambda_{1C}^L(s)/C_M^U(s)$	178.1	39.1
$\lambda_{1S}^U(s)/C_L^U(s)$	204.1	48.6
$\lambda_{1S}^L(s)/C_L^U(s)$	177.7	39.1
$\lambda_0^U(s)/C_T^L(s)$	85.3	3.6
$\lambda_0^L(s)/C_T^L(s)$	28.8	5.9
$\lambda_{1C}^U(s)/C_M^L(s)$	115.8	158.6
$\lambda_{1C}^L(s)/C_M^L(s)$	463.6	108.9
$\lambda_{1S}^U(s)/C_L^L(s)$	115.1	158.6
$\lambda_{1S}^L(s)/C_L^L(s)$	462.5	108.9
Average Cost	171.3	77.0

are clearly additional dynamics present in the frequency responses, but the form used captures accurately the key response characteristic.

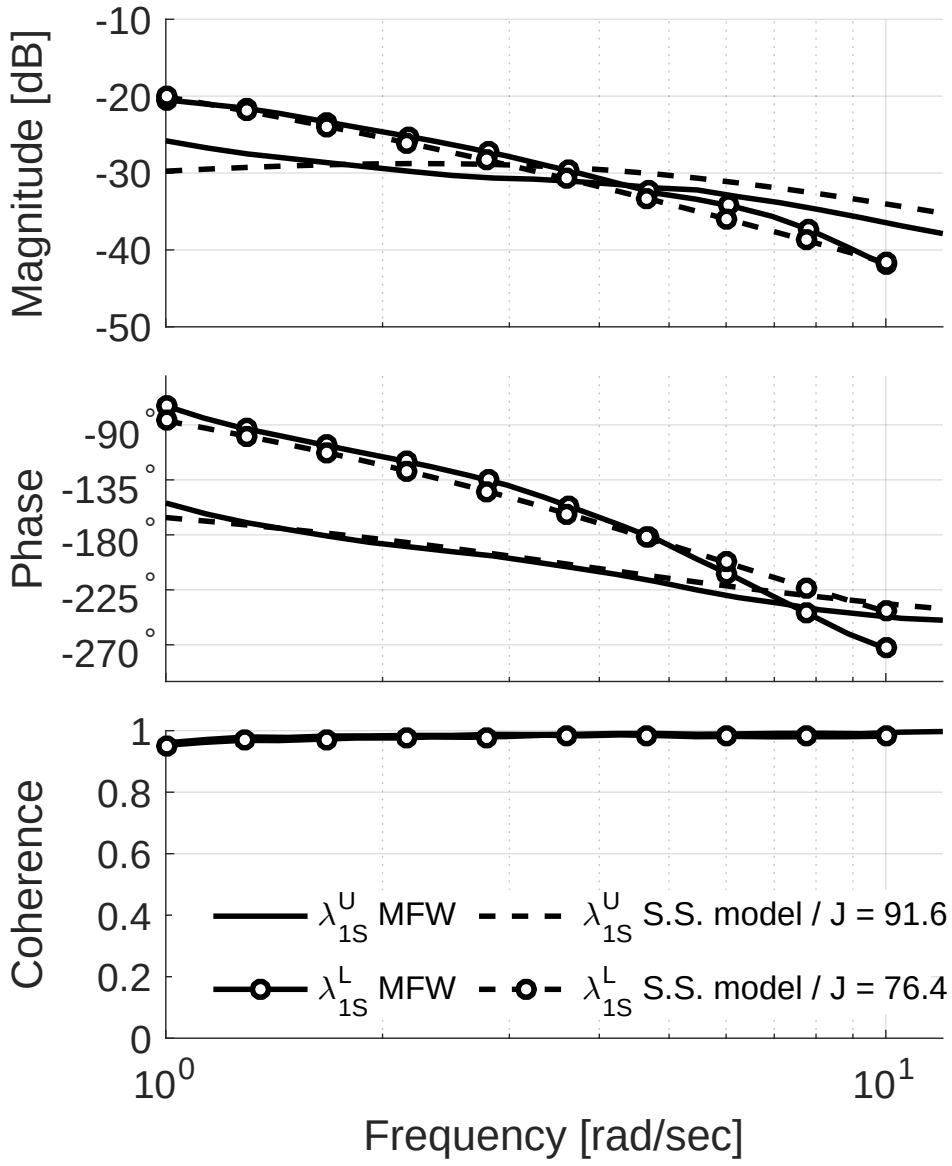

Figure 6.6: Inflow response of λ_{1S} on both rotors to upper rotor cyclic flapping rate $\dot{\beta}^{U}_{1S}$; Solid line, MFW, dashed line, state-space model.

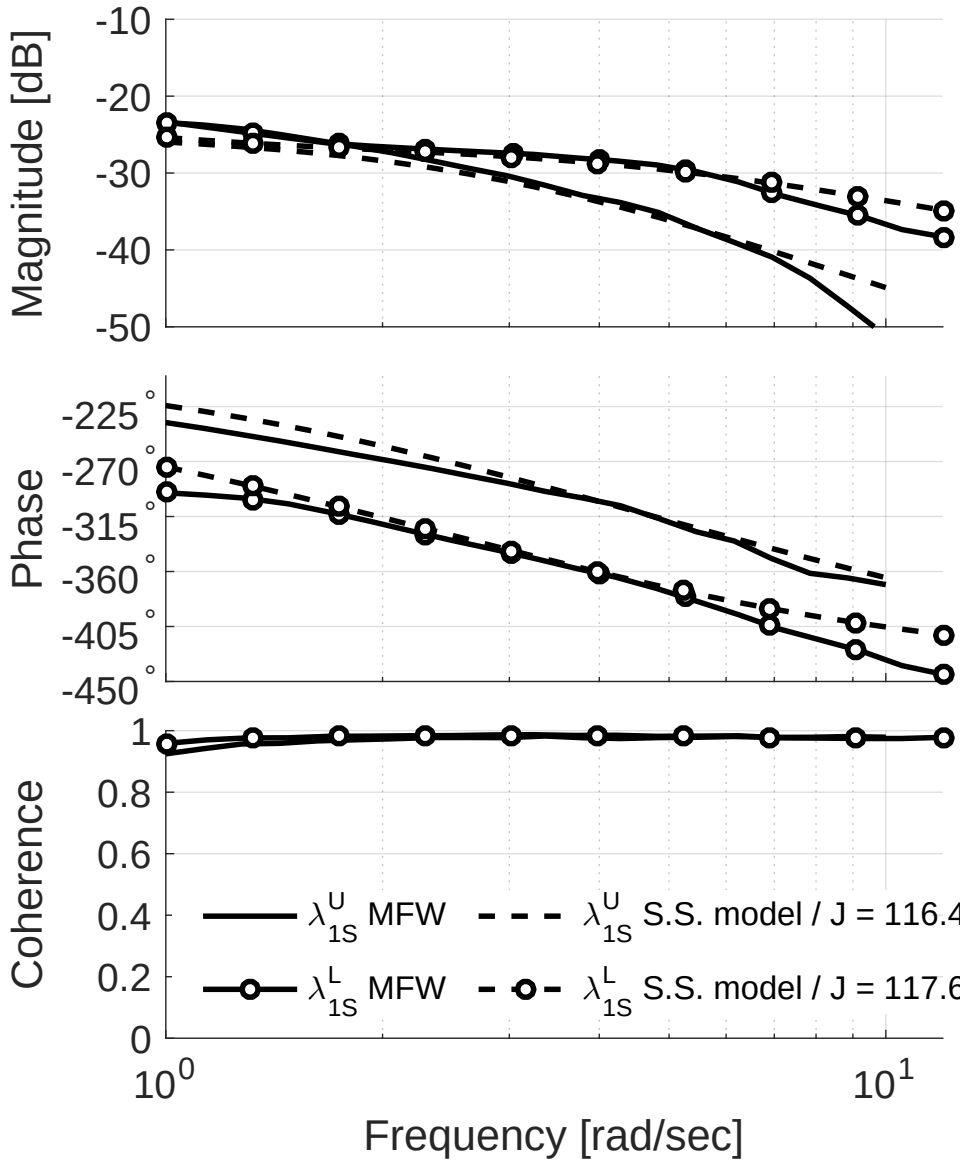

Figure 6.7: Inflow response of λ_{1S} on both rotors to lower rotor cyclic flapping rate $\dot{\beta}^{L}_{1S}$; Solid line, MFW, dashed line, state-space model.

were calculated and remained similar in value and form to those shown in Chap. 5, though small changes have occurred due to configuration changes and additional modeling considerations. The parametric models for each $\lambda(s)/C(s)$ pair have improved due to the better ability of the new second-order form to match the MFW data. The model follows the form shown in Eq.(2.30), with the final identification giving the matrices shown in Eqs.(6.8) and (6.9). The percentages listed in the matrices given by Eqs.(6.10) and (6.11) correspond to the identified model's Cramer-Rao Bound percentages for the parameter in the same row and column in Eqs.(6.8) and (6.9). These indices are a measure of parameter uncertainty and its importance to the model structure [63]. The low values for both Cramer-Rao show the model is well identified with minimal uncertainty and parameter correlation. Only heave and lateral axis results will be presented. Since the rotors are in hover, the longitudinal response matches the lateral one.

$$F = \tag{6.8}$$

$$\begin{bmatrix}
9.03 & 0 & 0 & 0 & 0 & 0 & -10.26 & 0 & 0 & 0 & 0 & 0 \\
0 & -6.85 & 0 & 0 & 0 & 0 & 0 & 0 & 0 & 0 & 0 & 0 \\
0 & 0 & -9.73 & 0 & 0 & 0 & 0 & 0 & 4.39 & 0 & 0 & 0 \\
0 & 0 & 0 & -4.83 & 0 & 0 & 0 & 0 & -2.40 & 0.394 & 0 & 0 \\
0 & 0 & 0 & 0 & -9.73 & 0 & 0 & 0 & 0 & 0 & 4.39 & 0 \\
0 & 0 & 0 & 0 & 0 & -4.83 & 0 & 0 & 0 & 0 & -2.40 & 0.394 \\
19.26 & 0 & 0 & 0 & 0 & 0 & -18.37 & 0 & 0 & 0 & 0 & 0 \\
0 & 0 & 0 & 0 & 0 & 0 & 0 & -5.27 & 0 & 0 & 0 & 0 \\
0 & 0 & 12.11 & 0 & 0 & 0 & 0 & 0 & -9.39 & 0 & 0 & 0 \\
0 & 0 & 0 & -5.60 & 0 & 0 & 0 & 0 & -3.27 & 0 & 0 & 0 \\
0 & 0 & 0 & 0 & 12.11 & 0 & 0 & 0 & 0 & 0 & -9.39 & 0 \\
0 & 0 & 0 & 0 & 0 & -5.60 & 0 & 0 & 0 & 0 & -3.27 & 0
\end{bmatrix}$$

$$G = \tag{6.9}$$

$$\begin{bmatrix}
7.08 & 0 & 0 & 0 & 0 & 36.12 & 0 & 0 & 0 & 0 \\
0 & 0 & 0 & 0 & 0 & -39.59 & 0 & 0 & 0 & 0 \\
0 & 94.12 & -0.165 & 0 & 0 & 0 & 0 & 0.287 & 0 & 0 \\
0 & 0 & -0.0840 & 0 & 0 & 0 & 0 & -0.254 & 0 & 0 \\
0 & 0 & 0 & -94.12 & -0.165 & 0 & 0 & 0 & 0 & -0.287 \\
0 & 0 & 0 & 0 & -0.0840 & 0 & 0 & 0 & 0 & 0.255 \\
0 & 0 & 0 & 0 & 0 & 44.43 & 0 & 0 & 0 & 0 \\
0 & 0 & 0 & 0 & 0 & -39.59 & 0 & 0 & 0 & 0 \\
0 & -43.13 & 0 & 0 & 0 & 0 & 90.0 & 0.586 & 0 & 0 \\
0 & 0 & 0 & 0 & 0 & 0 & 0 & -0.330 & 0 & 0 \\
0 & 0 & 0 & 43.13 & 0 & 0 & 0 & 0 & -90.0 & -0.586 \\
0 & 0 & 0 & 0 & 0 & 0 & 0 & 0 & 0 & 0.330
\end{bmatrix}$$

F matrix Cramer-Rao Bound % = (6.10)

$$\begin{bmatrix}
36.87 & 0 & 0 & 0 & 0 & 0 & 29.71 & 0 & 0 & 0 & 0 & 0 \\
0 & 16.17 & 0 & 0 & 0 & 0 & 0 & 0 & 0 & 0 & 0 & 0 \\
0 & 0 & 3.72 & 0 & 0 & 0 & 0 & 0 & 4.46 & 0 & 0 & 0 \\
0 & 0 & 0 & 3.99 & 0 & 0 & 0 & 0 & 7.23 & 14.42 & 0 & 0 \\
0 & 0 & 0 & 0 & 3.72 & 0 & 0 & 0 & 0 & 0 & 4.46 & 0 \\
0 & 0 & 0 & 0 & 0 & 3.99 & 0 & 0 & 0 & 0 & 7.23 & 14.42 \\
19.74 & 0 & 0 & 0 & 0 & 0 & 20.44 & 0 & 0 & 0 & 0 & 0 \\
0 & 0 & 0 & 0 & 0 & 0 & 0 & 11.81 & 0 & 0 & 0 & 0 \\
0 & 0 & 7.26 & 0 & 0 & 0 & 0 & 0 & 8.33 & 0 & 0 & 0 \\
0 & 0 & 0 & 7.93 & 0 & 0 & 0 & 0 & 7.44 & 0 & 0 & 0 \\
0 & 0 & 0 & 0 & 7.26 & 0 & 0 & 0 & 0 & 0 & 8.33 & 0 \\
0 & 0 & 0 & 0 & 0 & 7.93 & 0 & 0 & 0 & 0 & 7.44 & 0
\end{bmatrix}$$

G matrix Cramer-Rao Bound % = (6.11)

$$\begin{bmatrix}
15.63 & 0 & 0 & 0 & 0 & 24.63 & 0 & 0 & 0 & 0 \\
0 & 0 & 0 & 0 & 0 & 22.76 & 0 & 0 & 0 & 0 \\
0 & 4.10 & 6.25 & 0 & 0 & 0 & 0 & 8.47 & 0 & 0 \\
0 & 0 & 5.94 & 0 & 0 & 0 & 0 & 9.26 & 0 & 0 \\
0 & 0 & 0 & 4.10 & 6.25 & 0 & 0 & 0 & 0 & 8.47 \\
0 & 0 & 0 & 0 & 5.94 & 0 & 0 & 0 & 0 & 9.26 \\
0 & 0 & 0 & 0 & 0 & 19.62 & 0 & 0 & 0 & 0 \\
0 & 0 & 0 & 0 & 0 & 22.76 & 0 & 0 & 0 & 0 \\
0 & 12.01 & 0 & 0 & 0 & 0 & 5.33 & 6.64 & 0 & 0 \\
0 & 0 & 0 & 0 & 0 & 0 & 0 & 10.33 & 0 & 0 \\
0 & 0 & 0 & 12.01 & 0 & 0 & 0 & 0 & 5.323 & 6.64 \\
0 & 0 & 0 & 0 & 0 & 0 & 0 & 0 & 0 & 10.33
\end{bmatrix}$$

6.5.2 Time Verification

This section contain time domain responses of rotor flapping and inflow components. These are used as verification of the inflow state-space model with the form of Eq.(6.2) and the matrices shown in Eqs. (6.8) and (6.9).

In Fig. 6.8, the swashplate input (not shown in the figure) is a doublet of lateral cyclic stick at the upper rotor θ_{1s}^U of magnitude 1°. The top plot in the figure shows the aerodynamic roll moment coefficients C_L^U and C_L^L for upper and lower rotor, respectively. The second plot shows the corresponding lateral flapping rates $\dot{\beta}_{1s}^U$ and $\dot{\beta}_{1s}^L$. The third plot shows the response of the lateral inflow component λ_{1s}^U for the upper rotor. There are three curves: (i) the response computed using the full nonlinear MFW; (ii) the response computed using the identified state-space inflow model, including the wake distortion effects; and (iii) the same response as (ii) but without the wake distortion effects. The fourth and final plot contains the same

information, but for the lower rotor. The results indicate that neglecting the effects of wake distortion causes the identified model to overpredict the magnitude of the λ_{1s}^U peak, and to anticipate the second peak of both λ_{1s}^U and λ_{1s}^L.

Figure 6.9 has the same general arrangement as Fig. 6.8, except that it shows the responses to the same lateral cyclic doublet, but applied to the *lower* rotor, i.e., θ_{1s}^L. The $\dot{\beta}_{1s}^L$ response is very similar to the $\dot{\beta}_{1s}^U$ of Fig. 6.8, whereas the upper rotor flap rate is very small. The agreement of the MFW and the state-space predictions including wake distortion is nearly perfect for λ_{1s}^U, whereas neglecting wake distortion underpredicts and anticipates the response peaks. The agreement is generally not as good as for λ_{1s}^L, but in this case too including wake distortion effects improves the fit.

Finally, Fig. 6.10 shows the case of a swashplate doublet of both upper and lower rotor collective pitch θ_0 of magnitude 1°. The top plot in the figure shows the corresponding values of the thrust coefficients C_T^U and C_T^L. The lower two plots show the constant portion λ_0 of the inflow for the upper and lower rotor, respectively. Each of these plots shows only two curves, namely, the free wake predictions and those of the identified state-space model. In this essentially symmetric condition, the effects of wake distortion are negligible. For both inflow components, the state-space model matches almost perfectly the free wake results through the two peaks of the response. There is a small discrepancy (about 10% of the total excursion) in the transient following the end of the input, and agreement is again nearly perfect when returned to steady-state.

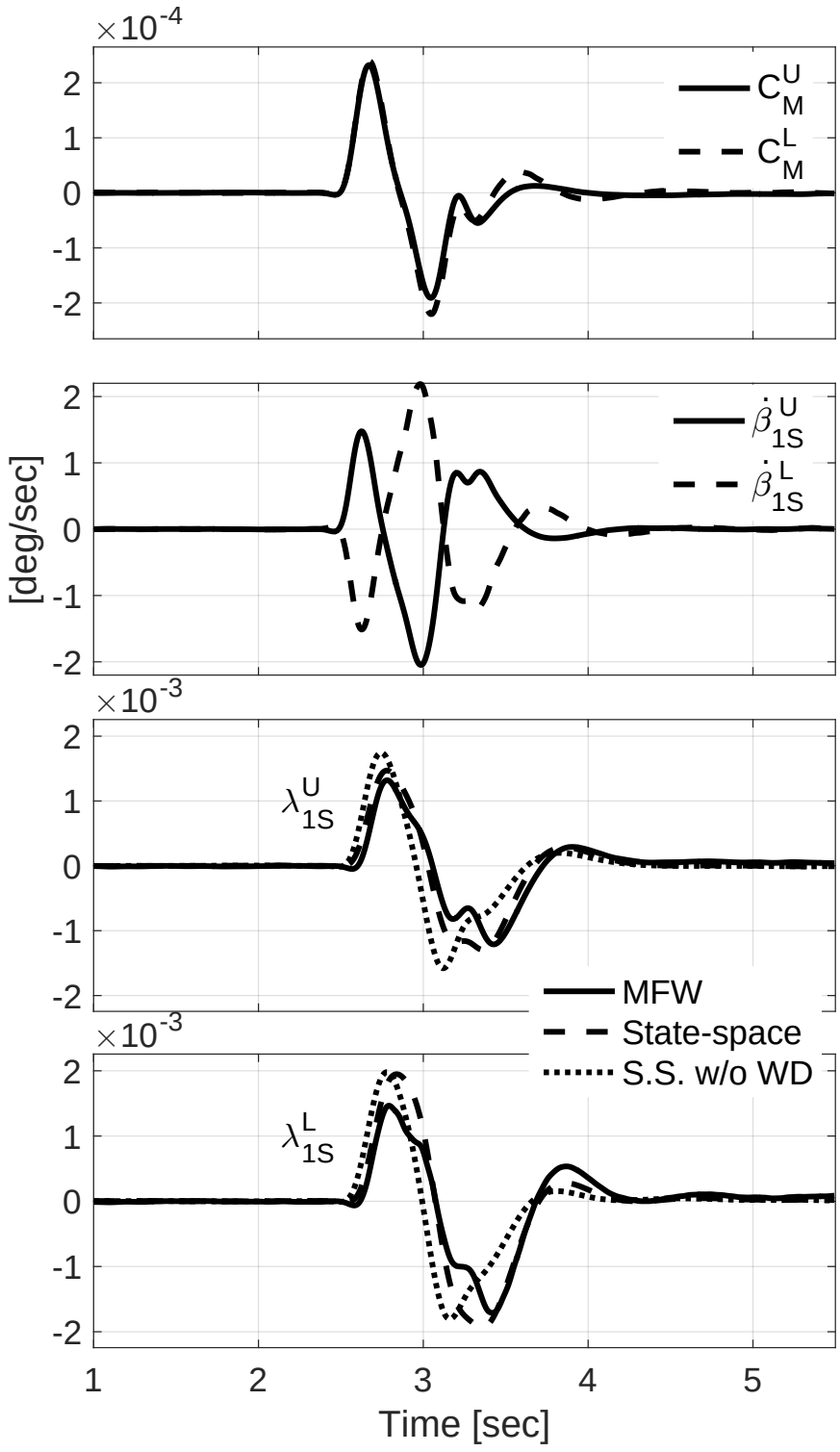

Figure 6.8: Time verification of the lateral inflow λ_{1S} response to roll moment C_L and cyclic flapping $\dot{\beta}_{1S}$ produced by a lateral stick doublet. State-space model with and without wake distortion (WD) shown.

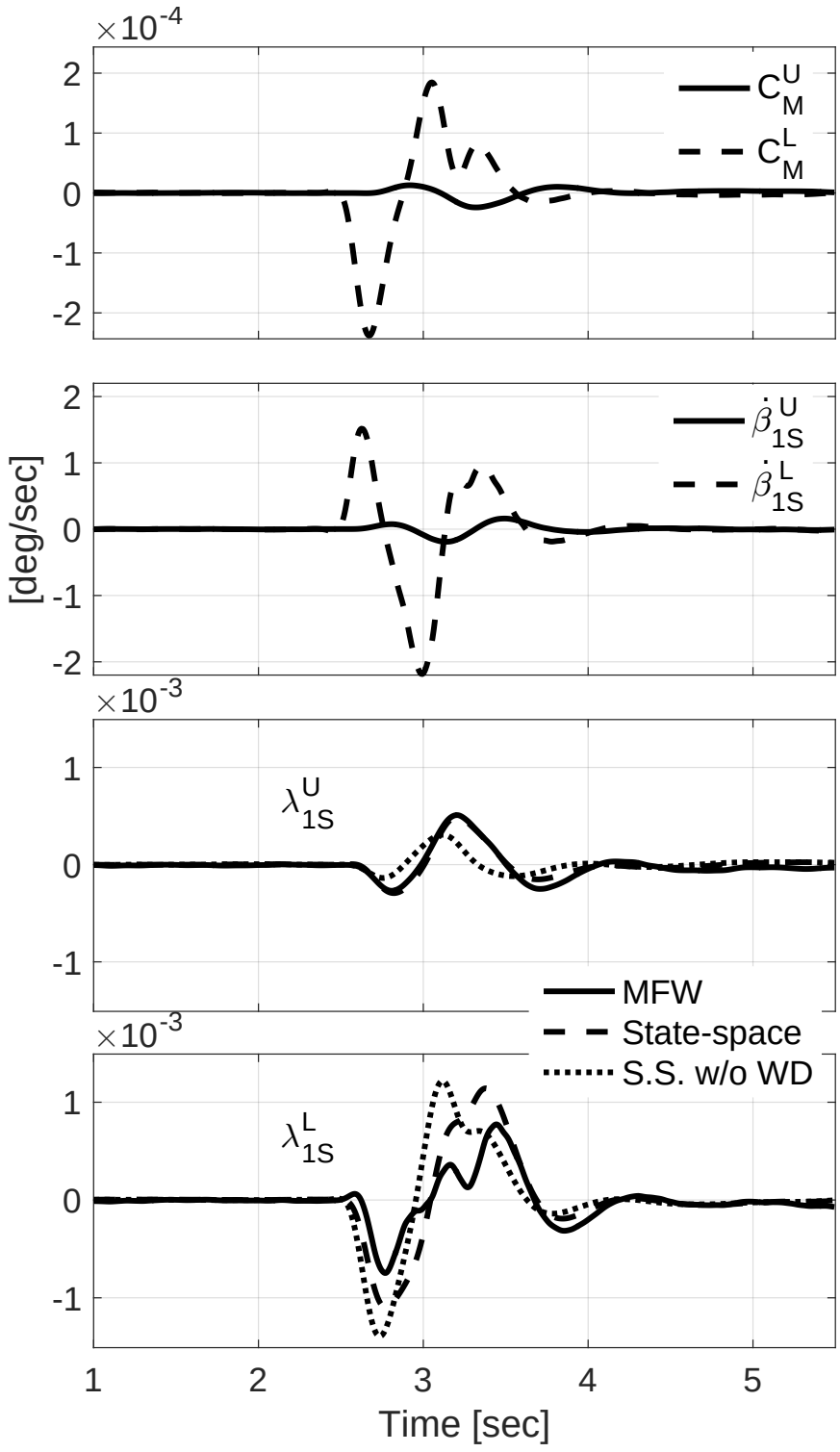

Figure 6.9: Time verification of the lateral inflow λ_{1S} response to roll moment C_L and cyclic flapping $\dot{\beta}_{1S}$ produced by a lower rotor swashplate doublet. State-space model with and without wake distortion (WD) shown.

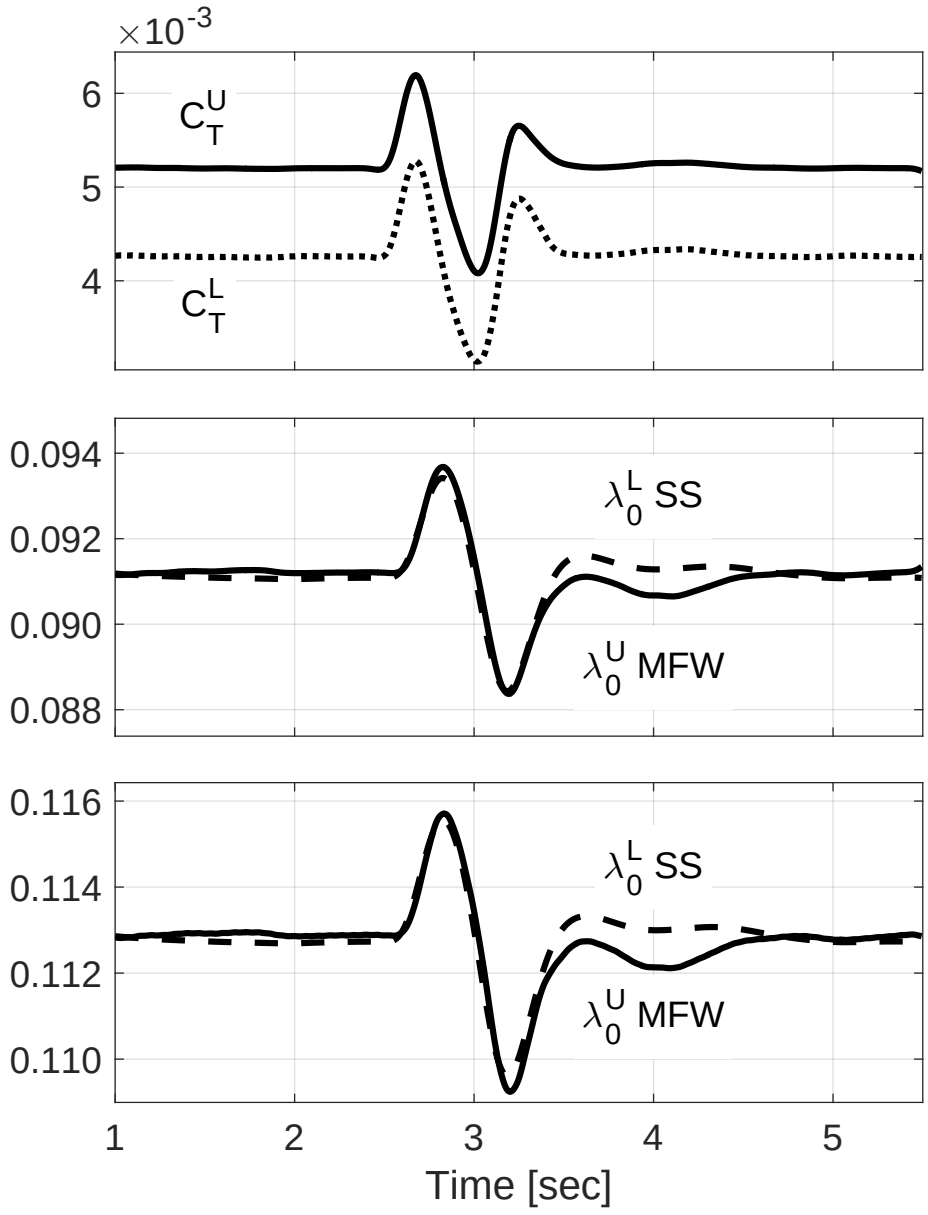

Figure 6.10: Time verification of the average inflow λ_0 response to thrust C_T due to collective doublet on both rotors

6.6 Results for Forward Flight

The coaxial rotor, described in Appendix B, was trimmed at 200 knots, with time averaged trim C_T for the upper and lower rotors of around 0.0073 and 0.0065, respectively. The coaxial rotor was trimmed with enough propeller thrust to meet a trim target angle of attack of $\alpha = 2°$. Frequency responses were then generated through frequency sweeps.

6.6.1 Frequency Responses

This section presents an extensive set of frequency responses for various combinations of aerodynamic loading inputs and inflow component outputs. In all figures, solid lines indicate the frequency responses obtained with the full, nonlinear MFW, the dashed lines those obtained with the identified state-space model. The specific combinations and the corresponding figures are listed here in tabular form:

Table 6.2: Table of figures for the different responses of inflow components to aerodynamic loading

		Outputs		
		λ_0^U, λ_0^L	λ_{1S}^U, λ_{1S}^L	λ_{1C}^U, λ_{1C}^L
Inputs	C_T^U	6.11	6.12	6.13
	C_T^L	6.14	6.15	6.16
	C_L^U	6.17	6.18	6.19
	C_L^L	6.20	6.21	6.22
	C_M^U	6.23	6.24	6.25
	C_M^L	6.26	6.27	6.28

The first observation is that for all the frequency responses, the coherence is relatively high. All are above .75 at all frequencies, which is well within the guidelines of acceptable coherence of [63], indicating that the inflow dynamics are well represented by a linear system.

The next very interesting observation that can be made is that, in general, a rotor aerodynamic loading perturbation has a larger effect on the inflow of that same rotor than on the the inflow of the other rotor. This is shown in the upper rotor aerodynamic loading responses (Figs. 6.11-6.13,6.17-6.19, and 6.23-6.25) by the magnitude curve for the upper rotor inflow coefficient always lying above the lower rotor inflow coefficient. Similarly, for the lower rotor aerodynamic loading responses (Figs. 6.14-6.16,6.20-6.22, and 6.26-6.28), the magnitude curve for the lower rotor inflow coefficient is generally below the lower rotor inflow coefficient. The gap between the magnitude of the responses varies in magnitude for each response, and within each response with frequency. At the low frequency, the difference is typically between 3.5 and 18 dB, which corresponds to the off-rotor responses being somewhere between 12 and 67 % of the magnitude of the response of the on-rotor inflow response. For example, Fig. 6.11 shows the average inflow response of λ_0 on both rotors to a perturbation of upper rotor thrust C_T^U. The upper rotor average inflow λ_0^U response magnitude is about 8.5 dB above that of the lower rotor inflow, or about a factor of 2.7. This means that when the thrust changes on the upper rotor, the average inflow on the upper rotor changes, but also the lower rotor average inflow changes about 38% as much. This is still a significant coupling between the two rotors, and should not be ignored when modeling inflow dynamics.

This general observation is also not always true. For example, Fig. 6.19, which shows the response of average inflow on both rotors to lower rotor roll moment C_L^L, looks different at some frequencies. At frequencies above 3 rad/sec, the on-rotor response (λ_0^L response to C_L^L) is larger in magnitude than the off-rotor response (λ_0^U response to C_L^L). But below 3 rad/sec, this is flipped, indicating that slow perturbations of lower rotor roll moment C_L^L have larger off-rotor effects than on-rotor effects when it comes to average inflow λ_0.

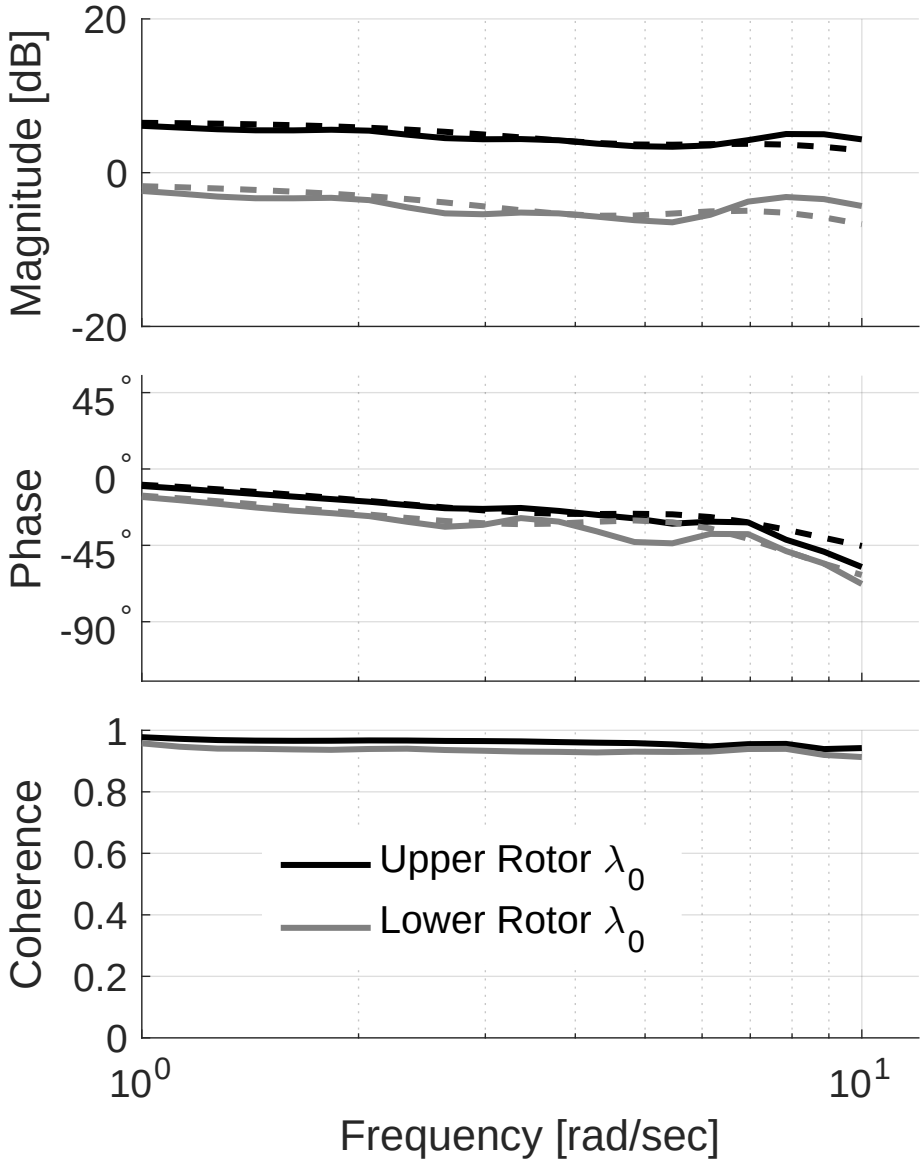

Figure 6.11: Inflow response of λ_0 on both rotors to upper rotor thrust C_T^U; Solid line, MFW, dashed line, state-space model.

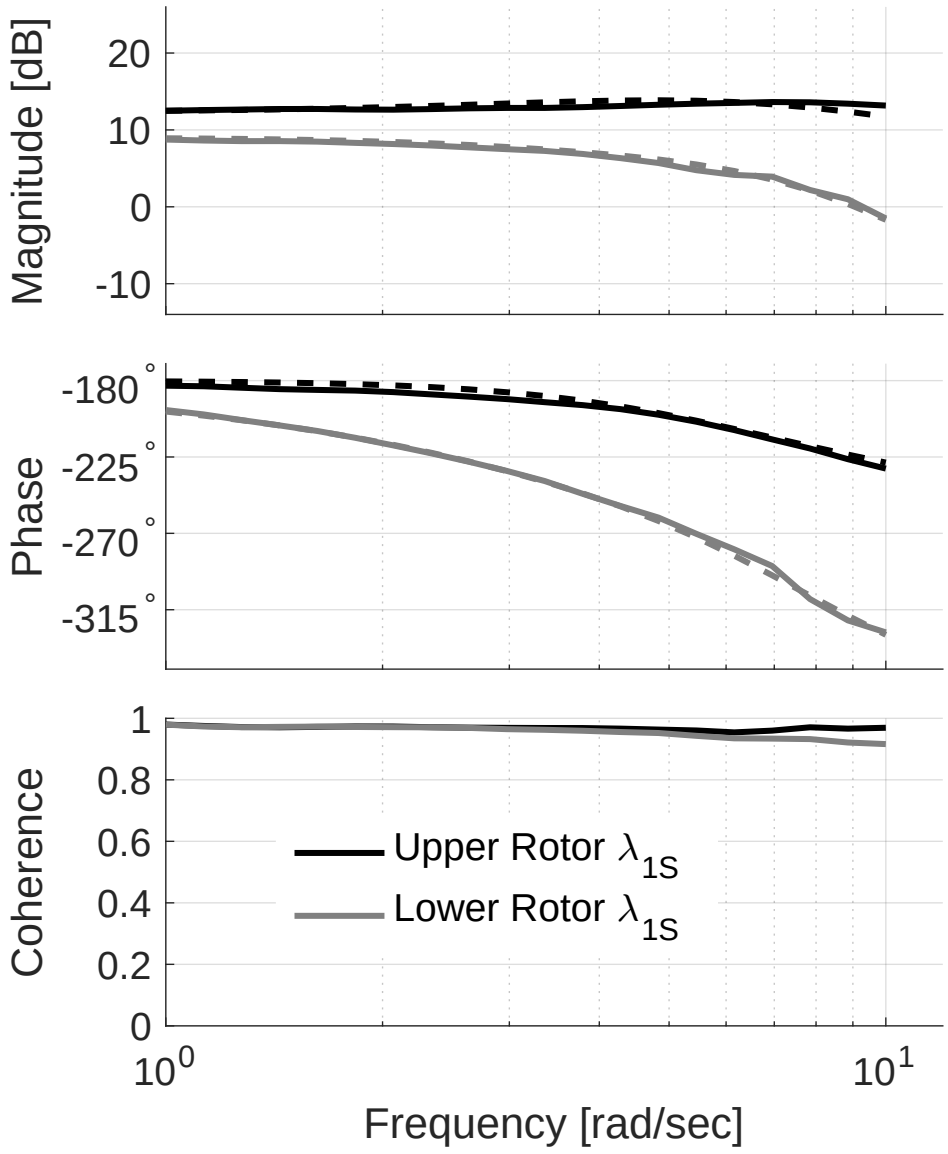

Figure 6.12: Inflow response of λ_{1S} on both rotors to upper rotor thrust C_T^U; Solid line, MFW, dashed line, state-space model.

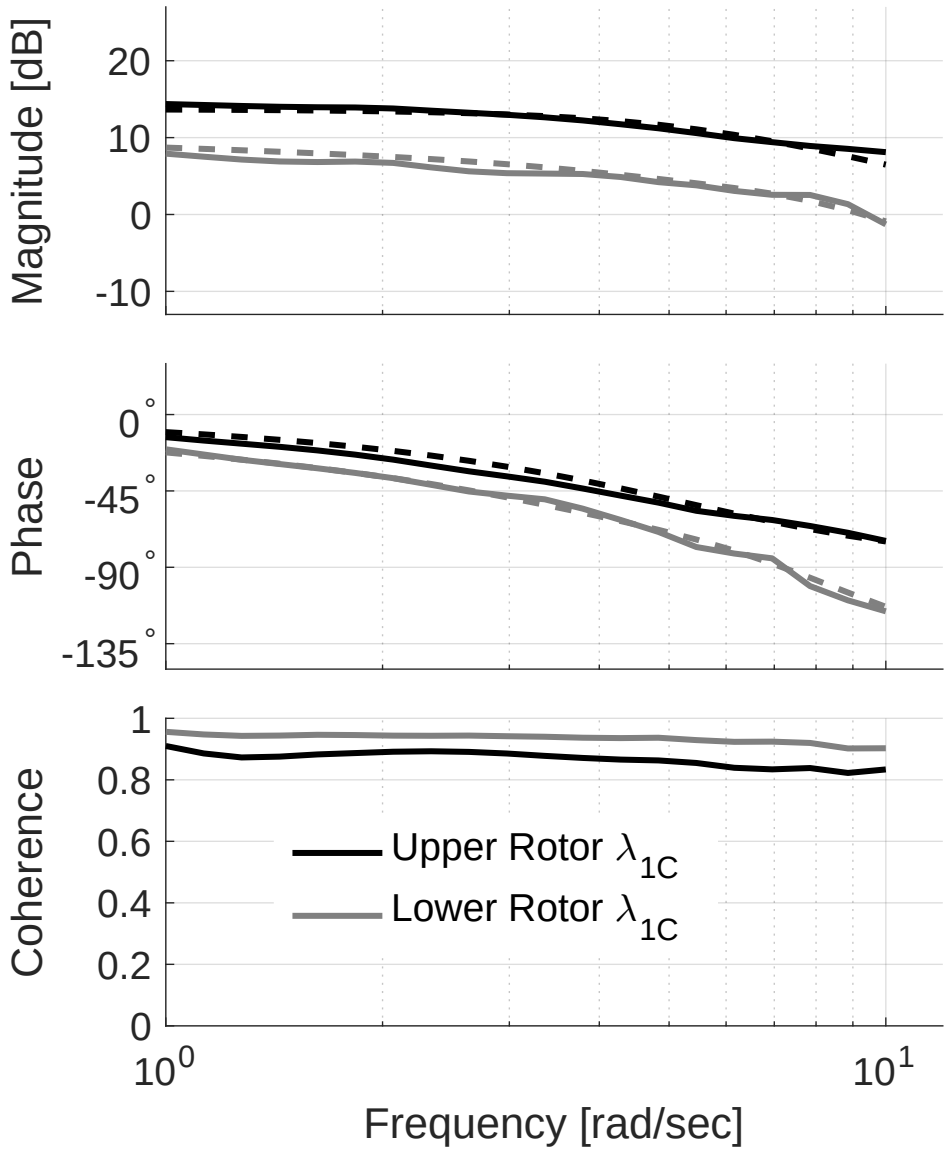

Figure 6.13: Inflow response of λ_{1C} on both rotors to upper rotor thrust C_T^U; Solid line, MFW, dashed line, state-space model.

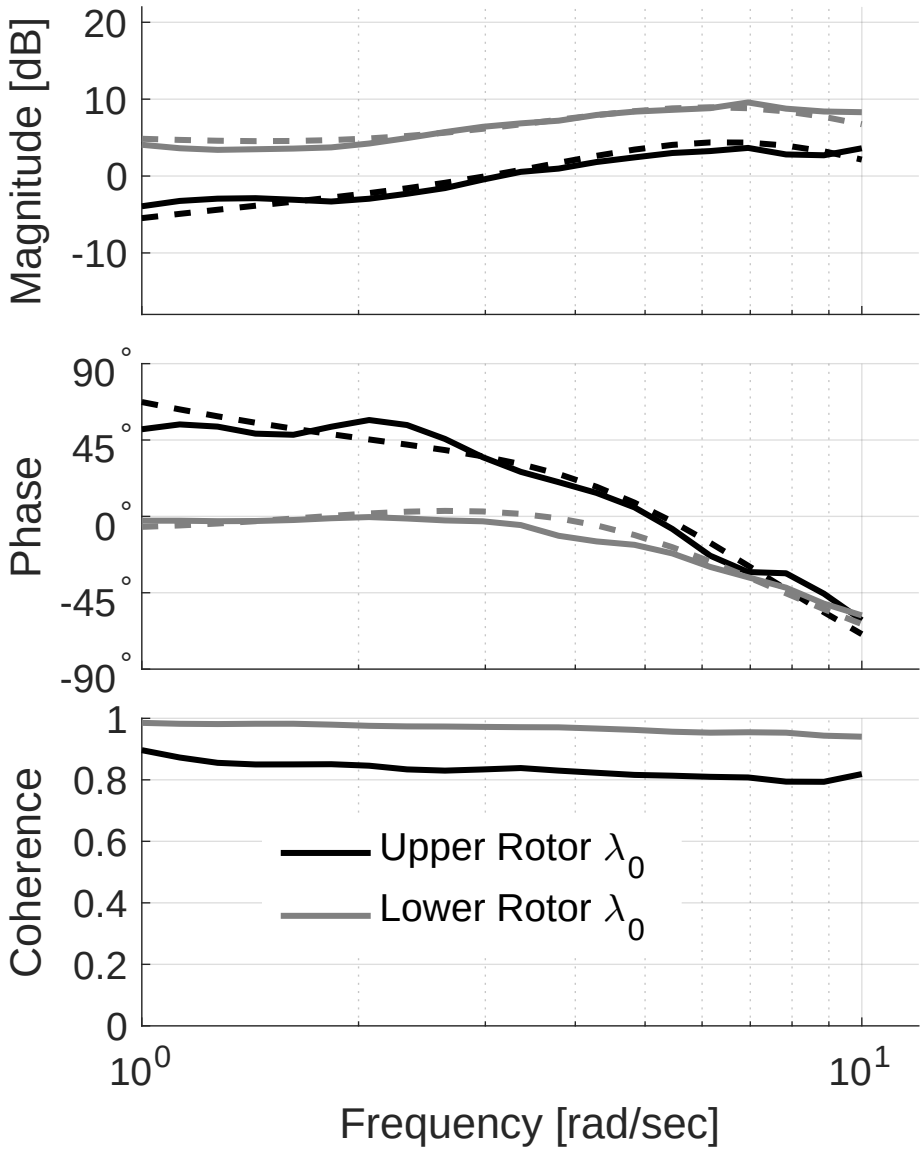

Figure 6.14: Inflow response of λ_0 on both rotors to lower rotor thrust C_T^L; Solid line, MFW, dashed line, state-space model.

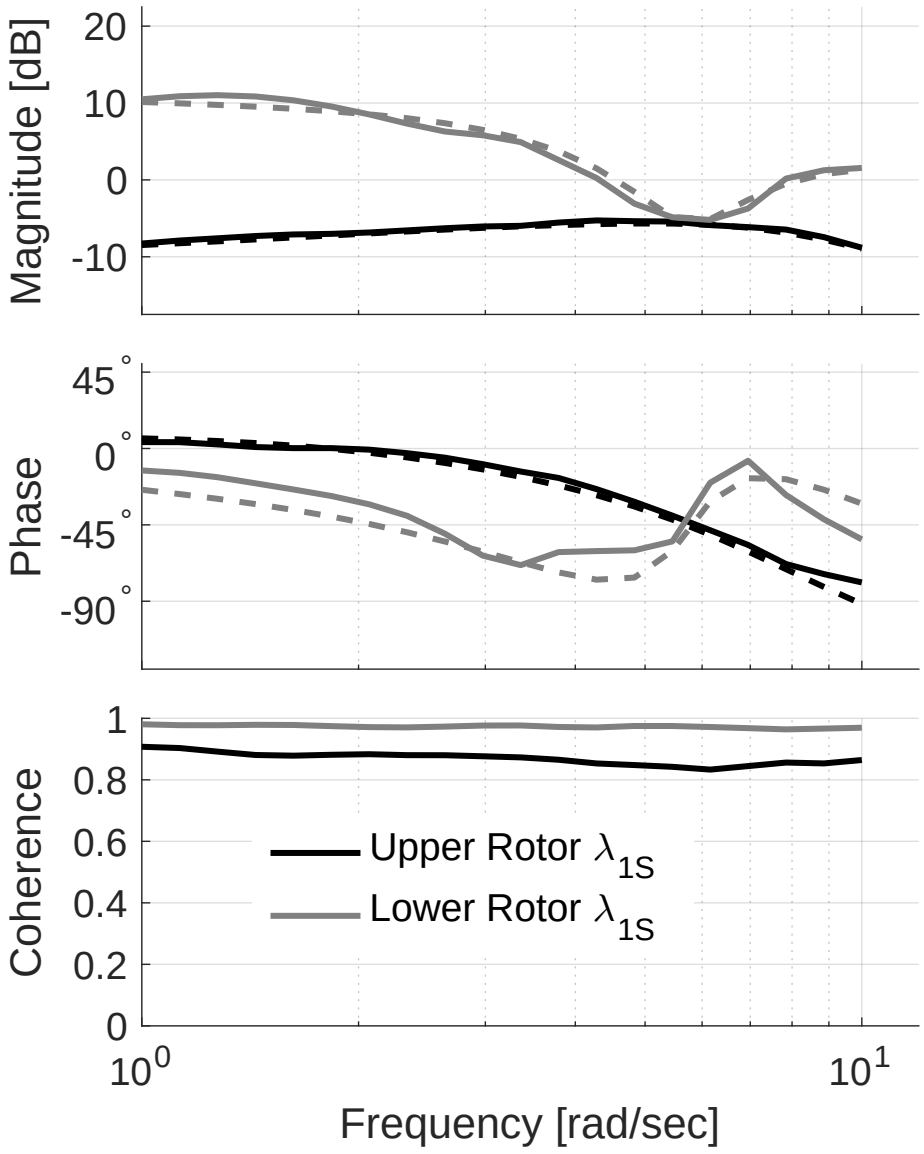

Figure 6.15: Inflow response of λ_{1S} on both rotors to lower rotor thrust C_T^L; Solid line, MFW, dashed line, state-space model.

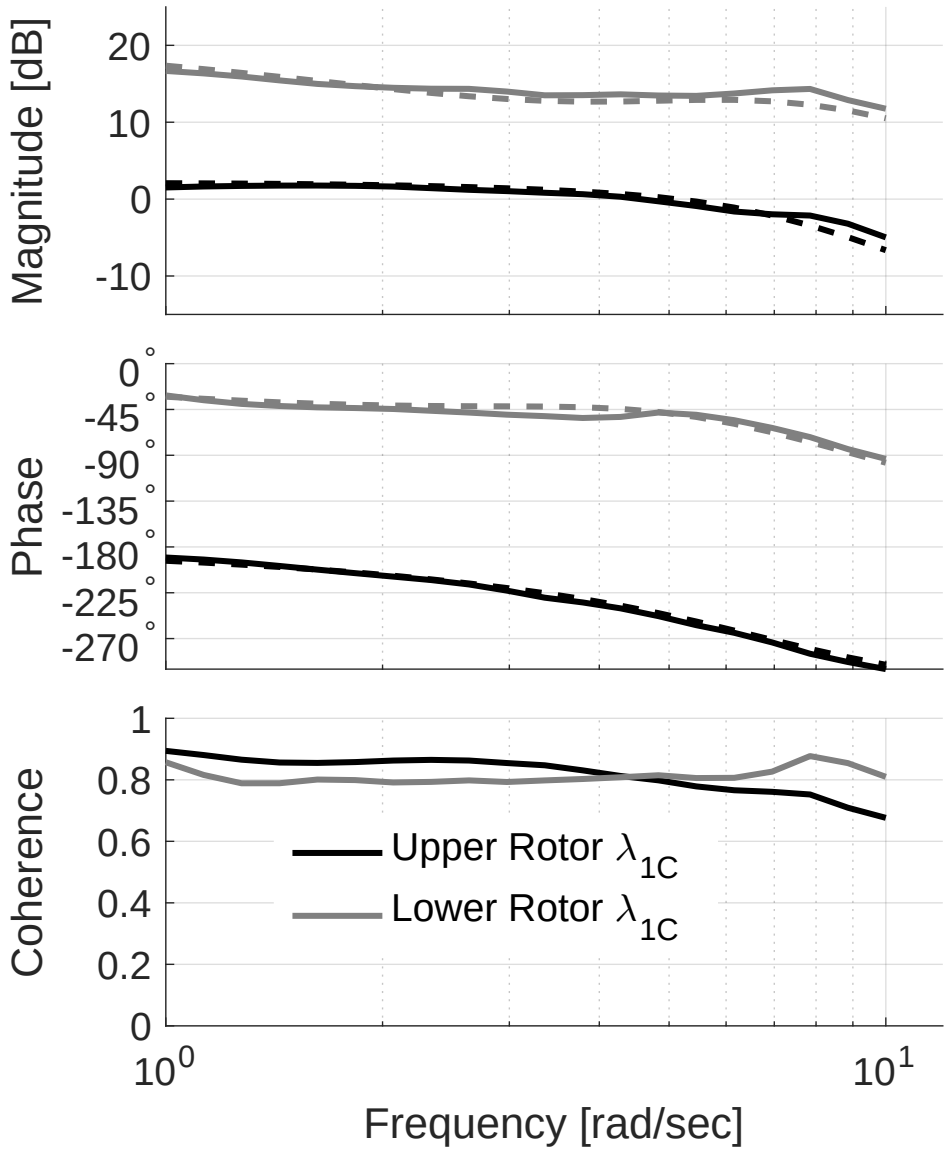

Figure 6.16: Inflow response of λ_{1C} on both rotors to lower rotor thrust C_T^L; Solid line, MFW, dashed line, state-space model.

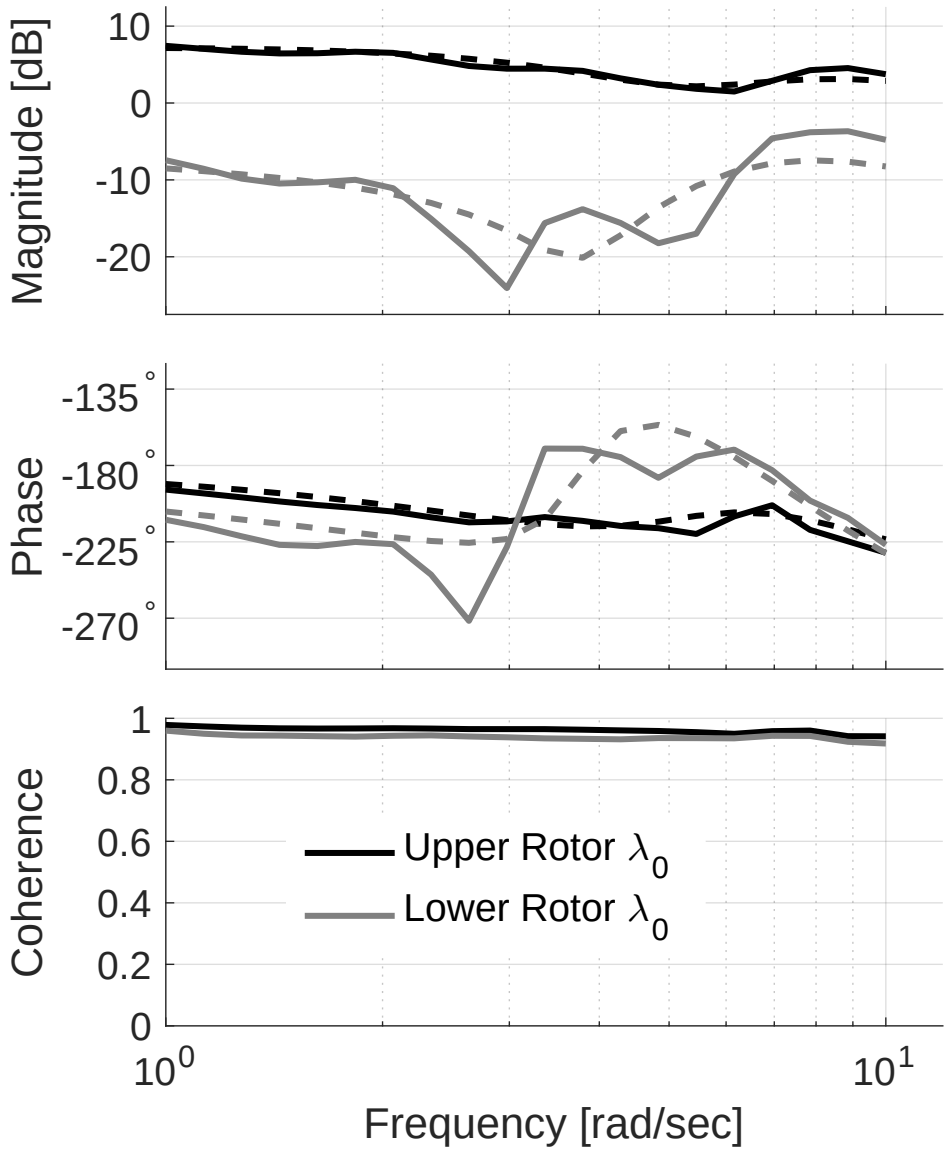

Figure 6.17: Inflow response of λ_0 on both rotors to upper rotor roll moment C_L^U; Solid line, MFW, dashed line, state-space model.

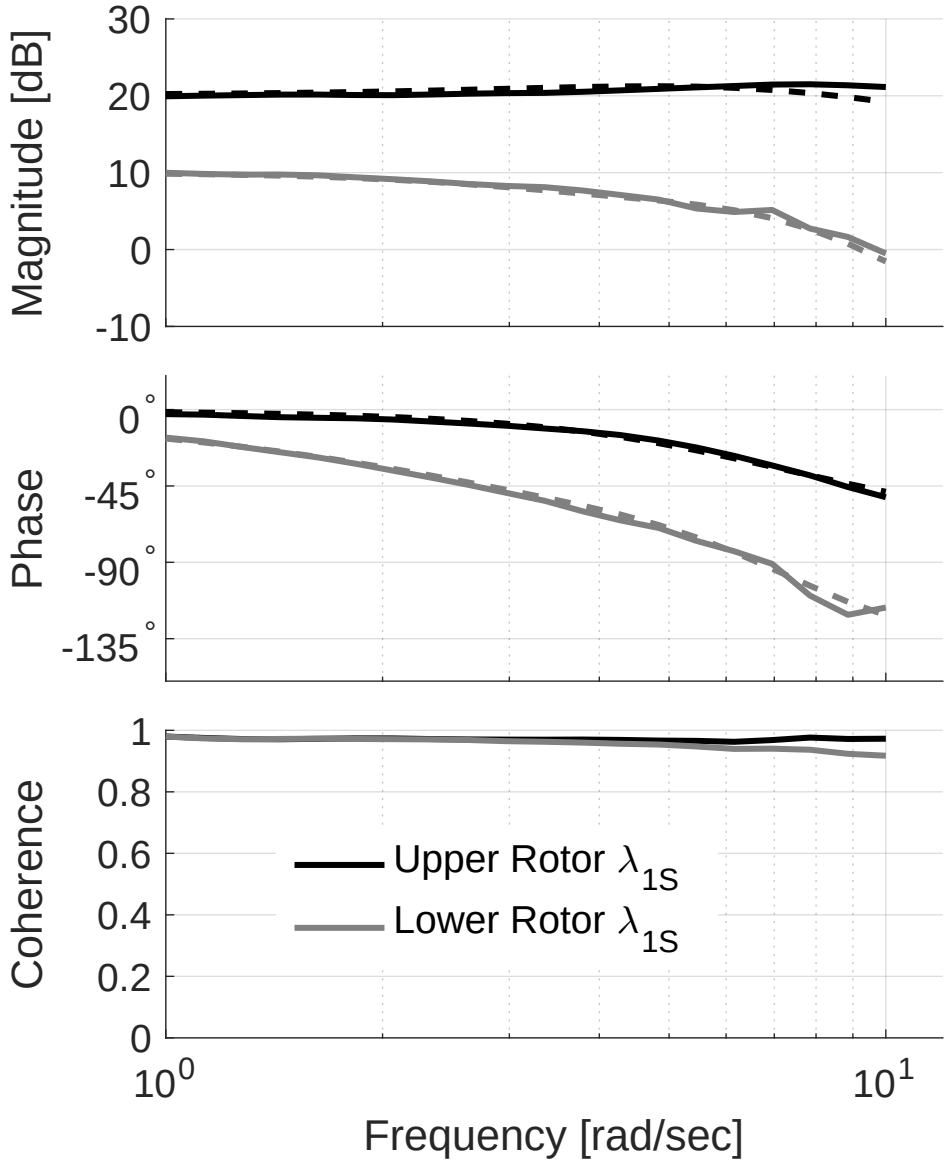

Figure 6.18: Inflow response of λ_{1S} on both rotors to upper rotor roll moment C_L^U; Solid line, MFW, dashed line, state-space model.

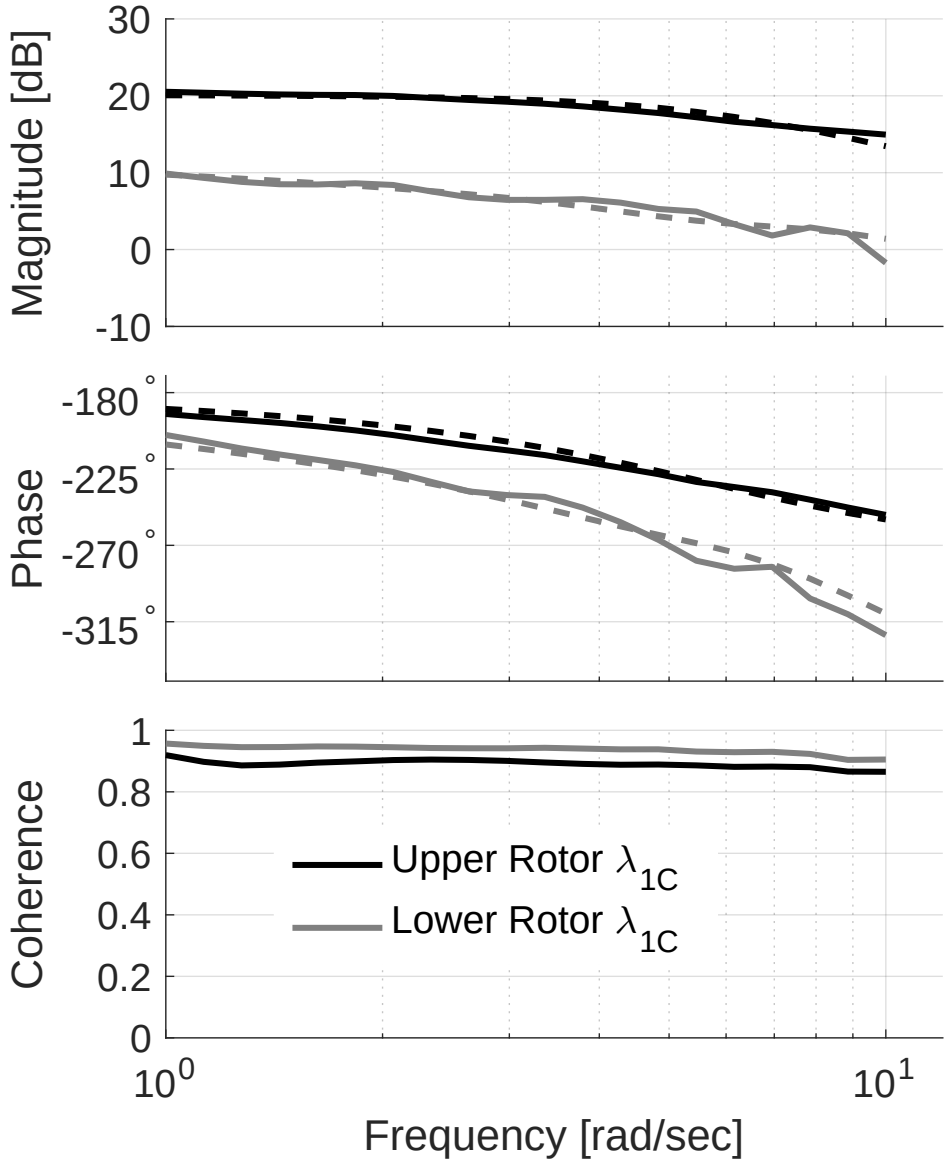

Figure 6.19: Inflow response of λ_{1C} on both rotors to upper rotor roll moment C_L^U; Solid line, MFW, dashed line, state-space model.

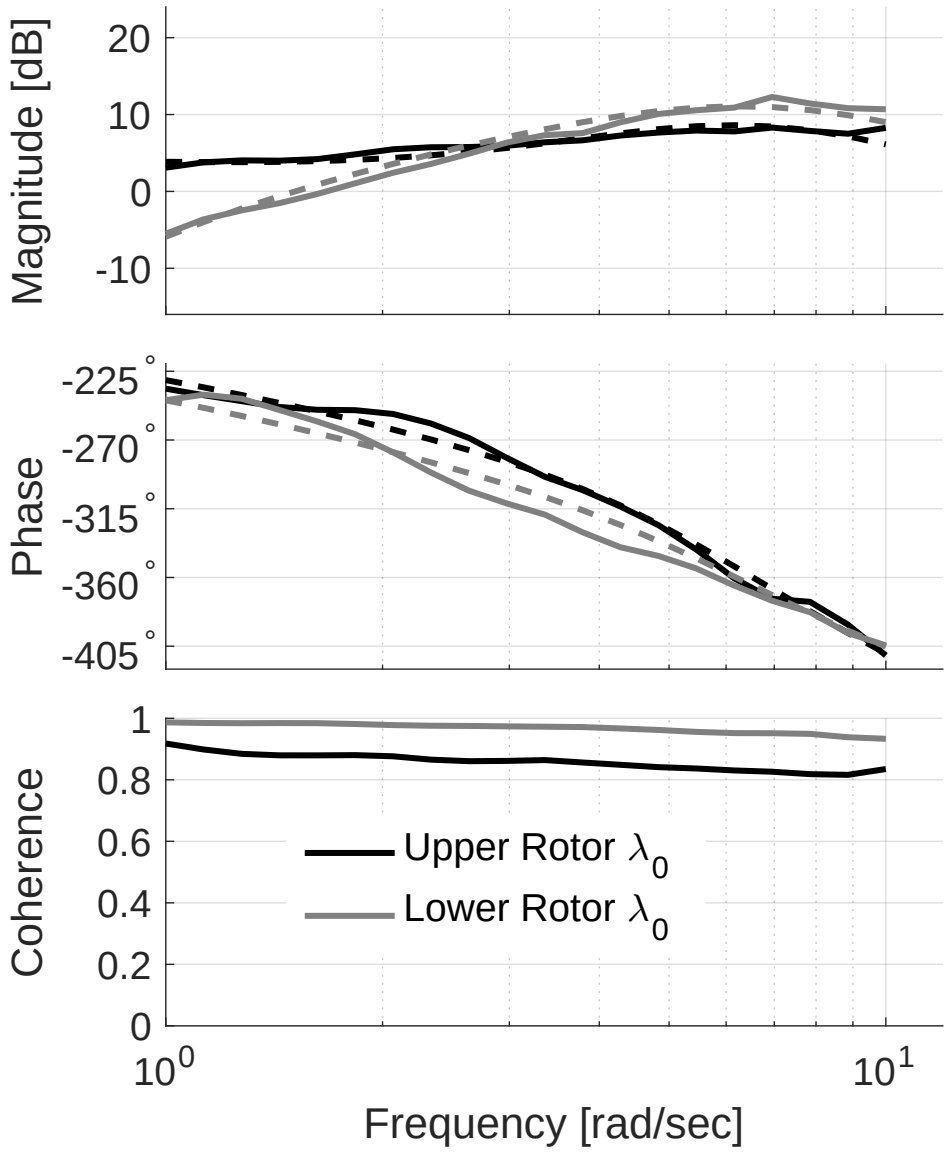

Figure 6.20: Inflow response of λ_0 on both rotors to lower rotor roll moment C_L^L; Solid line, MFW, dashed line, state-space model.

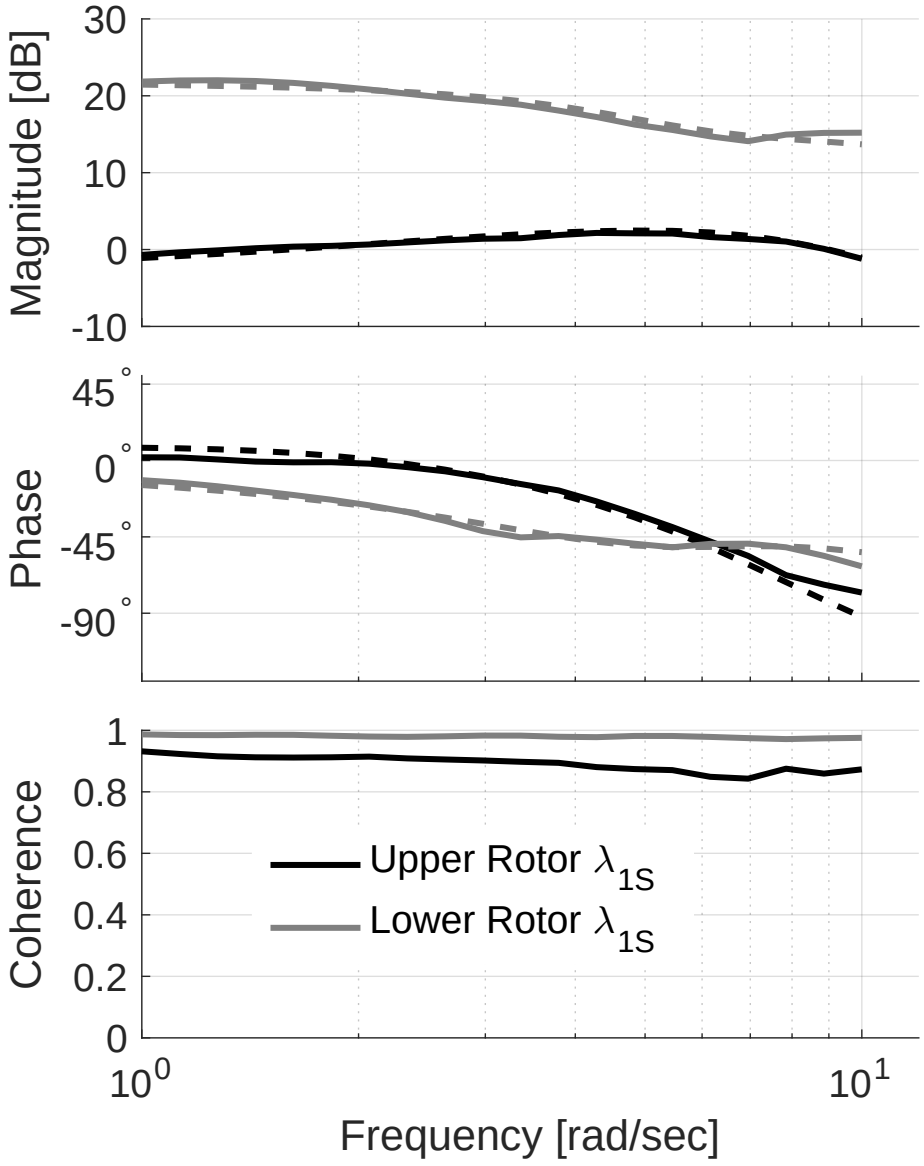

Figure 6.21: Inflow response of λ_{1S} on both rotors to lower rotor roll moment C_L^L; Solid line, MFW, dashed line, state-space model.

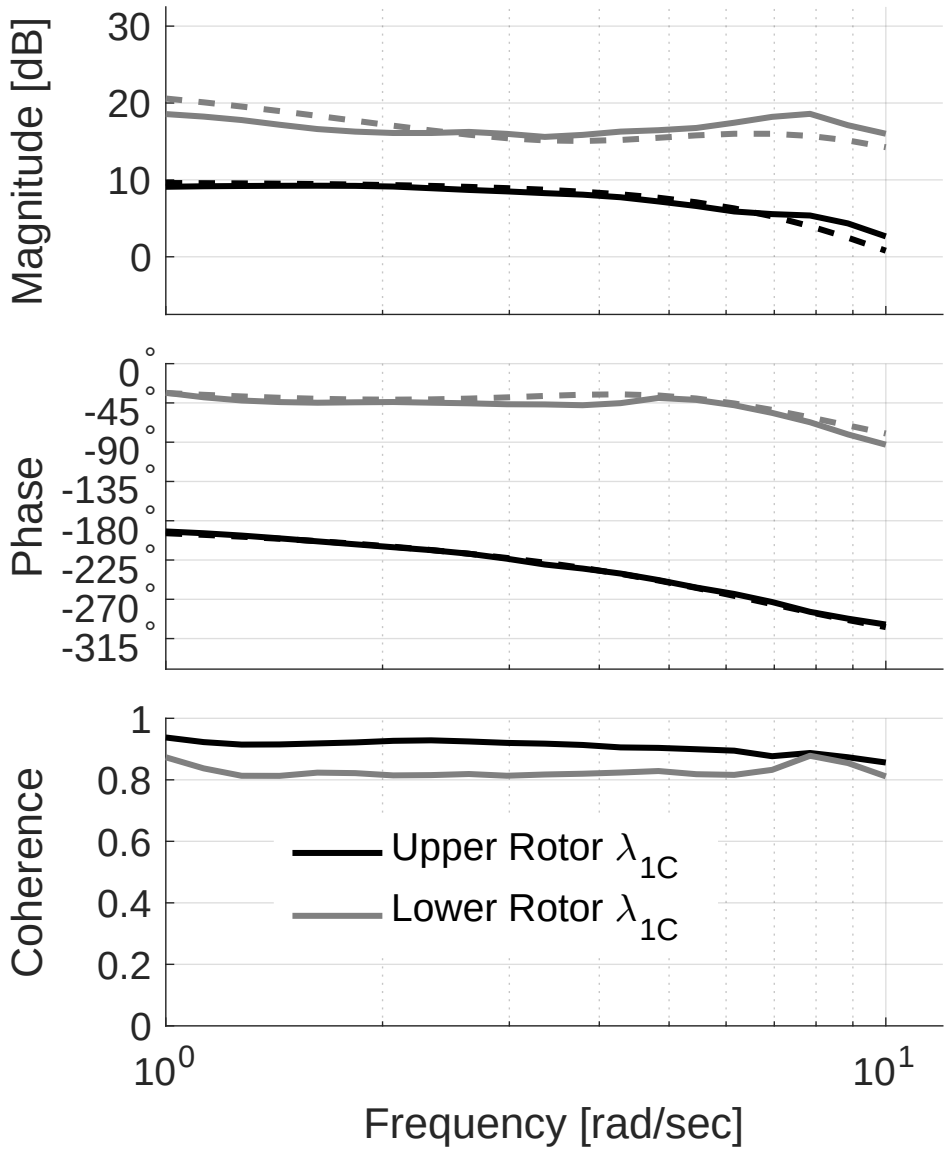

Figure 6.22: Inflow response of λ_{1C} on both rotors to lower rotor roll moment C_L^L; Solid line, MFW, dashed line, state-space model.

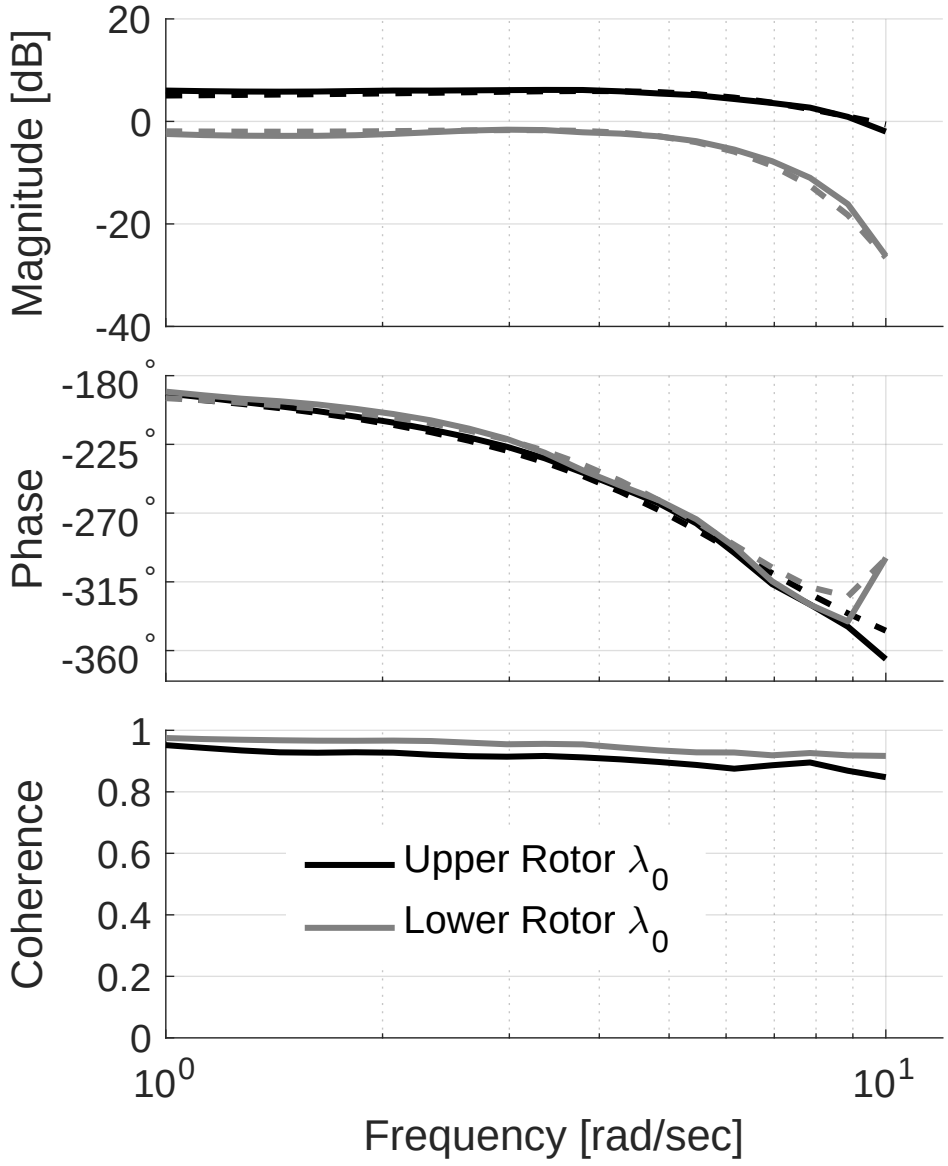

Figure 6.23: Inflow response of λ_0 on both rotors to upper rotor pitching moment C_M^U; Solid line, MFW, dashed line, state-space model.

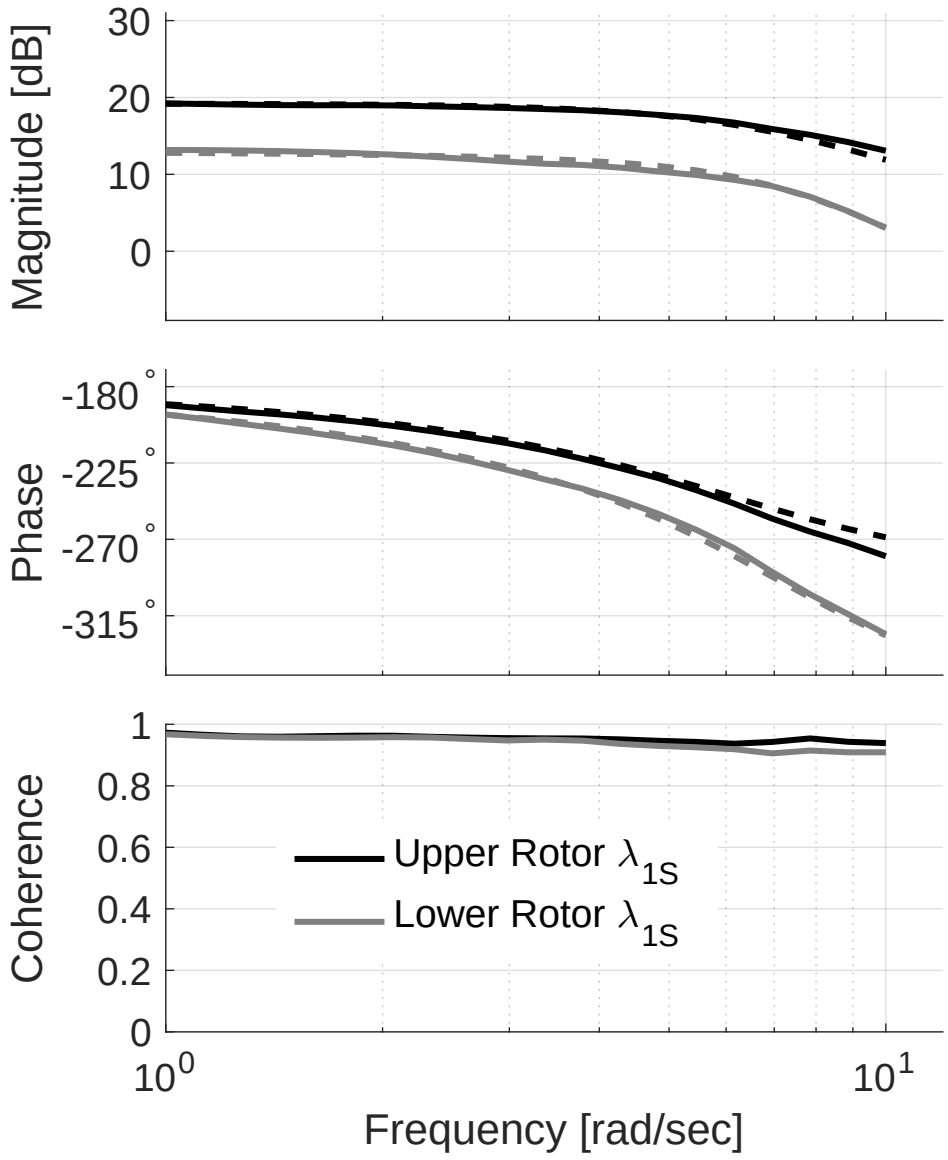

Figure 6.24: Inflow response of λ_{1S} on both rotors to upper rotor pitching moment C_M^U; Solid line, MFW, dashed line, state-space model.

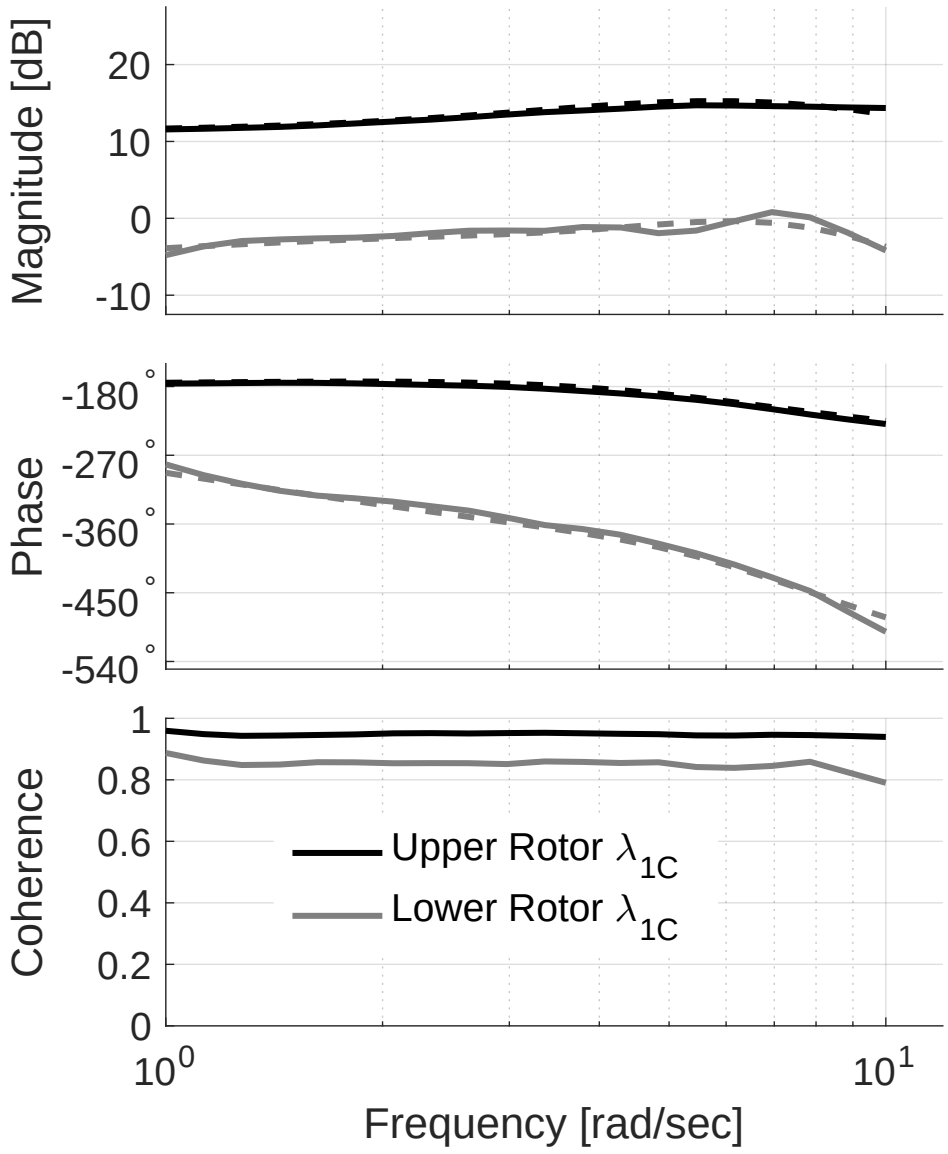

Figure 6.25: Inflow response of λ_{1C} on both rotors to upper rotor pitching moment C_M^U; Solid line, MFW, dashed line, state-space model.

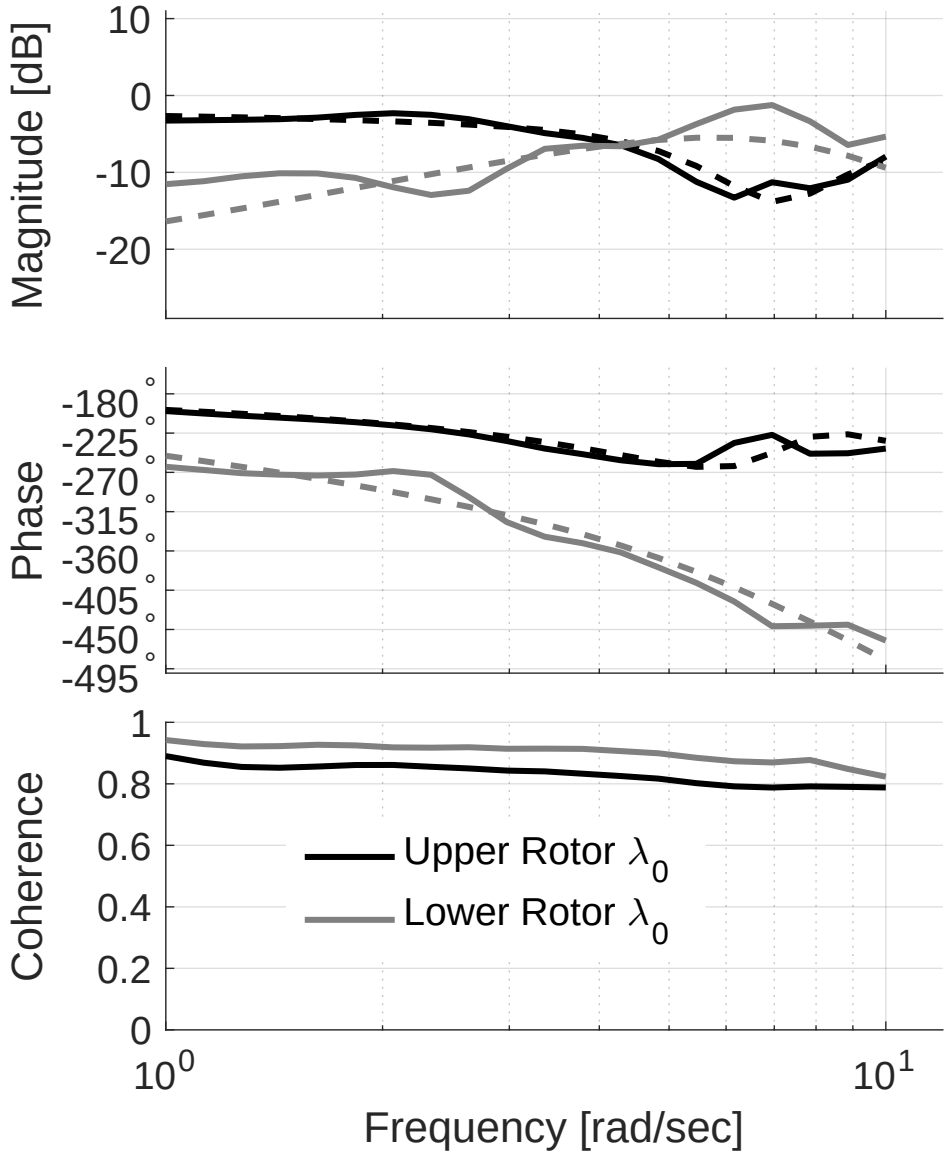

Figure 6.26: Inflow response of λ_0 on both rotors to lower rotor pitching moment C_M^L; Solid line, MFW, dashed line, state-space model.

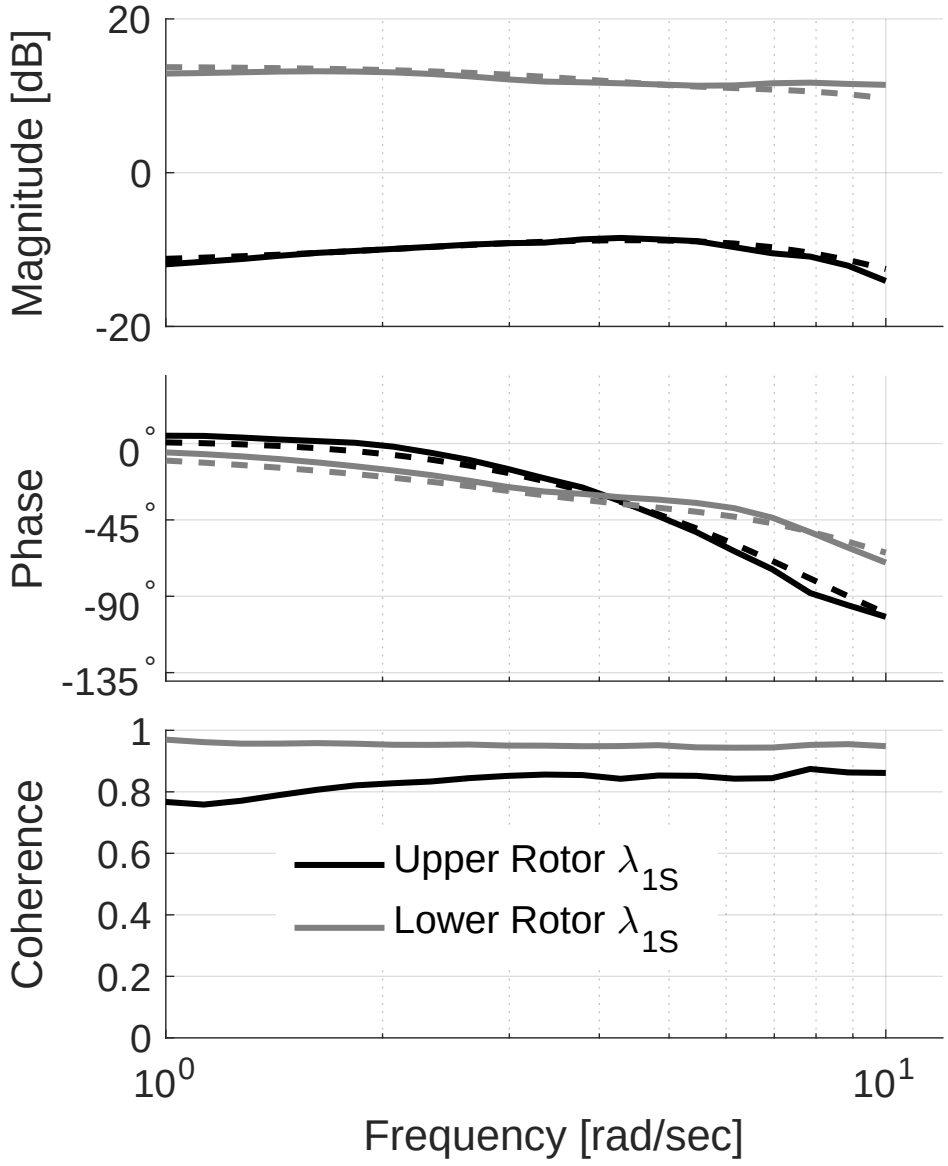

Figure 6.27: Inflow response of λ_{1S} on both rotors to lower rotor pitching moment C_M^L; Solid line, MFW, dashed line, state-space model.

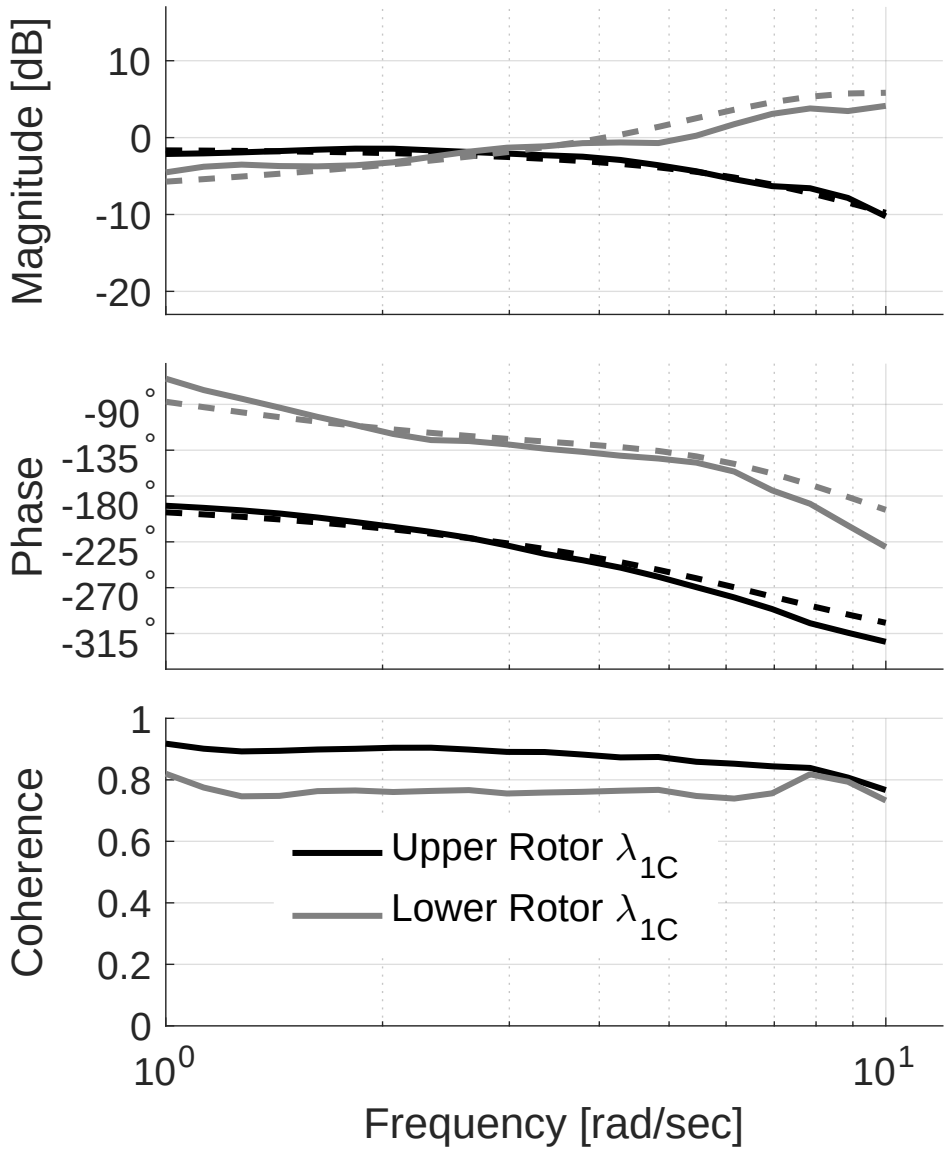

Figure 6.28: Inflow response of λ_{1C} on both rotors to lower rotor pitching moment C_M^L; Solid line, MFW, dashed line, state-space model.

The costs of the fits to each of the 36 frequency responses are grouped in Table 6.6.1. All of the costs are low except the lower rotor average inflow response λ_0^L to upper rotor roll moment C_L^U and to lower rotor pitching moment C_M^L. However, these are very small responses, and are only included in the best fit optimization for the purpose of keeping the same responses from the state-space model also low in magnitude. The high cost, i.e. the inaccuracy of the fit, is not particularly important because amplitude are very low.

Table 6.3: Cost of parameterizations of the frequency responses for the 12 state model in forward flight; each row corresponds to an output and each column corresponds to an input.

✕	C_T^U	C_L^U	C_M^U	C_T^L	C_L^L	C_M^L
λ_0^U	15.6	15.3	14.1	32.2	17.1	44.8
λ_{1S}^U	9.5	11.1	8.3	6.5	10.3	8.7
λ_{1C}^U	10.2	9.6	6.1	8.8	10.1	25.6
λ_0^L	32.4	337.4	20.1	17.7	42.0	217.2
λ_{1S}^L	3.4	6.2	4.3	64.4	12.0	15.6
λ_{1C}^L	14.8	27.9	20.2	20.4	49.2	79.4

Average Cost	77.0

The model follows the form shown in Eq.(6.5), with the identification giving the numerical value of the matrices shown in Eqs.(6.12) and (6.13).

$$F = \begin{bmatrix} F_{UU} & F_{UL} \\ F_{LU} & F_{LL} \end{bmatrix} \tag{6.12}$$

where:

$$F_{UU} = \begin{bmatrix} -4.85 & 0 & 0.95 & 0 & 0.99 & 0 \\ 0 & 2.76 & 0 & 1756.4 & -0.91 & 0 \\ -0.41 & 0 & -5.26 & 0 & 5.31 & 0 \\ -0.054 & -0.11 & 0 & -59.32 & 0.036 & -4.71 \\ 0 & 0 & -2.56 & 0 & -6.39 & 0 \\ 0 & 0.32 & 0 & 243.79 & -0.12 & 15.64 \end{bmatrix}$$

$$F_{UL} = \begin{bmatrix} 0 & 0 & 0.69 & 0 & -2.06 & 0 \\ 3.68 & -82.89 & 1.12 & -3.15 & 0 & 31.53 \\ 2.95 & 0 & 1.17 & 0 & 0.64 & 0 \\ 0 & 2.46 & 0 & 0.081 & 0 & -1.00 \\ -3.03 & 0 & -1.23 & 0 & -0.31 & 0 \\ 0.46 & -10.44 & 0 & -0.40 & 0 & 4.19 \end{bmatrix}$$

$$F_{LU} = \begin{bmatrix} 1.75 & 0 & 0 & 0 & 0 & 0 \\ 0 & -2.45 & 0 & 0 & 0 & -148.75 \\ -7.75 & 0 & 3.08 & 0 & 1.88 & 0 \\ 14.72 & 194.98 & 0 & 0 & -2.96 & -1072.7 \\ 0 & 0 & -1.79 & 0 & 0 & 0 \\ 2.34 & 0 & 0 & 0 & -0.63 & -425.11 \end{bmatrix}$$

$$F_{LL} = \begin{bmatrix} -5.80 & 0 & 0 & 0 & -1.65 & 0 \\ 0 & 0 & 2.01 & 0 & -0.057 & 0 \\ 0 & 0 & -5.30 & 0 & 0 & 0 \\ 0 & -315.92 & 0 & -12.19 & 0 & 59.07 \\ 10.44 & 0 & 1.55 & 0 & -3.08 & 0 \\ -3.47 & 0 & 5.84 & 0 & 0 & 0 \end{bmatrix}$$

$$G = \begin{bmatrix} 17.13 & -14.09 & 6.13 & 4.99 & 5.99 & -2.26 \\ 0 & 0 & 0 & -1.82 & 0 & 16.80 \\ -45.82 & 107.77 & -22.32 & 0 & 0 & 0 \\ 0 & 0 & 0 & 0 & 0 & -0.55 \\ 18.65 & -39.79 & -54.23 & 0 & 0 & 0 \\ 0 & 0 & 0 & -0.41 & 0 & 2.28 \\ 3.72 & 0 & -2.48 & 13.24 & 17.86 & 7.13 \\ 0 & 0 & 0 & 0 & 0 & 0 \\ 0 & -28.97 & 0 & 11.26 & 59.26 & 6.82 \\ 0 & 33.85 & 0 & 0 & 0 & 0 \\ 0 & 12.22 & 0 & 0 & 11.91 & 0 \\ 0 & 0 & -1.88 & 0 & 0 & 0 \end{bmatrix} \tag{6.13}$$

The percentages listed in the matrices of Eqs.(6.14) and (6.15) correspond to the Cramer-Rao Bound percentages for the parameter of the identified model in the same row and column in Eqs.(6.12) and (6.13).

$$\begin{matrix} F \text{ matrix} \\ \text{Cramer-Rao} \\ \text{Bound \%} \end{matrix} = \begin{bmatrix} F_{UU}^{CR} & F_{UL}^{CR} \\ F_{LU}^{CR} & F_{LL}^{CR} \end{bmatrix} \tag{6.14}$$

where:

$$F_{UU}^{CR} = \begin{bmatrix} 9.9 & 0 & 16.6 & 0 & 16.9 & 0 \\ 0 & 16.3 & 0 & 9.0 & 17.2 & 0 \\ 29.6 & 0 & 5.9 & 0 & 6.3 & 0 \\ 10.1 & 14.3 & 0 & 7.7 & 15.3 & 12.1 \\ 0 & 0 & 11.1 & 0 & 4.9 & 0 \\ 0 & 16.5 & 0 & 8.9 & 17.0 & 8.9 \end{bmatrix}$$

$$F_{UL}^{CR} = \begin{bmatrix} 0 & 0 & 31.0 & 0 & 14.1 & 0 \\ 17.8 & 6.0 & 16.7 & 7.7 & 0 & 2.3 \\ 9.2 & 0 & 12.4 & 0 & 25.4 & 0 \\ 0 & 8.9 & 0 & 10.6 & 0 & 8.4 \\ 9.2 & 0 & 11.8 & 0 & 45.1 & 0 \\ 13.7 & 6.3 & 0 & 8.5 & 0 & 3.0 \end{bmatrix}$$

$$F_{LU}^{CR} = \begin{bmatrix} 12.6 & 0 & 0 & 0 & 0 & 0 \\ 0 & 11.8 & 0 & 0 & 0 & 8.8 \\ 11.1 & 0 & 10.8 & 0 & 17.1 & 0 \\ 11.2 & 8.2 & 0 & 0 & 16.8 & 10.7 \\ 0 & 0 & 6.8 & 0 & 0 & 0 \\ 9.4 & 0 & 0 & 0 & 19.5 & 8.6 \end{bmatrix}$$

$$F_{LL}^{CR} = \begin{bmatrix} 7.7 & 0 & 0 & 0 & 13.4 & 0 \\ 0 & 0 & 10.7 & 0 & 17.2 & 0 \\ 0 & 0 & 8.1 & 0 & 0 & 0 \\ 0 & 9.4 & 0 & 9.1 & 0 & 12.7 \\ 8.9 & 0 & 18.5 & 0 & 7.1 & 0 \\ 25.4 & 0 & 10.1 & 0 & 0 & 0 \end{bmatrix}$$

$$
\begin{array}{c} G \text{ matrix} \\ \text{Cramer-Rao} \\ \text{Bound \%} \end{array} = \left[\begin{array}{cccccc}
5.6 & 12.7 & 18.7 & 14.0 & 29.8 & 17.4 \\
0 & 0 & 0 & 19.4 & 0 & 15.4 \\
4.2 & 4.3 & 14.6 & 0 & 0 & 0 \\
0 & 0 & 0 & 0 & 0 & 20.6 \\
9.1 & 9.7 & 5.1 & 0 & 0 & 0 \\
0 & 0 & 0 & 13.7 & 0 & 15.8 \\
9.8 & 0 & 10.4 & 6.8 & 8.0 & 7.1 \\
0 & 0 & 0 & 0 & 0 & 0 \\
0 & 18.5 & 0 & 14.0 & 5.5 & 20.1 \\
0 & 15.9 & 0 & 0 & 0 & 0 \\
0 & 12.0 & 0 & 0 & 19.6 & 0 \\
0 & 0 & 16.1 & 0 & 0 & 0
\end{array}\right] \tag{6.15}
$$

Some of the Cramer-Rao bound percentages were above the recommended level of 20% but the parameters could not be removed because doing so caused the cost function J_{ave} to increase too sharply, or caused the system to go unstable, after re-optimization. The insensitivities for all parameters were under 5%, well within the guidelines of 10% [63].

6.6.2 Time verification

This section contain time domain responses of rotor inflow components. These are used as verification of the inflow state-space model with the form of Eq.(6.5) and the matrices shown in Eqs. (6.12) and (6.13).

In Figs. 6.29 to 6.33, the swashplate input (not shown in the figure) is a doublet of lateral cyclic stick at the lower rotor θ_{1s}^{L} of magnitude 1°. Figure 6.29 shows the aerodynamic thrust, roll moment, and pitching moment coefficients, C_T^U,C_L^U and C_M^U respectively, for the upper rotor. Figure 6.30 shows those for the lower rotor.

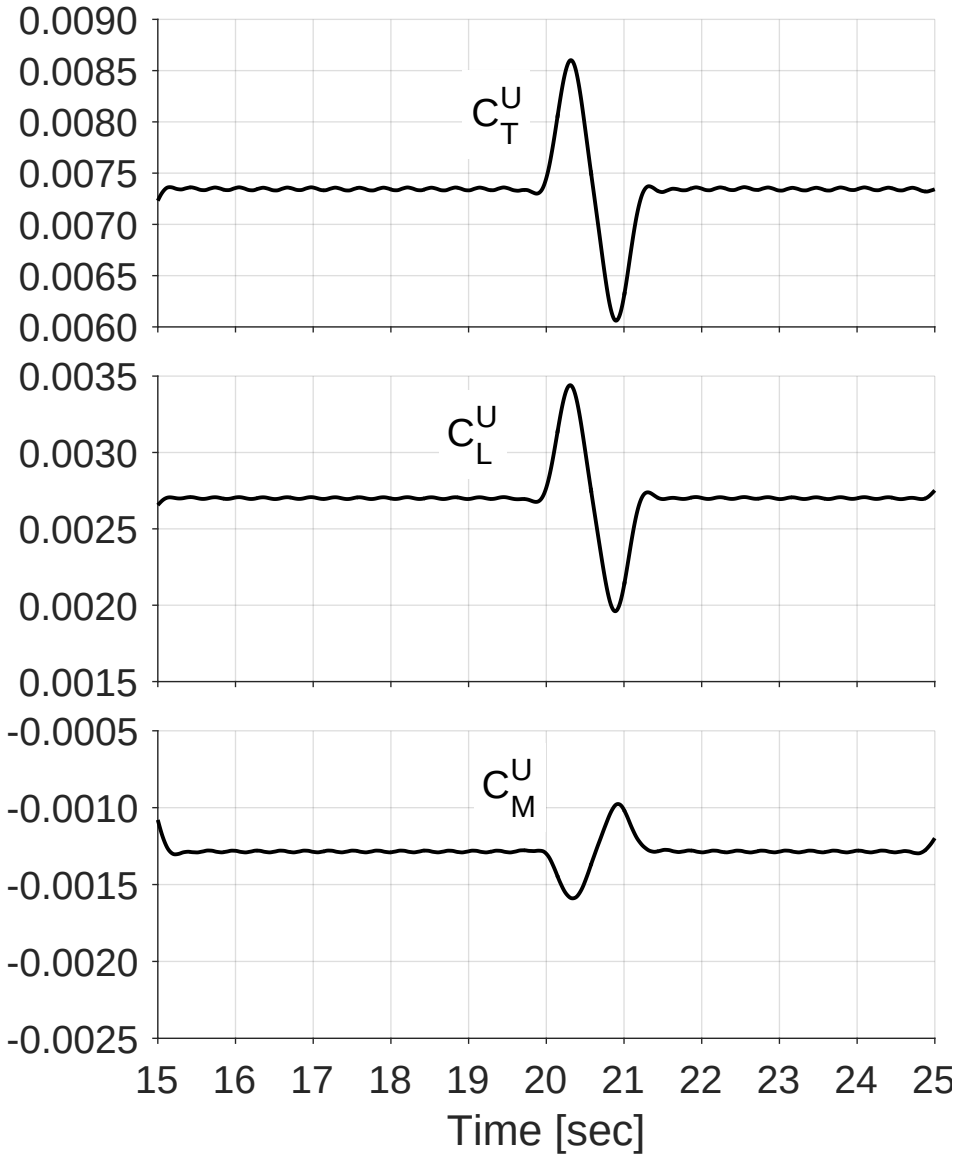

Figure 6.29: Upper rotor aerodynamic loading for time verification produced by a lower rotor lateral swashplate doublet in Forward Flight.

Each plot in Figs. 6.31 to 6.33 has two curves: (i) the response computed using the full nonlinear MFW; (ii) the response computed using the identified state-space inflow model. Figure 6.31 shows the response of the average inflow components, λ_0^U and λ_0^L for the both rotors. Figure 6.32 shows the response of the lateral inflow

components, λ_{1S}^{U} and λ_{1S}^{L}, for the both rotors. And lastly, Fig. 6.33 shows the response of the longitudinal inflow components, λ_{1C}^{U} and λ_{1C}^{L} for the both rotors.

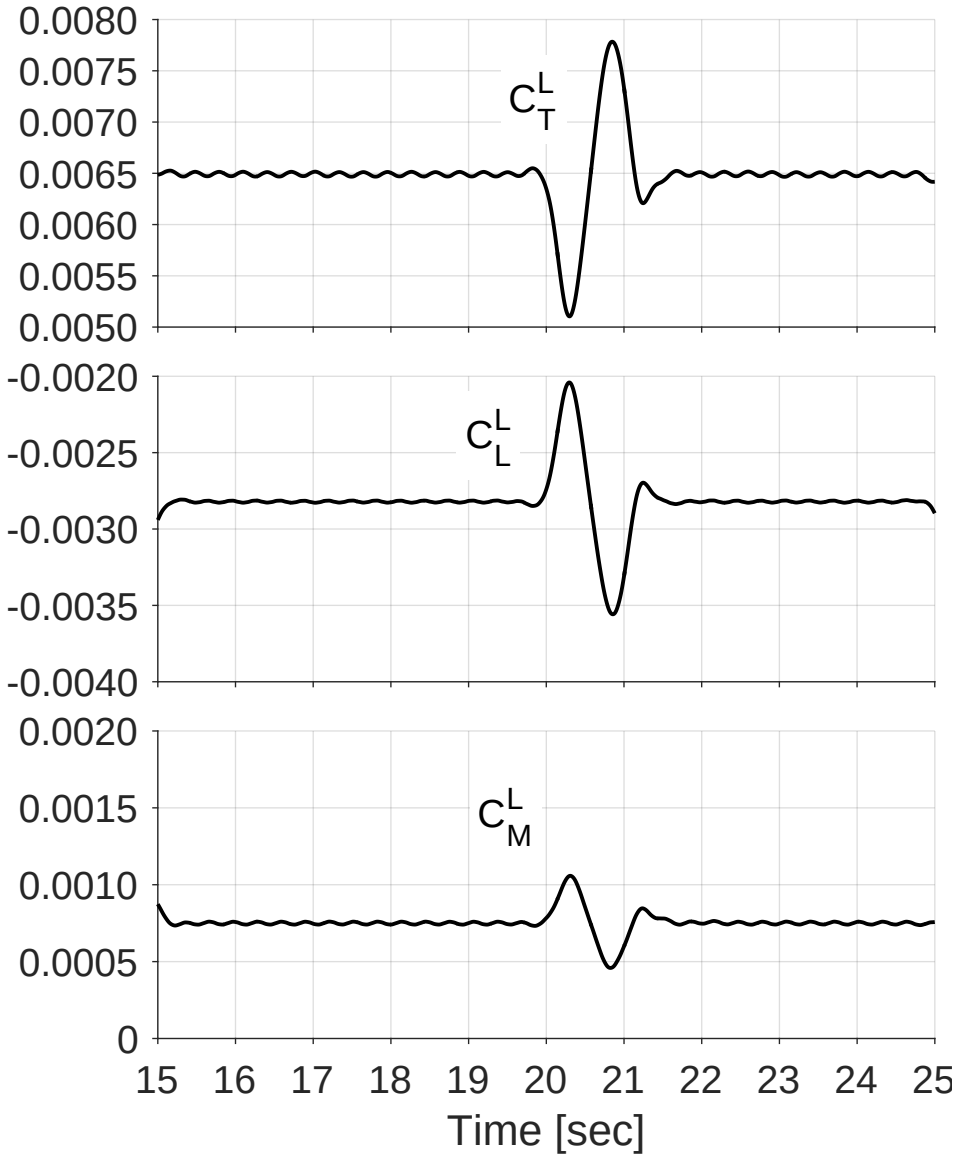

Figure 6.30: Lower rotor aerodynamic loading for time verification produced by a lower rotor lateral swashplate doublet in Forward Flight.

Overall these verifications show pretty good agreement between the identified model and the actual MFW data. In particular, the lateral inflow dynamics on

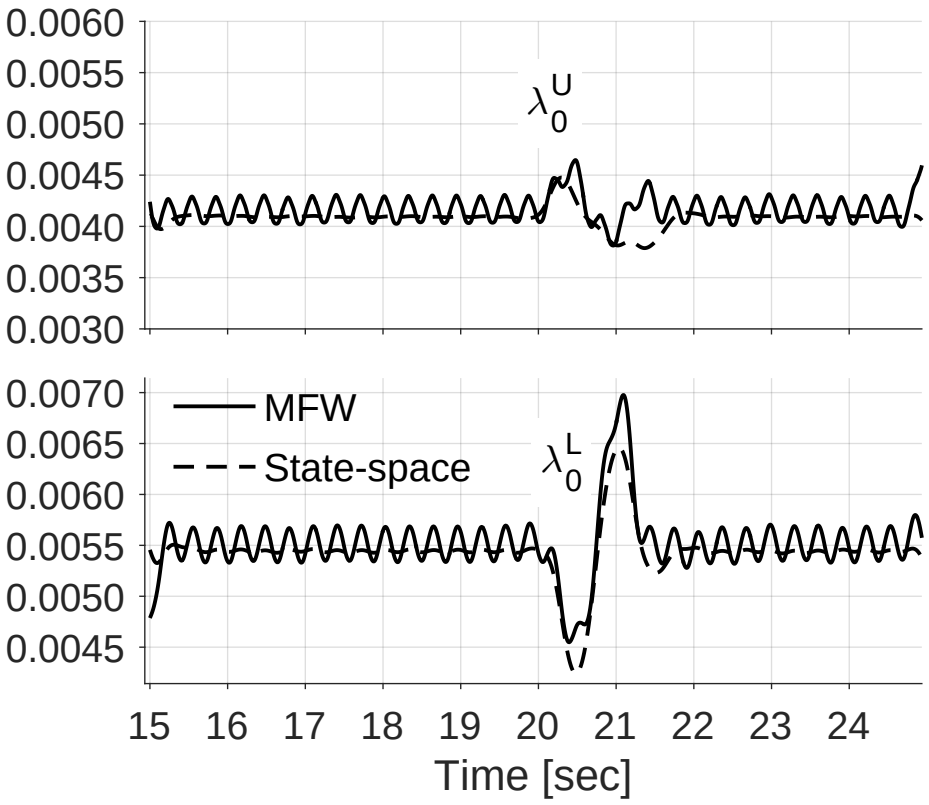

Figure 6.31: Time verification of the average inflow λ_0 response on both rotors for the lower rotor lateral swashplate doublet in forward flight

both rotors experience large perturbations and are well captured by the model. The average inflow shows some of the periodicity of a coaxial rotor in forward flight. The inflow clearly has a 1/rev oscillation (there is also a 4/rev and other higher frequency oscillations which are not shown because the time histories in the figures are attenuated through a high-pass filter) that cannot be captured by the simple first harmonic state-space model. However the identified model fits generally very well through the average of the higher frequency oscillations.

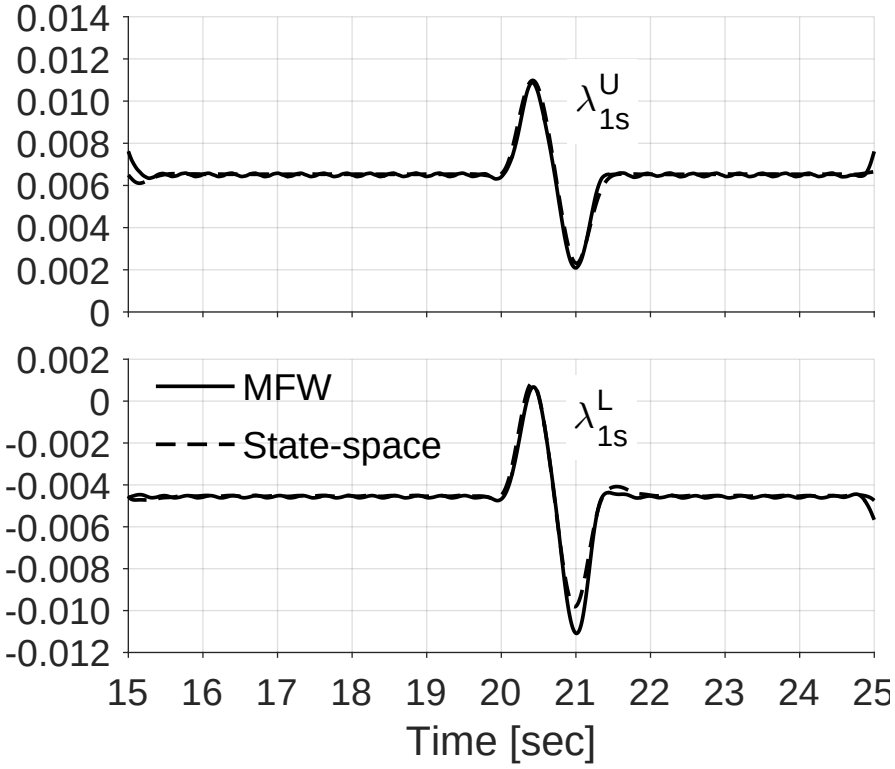

Figure 6.32: Time verification of the lateral inflow λ_{1S} response on both rotors for the lower rotor lateral swashplate doublet in forward flight

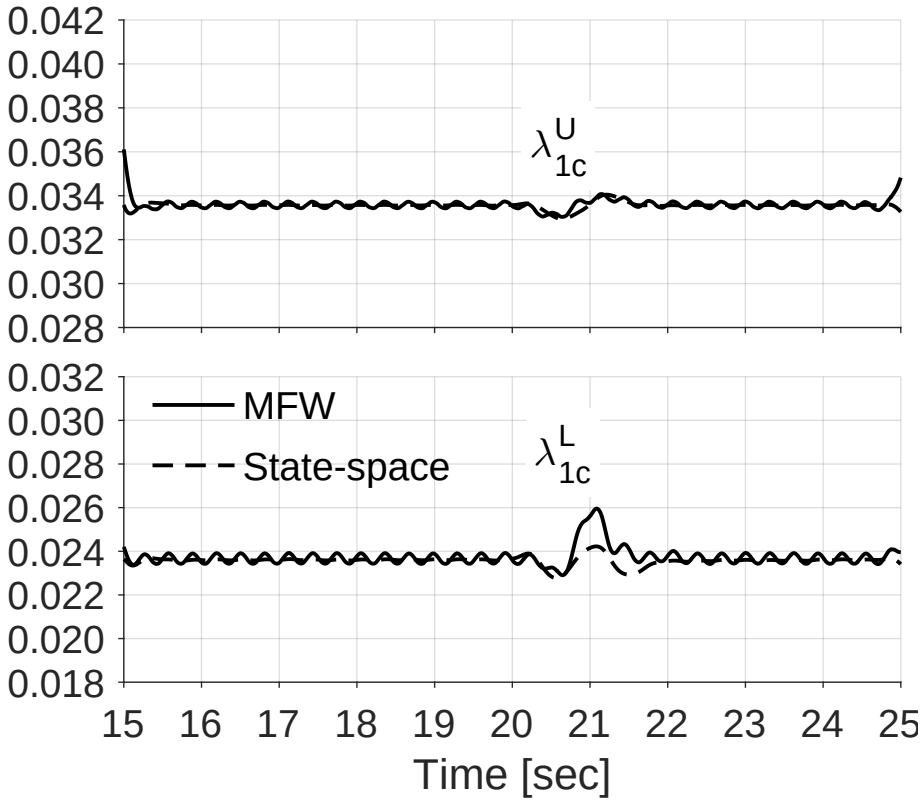

Figure 6.33: Time verification of the longitudinal inflow λ_{1C} response on both rotors for the lower rotor lateral swashplate doublet in Forward Flight

Figures 6.34 through 6.36 have the same general arrangement as Figs. 6.29 through 6.31, except that it shows the responses to the same size doublet, but applied to the upper rotor collective θ_0^U. The agreement is generally not as good as for θ_{1s}^L doublet and demonstrates the complexity of the true rotor flow. In general the lower rotor inflow is better predicted. The upper rotor lateral inflow λ_{1S}^U is particularly bad as it shows the incorrect sign for the inflow prediction, but the actual shape of the MFW perturbation suggests some complex higher order response. The inflow once again clearly has a 4 per rev vibration that is not captured by this model. This part not being captured may be leading to some of the discrepancies between the state-space model and the full, nonlinear MFW.

There are many more verifications that can be shown, but these two show the strengths and weaknesses of this particular model. With the current model form, this is still considered to be as good an approximation as can be attained.

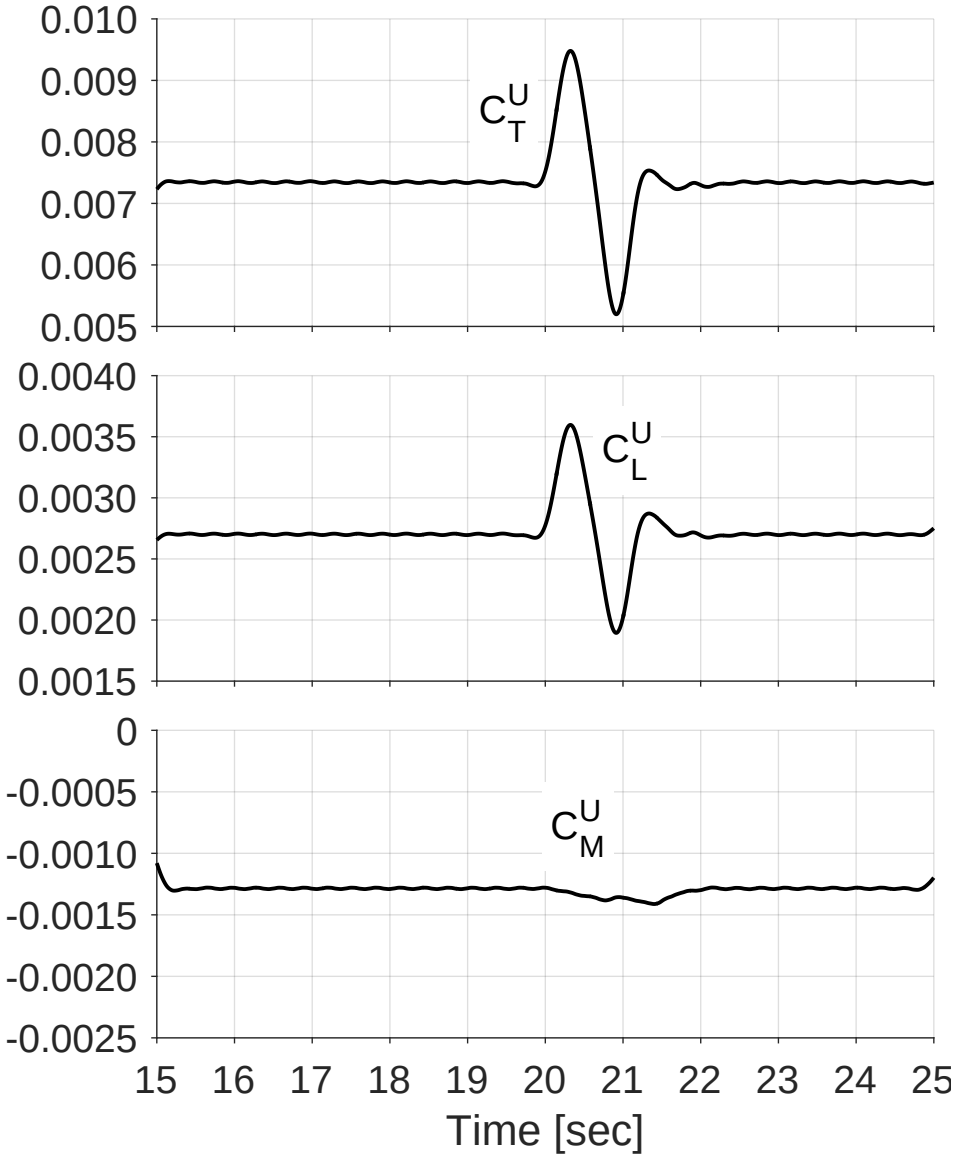

Figure 6.34: Upper rotor aerodynamic loading for time verification produced by a upper rotor collective swashplate doublet in forward flight.

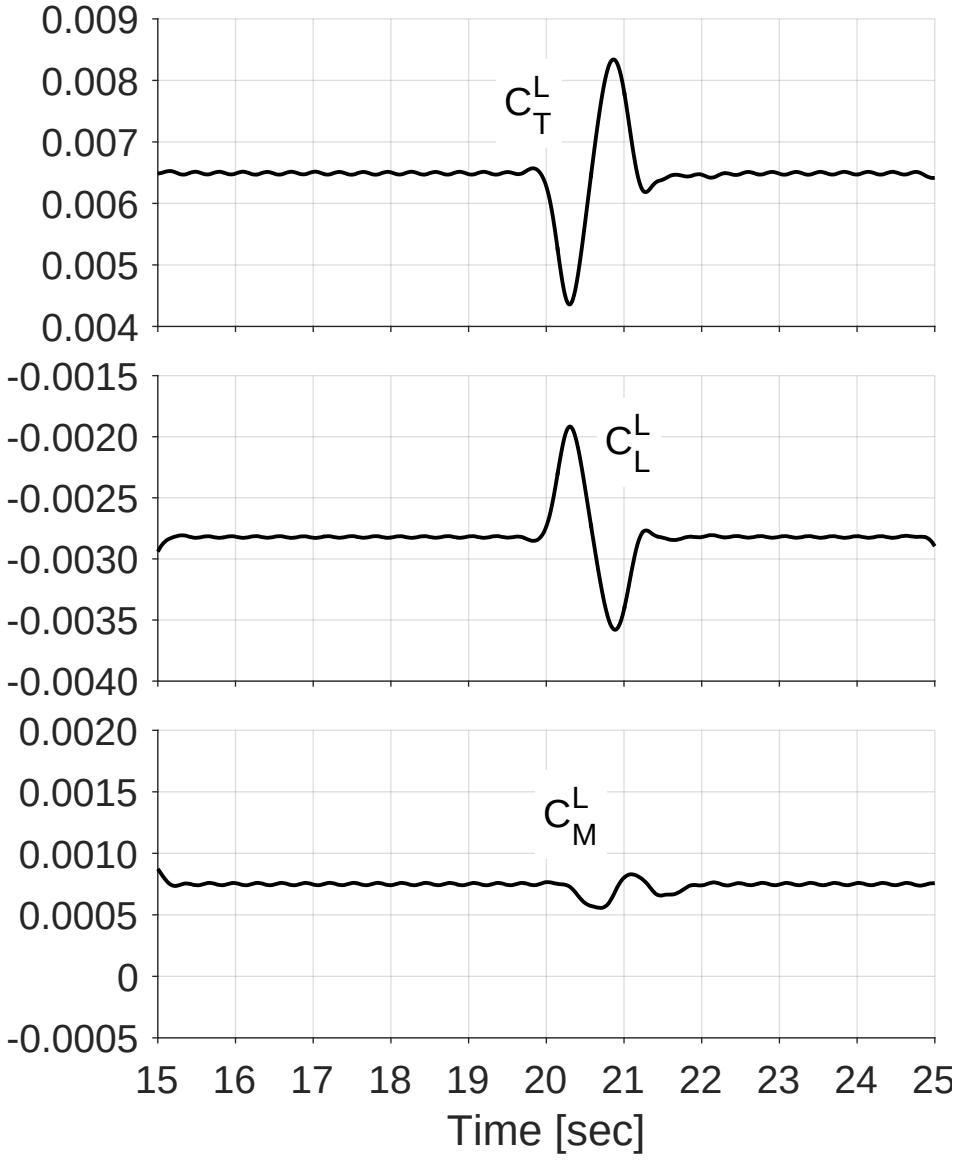

Figure 6.35: Lower rotor aerodynamic loading for time verification produced by a upper rotor collective in forward flight.

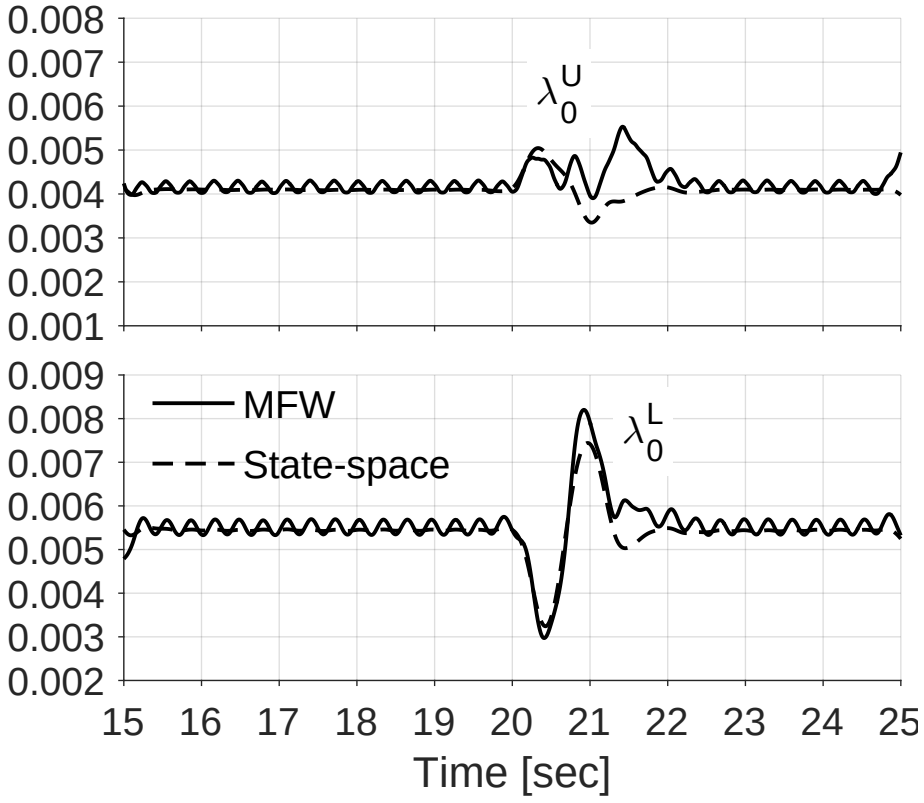

Figure 6.36: Time verification of the average inflow λ_0 response on both rotors for the upper rotor collective swashplate doublet in forward flight

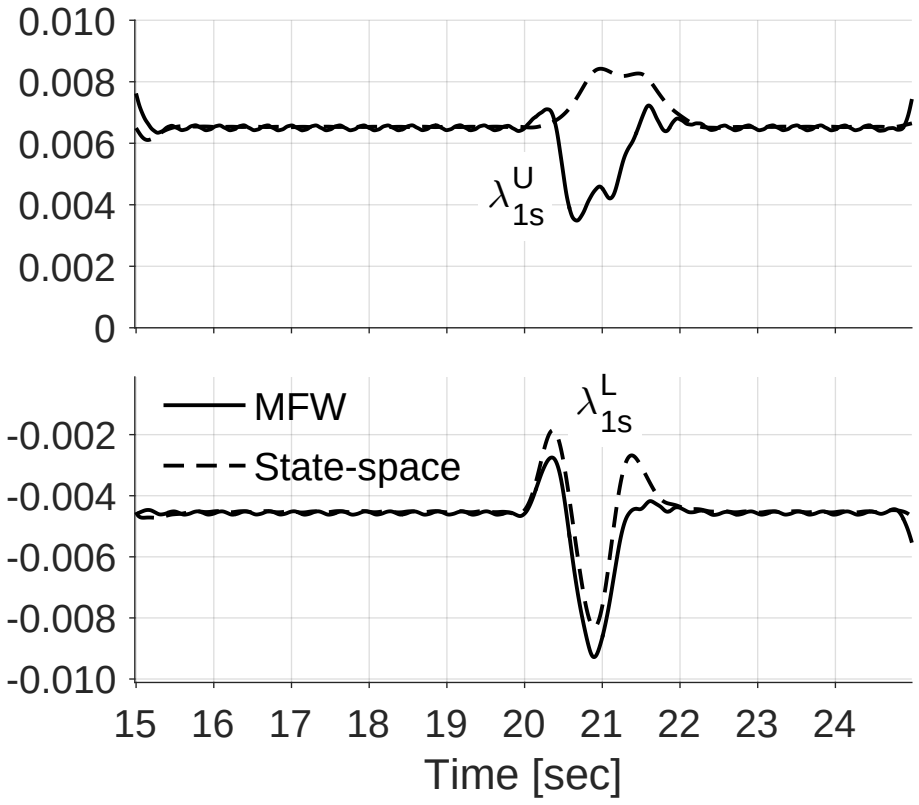

Figure 6.37: Time verification of the lateral inflow λ_{1S} response on both rotors for the upper rotor collective swashplate doublet in forward flight

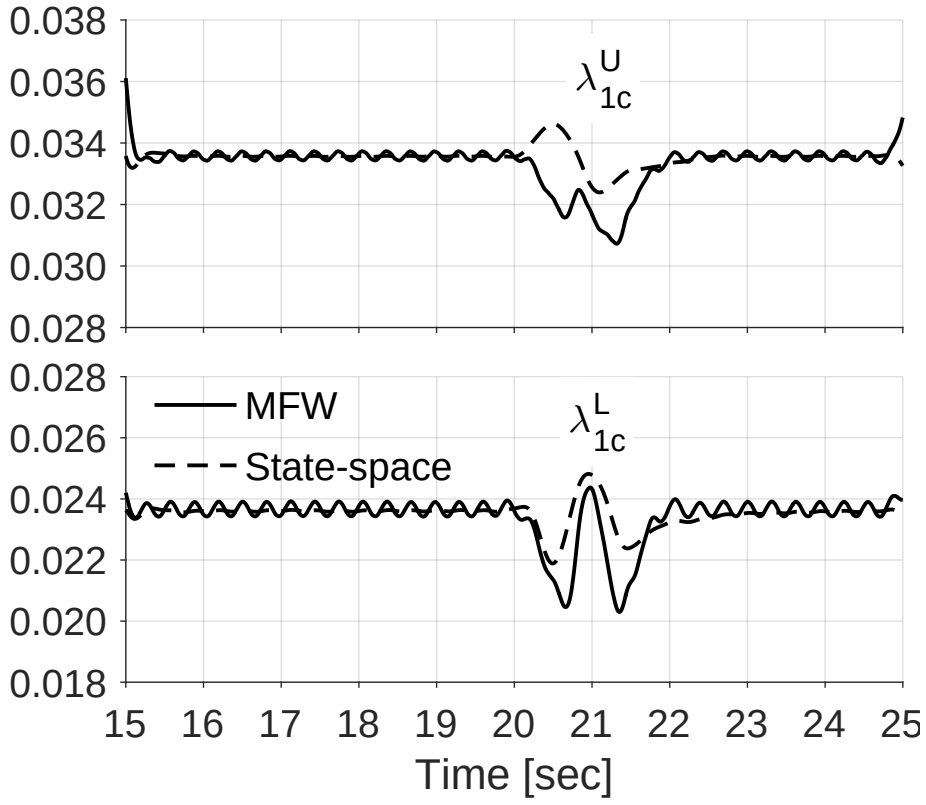

Figure 6.38: Time verification of the longitudinal inflow λ_{1C} response on both rotors for the upper rotor collective swashplate doublet in forward flight

6.7 Summary

A need for a second-order model of inflow was seen in Chapter. 5 for coaxial rotors, which exhibited more dynamics that were not captured but the first-order model. This was consistent with the findings of several other authors when identifying inflow model from other free-wake models [80], from viscous vortex particle methods [79], and from Boundary Element methods [77]. A second-order linear state-space model was defined and identified from the MFW solution, including the effects of wake distortion due to angular rates. This second-order model was shown to correctly capture the dynamic wake response of a coaxial rotor system in Hover. A version of this model was then used to capture a model of the complex inflow interactions of a coaxial rotor in forward flight with a slightly positive angle of attack, allowing flow from the free-stream to provide a climb to the rotors, but not so much as to be in autorotation. This model also proved capable of capturing proper wake dynamics.

Chapter 7: Coupled Aircraft Models

7.1 Overview

The results of the previous chapters were obtained for isolated rotors, and ignoring any couplings with the model of the rest of the aircraft. When the full aircraft simulation [98] was used, it was only to take advantage of the already existing rotor dynamic model, therefore, the aircraft rigid body degrees of freedom were locked and the simulation was not representative of free flight conditions.

This chapter present results obtained with the state-space inflow model fully coupled with the aircraft simulation. Section 7.2 describes how the state-space inflow model is coupled with the rest of the mathematical model of the aircraft, and how the different types of solutions are affected by the model. Section 7.3 and 7.4 present free flight results from the fully coupled simulations for the single main rotor and the coaxial configuration, respectively. Fixed-stick stability and frequency responses to pilot inputs are presented. Finally, section 7.5 shows an example of flight control system design for the coaxial rotorcraft configuration in hover.

7.2 Coupling of State-Space Inflow Models

The general architecture of the simulation model has been presented in Sec. 2.2. Additional details concerning the coupling of the inflow model with the different solution algorithms are presented below.

7.2.1 Trim Solution

As stated in Chapter 2, the trim problem is formulated as a coupled system of nonlinear algebraic equations, which enforce, for the present study: (i) force and moment equilibrium along and about the body axes; (ii) periodicity of the motion of the rotor blades; and iii) constant averages of inflow harmonics for momentum-theory based inflow models. A trim solution can be computed even if the wake model (or any other portion of the model) is not in state-space form. With a free wake model, a "loose" coupling procedure is used, in which wake geometry and inflow are updated at every trim iteration using the controls and blade motions of the previous revolution [98].

The state-space inflow models, such as those presented in the previous chapters, do not affect trim at all, because they are all perturbation models, where "perturbation" implies "perturbation from trim", therefore all their states are identically equal to zero at trim.

7.2.2 Time Marching Solution

Time marching solutions of the equations of motion of the entire rotorcraft do not require that the model be in state-space form, as long as the portions not in state-space form contain a mechanism to advance the solution in time, as is the case for the MFW.

For the inflow models used in the present study, three integration options are possible:

1. *MFW only* — The time histories of the inflow quantities are obtained from the full, nonlinear MFW solution:

$$\lambda^{(\cdots)}(\tilde{r},\psi) = \lambda^{(\cdots)}_{MFW}(\tilde{r},\psi) \tag{7.1}$$

   where the superscript is ignored for a single main rotor, and is "U" or "L" for the upper and lower rotor, respectively, of a coaxial configuration. This is expected to be the most accurate solution and, in the absence of flight test or wind tunnel data, it is considered as the "truth" model for the results of this dissertation.

2. *MFW trim solution plus state-space inflow model* — The inflow quantities are given by the sum of a steady, nonlinear inflow distribution over the rotor disk obtained from the MFW and a linear, time-dependent perturbation computed from one of the state-space models:

$$\lambda^{(\cdots)}(\tilde{r},\psi) = \lambda^{(\cdots)}_{eq}(\tilde{r},\psi) + \Delta\lambda^{(\cdots)}_{0} + \Delta\lambda^{(\cdots)}_{1S}\tilde{r}\sin(\psi) + \Delta\lambda^{(\cdots)}_{1C}\tilde{r}\cos(\psi) \tag{7.2}$$

$$\text{where: } \lambda_{eq}^{(\cdots)}(\tilde{r},\psi) = \lambda_{MFW}^{(\cdots)}(\tilde{r},\psi) \text{ at trim} \tag{7.3}$$

3. *State-space inflow model only* — The inflow quantities are given by the sum of a linear time-dependent perturbation computed from one of the state-space models and the initial conditions for the inflow harmonics (λ_{eq}):

$$\lambda^{(\cdots)}(\tilde{r},\psi) = \lambda_{eq}^{(\cdots)}(\tilde{r},\psi) + \Delta\lambda_0^{(\cdots)} + \Delta\lambda_{1S}^{(\cdots)}\tilde{r}\sin(\psi) + \Delta\lambda_{1C}^{(\cdots)}\tilde{r}\cos(\psi) \tag{7.4}$$

$$\text{where: } \lambda_{eq}^{(\cdots)}(\tilde{r},\psi) = \left(\lambda_0^{(\cdots)}\right)_{eq} + \left(\lambda_{1S}^{(\cdots)}\right)_{eq}\tilde{r}\sin(\psi) + \left(\lambda_{1C}^{(\cdots)}\right)_{eq}\tilde{r}\cos(\psi) \tag{7.5}$$

and $\left((\lambda_0^{(\cdots)}\right)_{eq}$, $\left(\lambda_{1C}^{(\cdots)}\right)_{eq}$, and $\left(\lambda_{1S}^{(\cdots)}\right)_{eq}$ are calculated from the full, nonlinear MFW inflow distribution ($\lambda_{MFW}^{(\cdots)}(\tilde{r},\psi)$) at trim using Eqs.(2.22), (2.25), and (2.26), respectively.

Depending on the specific problem and the inflow model used, slightly different state vectors have been used. All state vectors have the following structure:

$$\boldsymbol{x} = \left\{ \begin{array}{c} \boldsymbol{x_{rb}} \\ \boldsymbol{x_{inf}} \\ \boldsymbol{x_{rot}} \end{array} \right\} \tag{7.6}$$

The vector $\boldsymbol{x_{rb}}$ is the portion containing the rigid body states:

$$\boldsymbol{x}_{\boldsymbol{rb}}^T = [u \;\; v \;\; w \;\; p \;\; q \;\; r \;\; \phi \;\; \theta \;\; \psi] \tag{7.7}$$

where: u, v, and w are the velocity components of the aircraft along its body axes; p, q, and r are the roll, pitch, and yaw rates; and ϕ, θ, and ψ are the roll, pitch, and yaw Euler angles; for both the single main rotor and the coaxial configuration.

The vector $\boldsymbol{x_{rot}}$ contains the rotor states, which are the modal coefficients for each individual blade and their time derivatives. For the single main rotor configuration (which has four blades) the vector is written as:

$$\boldsymbol{x_{rot}} = \left\{ \begin{array}{l} q_1^1 \;\; q_2^1 \;\; q_3^1 \;\; q_4^1 \;\; \dot{q}_1^1 \;\; \dot{q}_2^1 \;\; \dot{q}_3^1 \;\; \dot{q}_4^1 \;\; \cdots \\ \qquad \cdots \;\; q_1^{NM} \;\; q_2^{NM} \;\; q_3^{NM} \;\; q_4^{NM} \;\; \dot{q}_1^{NM} \;\; \dot{q}_2^{NM} \;\; \dot{q}_3^{NM} \;\; \dot{q}_4^{NM} \end{array} \right\} \tag{7.8}$$

in which q_i^k and $\dot{q}_i^k$ are the generalized displacement and rate for the i-th blade and the k-th mode, and NM is the number of modes retained. For the single main rotor results in this chapter, only the first (predominantly) flap ($k = 1$) and lag ($k = 2$) modes are retained, so the rotor state vector becomes:

$$\boldsymbol{x_{rot}} = \left\{ q_1^1 \;\; q_2^1 \;\; q_3^1 \;\; q_4^1 \;\; \dot{q}_1^1 \;\; \dot{q}_2^1 \;\; \dot{q}_3^1 \;\; \dot{q}_4^1 \;\; q_1^2 \;\; q_2^2 \;\; q_3^2 \;\; q_4^2 \;\; \dot{q}_1^2 \;\; \dot{q}_2^2 \;\; \dot{q}_3^2 \;\; \dot{q}_4^2 \right\} \tag{7.9}$$

For the coaxial configuration, a U or L is added to the blade subscript to indicate whether the blade is on the upper or lower rotor, respectively. The rotor vector is written with all the upper rotor terms first, and then with all the lower rotor terms. For hover results, only the first flap mode ($k = 1$) was retained:

$$\boldsymbol{x_{rot}} = \left\{ \begin{array}{l} q_{1U}^1 \;\; q_{2U}^1 \;\; q_{3U}^1 \;\; q_{4U}^1 \;\; \dot{q}_{1U}^1 \;\; \dot{q}_{2U}^1 \;\; \dot{q}_{3U}^1 \;\; \dot{q}_{4U}^1 \;\; \cdots \\ \qquad q_{1L}^1 \;\; q_{2L}^1 \;\; q_{3L}^1 \;\; q_{4L}^1 \;\; \dot{q}_{1L}^1 \;\; \dot{q}_{2L}^1 \;\; \dot{q}_{3L}^1 \;\; \dot{q}_{4L}^1 \end{array} \right\} \tag{7.10}$$

Besides the first flap ($k = 1$) and lag ($k = 2$) modes, the results for the coaxial configuration in forward flight also include the second flap ($k = 3$) and lag ($k = 4$)

modes, so the rotor state vector becomes:

$$\boldsymbol{x_{rot}} = \Big\{ \begin{array}{cccccccc} q^1_{1U} & q^1_{2U} & q^1_{3U} & q^1_{4U} & \dot{q}^1_{1U} & \dot{q}^1_{2U} & \dot{q}^1_{3U} & \dot{q}^1_{4U} \ \cdots \\ q^2_{1U} & q^2_{2U} & q^2_{3U} & q^2_{4U} & \dot{q}^2_{1U} & \dot{q}^2_{2U} & \dot{q}^2_{3U} & \dot{q}^2_{4U} \ \cdots \\ q^3_{1U} & q^3_{2U} & q^3_{3U} & q^3_{4U} & \dot{q}^3_{1U} & \dot{q}^3_{2U} & \dot{q}^3_{3U} & \dot{q}^3_{4U} \ \cdots \\ q^4_{1U} & q^4_{2U} & q^4_{3U} & q^4_{4U} & \dot{q}^4_{1U} & \dot{q}^4_{2U} & \dot{q}^4_{3U} & \dot{q}^4_{4U} \ \cdots \\ q^1_{1L} & q^1_{2L} & q^1_{3L} & q^1_{4L} & \dot{q}^1_{1L} & \dot{q}^1_{2L} & \dot{q}^1_{3L} & \dot{q}^1_{4L} \ \cdots \\ q^2_{1L} & q^2_{2L} & q^2_{3L} & q^2_{4L} & \dot{q}^2_{1L} & \dot{q}^2_{2L} & \dot{q}^2_{3L} & \dot{q}^2_{4L} \ \cdots \\ q^3_{1L} & q^3_{2L} & q^3_{3L} & q^3_{4L} & \dot{q}^3_{1L} & \dot{q}^3_{2L} & \dot{q}^3_{3L} & \dot{q}^3_{4L} \ \cdots \\ q^4_{1L} & q^4_{2L} & q^4_{3L} & q^4_{4L} & \dot{q}^4_{1L} & \dot{q}^4_{2L} & \dot{q}^4_{3L} & \dot{q}^4_{4L} \end{array} \Big\} \tag{7.11}$$

Finally, the vector $\boldsymbol{x_{inf}}$ is the portion containing the inflow states. For single main rotors, the inflow states are the same states as in the state vector of Eqs. (2.11) or (2.12):

$$\boldsymbol{x_{inf}} = \left\{ \begin{array}{c} \Delta\lambda_0 \\ \Delta\lambda_{1s} \\ \Delta\lambda_{1c} \end{array} \right\} \tag{7.12}$$

Similarly for the coaxial rotor, the inflow state vector is the same as the state vector of the model which is being utilized. So for the 6-state inflow model for hover, the state vector is the same as in Eq.(2.30):

$$\boldsymbol{x_{inf}} = \left\{ \begin{array}{c} \Delta\lambda^U_0 \\ \Delta\lambda^U_{1s} \\ \Delta\lambda^U_{1c} \\ \Delta\lambda^L_0 \\ \Delta\lambda^L_{1s} \\ \Delta\lambda^L_{1c} \end{array} \right\} \tag{7.13}$$

whereas, for the higher order, 12-state inflow models, the inflow state vector is the same as Eq.(2.35):

$$\boldsymbol{x_{inf}} = \left\{ \begin{array}{c} \Delta\lambda^U_{0N} \\ \Delta\lambda^U_{0F} \\ \Delta\lambda^U_{1SN} \\ \Delta\lambda^U_{1SF} \\ \Delta\lambda^U_{1CN} \\ \Delta\lambda^U_{1CF} \\ \Delta\lambda^L_{0N} \\ \Delta\lambda^L_{0F} \\ \Delta\lambda^L_{1SN} \\ \Delta\lambda^L_{1SF} \\ \Delta\lambda^L_{1CN} \\ \Delta\lambda^L_{1CF} \end{array} \right\} \tag{7.14}$$

The inflow models presented in the previous chapters are all perturbation models, meaning that they are valid around a given equilibrium point or trim. Therefore the inflow states presented in Eqs.(7.12) through (7.14) are all *perturbation* states, and similarly the aerodynamic (or flap rate) inputs in the models are all perturbation inputs. The symbol Δ, which denotes perturbations, is usually dropped for convenience, but it is retained in the discussion that follows, for clarity.

When the identified state-space inflow models are used in the fully coupled aircraft model, the inflow state vector is a *perturbation* state, and so are the aerodynamic inputs $\Delta\mathbf{C}$ and the perturbation flap rates $\Delta\overset{*}{\boldsymbol{\beta}}$ that represent the forcing function for the model. However, the simulation typically computes the *total* aerodynamic forcing and flap rates. Therefore in order to advance in time the solution of the identified inflow models, the *perturbation* inputs must be calculated from the full values. This requires that the trim values, i.e., the value of the aerodynamic forcing at trim $\mathbf{C}_{eq}$ be known, together with (depending on the model) the flapping

rates at trim $\overset{*}{\boldsymbol{\beta}}_{eq}$. The perturbation values of the vector of aerodynamic forcing inputs, $\Delta\mathbf{C}(t)$, can then be calculated by:

$$\Delta\mathbf{C}(t) = \mathbf{C}(t) - \mathbf{C}_{eq}(t) \tag{7.15}$$

similarly, for the flapping rate perturbations $\Delta\overset{*}{\boldsymbol{\beta}}(t)$:

$$\Delta\overset{*}{\boldsymbol{\beta}}(t) = \overset{*}{\boldsymbol{\beta}}(t) - \overset{*}{\boldsymbol{\beta}}_{eq}(t) \tag{7.16}$$

Once $\Delta\mathbf{C}$ and $\Delta\overset{*}{\boldsymbol{\beta}}$ are available, the perturbation inflow $\boldsymbol{x_{inf}}$ can be calculated. Then, the full value $\lambda(x,\psi)$ of the inflow, needed by the simulation (e.g., for the calculation of the blade aerodynamic loads) can be reconstructed at every spanwise station x and azimuth angle ψ by either Eq.(7.2) or Eq.(7.4).

For single main rotor configurations, the input vector $\boldsymbol{u}$ consists of:

$$\boldsymbol{u} = \left\{ \begin{array}{c} \theta_0 \\ \theta_{1s} \\ \theta_{1c} \\ \theta_{TR} \end{array} \right\} \tag{7.17}$$

where θ_0, θ_{1s}, and θ_{1c} are the swashplate collective, longitudinal and lateral cyclic, respectively, and θ_{TR} is the tail rotor collective.

For the coaxial configuration, there are two sets of swashplate controls, one for each rotor. Also there is an additional control for the propeller collective. So control vector can be written as:

$$\boldsymbol{u} = \left\{ \begin{array}{c} \theta_0^U \\ \theta_{1s}^U \\ \theta_{1c}^U \\ \theta_0^L \\ \theta_{1s}^L \\ \theta_{1c}^L \\ \theta_{PR} \end{array} \right\} \tag{7.18}$$

where θ_0, θ_{1s}, and θ_{1c} are the swashplate collective, longitudinal and lateral cyclic, respectively, the superscripts "U" and "L" refer to upper and lower rotor, and and θ_{PR} is the collective of the pusher propeller (not used in this study). For this coaxial configuration, which has no hinge and a flap frequency closer to 1.5/rev, the role of swashplate cyclics are mostly reversed: θ_{1s} produces primarily roll response and θ_{1c} produces primarily pitch response, albeit with much more off-axis response than with a single main rotor.

The six swashplate controls in coaxial rotorcraft are generally not independent, but are constrained in such a way that only four pilot controls, namely, lateral stick δ_{lat}, longitudinal stick δ_{lon}, collective stick δ_{col}, and pedal δ_{ped}, are independent. For the present study, the pilot input vector is defined as follows:

$$\boldsymbol{\delta} = \begin{Bmatrix} \delta_{col} \\ \delta_{lon} \\ \delta_{lat} \\ \delta_{ped} \\ \delta_{PR} \end{Bmatrix} = K \begin{Bmatrix} \theta_0^U + \theta_0^L \\ \theta_{1c}^U + \theta_{1c}^L \\ \theta_{1s}^U + \theta_{1s}^L \\ \theta_0^U - \theta_0^L \\ \theta_{PR} \end{Bmatrix} \tag{7.19}$$

where K is a simple proportionality constant, which is meant to represent in an elementary way the stick-to-swashplate connection. For all the bare airframe cases of this study it is simply $K = 0.5$.

The difference in lateral cylic swashplate angles ($\delta_{\Delta lat} = \theta_{1s}^U - \theta_{1s}^L$) is used in trim only to produce a desired lift-offset. Once this value is set in trim it is not changed for time integration purposes. It can, in theory, be used but it is generally not considered a pilot control. This control can however be perturbed for linearized analysis purposes, to allow exploration of the aircraft behavior produced by such a swashplate control combination. Finally the longitudinal cyclic swashplate angles

are constrained in trim such that $\delta_{\Delta lon} = \theta_{1c}^{U} - \theta_{1c}^{L} = 0$. Once again this value is held fixed in time integration, but can be utilized in linearized anaylsis.

7.2.3 Linearized Analysis Solution

Linearized analysis utilizes the same ODE kernel as used for the time-marching solutions, except that the ODEs are not integrated in time, but are perturbed numerically about a trimmed equilibrium position [98]. Of the three time integration options listed above, the model used in the "*MFW only*" option cannot be used because the MFW is not in state-space form. The models used in the other two time integration options can be used because the overall aircraft model ends up being fully in ODE form. Therefore the procedure can be carried out exactly as described in Appendix A. The state-space inflow models are not inserted directly into the the $[A]$ an $[B]$ matrices of the entire aircraft, but rather the state-space models effects are quantified when the ODE kernel (containing the inflow equations and inflow states) is perturbed. As such, full aircraft models created through linearized analysis are only valid at the equilibrium, or trim, condition at which the state-space inflow model was identified. The main result of linearized analysis are the state and control matrices, $[A]$ and $[B]$ respectively, which describe the full aircraft motion when used in the equation:

$$\dot{\boldsymbol{x}} = [A]\boldsymbol{x} + [B]\boldsymbol{u} \tag{7.20}$$

where $\boldsymbol{x}$ and $\boldsymbol{u}$ are the state and input vectors, as described in the previous section. The results of this chapter are exclusively from linearized anaylsis of HeliUM with the identified state-space models of inflow inserted as described in the "State-space inflow model only" integration option. The $[A]$ and $[B]$ matrix results of linearized analysis can be alternatively shown as Bode plots of full aircraft responses, such as roll response to pilot stick. Another important result that can be obtained are the eigenvalues of the $[A]$ matrix, which are the poles of the full aircraft and describe the aircraft stability. Controllers can be augmented to the state and control matrices to demonstrate the stability of the aircraft in the presence of feedback control.

Lastly, Eq.(7.20) can time-integrated, starting from the HeliUM trim solution corresponding to this linearized model, to create time histories of helicopter responses, in particular the response of any one of the states in $\boldsymbol{x}$ to any one of the controls in $\boldsymbol{u}$. This can be performed with or without the feedback control, but as with the full HeliUM simulation, a helicopter without feedback control is often unstable, rendering its time histories divergent. However, time integration performed with a controller can give well behaved time histories that stay within the acceptable bounds of a small perturbation model. Showing comparisons between two time histories computed with different controllers can show, in a practical sense, the difference between the performance of the controllers. All the time integration results that will be shown in this chapter are performed by time-marching the state $[A]$ and control $[B]$ matrices obtained using linearized analysis, with various feedback controllers applied to them which will be described in detail.

7.3 Single Main Rotor

7.3.1 Hovering Aircraft Responses

For a single main rotor in hover, first the full nonlinear MFW simulation was compared against flight tests and other models, to see how the models compare before state-space idnetification. The aircraft response of coning flapping β_0 to to collective pitch θ_0 was compared in Figure 7.1. The first frequency response, labeled "Flight", is from a collective pitch θ_0 frequency sweep flight test data [120]. The next is from HeliUM with the Pitt-Peters model. The third frequency response is from collective pitch θ_0 sweep of HeliUM with the MFW. The last frequency response, labeled "Chen", is a single-axis analytical model (also from Ref. 120). These responses were *not* found through linearized analysis, but rather through frequency sweeps of the collective pitch (shaft-fixed), and then frequency response generation (Fig. 7.1 leaves them in non-parametric form). The agreement is generally good with the same dynamics present in all the models. The MFW (not the identified state-space model but rather the full simulation) model correctly captures the coupled inflow-coning mode at 20 rad/sec. The low-frequency dynamics in the flight data (0.1 - 3 rad/sec) correspond to fuselage motion of the aircraft, which is not present in the other wind-tunnel type models.

Next, the coefficients from Table 4.1 were implemented into the HeliUM simulation (see Sec. 2.2.2). The linearized analysis extracts linearized models of the full aircraft dynamics in state space form. To accomplish this, the entire simula-

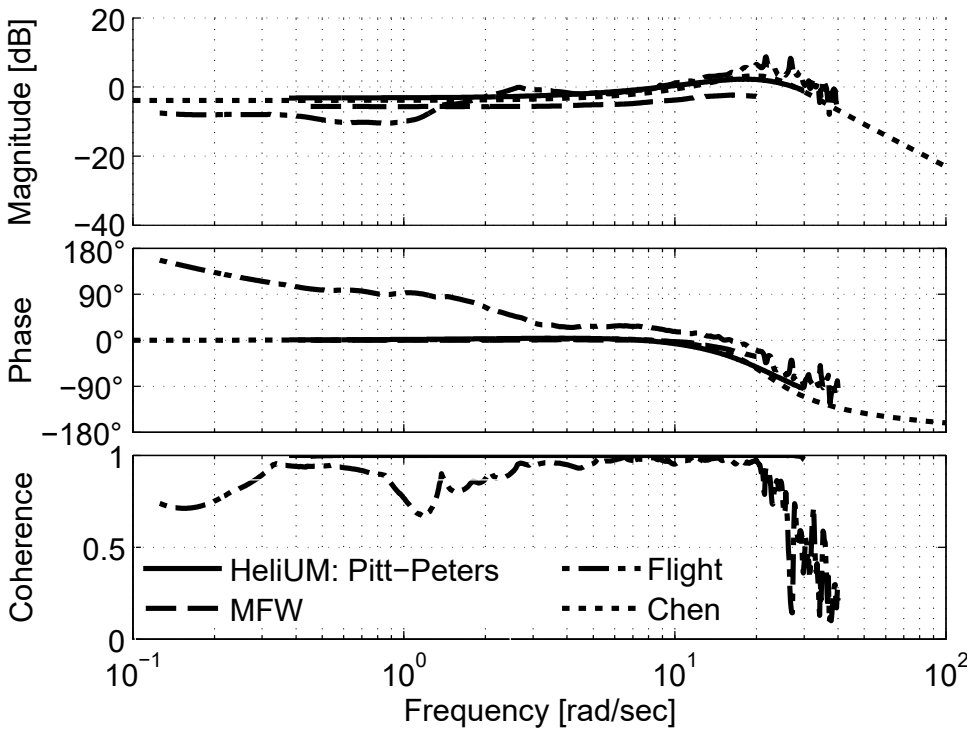

Figure 7.1: Coning β_0 response to collective θ_0 input.

tion model must be in state-space form, therefore not allowing the full nonlinear MFW or RFW simulations. A comparison between the full aircraft linearized models shows the effect of the various extracted inflow models on overall rotor system behavior. Figure 7.2 shows the coning response for the different inflow models used in HeliUM: the Peters inflow model, identified state-space model from MFW, the identified state-space model from RFW, as well as a static inflow model. The free wake state space models match very well with the Peters-He dynamic inflow model. The only noticeable difference is that the steady-state coning response of the RFW mode is slightly under-predicted. The static inflow model is inaccurate over the entire frequency range. At low frequency, the model over predicts the coning (and thus thrust) generated by the rotor, and the phase is incorrectly predicted at higher

frequencies. This provides further evidence that inflow dynamics are necessary for accurate computation of aircraft responses and that the inflow state space models identified are able to provide said dynamics.

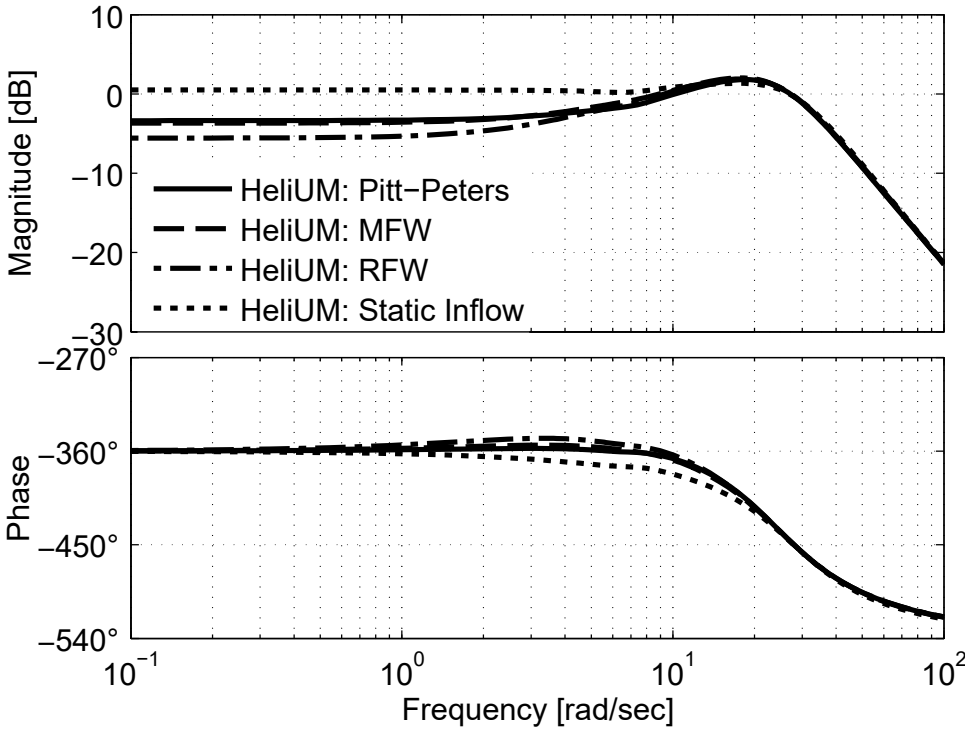

Figure 7.2: Comparison of coning response β_0 to collective θ_0 using different inflow models.

7.4 Coaxial Rotor

7.4.1 Hovering Aircraft Responses with Six-State Inflow Model

Next comparisons between coaxial rotorcraft modeled with different inflow models are performed. The linearized full aircraft results of this section were obtained using two types of state-space rotor inflow models in hover.

The first type, used for most results, is the state-space model extracted from the MFW using frequency domain system identification, as described in the Chap. 5. The model required nine time delays which became 26 time delay states after being converted using the Padé approximant (See Sec. 2.2.2.5). The simplicity of the 26 time delay equations ensures that they are simple for the ODE solver to solve and there is no noticeable effect on computation time. With the free-wake simplified into ODE form, the linearized analysis of the full aircraft now properly includes the effects of the wake and rotor-on-rotor interference. The second type of inflow model, used for comparison for a few coaxial results, is the "Climbing Lower Rotor" model (see Sec. 2.2.2), obtained by putting the lower rotor into a climb equivalent to the upper rotor trim average induced inflow from MFW.

Linearized analysis produce two sets of linearized state and controls matrices. One for the full aircraft using the identified inflow model from MFW (Eq.(5.3)) and the other for the full aircraft using the Climbing Lower Rotor theory. The state and controls matrices make up the full aircraft model (linearized) which describes the response of all the helicopter states to the pilot controls. Key aircraft responses can be shown as frequency responses. Figure 7.3 shows the heave velocity response to the symmetric collective or collective stick δ_{col}.

Very close agreement is shown between the two responses, meaning the identified hover inflow model aligns well with the Climbing Lower Rotor model. Figure 7.4 shows almost perfect agreement for the yaw rate response to foot pedal.

The roll and pitch response using the identified state-space model differ from the Climbing Lower Rotor model. As shown in Fig. 7.5, the MFW state-space inflow

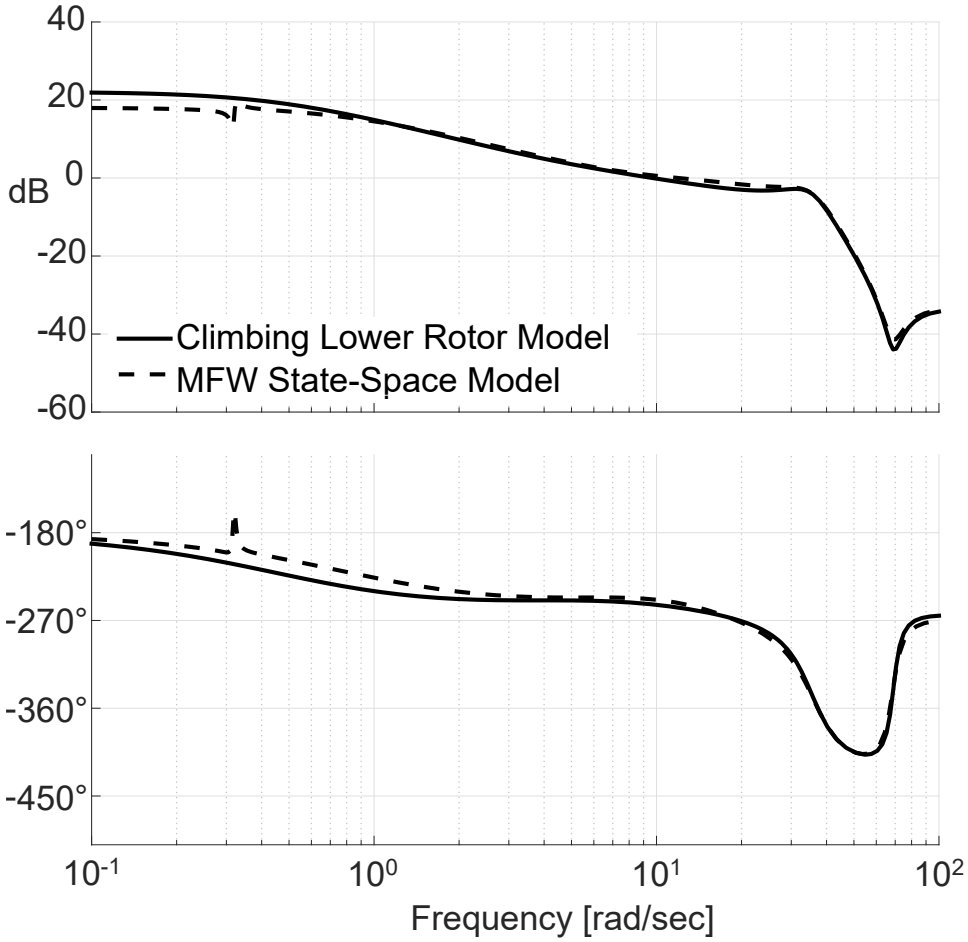

Figure 7.3: Responses of heave velocity w to δ_{col} showing comparison between MFW identified state-space model and Climbing Lower Rotor model; magnitude(top), phase(bottom)

model shows the aircraft having a higher response in roll due to δ_{lat} than is predicted with the Climbing Lower Rotor model with the lower rotor in climb. This response elevation occurs right around the frequency range of control system crossover (1-10 rad/sec), and would have a direct impact on predicted aircraft stability margins.

Figure 7.6 shows a similar result for the response of pitch rate to δ_{lon}. This response is not exactly the same as the roll rate due to the large variation in pitch and roll inertia of the aircraft. There are also small but non-zero off-axis responses,

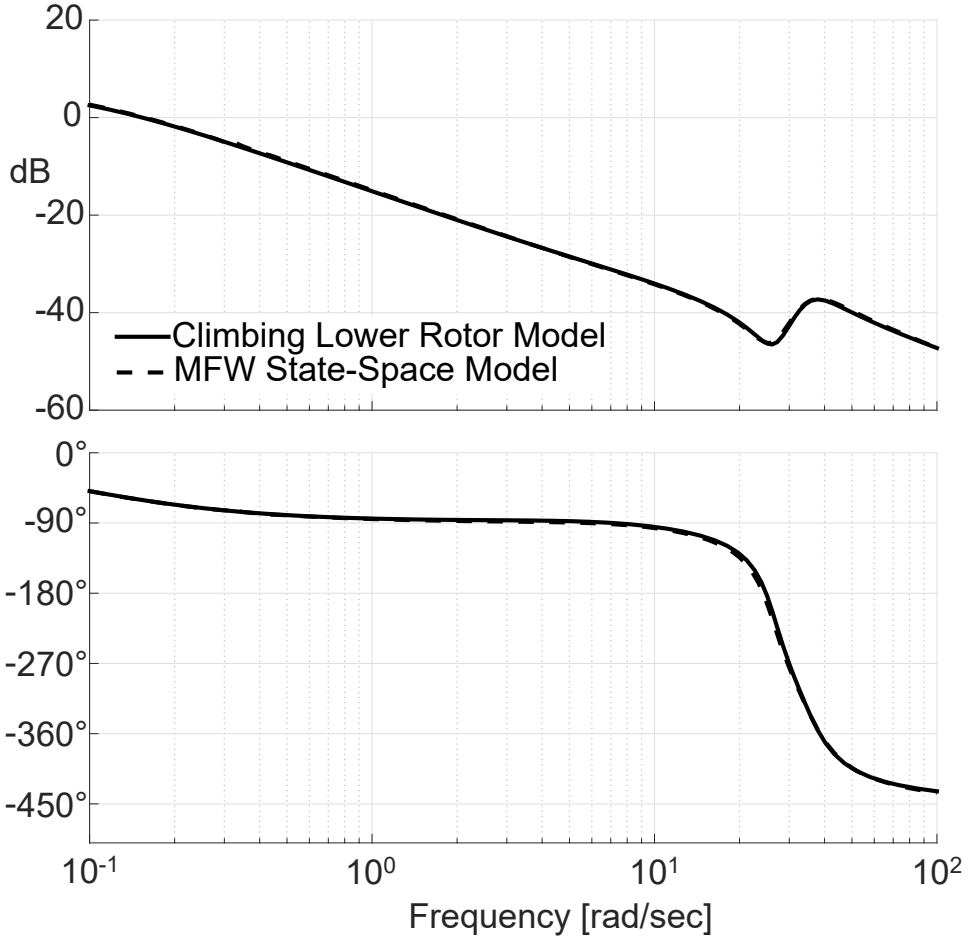

Figure 7.4: Responses of yaw rate r to δ_{ped} showing comparison between MFW identified state-space model and Climbing Lower Rotor model; magnitude(top), phase(bottom)

as in δ_{lat} causes some pitch rate and δ_{lon} causes some roll rate. This is indicative of the fact that the swash-plate angle is set to zero for both cases to allow comparison. Practically, the differences in the two responses may indicate that the design of the swash-plate phasing would be different depending on which inflow model is used.

Looking at the previous bode plots it is clear that the heave and directional responses are pretty much the same at high frequency, regardless of the inflow model used. The low frequency poles are different but poles above 10 rad/sec are essentially

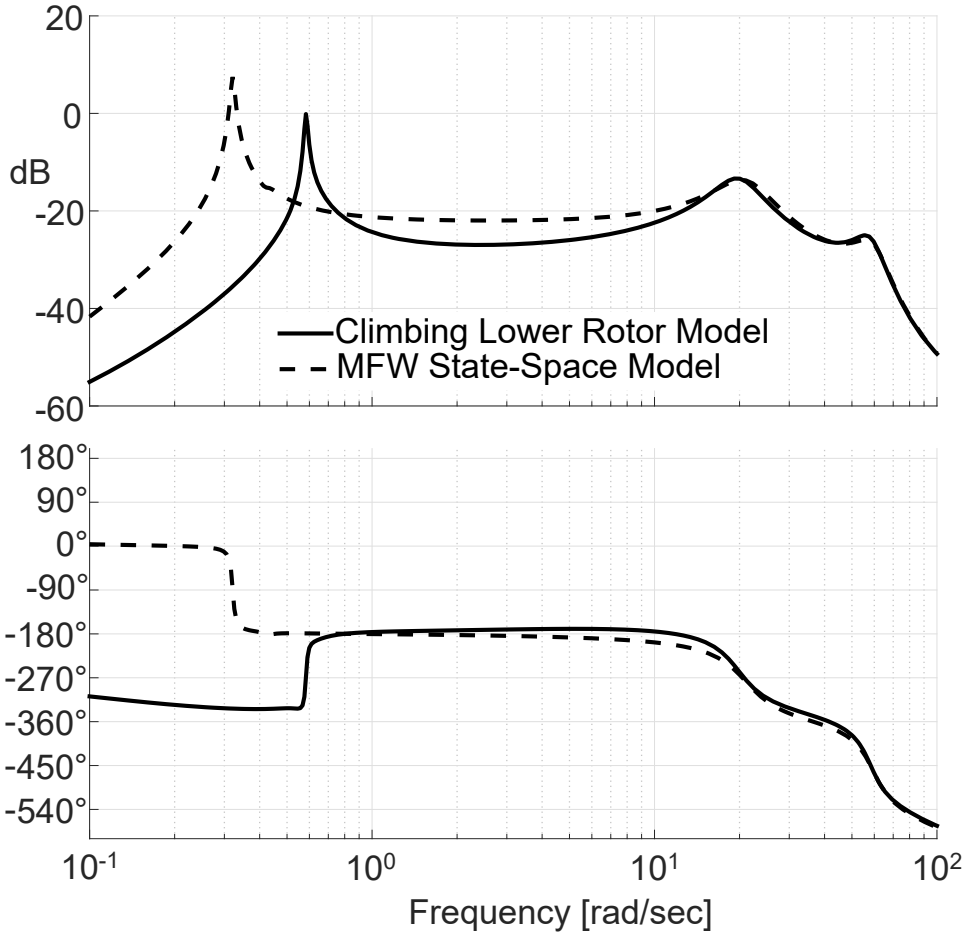

Figure 7.5: Responses of roll rate p to δ_{lat} showing comparison between MFW identified state-space model and Climbing Lower Rotor model; magnitude(top), phase(bottom)

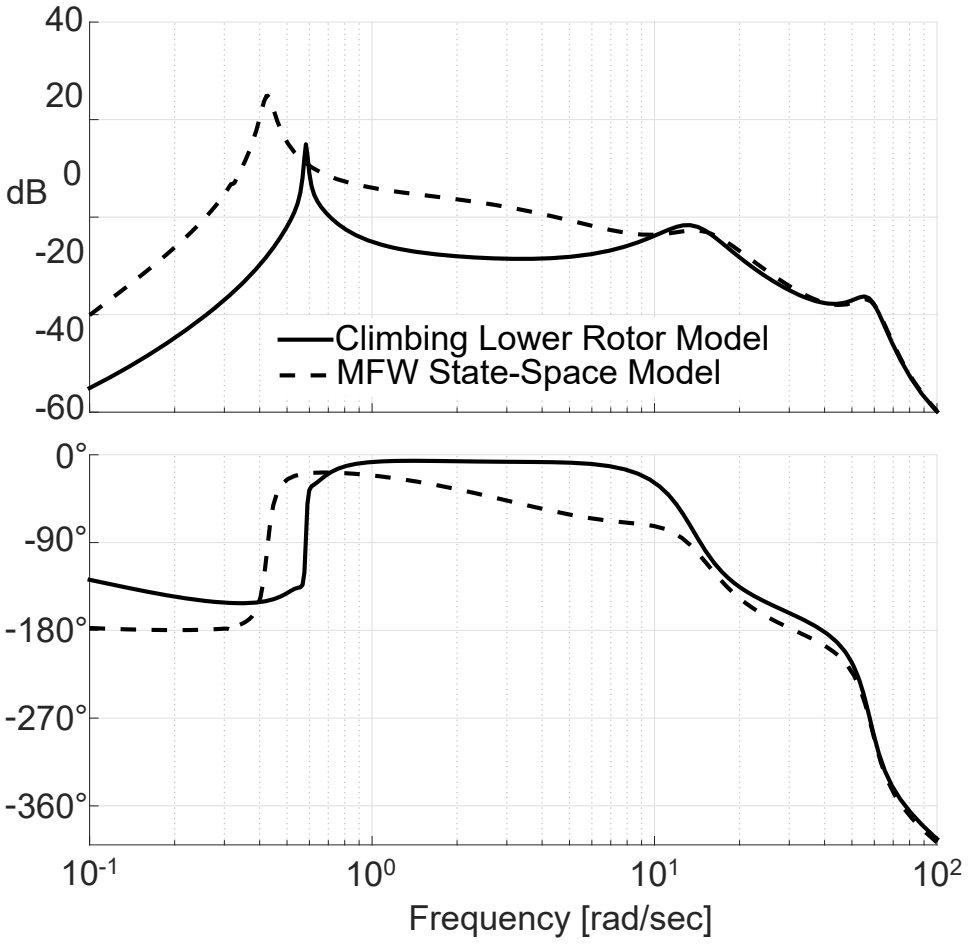

Figure 7.6: Responses of pitch rate q to δ_{lon} showing comparison between MFW identified state-space model and Climbing Lower Rotor model; magnitude(top), phase(bottom)

unchanged. This is further shown in Tables 7.1 and 7.2, which show the poles of the linearized state matrices for the two different systems. The high frequency rotor modes are very close in value when using either inflow model.

Table 7.1: Aircraft poles with Climbing Lower Rotor model.

Freq. (rad/sec)	Pole		Description
0	0		heading
0.08656	-0.08656		heave
0.478	-0.478		yaw
0.5833	0.007835	± 0.5833i	phugoid
0.5858	0.0852	± 0.5796i	phugoid
2.788	-2.788		spiral
4.18	-4.18		pitch
10.29	-10.29		inflow
11.44	-11.44		inflow
13.68	-3.705	± 13.17i	Regressive Flap
19.28	-19.28		inflow
19.79	-19.79		inflow
19.87	-3.747	± 19.51i	Regressive Flap
21.4	-21.4		inflow
21.71	-21.71		inflow
34.71	-7.631	± 33.86i	Coning Flap
35.36	-7.975	± 34.45i	Reactionless Flap
35.43	-7.34	± 34.66i	Reactionless Flap
35.53	-6.849	± 34.86i	Coning Flap
57.92	-7.262	± 57.46i	Progressive Flap
58.34	-6.572	± 57.97i	Progressive Flap

Table 7.2: Aircraft poles with MFW identified state-space model inflow.

Freq. (rad/sec)	Pole		Description
0	0		heading
0.08606	-0.08606		heave
0.321	-0.005125	± 0.3209i	phugoid
0.4252	0.02015	± 0.4247i	phugoid
0.8566	-0.8566		yaw
3.23	-3.23		pitch
3.799	-3.798	± 0.0969i	inflow
3.853	-3.853		inflow
3.853	-3.853		inflow
4.455	-4.455		pitch
4.93	-4.93		pitch
7.408	-7.408		inflow
9.985	-9.179	± 3.931i	inflow
10.89	-10.89		inflow
12.44	-10.93	± 5.95i	inflow
13.62	-12.93	± 4.284i	inflow
13.79	-13.79		inflow
13.79	-13.79		inflow
14.43	-11.58	± 8.604i	inflow
14.94	-4.736	± 14.17i	Regressive Flap
21.05	-4.601	± 20.54i	Regressive Flap
21.85	-21.85		inflow
25.54	-22.07	± 12.86i	inflow
28.47	-23.85	± 15.54i	inflow
34.83	-8.367	± 33.81i	Coning Flap
35.08	-30.72	± 16.93i	inflow
35.36	-7.804	± 34.49i	Reactionless Flap
35.39	-7.576	± 34.57i	Reactionless Flap
35.92	-7.663	± 35.1i	Coning Flap
41.47	-35.94	± 20.68i	inflow
42.91	-37.06	± 21.63i	inflow
49.94	-49.94		inflow
58.92	-7.512	± 58.43i	Progressive Flap
59.3	-7.376	± 58.84i	Progressive Flap
68.53	-68.53		inflow
88.76	-88.73	± 2.535i	inflow

7.4.2 Aircraft Responses with Twelve-State Inflow Models

Next comparisons are made with coaxial rotorcraft modeled with the higher order state-space models extracted from the MFW, as described in the Chap. 6, for both hover and forward flight (200 kts). For hover the identified modeled is compared against the "Dynamic Climb" model described in Sec. 2.2.2. For forward flight, the identified model is compared against the "Isolated Rotor" model, also described in Sec. 2.2.2.

The identified state-space inflow models were inserted into HeliUM as an option for the calculation of the inflow. Since no time delays were used, no Padé approximations were needed, and the system need only 12 inflow states. A linearized model of the full helicopter was extracted using linearized analysis at each flight condition (hover and 200 kts), which will be referred to as the MFW ID aircraft models. This MFW ID aircraft model describes the response of all the helicopter states to the pilot controls. A similar linearized model of the helicopter can be created using the Dynamic Climb (DC) inflow model for hover and Isolated Rotor inflow model for 200 knots, which were described in Sec. 2.2.2. These linearized full aircraft models provide a basis of comparison for the free-wake based identification models and dynamic inflow based approaches (Dynamic Climb and Isolated Rotors) and will be referred to the Dynamic Climb aircraft model and the Isolated Rotor aircraft model. The bare airframe frequency responses such as roll rate to lateral swashplate, p/δ_{lat}, can be shown and compared and key poles of the rotor dynamics and body dynamics can be identified. These dynamics will be different depending

on which inflow model is used. Note that for the rest of this chapter the models described are all full aircraft (linearized) models unless explicitly stated as an inflow model.

7.4.2.1 Forward Flight Bare-airframe Responses

The dynamic response of the two aircraft models in forward flight, one with the Isolated Rotors inflow model and the other with the MFW Identified inflow model can now be compared. Figure 7.7 shows the bare airframe response of pitch rate to longitudinal swashplate, q/δ_{lon}. Figure 7.8 shows the bare airframe response of roll rate to lateral swashplate, p/δ_{lat}.

Figure 7.9 shows the bare airframe response of roll rate to lateral swashplate, p/δ_{lat}. Figure 7.10 shows the bare airframe response of roll rate to lateral swashplate, p/δ_{lat}.

The two models have quite different characteristics. Interestingly, The MFW ID model has more control power than the Isolated Rotor model in roll and yaw but has less control power in pitch and heave. Also of particular note is that Figs. 7.8 and 7.10 do have 2-3 decibel (25-40%) differences between 5 and 20 rad/sec indicating that the inflow models do have a strong influence directly in the flight dynamics range of interest.

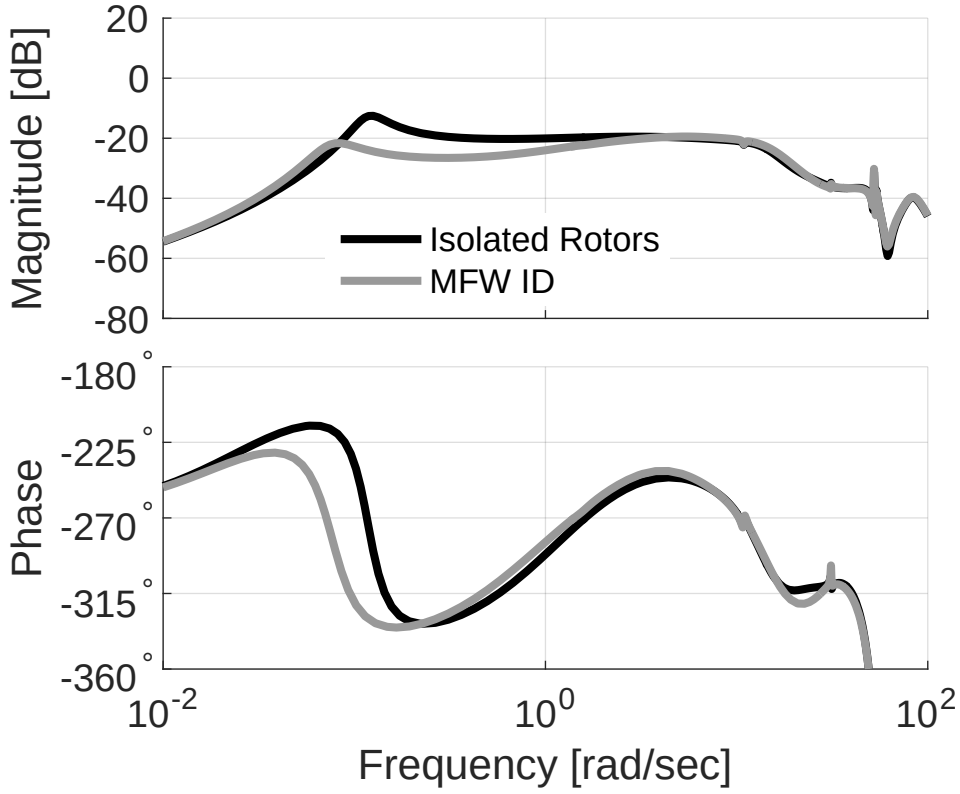

Figure 7.7: Bare Airframe: pitch rate (deg/s) response to longitudinal swashplate: q/δ_{lon}

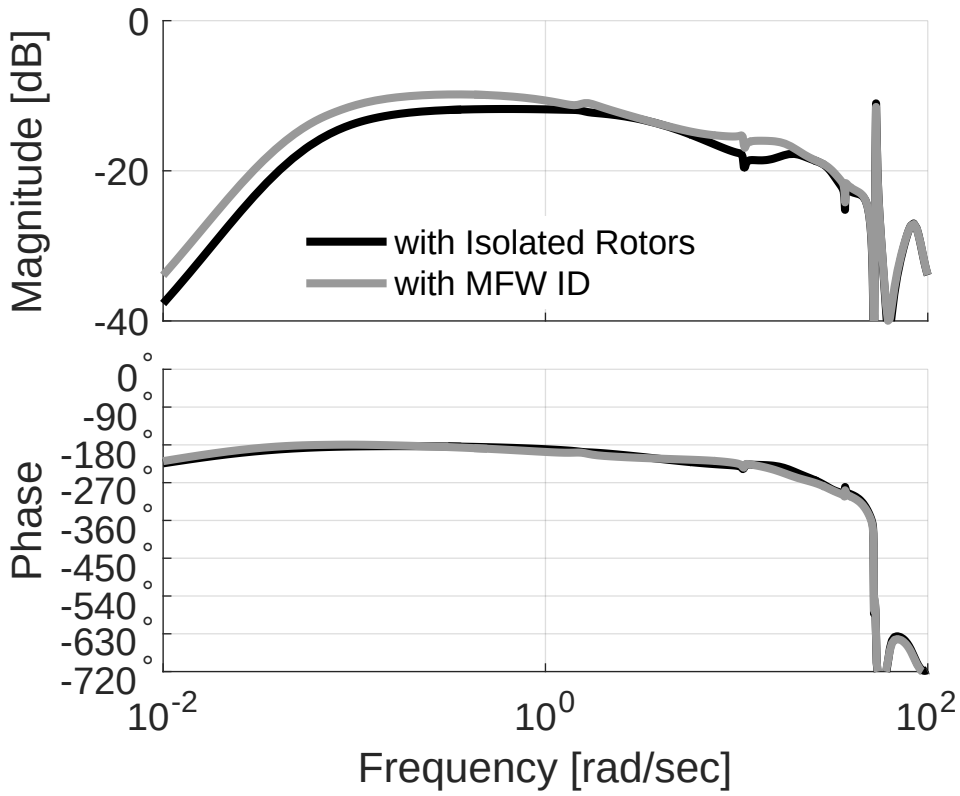

Figure 7.8: Bare Airframe: roll rate (deg/s) response to lateral swashplate: p/δ_{lat}

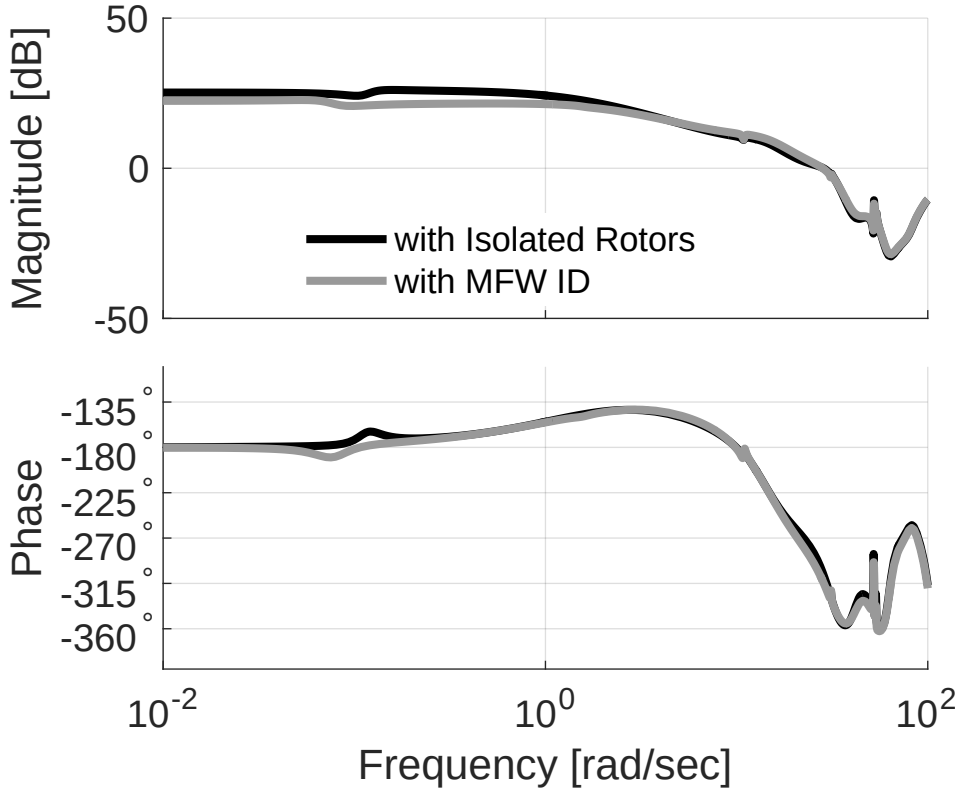

Figure 7.9: Bare Airframe: heave rate (ft/s) response to symmetric collective swashplate: w/δ_{col}

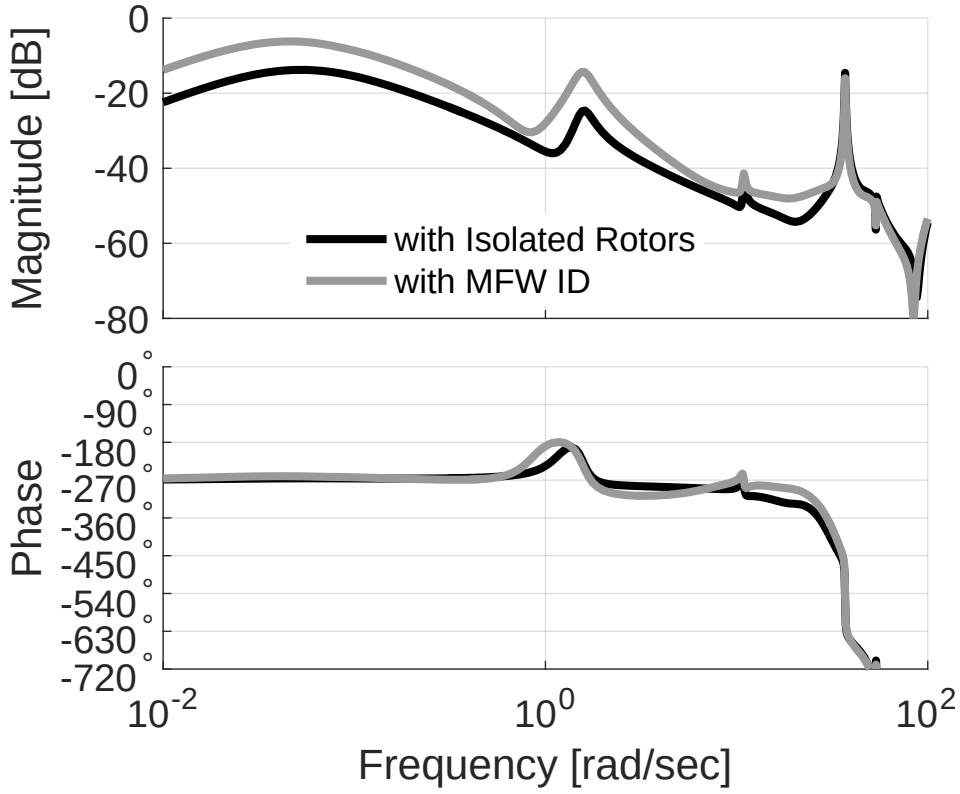

Figure 7.10: Bare Airframe: yaw rate (deg/s) response to differential collective swashplate: p/δ_{lat}

7.4.2.2 Hover bare-airframe responses

The dynamic response of the two aircraft models, one with the Dynamic Climb (DC) inflow model and the other with the MFW Identified inflow model can now be compared. Figure 7.11 shows the bare airframe response of roll rate to lateral swashplate, p/δ_{lat}. The proceeding analysis is for the lateral axis only, the other axes have been stabilized using coupling-numerators as described previously.

The two models have quite different characteristics. The response of the MFW ID model tends to be a lot flatter than that of the DC model. Of particular note is that the regressive flap mode of the DC model is far more lightly damped than in the MFW ID model ($[\zeta, \omega_n] = [.175, 17.7]$ vs. $[.288, 19.7]$). Also, the low frequency body mode of the DC model is unstable whereas it is not for the MFW ID model ($[\zeta, \omega_n] = [-.176, 0.756]$ vs. $[.192, .27]$).

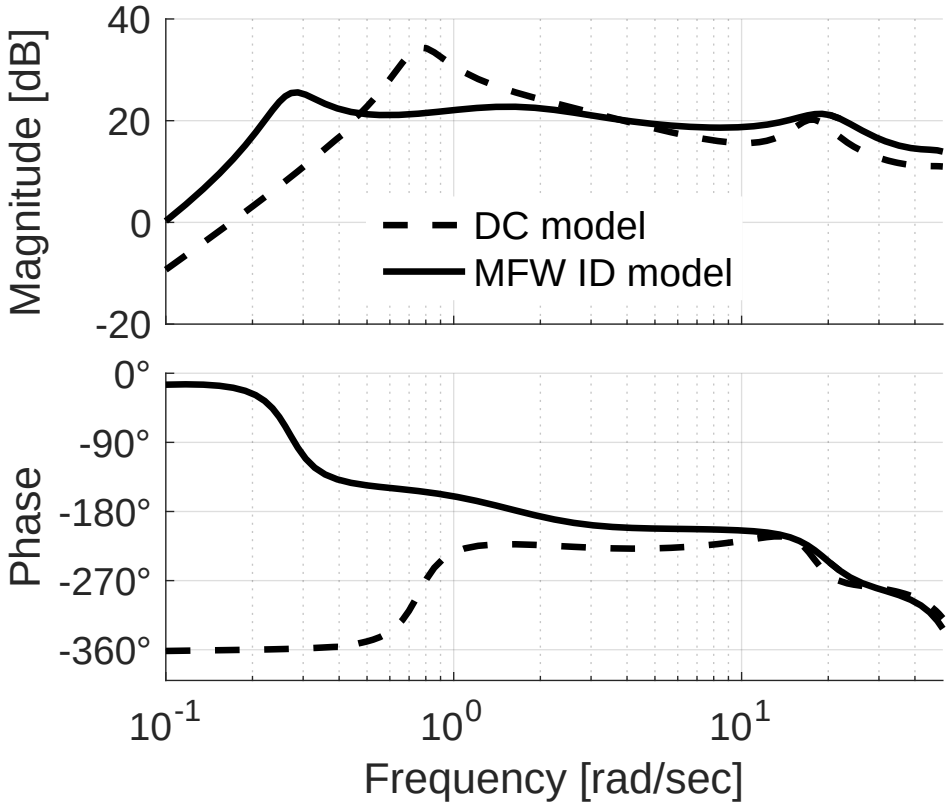

Figure 7.11: Bare Airfame: roll rate (deg/s) response to swashplate: p/δ_{lat}

7.5 Impact of Dynamic Inflow Modeling on Control Design in Hover

With the Hover MFW ID model and the Dynamic Climb model, explicit model-following control (EMF) systems were designed and compared. Explicit model-following is a well established control method in which the controller attempts to follow the response of a prescribed model with desirable attributes [121–123]. The basic elements and form of the EMF controller are shown in Fig. 7.12.

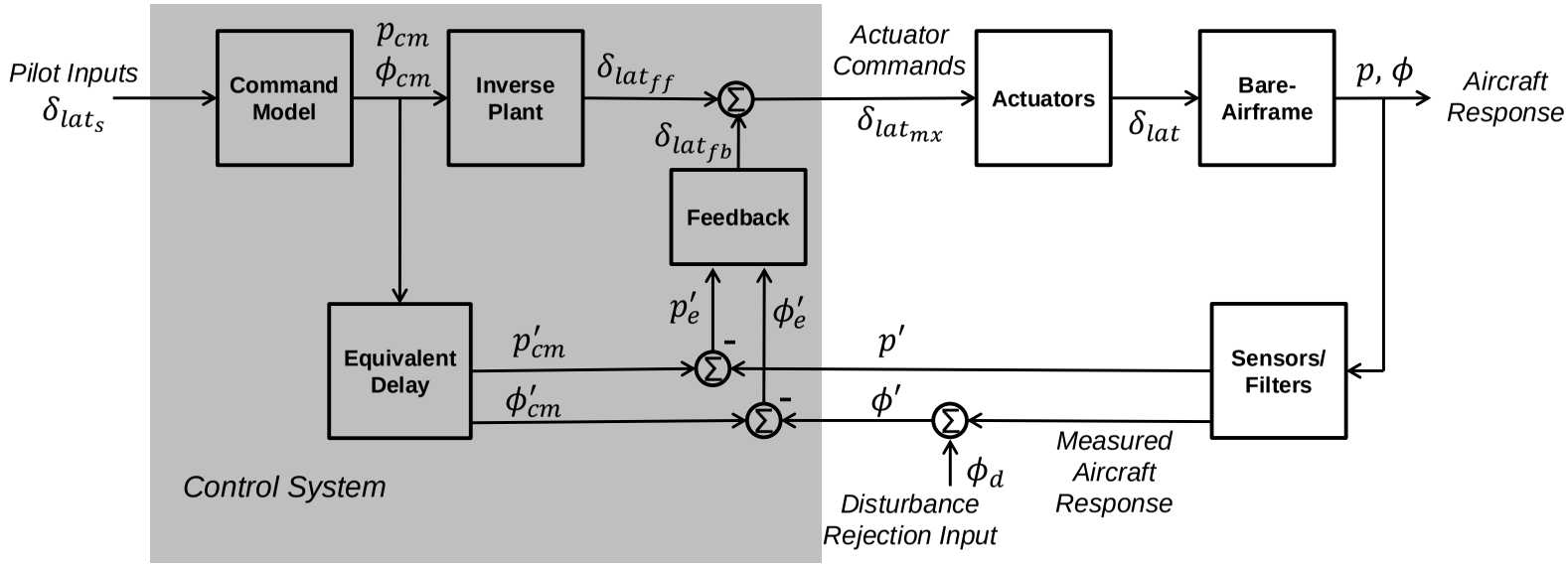

Figure 7.12: Explicit Model-Following Scheme adapted from Ref. 122

This control system first takes in commands from pilot inputs p/δ_{lat_s} and converts them into desired aircraft responses by way of a command model. The commanded aircraft response is then fed through an inverse plant to obtain feed-forward actuator commands $\delta_{lat_{ff}}$. The inverse plant is usually a low order (first or second) transfer function fit to the bare-airframe response in the flight dynamics frequency range of interest, from about 1 to 12 rad/sec. This feed-forward command is mixed with feed-back commands $\delta_{lat_{fb}}$ given by a proportional–integral–derivative (PID) controller. These mixed commands $\delta_{lat_{mx}}$ are fed into the actuators for the swashplate and then fed into the Bare-Airframe model P to produce the aircraft response. This response is sensed by sensors and filtered to produce measured aircraft responses. These are mixed with equivalent delays, used to synchronize the feedback with the feed forward, before being fed into the PID feedback gains.

The baseline case is the Dynamic Climb (DC) model, which represents a simpler approximation that a designer might utilize without identification from a high fidelity simulation. The MFW ID model is considered a more rigorous flight dynamics model and is considered to be a better representative of flight. Therefore a design optimized to the DC aircraft model but analyzed on the better representative model, gives an idea for how poor initial controller design could be. So to compare the impact of using the simplified inflow representation, three cases were presented in this investigation:

case (A) - An optimal controller for the DC model applied to the DC model

case (B) - The same optimal controller for the DC model applied to the MFW ID model

case (C) - An optimal controller for the MFW ID model applied to the MFW ID model

All three cases used the same explicit model-following form shown in Fig. 7.12 and differed in their bare-airframe model (P), the inverse plant ($\hat{P}^{-1}$) and equivalent delay for synchronization (τ_{Eq}), and the feedback PID gains. Case(A) and Case(B) differ only in the plant. Case(C) differs from Case(A) in the plant, inverse plant and equivalent delay. The command model and sensor and actuator dynamics were the same between the three cases.

To allow for the optimization and analysis of a single axis, coupling numerators [123, 124] were used to constrain the pitch, heave, and yaw axes for both the DC model and the MFW ID model. This left only the roll axis free. Coupling numerators are a way of constraining responses by assuming tight feedback from one response to a control input. This freezes the constrained response while leaving the dynamics of the other axes free. For this investigation, the coupling numerator used was:

$$\frac{p}{\delta_{lat}}(s)\Bigg|_{\substack{q \to \delta_{lon} \\ r \to \delta_{ped} \\ w \to \delta_{col}}} = \frac{N^{p}_{\delta_{lat}} N^{q}_{\delta_{lon}} N^{r}_{\delta_{ped}} N^{w}_{\delta_{col}}(s)}{N^{q}_{\delta_{lon}} N^{r}_{\delta_{ped}} N^{w}_{\delta_{col}}(s)} \tag{7.21}$$

For case (A), the inverse model was calculated by fitting a 0^{th} over 1^{st} transfer function to the portion of the bare airframe, plus sensor and actuator dynamics, in the frequency range of 1-12 rad/sec. The equivalent time delay of the system was

found by removing the command model and the feedback loop and evaluating the response from stick to roll rate (p) in the 1-12 rad/sec frequency range. Because the system in this state is mostly the inverse model multiplied by the model, it is a relatively flat frequency response ($\hat{P}^{-1}P \approx 1$) with a lot of phase roll-off. This can be fit with a gain of one and a time delay, which becomes the synchronization delay [122].

The flight control design software CONDUIT [122] was used to optimize the controllers, so that they meet the quantitative flight control requirements to achieve desirable handling qualities as defined in ADS-33E [90] as well as stability and robustness metrics [125–128] . The specifications are listed in Table 7.3 and are each discussed in detail in Ref. 122. Design margin optimization (DMO) is then performed to maximize the minimum cross-over frequency and the disturbance rejection bandwidth (DRB) to achieve the maximum performance attainable from the control system [122]. The DMO increases the minimum crossover and DRB Level 1/Level 2 specification boundary until a feasible solution that meets all specifications can no longer be met.

With the different aircraft models, the lateral axis broken loop responses, $\delta_{lat_{fb}}/\delta_{lat_{mx}}$, and associated stability and robustness metrics can be compared. Similarly, with the two optimized controllers, the closed-loop comparisons p/δ_{lat_s} between the cases can be performed to look at performance metrics such as bandwidth. The roll angle disturbance rejection frequency response, ϕ'/ϕ_d, is shown to quantify adequate rejection. Closed-loop lateral stick impulse responses and roll angle distur-

Table 7.3: Controller Optimization Specifications for Roll Axes; adapted from Ref. 122

Description	Motivation	Short Name	Source
Hard Constraints			
All eigenvalues in left-half plane	Stability	EigLcG1	Generic
Nichols margin for loop broken at mixer input	Stability	NicMgG1	Ref. 125
Gain and phase margin for loop broken at mixer input	Stability	StbMgG1	Ref. 126
Soft Constraints			
Roll attitude Bandwidth	Handling Qualities	BnwAtH1	Ref. 90
Performance of aircraft as compared to command model; Model-following control system only	Handling Qualities	ModFoG2	Generic
Roll attitude disturbance rejection; Attitude hold	Hold Characteristics	DrbRoH1	Ref. 127
Disturbance rejection peak magnitude; Attitude hold	Loads, Ride Quality	DrpAvH1	Ref. 127
Eigenvalue damping ratio $\zeta > .1$ for freq = 4-20 rad/sec	Handling Qualities, Loads	EigDpG1	Ref. 90
Eigenvalue damping ratio $\zeta > .35$ for freq = 0.5-4 rad/sec	Handling Qualities, Loads	EigDpG1	Ref. 90
Open-Loop Onset Point spec for piloted input	Pilot-induced Oscillation	OlpOpG1	Ref. 128
Open-Loop Onset Point spec for disturbance input	Limit Cycle	OlpOpG1	Ref. 128
Minimum crossover freq for loop broken at mixer input	Robustness	CrsMnG2	Generic
Summed Objectives			
Minimize crossover freq for loop broken at mixer input	Actuator Activity	CrsLnG1	Generic
Minimize mixer input RMS for pilot input	Actuator Activity	RmsAcG1	Generic
Minimize mixer input RMS for disturbance input	Actuator Activity	RmsAcG1	Generic

bance step responses are shown for each model to demonstrate the model following and disturbance rejection performance in the time domain.

7.5.1 Control Optimization Results

The linearized MFW ID and DC flight dynamics models were used to create three different control evaluation cases, as previously stated:

case (A) - An optimal controller for the DC model applied to the DC model

case (B) - The same optimal controller for the DC model applied to the MFW ID model

case (C) - An optimal controller for the MFW ID model applied to the MFW ID model

case (A) shows the type of design a designer would get without using a system identification technique and rather relying on simpler approximations. Case (B) shows how the design from case (A) would work when utilized in a more realistic flight simulation. Case (C) shows the type of controller that could be designed if a designer optimized to a model identified from higher fidelity aerodynamic solvers. The feedback block in figure 7.12 is a simple PID controller with proportional, integral and derivative gains, named K_ϕ, K_{I_ϕ}, and K_p respectively. Their values for each of these cases, after optimization, are listed in table 7.4. Also shown here are the equivalent time delays.

Table 7.4: Optimal Controller Parameters.

Parameter	cases (A) & (B)	case (C)
K_P	0.0413	0.0326
K_ϕ	0.303	0.582
K_{I_ϕ}	0.212	0.626
τ_{Eq}	0.0265	0.0454

Table 7.5: Optimal Controller Characteristics.

Characteristic	case (A)	case (B)	case (C)
ω_c (rad/sec)	3.53	3.47	5.38
GM (dB)	7.2	6.25	6.00
PM (deg)	45.0	73.0	47.7
min ζ (4-20 rad/sec)	0.1048	0.148	0.193
ω_{DRB} (rad/sec)	1.89	1.97	2.91
DRP (dB)	4.38	2.35	4.87

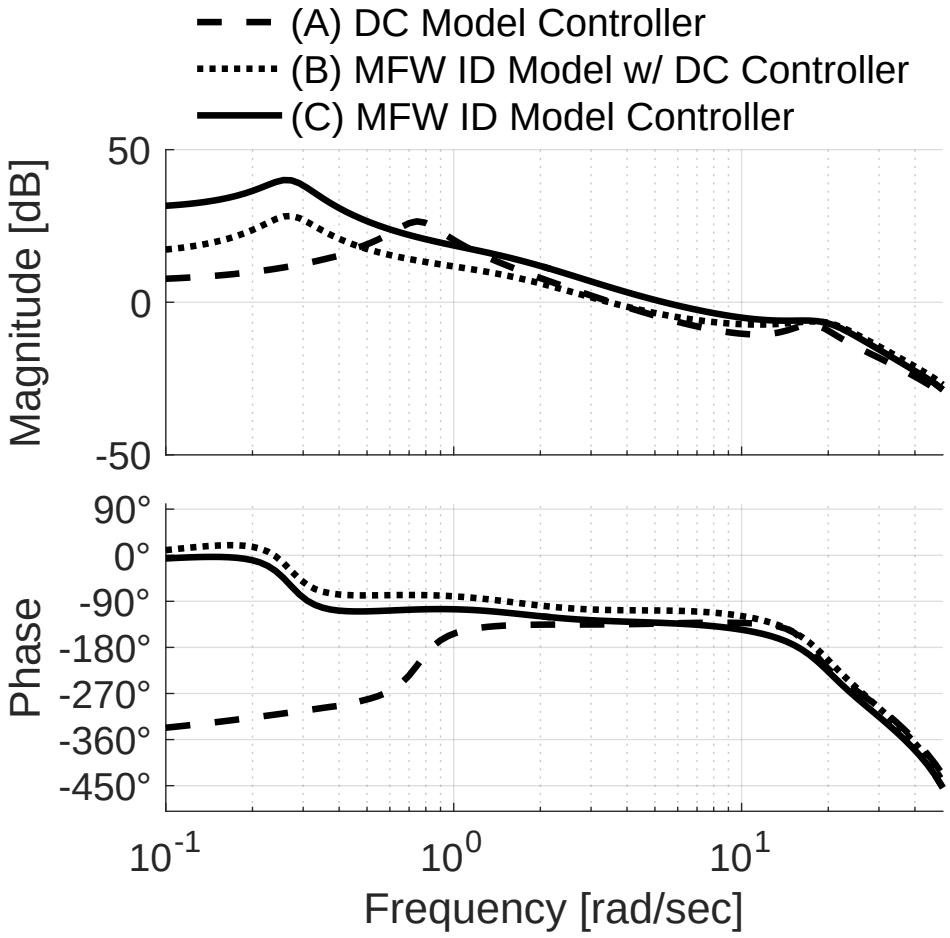

Figure 7.13: Broken Loop: $\delta_{lat_{fb}}/\delta_{lat_{mx}}$

Figure 7.13 shows the lateral-axis broken-loop response, $\delta_{lat_{fb}}/\delta_{lat_{mx}}$. This plot shows 3 lines which represent the three cases defined above. Case (B) and (C)

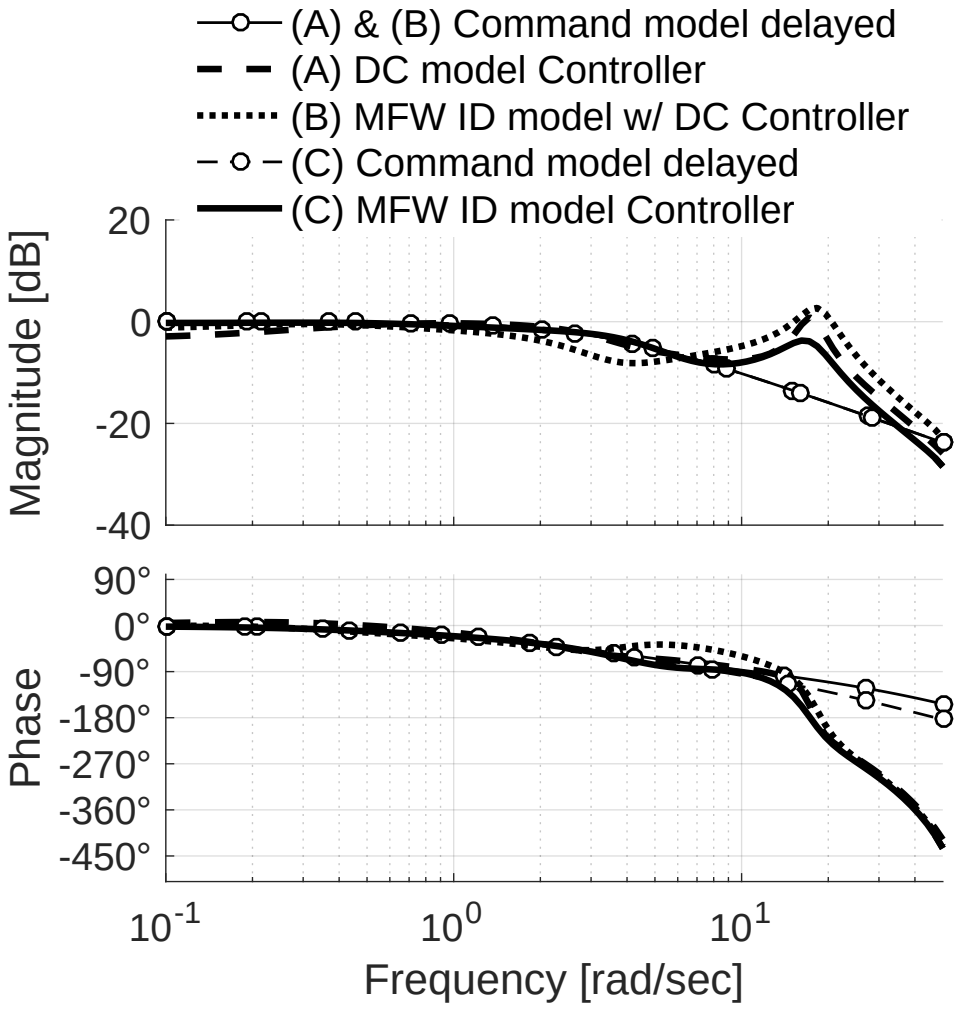

Figure 7.14: Closed Loop: p/δ_{lat_s}

have the same MFW ID model for the bare airframe, but the different feedback gains provide different broken loop responses. All the models are able to have good stability margins, and the MFW model and controller was able to reach the highest crossover frequency. This is because the DC model has the lightly damped regressive lag modes, which limit the allowable gains before stability margin boundaries are reached.

Figure 7.14 shows the closed loop response of roll rate to lateral stick, p/δ_{lat_s}. There are also an additional two lines labeled as the commanded lines which show what the command model is requesting after the given equivalent time delay, $\theta'_{cm}/\delta_{lat_s}$. These lines differ only in their phase response due to the different equivalent delay for each case. With a perfect controller, the other lines should lay on top of the commanded response, and so the difference provides a metric for the model-following capability of the system. The regressive flap mode again plays prominently into these responses and is the limiting factor in the performance of the controllers. This is a characteristic similar to that seen in Ref. 38.

The controllers reduce the damping ratio of the regressive lag mode. The damping of the mode by the DC model controller (case(A)) is reduced from $\zeta = 0.175$ to $\zeta = 0.1048$. The DC model controller (case (A)) works well in a broad frequency range up to the regressive lag mode. At low frequency the response of the DC model controller tends to lie slightly lower than the commanded value. Additional integrator gain would be required to improve this response, but the current analysis ties the integral/proportion gain ratio to be 1/5 of crossover frequency. This minimizes phase loss at crossover from the integrator [122].

In cases (B) and (C), the bare-airframe response is greater so model following fairs better at low frequency. Case (B) uses the inverse model from the DC model and therefore has degraded model following performance, since the bare-airframe responses are different. Case (C) allows for better model following across the frequency range with an updated inverse. Because the damping ratio for the bare-airframe lag modes starts at $\zeta = 0.28$ there is more room for optimization, and more latitude

for increasing the integrator gain due to the higher crossover frequency. In fact, that damping ratio is only reduced to $\zeta = 0.193$ and is not really the limiting factor of the controller optimization and therefore allows the DMO to achieve higher performance.

In the time domain, various responses can also be compared. Figure 7.15 shows the response of the helicopter to a lateral stick impulse. There are three different plots to show the three different cases. The dashed line on each indicates the lateral stick position in degrees over time. The dotted line shows the desired response produced by the command model. The solid black line shows the aircraft response, with the controller attempt to track the dotted line.

Case (A), for the DC controller applied to the DC model, is the top plot. The response does not capture the max commanded response and also has quite a bit of overshoot when returning to steady state. It also shows oscillations with periods of around 1/3 of a second, which correspond to the frequency of the low damped regressive flap mode. Case (B), for the DC controller applied to the MFW ID model, is shown in the middle plot and clearly contains sustained oscillations with the response not tracking the command model, as was suggested by Fig. 7.14. Case (C), for the MFW ID controller applied to the MFW ID model, is shown in the bottom plot and shows much better model following. There is still an influence from the regressive flap mode but it is much smaller due to the mode's higher damping.

The integration of this time response provides the roll angle response to the same lateral stick input, and this is shown in Fig. 7.16 for each of the three cases. Here the dashed line indicates the desired roll angle from the command model, which

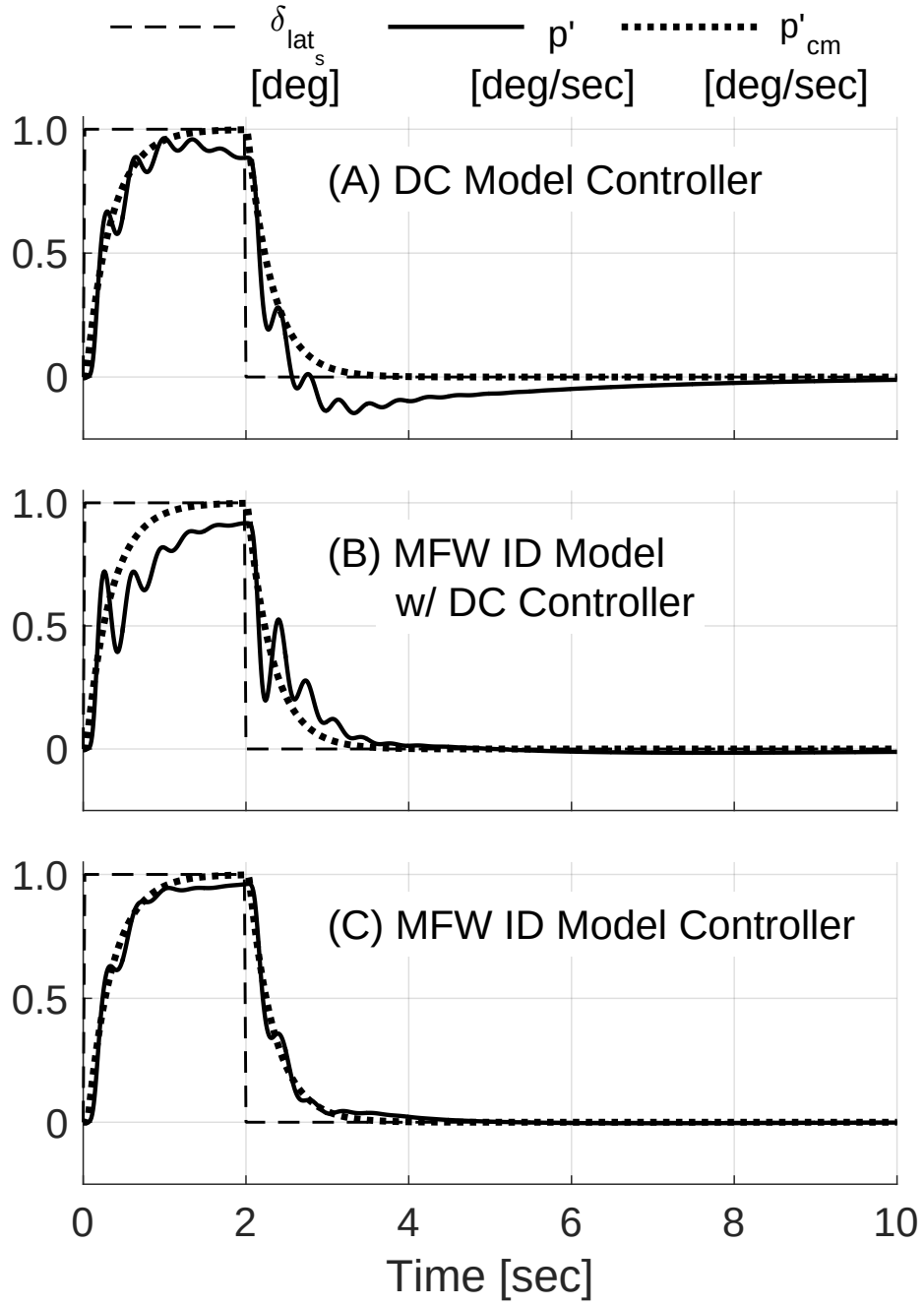

Figure 7.15: Comparison of lateral stick δ_{lat_s} impulses of three different cases. p' (measured roll rate) aircraft response is shown and compared to the p'_{cm} (commanded roll rate from the command model).

is to approach and hold a roll angle of about 2 degrees. Case (A) is shown in the top plot and the solid line indicates the actual measured roll angle of the aircraft. Case

(A) shows significant inability to track the desired steady-state roll angle, steadying out at a roll angle which is about 71% of the desired angle. Case (B), in the middle plot, shows that even though the model following is worse, a better response is still produced, achieving about 90% of the desired roll angle. Case (C) (the bottom plot) shows the best tracking, achieving about 98% of the desired roll angle.

Figure 7.17 show the disturbance rejection frequency response ϕ'/ϕ_d for the 3 cases. Case (A), shown by the dashed line, has a disturbance rejection bandwidth of $\omega_{DRB} = 1.89$ rad/sec and a disturbance rejection peak of $DRP = 4.38$ dB. it is relatively flat at low frequency with a value around -10 dB meaning that a disturbance attenuation of only roughly 30% is expected. Case (B) and (C) (dotted and solid) have disturbance rejection bandwidth of $\omega_{DRB} = 1.97$ rad/sec and $\omega_{DRB} = 2.91$ rad/sec respectively. Their disturbance rejection peaks are $DRP = 2.35$ dB and $DRP = 4.87$ dB. The control systems for these cases do a better job at rejecting low frequency disturbances while still giving a small peak response. All of these disturbance rejection bandwidths are well above the current criteria for the roll axis, which is $\omega_{DRB} = 0.9$ rad/sec [122].

Step disturbances to roll angle are shown in Fig. 7.18 to demonstrate the disturbance rejection. Once again there are three plots comparing the three cases. The input disturbance is a 1 degree disturbance in roll angle, shown by the dashed line. The desired response would be controller to completely and quickly reject this disturbance and produce a zero measured roll angle ϕ' response (solid line). Case (A), in the top plot, shows the 30% steady-state disturbance rejection error that was seen in Fig. 7.17, as well as about 20% overshoot on the return to steady state.

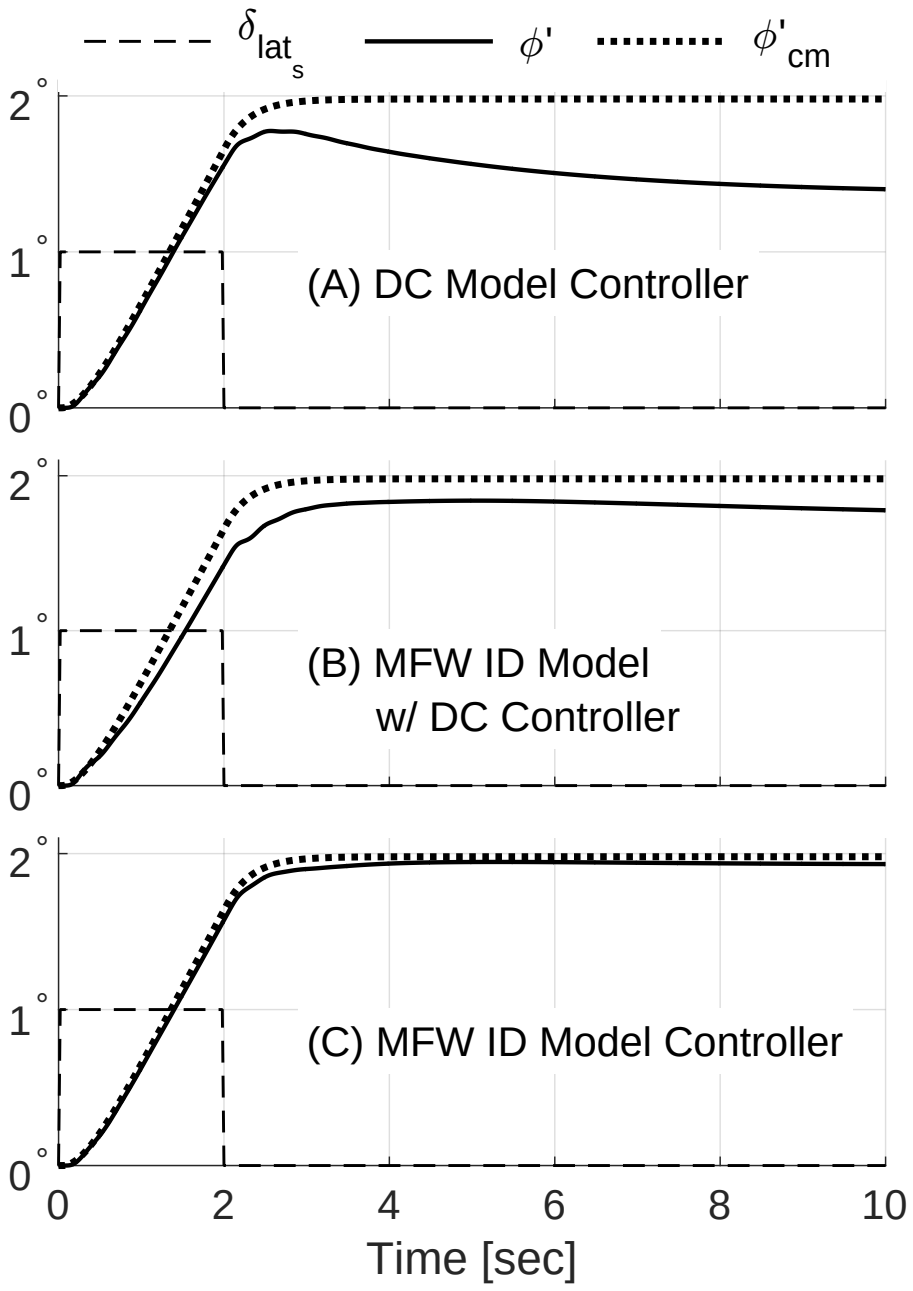

Figure 7.16: Comparison of lateral stick δ_{lat_s} impulses of three different cases. ϕ' (measured roll angle) aircraft response is shown and compared to the ϕ'_{cm} (commanded roll angle from the command model).

The middle plot, showing case (B), presents better overall rejection qualities. The error is reduced to about 10% and the undershoot is gone because of the much lower

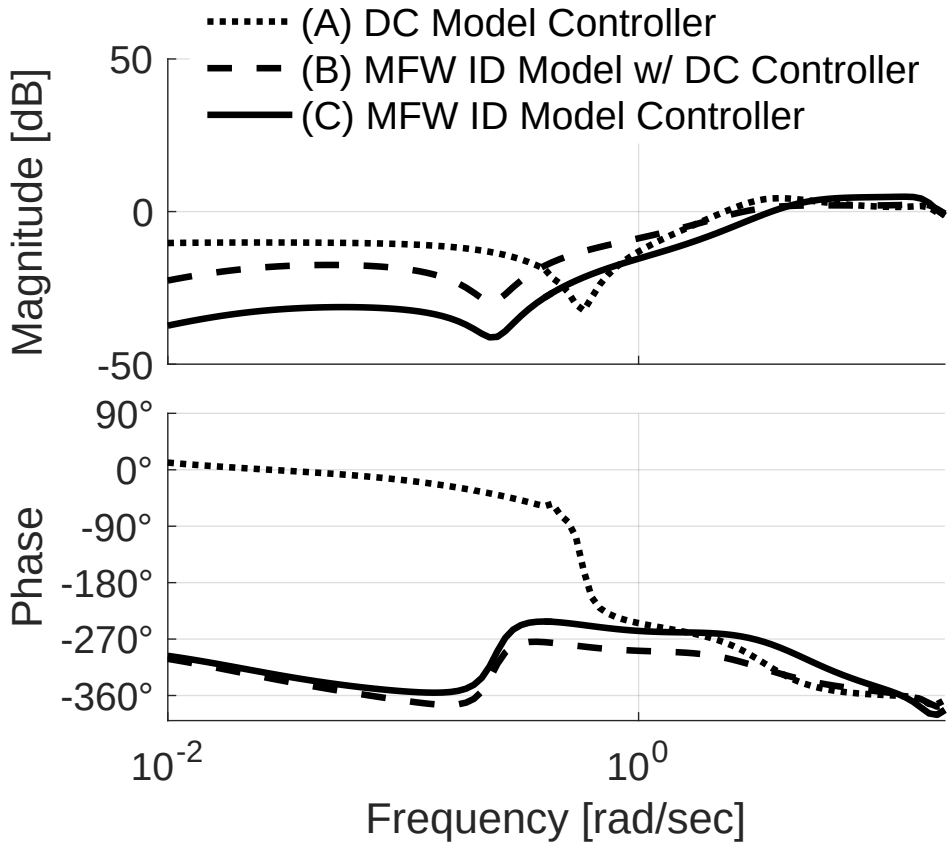

Figure 7.17: Disturbance Rejection to ϕ Disturbances for different models, ϕ'/ϕ_d

disturbance rejection peak. The bottom plot shows the disturbance rejection of the MFW ID model controller (case (C)), which has excellent steady-state rejection. The rejection also occurs quite a bit faster for this case, but the undershoot is about equivalent to that of case (A).

7.6 Summary

When the single main rotor state space models of inflow were utilized in HeliUM, they produced similar coning responses to that of the full MFW model, and matched closely with coning responses produced with Pitt-Peters inflow model. In

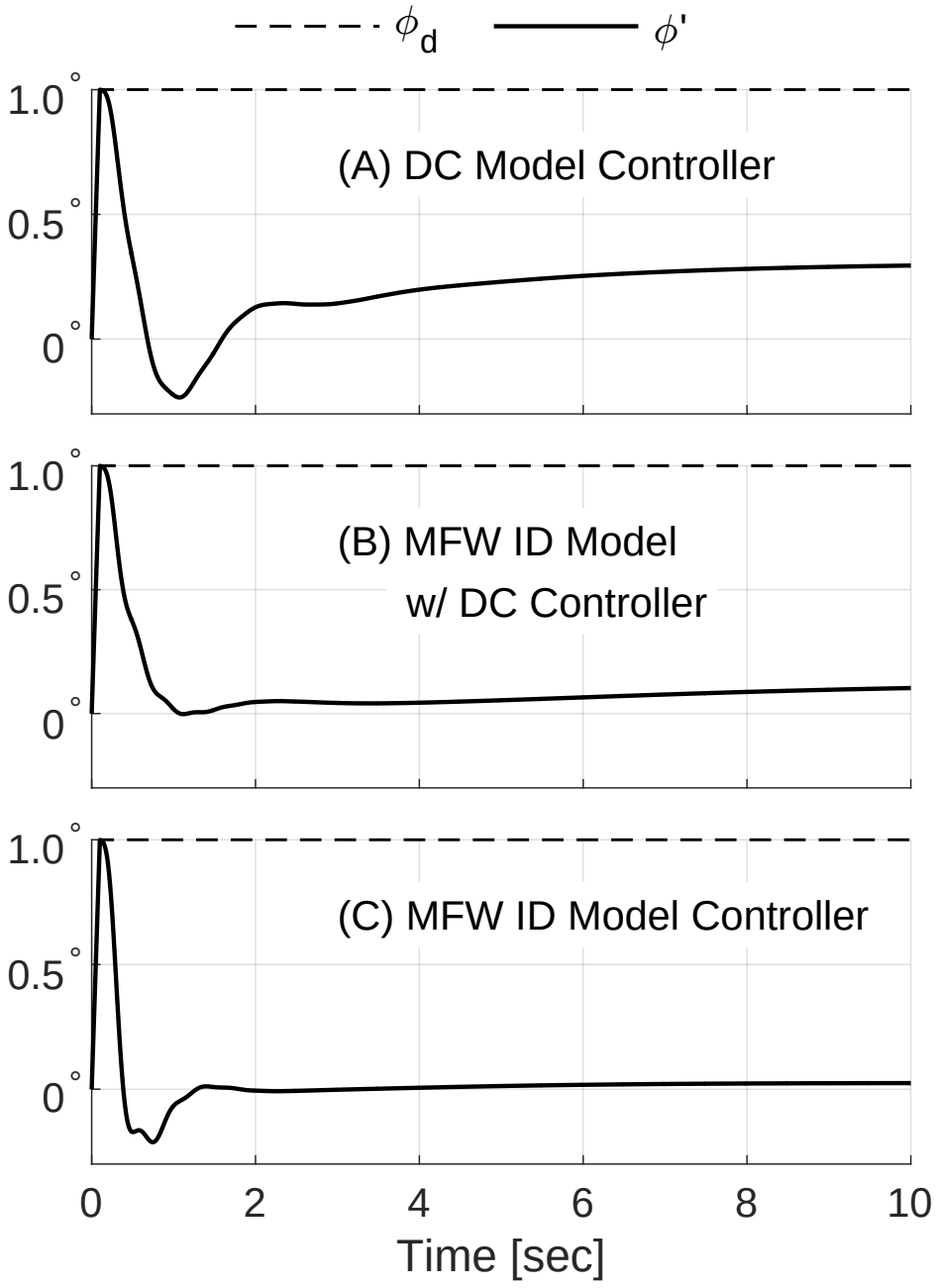

Figure 7.18: Step Disturbance in ϕ for different models

particular, the state space model from MFW differentiated itself from the static inflow model, and produced the behavior that inflow dynamics are well known to provide.

The lower order identified state-space model for a coaxial was then used in a full aircraft simulation. Comparisons of the predicted aircraft response to controls using the identified state space model and a simple Climbing Lower Rotor model were given. The results show that for the heave and yaw responses, the inflow models predicted very similar behavior. The responses to pitch and roll inputs show quite different responses, indicating that a more complex model with rotor-rotor interactions is needed to properly predict the aircraft behavior.

A need for a higher-order model of inflow was seen for coaxial rotors in Chapter. 5, and was then identified in Chapter. 6, for both hover and forward flight. After being combined with a flight dynamics solution, rotorcraft responses were compared using this identified model and a momentum-based approaches. For forward flight, the model was compared against an assumption typically made for coaxial in high speed flight, i.e. that the rotors do not interfere with eachother and can therefore be modeled as isolated rotors. In hover, the identified state-space model was used to create and aircraft model that was compared against an aircraft model created using a momentum-based inflow model with dynamic interference. These results showed that the identified state-space models have a significant impact on the overall flight dynamics of the aircraft.

Using these two hover aircraft models, Explicit model-following controllers, which are a common, well vetted approach, were created, and the controller for the momentum-based approach was applied to the free-wake identified model in order to evaluate its shortcomings. The free-wake identified inflow model enables a more aggressive control system design. The regressive flap mode is more damped, opening

the control system design space. This led to an over 50% increase in the crossover frequency when using the free-wake identified inflow model, as well as drastically improved disturbance rejection and steady-state tracking.

Chapter 8: Conclusions and Recommendations

8.1 Conclusions

The main conclusion of the research described in this dissertation is that frequency domain system identification is a new, effective technique for the extraction of mathematical models of rotor wake dynamics in state-space form, i.e., in the form of Ordinary Differential Equations (ODEs), from any kind of aerodynamic model not in state-space form. The availability of wake models in this specific mathematical form is a key ingredient for the study of the flight dynamic characteristics of rotorcraft, and for the design of flight control systems, and it was a largely unmet need, especially for advanced rotor configurations such as coaxial rotors. The research described in the dissertation largely closes this important practical gap, and this is its most significant contribution to the state-of-the-art.

Additional comments and conclusions from this study are:

1. For the configurations for which state-space wake models were already available, such as for single main rotor configurations, there was generally good agreement between these models and those extracted from systems identification. At the frequencies at the upper end of the range of interest for flight

dynamics, i.e., 10-15 rad/sec, good agreement required including additional dynamics beyond constant and first harmonics of the inflow, either in the form of additional states or as additional time delays.

2. It is possible to extract low order inflow models for both single and coaxial rotors that match very well the inflow responses to aerodynamic loading predicted by a full, nonlinear free vortex wake, both in the time and in the frequency domains. Not only are these models accurate, but they are also computationally very efficient, and therefore are suitable for real-time applications such as pilot-in-the-loop simulation.

3. For closely spaced coaxials, the aerodynamic couplings between the rotors are strong not only in hover, but also in forward flight, including high speed flight. The traditional simplifying assumption that at high speed the rotor wake will be quickly swept away by the free stream, and that the two rotors will behave as isolated rotors, is not necessarily valid and needs to be verified for each individual case. Similarly, it is not necessarily true that the direction of the flow will be from upper to lower rotor, especially for configurations with auxiliary propulsion at high speed.

4. The nature of the coaxial identification problem, where the physical inputs to the swashplate generate two outputs, aerodynamic loads and inflow harmonics, the first of which becomes the input of the identification, leads to strong input correlation. The traditional approach to removing the correlation, based on the use of crossfeeds, was impractical because of the large number of input-

output pairs and the extent of the correlation. A new approach, developed as part of this research (and later rediscovered in earlier signal processing literature as the "joint input-output" method) proved easier to use, computationally less demanding, and of very broad applicability.

5. For coaxial rotors, the relationship between the aerodynamic loading input and the inflow harmonic output was linear, as clearly indicated by a coherence essentially equal to 1 for most frequencies of interest. This result was rather unexpected because of the strong nonlinearities of the free wake model and the complexity of the coupled flow field. Even though it might not hold for all possible rotor configurations and flight conditions, this conclusion is especially interesting.

6. Because the inflow state-space models were extracted from free wake models that contained the physics of wake geometry distortion, they also correctly modeled the effects of distortion due to angular body rates or blade flapping on inflow dynamics in hover and low speed flight. For single main rotors, these effects are generally captured by a constant parameter often denoted with K_R. Not only was this parameter recovered in the identified state-space model, with an average value in good agreement with the literature, but it was discovered for the first time that K_R is actually frequency-dependent and, in a sense, it has its own dynamics.

7. Somewhat surprisingly, the effects of wake geometry distortion on inflow dynamics mentioned above are present in coaxial configurations as well, and can

be significant. Clearly, the presence of the wakes of two counter-rotating rotors does not lead to cancellation of these effects. They were correctly captured by the identified state-space models.

8. A 6-state coaxial inflow model, i.e., the natural extension of 3-state single rotor models, is not sufficiently accurate to properly match the response predicted by a full nonlinear free wake simulation. Instead, a 12-state model, in which (with a somewhat arbitrary interpretation) each inflow state is allowed a second order dynamics, or a split between a near- and a far-wake contribution, provides a much better match with the free wake response in the range of frequencies of interest for flight dynamics and control.

9. With the free vortex model used in this study it was straightforward to compute the velocity induced by the rotor at any point of the flow field. Therefore, it was possible to apply the same methodology to the extraction of inflow dynamic models at arbitrary points, such as the horizontal tail and a point representative of the fuselage. Simple models consisting of constants and time delays applied to rotor inflow, with no additional dynamics, proved quite adequate to model the low frequency rotor effects on tail and fuselage.

10. As far as the predicted flight dynamics characteristics of a coaxial rotorcraft configuration are concerned, there are considerable differences between the second-order inflow model identified in the present study, and a simplified dynamic inflow model based on momentum theory, in which each rotor is modeled independently, and with a climb velocity meant to approximate rotor-

rotor aerodynamic interference. The latter model, referred to as the "dynamic climb model" in the present study, is attractive for its simplicity, and it has been used in some industry studies, but its predictions are not accurate enough, compared with those of a free vortex wake model.

11. The use of the simpler dynamic climb inflow model in the full aircraft simulation leads to flight control designs that are too conservative, compared with the identified state space models. Higher performance controllers can be obtained when the latter are used. The results presented in this dissertation also show degradation in performance of the high-fidelity model when a momentum-based model is used for control system design.

12. Because of the strong rotor-rotor couplings, the extraction of even a low order coaxial inflow model required the identification of a large number of parameters. The limit of 100 parameters was due to the specific system identification software used. The identification problem solved for this research was significantly larger than most, if not all, rotorcraft problem solved in the past. Still, the basic approach of identifying initially a large number of parameters, and then reducing the number using metrics such as insensitivities and Cramer-Rao bounds, remained very effective even at this larger scale. The resulting state-space model was accurate and not over parameterized.

8.2 Recommendations

The development of the methodology described in this dissertation required that certain assumptions be made, which should addressed in future research. Other limitations of the state-of-the-art and ideas for future work were also identified, and are listed below.

1. There is currently a very critical gap in the state-of-the-art of inflow dynamic modeling, namely, the nearly complete absence of inflow measurements in dynamic conditions. This is true for any rotor configuration and any flight condition. Inflow dynamics can be to some extent reconstructed from blade dynamic measurements, but this can provide only an indirect, partial validation. As a consequence, the inflow models generated as part of this research could not be validated by comparison with experimental results.

2. Only a small number of flight conditions were considered in this study. While these conditions were adequate for the development of the methodology, it would be very interesting to extend the spectrum to study, for example, effects of parameters such as disk loading C_T/σ, flight path angle γ, and turn rate $\dot{\psi}$. The effects of design parameters such as rotor spacing, number of blades, twist, radius, and angular velocity could also be studied systematically.

3. Inflow models in state-space form are generally based on small perturbation equations such as the acceleration potential equations, and therefore have some intrinsic theoretical limitations. Their validity can sometimes be ex-

tended through the use of ad-hoc empirical or theoretical corrections. The methodology developed in this dissertation is applicable without limitation to any flow field, as long as the aerodynamic model from which the inflow model is extracted contains the required physics. Therefore, for example, it would be possible for the first time to extract state-space models that contain the physics of rotor-fuselage or rotor-wing interaction, ground effect, high rate of descent flight including the vortex ring state, autorotation, and of any type of maneuver. It would be very interesting to explore such conditions. In some of these conditions, a linear inflow model may not be adequate, however the examination of the coherence of the response will help assess the accuracy of the model.

4. The input to all inflow models of the study were the aerodynamic thrust and moment components. This was done to maintain a measure of compatibility with the inflow dynamics theories commonly used by the rotorcraft community. However, this is not the only possible set of inputs. Alternate types, such as swashplate inputs and rotor and body states, alone or in combination, could also be explored.

5. The range of frequencies studied in this dissertation was that of interest for flight dynamics and control, i.e., typically well below 1/rev, and often even below 0.5/rev. The same methodology could be applied at a higher frequency range, i.e., that of interest for rotor aeroelastic stability and response, where

availability of accurate inflow models in state-space form is also very limited, especially for advanced rotor configurations.

6. The identification methodology was applied in this study to a free vortex wake model, but it is completely general, and applicable to any aerodynamic model from which a time history can be computed. Therefore, it would be interesting to apply to state-of-the-art high fidelity CFD solvers. Since the computational effort required to simulate the several hundred revolutions needed for the identification could still be prohibitive at this time, it would be worth exploring approaches that reduce computer time, such carrying out the identification on a small number of isolated frequencies, instead of a full sweep, or somehow blending the CFD-based method with a less computationally demanding method.

7. The system identification procedure used in this study, especially in the more complex cases such as the identification of a coaxial inflow model in forward flight, required a nontrivial amount of trial-and-error to reduce the number of parameters and avoid overparameterization. It would be beneficial to devise techniques to automate this process as much as possible, also to make the entire methodology more accessible to individuals with a limited systems identification background. Several recent machine learning techniques appear promising, and could be explored.

Appendix A: Derivation of Linearized Perturbation Analysis

For the purposes of linearized analysis (and also transient analysis), the equations of motion for a helicopter can be written as:

$$f(\dot{\boldsymbol{y}}, \boldsymbol{y}, \boldsymbol{u}, t) = 0 \tag{A.1}$$

For trim, the condition is denoted with a subscript $(...)_0$ and the equation is written as:

$$f(\dot{\boldsymbol{y}}_0, \boldsymbol{y}_0, \boldsymbol{u}_0, t) = 0 \tag{A.2}$$

Expanding Eq. (A.1) with a Taylor Series expansion gives:

$$f(\dot{\boldsymbol{y}}_0, \boldsymbol{y}_0, \boldsymbol{u}_0, t) + \left.\frac{\partial f}{\partial \dot{\boldsymbol{y}}}\right|_0 \Delta\dot{\boldsymbol{y}} + \left.\frac{\partial f}{\partial \boldsymbol{y}}\right|_0 \Delta\boldsymbol{y} + \left.\frac{\partial f}{\partial \boldsymbol{u}}\right|_0 \Delta\boldsymbol{u} + \mathcal{O}(\|\Delta\dot{\boldsymbol{y}}\|^2, \|\Delta\boldsymbol{y}\|^2, \|\Delta\boldsymbol{u}\|^2) = 0 \tag{A.3}$$

Where:

$$\Delta\dot{\boldsymbol{y}} = \dot{\boldsymbol{y}} - \dot{\boldsymbol{y}}_0, \qquad \Delta\boldsymbol{y} = \boldsymbol{y} - \boldsymbol{y}_0, \qquad \Delta\boldsymbol{u} = \boldsymbol{u} - \boldsymbol{u}_0 \tag{A.4}$$

The three partial derivatives shown in Eq. (A.1) are the partial derivatives of f with respect to the state derivatives, the states, and the controls. These can be approximated through finite difference calculations where a perturbation to one of

either the states derivatives, states, or controls from trim is calculated and the resulting f perturbation can be used to calculate the partial derivative as:

$$\begin{aligned}
\frac{\partial f}{\partial \dot{\boldsymbol{y}}} &\approx \frac{f(\dot{\boldsymbol{y}}_0 + \Delta\dot{\boldsymbol{y}}, \boldsymbol{y}_0, \boldsymbol{u}_0, t) - f(\dot{\boldsymbol{y}}_0, \boldsymbol{y}_0, \boldsymbol{u}_0, t)}{\Delta\dot{\boldsymbol{y}}} && \text{state derivative perturbations} \\
\frac{\partial f}{\partial \boldsymbol{y}} &\approx \frac{f(\dot{\boldsymbol{y}}_0, \boldsymbol{y}_0 + \Delta\boldsymbol{y}, \boldsymbol{u}_0, t) - f(\dot{\boldsymbol{y}}_0, \boldsymbol{y}_0, \boldsymbol{u}_0, t)}{\Delta\boldsymbol{y}} && \text{state perturbations} \\
\frac{\partial f}{\partial \dot{\boldsymbol{u}}} &\approx \frac{f(\dot{\boldsymbol{y}}_0, \boldsymbol{y}_0, \boldsymbol{u}_0 + \Delta\boldsymbol{u}, t) - f(\dot{\boldsymbol{y}}_0, \boldsymbol{y}_0, \boldsymbol{u}_0, t)}{\Delta\boldsymbol{u}} && \text{control perturbations}
\end{aligned} \tag{A.5}$$

The second order and higher terms in the Taylor Series (Eq. (A.3)) are truncated and the resultant linearized model equation is:

$$\left.\frac{\partial f}{\partial \dot{\boldsymbol{y}}}\right|_0 \Delta\dot{\boldsymbol{y}} + \left.\frac{\partial f}{\partial \boldsymbol{y}}\right|_0 \Delta\boldsymbol{y} + \left.\frac{\partial f}{\partial \boldsymbol{u}}\right|_0 \Delta\boldsymbol{u} = 0 \tag{A.6}$$

Define the following matrices:

$$[E(t)] \stackrel{\text{def}}{=} \left.\frac{\partial f}{\partial \dot{\boldsymbol{y}}}\right|_0, \qquad [F(t)] \stackrel{\text{def}}{=} \left.\frac{\partial f}{\partial \boldsymbol{y}}\right|_0, \qquad [G(t)] \stackrel{\text{def}}{=} \left.\frac{\partial f}{\partial \boldsymbol{u}}\right|_0 \tag{A.7}$$

And now rearrange to obtain:

$$\begin{aligned}
\Delta\dot{\boldsymbol{y}} &= -[E(t)]^{-1}[F(t)]\Delta\boldsymbol{y} - [E(t)]^{-1}[G(t)]\Delta\boldsymbol{u} \\
&= [A(t)]\Delta\boldsymbol{y} + [B(t)]\Delta\boldsymbol{u}
\end{aligned} \tag{A.8}$$

In general, the equations are time-varying and periodic. The rotor portion is particularly periodic and therefore the rotor portions of the state vector and of the linearized matrices must be transformed to the body fixed non-rotating frame, resulting in a linearized system that is written entirely in a non-rotating system. This removes most but not all of the time dependency, so the remainder is removed by averaging the $[A(t)]$ and $[B(t)]$ matrices around one rotor revolution to obtain the constant $[A]$ and $[B]$ in Eq. (1.1).

Appendix B: Rotorcraft Configurations

B.1 Single Main Rotor Model

The rotor configuration used in the present study is broadly representative of the main rotor of a Sikorsky UH-60 [119]. The aricraft weighs 17150 lbs, which corresponds to the rotor initially being trimmed to a nominal $C_T = .0061$ at sea level, and in standard atmosphere. The 4 bladed rotor has a radius of 26.83 feet and a rotor speed of $\Omega = \Omega_0 = 27$ rad/sec. The blades are assumed to be uniform with no spanwise airfoil variation, no cross-sectional offsets, a total linear twist of 17° and a rectangular tip. The chord is a constant value of 1.73 ft, giving a solidity of $\sigma = 0.0821$, and therefore a disk loading $C_T/\sigma = 0.0740$. Each blade is modeled with 4 flexible finite elements, each of which has 8 Gaussian quadrature points at which aerodynamic and inertial loads are calculated. There is a flap, lag, and pitch hinge modeled at 1.25 feet from the blade root. The first 3.83 feet after the hinge are considered a spar which produce no lift or pitching moment, but does produce a drag coefficient of $C_D = 0.05$. The remainder of the blade produces lift, drag and pitching moment based on airfoil tables obtained for the SC1095 airfoil. The tail rotor is modeled as a Bailey momentum theory type rotor [131] with a radius of 6.6

ft. and a rotational speed of 136 rad/sec. Fuselage and empennage aerodynamics are modeled as found in Ref. 119.

The MFW results were obtained using tip trailed vortex filaments discretized with straight segments of length $\Delta\psi = 10°$, with the length of each filament equal to six rotor revolutions or 2160°. Shed vorticity was neglected.

B.2 Coaxial Aircraft Model

A coaxial aircraft model was developed to be utilized for the extraction of coaxial inflow models. Gross sizing and rotor geometry data of the aircraft come from the "regression" military model found in Ref. 129. Blade structural and mass properties were scaled using data from the Sikorsky XH-59 Advancing Blade Concept [83] so that the 1st lag and flap modes match those of the ABC, roughly 1.3/rev for lag and 1.5/rev for flap. The same airfoils were used as in the XH-59 [83].

Fuselage and empennage component sizes and locations are based on Ref. 129, but the aircraft has been shortened to be more consistent with publicly available images of modern coaxial-pusher aircraft, such as the Sikorsky X2 Technology^{TM} Demonstrator [38]. General fuselage aerodynamics also come from Ref. 129. Look-up tables for horizontal and vertical stabilizer aerodynamics are based on wind-tunnel data obtained for the XV-15 [130] and contain effects of elevator and rudder deflection, respectively. However, the lack of free-stream velocity in hover means that the fuselage and stabilizers are essentially inactive for this chapter's results, but will come into effect in Chap. 5. The pusher-propeller is modeled as a Bailey

momentum theory type rotor [131]. The aerodynamic interference between the pusher propeller and the coaxial rotor and the fuselage was neglected. Propeller radius was 6.6 ft. and rotational speed 136 rad/s. The propeller was assumed to generate only a force directed along the x-body axis of the aircraft, and a torque about the same axis. In hover, the pusher is assumed to be inactive. In forward flight, the propeller thrust provides a key control redundancy allowing the aircraft to trim to a desired angle of attack. The final configuration is shown in Fig. B.1 and key sizing data is found in Table B.1.

Figure B.1: Generic coaxial aircraft model (modified from original found in Ref. 132)

Table B.1: Coaxial aircraft characteristics

Characteristic	English	Metric
Gross Weight	35,185 lb	15,960 kg
# Rotors	2	
Rotor Radius	30.55 ft	9.31 m
Hover Rotor Ω	23.7 rad/sec	
Forward Flight Rotor Ω	20.3 rad/sec	
Rotor Spacing	14% of Radius	
# Blades per Rotor	4	
Blade Weight	1133 lb	513 kg
1st Flap Freq.	1.5/rev	

Bibliography

[1] Cheney, M. C., "The ABC Helicopter," *Journal of the American Helicopter Society*, Vol. 14, (4), Oct 1969, pp. 10–19.

[2] Paglino, V. M., "Forward Flight Performance of a Coaxial Rigid Rotor," American Helicopter Society 27th Annual Forum, Washington, D.C., May 1971.

[3] Blackwell, R., and Millott, T., "Dynamics Design Characteristics of the Sikorsky X2 Technology™ Demonstrator Aircraft," American Helicopter Society 64th Annual Forum, Montreal, Quebec, May 2008.

[4] Walsh, D., Weiner, S., Bagai, A., Lawrence, T., and Blackwell, R., "Development Testing of the Sikorsky X2 Technology™ Demonstrator," American Helicopter Society 65th Annual Forum, Grapevine, TX, May 2009.

[5] Walsh, D., Weiner, S., Arifian, K., Lawrence, T., Wilson, S., Millott, T., and Blackwell, R., "High Airspeed Testing of the Sikorsky X2 Technology™ Demonstrator," American Helicopter Society 67th Annual Forum, Virginia Beach, VA, May 2011.

[6] Lorber, P. F., Law, G. K., O'Neill, J. J., Matalanis, C., and Bowles, P., "Overview of S-97 Raider™ Scale Model Tests," American Helicopter Society 72nd Annual Forum, West Palm Beach, FL, May 2016.

[7] Lorber, P., Bowles, P., Fox, E., Wang, Z. K., Hein, B., and Mayrides, B., "Wind Tunnel Testing for the SB>1 Defiant™ Joint Multi-Role Technology Demonstrator," American Helicopter Society 73rd Annual Forum, Fort Worth, TX, May 2017.

[8] Harrington, R. D., "Full-scale-tunnel Investigation of the Static-thrust Performance of a Coaxial Helicopter Rotor," NACA TN 2318, Mar 1951.

[9] Dingeldein, R. C., "Wind-tunnel Studies of the Performance of Multirotor Configurations," NACA TN 3236, Aug 1954.

[10] Payne, P. R., *Helicopter Dynamics and Aerodynamics*, Macmillan, New York, NY, 1959, pp. 90–98.

[11] Sweet, G. E., "Static Stability Measurements of a Stand-on Type Helicopter with Rigid Blades, including a Comparison with Theory," NASA TN D-189, 1960.

[12] Leishman, J. G., *Principles of Helicopter Aerodynamics*, Cambridge University Press, New York, NY, second edition, 2006.

[13] Leishman, J. G., and Syal, M., "Figure of Merit Definition for Coaxial Rotors," *Journal of the American Helicopter Society*, Vol. 53, (3), 2008, pp. 290.
doi: 10.4050/JAHS.53.290

[14] Leishman, J. G., and Ananthan, S., "An Optimum Coaxial Rotor System for Axial Flight," *Journal of the American Helicopter Society*, Vol. 53, (4), 2008, pp. 366.
doi: 10.4050/JAHS.53.366

[15] Johnson, W., *Rotorcraft Aeromechanics*, Cambridge Aerospace Series, Cambridge University Press, Cambridge, United Kingdom, 2013, pp. 112–115.

[16] Nagashima, T., and Nakanishi, K., "Optimum Performance and Wake Geometry of a Co-axial rotor in Hover," *Vertica*, Vol. 7, (3), 1983, pp. 225–239.

[17] Valkov, T., "Aerodynamic Loads Computation on Coaxial Hingeless Helicopter Rotors," 28th AIAA Aerospace Sciences Meeting, Reno, Nevada, Jan 1990.
doi: 10.2514/6.1990-70

[18] Bourtsev, B., Kvokov, V., Vainsein, I., and Petrosian, E., "Phenomenon of a Coaxial Helicopter High Figure of Merit at Hover," 23rd European Rotorcraft Forum, Dresden, Germany, 1997.

[19] Rand, O., and Khromov, V., "Optimal Aerodynamic Design of a Coaxial Rotor System in Hover and Axial Flight," American Helicopter Society 66th Annual Forum, Phoenix, AZ, May 2010.

[20] Juhasz, O., Syal, M., Celi, R., Khromov, V., Rand, O., Ruzicka, G. C., and Strawn, R. C., "Comparison of Three Coaxial Aerodynamic Prediction Methods Including Validation with Model Test Data," *Journal of the American Helicopter Society*, Vol. 59, (3), Jul 2010.

[21] Carpenter, P. J., and Friedovich, B., "Effect of a Rapid Blade-Pitch Increase on the Thrust and Induced-Velocity Response of a Full-Scale Helicopter Rotor," NACA TN 3044, 1953.

[22] Johnson, W., "Feasibility Investigation of General Time-Domain Unsteady Aerodynamics of Rotors," NASA CR 177570, Oct 1990.

[23] Betoney, P., Celi, R., and Leishman, J. G., "Development of a Free-vortex Wake Model in State-space Form," 35th European Rotorcraft Forum, Hamburg, Germany, Sep 2009.

[24] Betoney, P., Celi, R., and Leishman, J. G., "The State-Space Free-Vortex Wake: A Control-Oriented Model," American Helicopter Society 66th Annual Forum, May 2010.

[25] Pitt, D. M., and Peters, D. A., "Theoretical Prediction of Dynamic Inflow Derivatives," *Vertica*, Vol. 5, (1), 1981, pp. 21–34.

[26] Peters, D. A., and HaQuang, N., "Dynamic Inflow for Practical Applications," *Journal of the American Helicopter Society*, Vol. 33, (4), Oct 1988, pp. 64–68.

[27] Gaonkar, G., and Peters, D., "Review of Dynamic Inflow Modeling for Rotorcraft Flight Dynamics," 27th Structures, Structural Dynamics and Materials Conference, San Antonio, TX, May 1986.
doi: 10.2514/6.1986-845

[28] Peters, D. A., Boyd, D. D., and He, C. J., "Finite-State Induced-Flow Model for Rotors in Hover and Forward Flight," *Journal of the American Helicopter Society*, Vol. 34, (4), Oct 1989, pp. 5–17.
doi: 10.4050/JAHS.34.5

[29] Peters, D. A., and He, C. J., "Correlation of Measured Induced Velocities with a Finite-State Wake Model," *Journal of the American Helicopter Society*, Vol. 36, (3), Jul 1991, pp. 59–70.

[30] Prasad, J. V. R., Nowak, M., and Xin, H., "Finite State Inflow Models for a Coaxial Rotor in Hover," 38th European Rotorcraft Forum, Amsterdam, Netherlands, Sep 2012.

[31] Morillo, J. A., and Peters, D. A., "Convergence of a Complete Finite-State Inflow Model of a Rotor Flow Field," 28th European Rotorcraft Forum, Bristol, England, Sep 2002.

[32] McAlister, K. W., and Tung, C., "Experimental Study of a Hovering Coaxial Rotor with Highly Twisted Blades," American Helicopter Society 64th Annual Forum, Montreal, Quebec, May 2008.

[33] Nowak, M., Prasad, J. V. R., and Peters, D. A., "Development of a Finite State Model for a Coaxial Rotor in Forward Flight," American Helicopter Society 70th Annual Forum, American Helicopter Society 70th Annual Forum, Montreal, Quebec, May 2014.

[34] Xin, H., Goss, J., and Parkes, C., "Development of a Three-State Rotor Interference Model and Application to Coaxial Rotor Inflow Modeling," Fifth Decennial AHS Aeromechanics Specialists' Conference, San Francisco, CA, Jan 2014.

[35] Yong-Boon, K., Prasad, J., Sankar, L., and Kim, J., "Finite State Coaxial Rotor Inflow Model Improvements via System Identification," American Helicopter Society 72nd Annual Forum, West Palm Beach, FL, May 2016.

[36] Prasad, J. V. R., Kong, Y.-B., and Peters, D., "Analytical Methods for Modeling Inflow Dynamics of a Coaxial Rotor System," 42nd European Rotorcraft Forum, Lille, France, Sep 2016.

[37] Yong-Boon, K., Prasad, J. V. R., and Peters, D., "Development of a Finite State Dynamic Inflow Model for Coaxial Rotor using Analytical Methods," American Helicopter Society 73rd Annual Forum, American Helicopter Society 73rd Annual Forum, Fort Worth, TX, May 2017.

[38] Fegely, C., Field, M., Tischler, M. B., and Field, M., "Flight Dynamics and Control Modeling with System Identification Validation of the Sikorsky X2 Technology^{TM} Demonstrator," American Helicopter Society 72nd Annual Forum, West Palm Beach, FL, May 2016.

[39] Saito, S., and Azuma, A., "A Numerical Approach to Co-Axial Rotor Aerodynamics," Seventh European Rotorcraft and Powered Lift Aircraft Forum, Garmisch-Partenkirchen, Germany, 1981.

[40] Andrew, M. J., "Coaxial Rotor Aerodynamics in Hover," *Vertica*, Vol. 5, 1981, pp. 163–172.

[41] Zimmer, H., "The Aerodynamic Calculation of Counter Rotating Coaxial Rotors," Eleventh European Rotorcraft Forum, London, England, 1985.

[42] Bagai, A., and Leishman, J. G., "Free-Wake Analysis of Tandem, Tilt-Rotor and Coaxial Rotor Configurations," *Journal of American Helicopter Society*, Vol. 41, (3), 1996, pp. 196–207.

[43] Wachspress, D. A., and Quackenbush, T. R., "Impact of Rotor Design on Coaxial Rotor Performance, Wake Geometry and Noise," American Helicopter Society 62nd Annual Forum, May 2006.

[44] Lee, J., Yee, K., and Oh, S., "Numerical Investigation of Dual Rotors Using a Time-Marching Free-Wake Method," American Helicopter Society 64th Annual Forum, Vol. 64, Montreal, Quebec, May 2008.

[45] Lim, J. W., Mcalister, K. W., and Johnson, W., "Hover Performance Correlation for Full-Scale and Model-Scale Coaxial Rotors," *Journal of the American Helicopter Society*, Vol. 54, 2009, pp. 32005.
doi: 10.4050/JAHS.54.032005

[46] Belotserkovskiy, S., and Loktev, B., "Computer Simulation of Unsteady Flow Past Lifting Rotors of Coaxial Configuration," *Doklady akademii nauk SSSR*, Vol. 256, (4), 1981, pp. 810–814.

[47] Burtsev, B. N., "Aeroelasticity of a Coaxial Helicopter Rotor," 17th European Rotorcraft Forum, Berlin, Germany, 1991.

[48] Kim, H. W., and Brown, R. E., "Coaxial Rotor Performance and Wake Dynamics in Steady and Manoeuvring Flight," American Helicopter Society 62nd Annual Forum, Phoenix, AZ, May 2006.

[49] Rajmohan, N., Zhao, J., and He, C., "A Coupled Vortex Particle / CFD Methodology for Studying Coaxial Rotor Configurations," Fifth Decennial AHS Aeromechanics Specialists' Conference, San Francisco, CA, Jan 2014.

[50] Singh, P., and Friedmann, P. P., "Application of Vortex Methods to Coaxial Rotor Wake and Load Calculations in Hover," *Journal of Aircraft*, Vol. 55, (1), Jan 2018, pp. 373–381.
doi: 10.2514/1.C034520

[51] Cameron, C. G., Karpatne, A., and Sirohi, J., "Performance of a Mach-Scale Coaxial Counter-Rotating Rotor in Hover," *Journal of Aircraft*, Vol. 53, (3), May 2016, pp. 746–755.
doi: 10.2514/1.C033442

[52] Lakshminarayan, V. K., and Baeder, J. D., "High-Resolution Computational Investigation of Trimmed Coaxial Rotor Aerodynamics in Hover," *Journal of the American Helicopter Society*, Vol. 54, (4), 2009, pp. 042008.
doi: 10.4050/JAHS.54.042008

[53] Ruzicka, G. C., and Strawn, R. C., "Computational Fluid Dynamics Analysis of a Coaxial Rotor Using Overset Grids," AHS Specialists Conference on Aeromechanics, San Francisco, CA, Jan 2008.

[54] Singh, R., and Kang, H., "Computational Investigations of Transient Loads and Blade Deformations on Coaxial Rotor Systems," 33rd AIAA Applied Aerodynamics Conference, Dallas, TX, Jun 2015.
doi: 10.2514/6.2015-2884

[55] Singh, R., Kang, H., Cameron, C., and Sirohi, J., "Computational and Experimental Investigations of Coaxial Rotor Unsteady Loads," 54th AIAA Aerospace Sciences Meeting, San Diego, California, Jan 2016.
doi: 10.2514/6.2016-1787

[56] Barbely, N. L., Field, M., Komerath, N. M., and Novak, L. A., "A Study of Coaxial Rotor Performance and Flow Field Characteristics," American Helicopter Society Technical Meeting on Aeromechanics Design for Vertical Lift, San Francisco, CA, Jan 2016.

[57] Cornelius, J. K., Kinzel, M. P., and Schmitz, S., "An Efficient CFD Approach for Co-Axial Rotor Simulations," AIAA Scitech 2019 Forum, San Diego, California, Jan 2019.
doi: 10.2514/6.2019-1658

[58] Feik, R. A., and Perrin, R. H., "Identification of an Adequate Model for Collective Response Dynamics of a Sea King Helicopter," *Vertica*, Vol. 13, (3), 1989, pp. 251–266.

[59] Blackwell, J., Feik, R. A., Perrin, R. H., and Blackwell, A. J., "Identification of Rotor Dynamic Effects in Flight Data," Fifteenth European Rotorcraft Forum, Amsterdam, Netherlands, Sep 1989.

[60] Houston, S. S., "Identification of a coupled body/coning/inflow model of Puma vertical response in the hover," *Vertica*, Vol. 13, (3), 1989, pp. 229–249.

[61] Houston, S. S., and Thomson, D. G., "Calculation of Rotorcraft Inflow Model Coefficients Using Blade Flapping Measurements," *Journal of Aircraft*, Vol. 46, (5), 2009, pp. 1569–1576.
doi: 10.2514/1.40540

[62] Tomashofski, C. A., and Tischler, M. B., "Flight Test Identification of SH–2G Dynamics in Support of Digital Flight Control System Development," American Helicopter Society 55th Annual Forum, Montreal, Canada, 1999.

[63] Tischler, M. B., and Remple, R. K., *Aircraft and Rotorcraft System Identification: Engineering Methods with Flight Test Examples—Second Edition*, AIAA, Reston, VA, 2012.

[64] Tischler, M. B., "Identification of Bearingless Main Rotor Dynamic Characteristics from Frequency-Response Wind-Tunnel Test Data," *Journal of the American Helicopter Society*, Vol. 44, (1), Jan 1999, pp. 63–76.
doi: 10.4050/JAHS.44.63

[65] Bhagwat, M. J., and Leishman, J. G., "Time-Accurate Modeling of Rotor Wakes Using A Free-Vortex Wake Method," 18th Applied Aerodynamics Conference, Denver, CO, Aug 2000.
doi: 10.2514/6.2000-4120

[66] Bhagwat, M. J., and Leishman, J. G., "Transient Rotor Inflow Using a Time-Accurate Free-Vortex Wake Model," 39th AIAA Aerospace Sciences Meeting & Exhibit, Reno, NV, Jan 2001.
doi: 10.2514/6.2001-993

[67] Ellenrieder, T. J., and Brinson, P. R., "Experimental Investigation of Helicopter Coning / Inflow Dynamics in Hover," Twentieth European Rotorcraft Forum, Amsterdam, Netherlands, Oct 1994.

[68] Ellenrieder, T. J., and Brinson, P. R., "The Dynamic Induced Velocity Field of a Model Rotor in Hover Conditions," *The Aeronautical Journal*, Vol. 102, (1016), 1998, pp. 331–336.
doi: 10.1017/S0001924000027573

[69] Vepa, R., "Finite State Modeling of Aeroelastic Systems," NASA CR 2779, Feb 1977.

[70] Edwards, J. W., Ashley, H., and Breakwell, J. V., "Unsteady Aerodynamic Modeling for Arbitrary Motions," *AIAA Journal*, Vol. 17, (4), 1979, pp. 365–374.
doi: 10.2514/3.7348

[71] Venkatesan, C., and Friedmann, P. P., "New approach to finite-state modeling of unsteady aerodynamics," *AIAA Journal*, Vol. 24, (12), Dec 1986, pp. 1889–1897.
doi: 10.2514/3.9545

[72] Liu, L., Padthe, A. K., Friedmann, P. P., Quon, E., and Smith, M. J., "Unsteady Aerodynamics of an Airfoil/Flap Combination on a Helicopter Rotor Using Computational Fluid Dynamics and Approximate Methods," *Journal of the American Helicopter Society*, Vol. 56, (3), Jul 2011, pp. 1–13.
doi: 10.4050/JAHS.56.032003

[73] Tran, C. T., and Petot, D., "Semi-empirical model for the dynamic stall of airfoils in view of the application to the calculation of responses of a helicopter in forward flight," *Vertica*, Vol. 5, Jan 1981, pp. 35–53.

[74] Gennaretti, M., Gori, R., Serafini, J., Bernardini, G., and Cardito, F., "Rotor Dynamic Wake Inflow Finite-State Modelling," 33rd AIAA Applied Aerodynamics Conference, Dallas, TX, Jun 2015.

[75] Cardito, F., Gori, R., Bernardini, G., Serafini, J., and Gennaretti, M., "Identification of Coaxial-Rotors Dynamic Wake Inflow for Flight Dynamics and Aeroelastic Applications," 42nd European Rotorcraft Forum, Lille, France, Sep 2016.

[76] Gennaretti, M., Gori, R., Serafini, J., Cardito, F., and Bernardini, G., "Identification of rotor wake inflow finite-state models for flight dynamics simulations," *CEAS Aeronautical Journal*, Vol. 8, (1), Mar 2017, pp. 209–230.

[77] Cardito, F., Gori, R., Bernardini, G., Serafini, J., and Gennaretti, M., "Finite-State Dynamic Wake Inflow Modelling for Coaxial Rotors," 41st European Rotorcraft Forum, Munich, Germany, Sep 2015.

[78] Cardito, F., Gori, R., Bernardini, G., Serafini, J., and Gennaretti, M., "State-space coaxial rotors inflow modelling derived from high-fidelity aerodynamic simulations," *CEAS Aeronautical Journal*, Vol. 9, (4), Dec 2018, pp. 587–606.
doi: 10.1007/s13272-018-0301-8

[79] He, C. J., Syal, M., Tischler, M. B., and Juhasz, O., "State-Space Inflow Model Identification from Viscous Vortex Particle Method for Advanced Rotorcraft Configurations," American Helicopter Society 73rd Annual Forum, Fort Worth, TX, May 2017.

[80] Keller, J. D., McKillip, R. M., Wachspress, D. A., Tischler, M. B., and Juhasz, O., "A Free Wake Linear Inflow Model Extraction Procedure for Rotorcraft Analysis," American Helicopter Society 73rd Annual Forum, Fort Worth, TX, May 2017.

[81] Keller, J. D., "An Investigation of Helicopter Dynamic Coupling Using an Analytical Model," *Journal of the American Helicopter Society*, Vol. 41, (4), Oct 1995, pp. 322–330.
doi: 10.4050/JAHS.41.322

[82] Arnold, U. T. P., Keller, J. D., Curtiss, H. C., and Reichert, G., "The Effect of Inflow Models on the Predicted Response of Helicopters," *Journal of the American Helicopter Society*, Vol. 43, (1), Jan 1998, pp. 25–36.
doi: 10.4050/JAHS.43.25

[83] Ruddell, A. J., "Advancing Blade Concept (ABC) Technology Demonstrator," USAAVRADCOM TR-81-D-5, Apr 1981.

[84] Bourtsev, B. N., Guendline, L. Y., and Selemenev, S. V., "Method and Examples for Calculation of Flight Path and Parameters While Performing Aerobatic Maneuvers by the KA-50 Helicopter Based on Flight Data Recorded Information," 24th European Rotorcraft Forum, Marseilles, France, Sep 1998.

[85] Mikheyev, S. V., Bourtsev, B. N., and Selemenev, S. V., "Ka-50 Attack Helicopter Acrobatic Flight," American Helicopter Society 55th Annual Forum, Montreal, Quebec, May 1999.

[86] Bourtsev, B. N., Selemenev, S. V., and Vagis, V. P., "Coaxial Helicopter Rotor Design & Aeromechanics," 25th European Rotorcraft Forum, Rome, Italy, Sep 1999.

[87] Ferguson, K., and Thomson, D., "Flight Dynamics Investigation of Compound Helicopter Configurations," *Journal of Aircraft*, Vol. 52, (1), 2015, pp. 156–167.
doi: 10.2514/1.C032657

[88] Wu, M., Chen, M., Wang, F., and Wang, Q., "Small-scale coaxial armed unmanned helicopter flight dynamics investigation," AIAA Modeling and Simulation Technologies Conference, Washington, D.C., Jun 2016.
doi: 10.2514/6.2016-3377

[89] Chang, C., Hasbun, M., Saberi, H., He, C., Lindsey, J., and Fortenbaugh, R., "Modeling and Simulation in Support of Handling Quality Evaluation of AVX Joint-Multi-Role (JMR) Coaxial Compound Helicopter (CCH)," American Helicopter Society 74th Annual Forum, Phoenix, AZ, May 2018.

[90] Anonymous, "Aeronautical Design Standard-33E-PRF, Performance Specification, Handling Qualities Requirements for Military Rotorcraft," US Army AMCOM, Mar 2000.

[91] Husnić, Ž., "Modelling the Micro Coaxial Helicopter," Advanced Technologies, Systems, and Applications II IAT 2017, Vol. 28, Banja Vrućica, Teslić, Bosnia and Herzegovina, May 2017.

[92] Fankhauser, P., Bouabdallah, S., Leutenegger, S., and Siegwart, R., "Modeling and Decoupling Control of the CoaX Micro Helicopter," IEEE International Conference on Intelligent Robots and Systems, San Francisco, CA, Sep 2011. doi: 10.1109/IROS.2011.6048352

[93] Lee, R., Sreenath, K., and Scherer, S., "Modeling and Control of Coaxial UAV with Swashplate Controlled Lower Propeller," Carnegie Mellon University Robotics Institue Technical Report 16-33, Pittsburgh, PA, 2016.

[94] Grip, H. F., Scharf, D. P., Malpica, C., Johnson, W., Mandic, M., Singh, G., and Young, L. A., "Guidance and Control for a Mars Helicopter," 2018 AIAA Guidance, Navigation, and Control Conference, Reston, Virginia, Jan 2018. doi: 10.2514/6.2018-1849

[95] Rand, O., Khromov, V., Hersey, S., Celi, R., Juhasz, O., and Tischler, M. B., "Linear Inflow Model Extraction from High-Fidelity Aerodynamic Models for Flight Dynamics Applications," American Helicopter Society 71st Annual Forum, Virginia Beach, VA, May 2015.

[96] Hersey, S., Celi, R., Juhasz, O., Tischler, M. M. B., Rand, O., and Khromov, V., "State-Space Inflow Model Identification and Flight Dynamics Coupling for an Advanced Coaxial Rotorcraft Configuration," American Helicopter Society 73rd Annual Forum, Fort Worth, TX, May 2017.

[97] Hersey, S., Celi, R., Juhasz, O., and Tischler, M. B., "Accurate State-Space Inflow Modeling for Flight Dynamics and Control of a Coaxial-Pusher Rotorcraft," AHS International 74th Annual Forum & Technology Display, Phoenix, AZ, May 2018.

[98] Celi, R., "HeliUM 2 Flight Dynamic Simulation Model: Developments, Technical Concepts, and Applications," American Helicopter Society 71st Annual Forum, Virginia Beach, Virginia, May 2015.

[99] Rosen, A., and Friedmann, P. P., "Nonlinear Equations of Equilibrium for Elastic Helicopter of Wind Turbine Blades Undergoing Moderate Deflections," NASA CR 159478, Dec 1978.

[100] Hodges, D. H., and Dowell, E. H., "Nonlinear equations of motion for the elastic bending and torsion of twisted nonuniform rotor blades," NASA Technical Note D-7818, 1974.

[101] Celi, R., "Helicopter Rotor Blade Aeroelasticity in Forward Flight with an Implicit Structural Operator," *AIAA Journal*, Vol. 30, (9), 1992.

[102] Johnson, W., *Helicopter Theory*, Princeton University Press, Princeton, NJ, 1980, pp. 808–813.

[103] Leishman, J. G., Bhagwat, M. J., and Bagai, A., "Free-Vortex Filament Methods for the Analysis of Helicopter Rotor Wakes," *Journal of Aircraft*, Vol. 39, (5), 2002.
doi: 10.2514/2.3022

[104] Truesdell, C., *The Kinematics of Vorticity*, Indiana University Publications Science Series No 19, Indiana University Press, Bloomington, IN, 1954.

[105] Weissinger, J., "The Lift Distribution of Swept-Back Wings," NACA TM 1120, 1947.

[106] Bhagwat M. J., and Leishman, J. G., "Accuracy of Straight-Line Segmentation Applied to Curvilinear Vortex Filaments," *Journal of the American Helicopter Society*, Vol. 46, (2), Apr 2001, pp. 166–169.

[107] Franklin G.F., Powell D.J., and Emani-Naeini, A., *Feedback Control of Dynamic Systems*, Prentice Hall, Upper Sadle River, NJ, fourth edition, 2002, pp. 331–334.

[108] Williams, R. L., and Lawrence, D. A., *Linear State-space Control Systems*, John Wiley & Sons, Hoboken, NJ, 2007, pp. 185–196.

[109] Joglekar, M., and Loewy, R., "An Actuator-Disc Analysis of Helicopter Wake Geometry and the Corresponding Blade Response," USAAVLABS Technical Report 69-66, Dec 1970.

[110] Takahashi, M. D., "A Flight-Dynamic Helicopter Mathematical Model with a Single Flap-Lag-Torsion Main Rotor," NASA TM 102267, 1990.

[111] Ballin, M. G., and Dalang-Secrétan, M.-A., "Validation of the Dynamic Response of a Blade-Element UH-60 Simulation Model in Hovering Flight," *Journal of the American Helicopter Society*, Vol. 36, (4), Jun 1990, pp. 77–88.
doi: doi:10.4050/JAHS.36.77

[112] Chaimovich, M., Rosen, A., Rand, O., Mansnr, M. H., and Tischler, M. B., "Investigation of the Flight Mechanics Simulation of a Hovering Helicopter," American Helicopter Society 48th Annual Forum, Washington, D.C., Jun 1992.

[113] Takahashi, M. D., Fletcher, J. W., and Tischler, M. B., "Development of a Model Following Control Law for Inflight Simulation Using Analytical and Identified Models," American Helicopter Society 51st Annual Forum, Fort Worth, TX, May 1995.

[114] Bendat, J. S., and Piersol, A. G., *Random Data: Analysis and Measurement Procedures*, John Wiley and Sons, Inc., second edition, 1986.

[115] Rabiner, L. R., Schafer, R. W., and Rader, C. M., "The Chirp z-Transform Algorithm and Its Application," *Bell System Technical Journal*, Vol. 48, (5), May 1969, pp. 1249–1292.
doi: 10.1002/j.1538-7305.1969.tb04268.x

[116] Bendat, J. S., and Piersol, A. G., *Engineering Applications of Correlation and Spectral Analysis*, Wiley, Hoboken, NJ, second edition, 1993, p. 458.

[117] Otnes, R. K., and Enochson, L., *Applied Time Series Analysis, Vol 1: Basic Techniques*, Wiley, New York, 1978.

[118] Bretthauer, G., "New Results for the Joint Input-Output Identification Method," *IFAC Proceedings Volumes*, Vol. 14, (2), Aug 1981, pp. 693–697.
doi: 10.1016/S1474-6670(17)63565-1

[119] Howlett, J. J., "UH-60A Black Hawk Engineering Simulation Program - Volume II - Mathematical Model," NASA CR 166309, Dec 1981.

[120] Chen, R. T. N., and Hindson, W. S., "Influence of Dynamic Inflow on the Helicopter Vertical Response," NASA TM 88327, Jun 1986.

[121] Stengel, R. F., *Optimal Control and Estimation*, Dover Publications, Inc., Mineola, NY, 1994.

[122] Tischler, M. B., Berger, T., Ivler, C. M., Mansur, M. H., Cheung, K. K., and Soong, J. Y., *Practical Methods for Aircraft and Rotorcraft Flight Control Design: An Optimization-Based Approach*, American Institute of Aeronautics and Astronautics, Inc., Washington, DC, Mar 2017.
doi: 10.2514/4.104435

[123] Landis, K. H., Davis, J. M., Dabundo, C., and Keller, J. F., "Advanced Flight Control Research and Development at Boeing Helicopters," *Advances in Aircraft Flight Control (M.B. Tischler Ed)*, Taylor and Francis, Philadelphia, PA, 1996.

[124] McRuer, D. T., Ashkenas, I. L., and Graham, D., *Aircraft Dynamics and Automatic Control*, Princeton University Press, Princeton, NJ, 1973.

[125] Magni, J.-F., Bennani, S., and Terlouw, J., *Robust Flight Control: A Design Challenge*, Vol. 224, Lecture Notes in Control and Information Sciences, Springer-Verlag Berlin Heidelberg, Berlin, Germany, 1997.
doi: 10.1007/BFb0113842

[126] Anonymous, "Flight Control Systems - Design, Installation, and Test of Piloted Aircraft, General Specifications for," MIL-DTL-9490E, Department of Defense Interface Standard, Feb 2006.

[127] Berger, T., Ivler, C., Berrios, M., Tischler, M., and Miller, D., "Disturbance Rejection Handling Qualities Criteria for Rotorcraft," American Helicopter Society 72nd Annual Forum, West Palm Beach, FL, May 2016.

[128] Duda, H., "Prediction of Pilot-in-the-Loop Oscillations due to Rate Saturation," *Journal of Guidance, Navigation, and Control*, Vol. 20, (3), 1997.

[129] Johnson, W., "A History of Rotorcraft Comprehensive Analyses," American Helicopter Society 69th Annual Forum, Phoenix, AZ, May 2013.

[130] Harendra, P. B., Joglekar, M. J., Gaffey, T. M., and Marr, R. L., "Final Report V/STOL Tilt Rotor Study - Volume V: A Mathematical Model for Real Time Flight Simulation of the Bell Model 301 Tilt Rotor Research Aircraft," NASA CR 114614, Apr 1973.

[131] Bailey Jr., F. J., "A Simplified Theoretical Method of Determining the Characteristics of a Lifting Rotor in Forward Flight," NACA TR 716, Jan 1941.

[132] Johnson, W., Moodie, A. M., and Yeo, H., "Design and Performance of Lift-Offset Rotorcraft for Short-Haul Missions," Vertical Lift Aircraft Design Conference, San Francisco, CA, Jan 2012.